Multi-mass imaging in chemical reaction dynamics



Hansjochen Köckert
Lincoln College
University of Oxford

A thesis submitted for the degree of
Doctor of Philosophy

Trinity Term, 2019

Multi-mass imaging in chemical reaction dynamics

Hansjochen Köckert, Lincoln College

A thesis submitted for the degree of Doctor of Philosophy

Trinity Term, 2019

The work described in this thesis illustrates the application of multi-mass velocity-map imaging in the investigation of molecular fragmentation dynamics. Results from three experiments, focussing on three types of fragmentation processes, are reported.

Firstly, a photofragmentation and photoionization study of niobium oxide (NbO) is presented. Analysis of the recorded velocity-map images yields refined values for the dissociation energies of NbO and NbO^+, which are found to be $60,650 \pm 124$ cm^{-1} and $57,414 \pm 124$ cm^{-1}, respectively. In addition, the first steps towards the study of charged metal-ligand clusters are outlined using the example of the photofragmentation of the VCO_2^+ complex.

In Chapter 3, the UV-induced photofragmentation dynamics of the CH_2BrI molecule are studied in a time-resolved UV-pump XUV-probe experiment. While the findings are largely consistent with previous studies on this system, evidence for charge transfer processes between the XUV ionized halogen photoproducts and neutral rotationally excited CH_2Br fragments are found.

Finally, Chapter 4 presents an experimental study of the dissociative electron ionization of CF_3I. Following the ionization step, dissociation of singly-charged parent ions proceeds *via* either the C-I bond or C-F bond breaking with very different dynamics. A mixture of 'statistical' and 'direct' bond breaking dynamics is observed, and can be rationalized by comparison with photoionization studies. Evidence for the fragmentation of doubly and triply charged ions is also found, with these processes apparently proceeding *via* a two-body Coulomb explosion followed by further fragmentation of the molecular product ion.

Publications

The following articles arising from this work have been published as follows.

(1) *Photodissociation Dynamics and the Dissociation Energy of Vanadium Monoxide, VO, Investigated using Velocity Map Imaging* A. S. Gentleman, A. Iskra, **H. Köckert** and S. R. Mackenzie, *Phys. Chem. Chem. Phys.* **2019**, 21, 15560-15567.

(2) *C–I and C–F bond-breaking dynamics in the dissociative electron ionization of CF_3I* **H. Köckert**, D. Heathcote, J. W. L. Lee, W. Zhou, V. Richardson and C. Vallance, *Phys. Chem. Chem. Phys.* **2019**, 21, 14296-14305.

(3) *Coulomb explosion imaging of CH_3I and CH_2ClI photodissociation dynamics* F. Allum, M. Burt, K. Amini, R. Boll, **H. Köckert**, [43], D. Rolles *J. Chem. Phys.* **2018**, 149, 204313.

(4) *Time-resolved inner-shell photoelectron spectroscopy: From a bound molecule to an isolated atom* F. Braße, G. Goldsztejn, [16], **H. Köckert**, [29], D. Rolles *Phys. Rev. A* **2018**, 97, 043429.

(5) *Coulomb-explosion imaging of concurrent CH_2BrI photodissociation dynamics* M. Burt, R. Boll, J. W. L. Lee, K. Amini, **H. Köckert**, [44], D. Rolles *Phys. Rev. A* **2017**, 96, 043415.

Furthermore, multiple publications based on the work presented in Chapter 3 and 4, and recent work not featured in this thesis including the investigating the photofragmentation dynamics of poly-aromatic hydrocarbons and development of three-dimensional covariance analysis in slice imaging velocity-map imaging experiments are currently in preparation.

Acknowledgements

This work was prepared in the research-groups of Prof Claire Vallance, Prof Mark Brouard and Prof Stuart Mackenzie and it would not have been possible without the support and companionship of each and every group member.

I would like to especially thank my three advisors for their enthusiasm for my project, and an endless stream of ideas, useful tips, and shared experiences. Additionally, I am very grateful to Dr Jason Lee, Dr Michael Burt and Dr Alexander Gentleman for their support inside and outside the lab.

During my work at Oxford Chemistry, I had the opportunity to work with the exceptional final year undergraduate students, David Heathcote, Vincent Richardson and Jack Pickering, and my work has greatly benefited from their dedication towards science.

I am very grateful to the members of the electronic and mechanical workshops, and the facility staff of the department of Chemistry. None of this work would have been possible without their experience and support in the construction and maintenance of my experiments.

I would like to express my gratitude to collaborators at the *Deutsches Elektronen Synchrotron* (DESY). During my DPhil work, I had the opportunity to work together with the research groups of Prof Daniel Rolles, Prof Artem Rudenko, Dr Rebecca Boll, Dr Tatiana Marchenko, Prof Melanie Schnell and Dr Sadia Bari. The work presented

in Chapter 3 benefitted considerably from long and detailed discussions with Rebecca and Daniel and I would like to thank them for their help and patience.

I am very grateful to Ethan Cunningham, Cornelia Heid, Shazeaa Ishmael, and Dean James for proof-reading my thesis. They greatly improved this work with their attention to detail.

I could never thank my friends and family enough for supporting me on every step along the way for the past four years. I particularly would like to thank Michael Ben-Yehuda, Kate Beare, Robert Burleigh, Ethan Cunningham, Shazeaa Ishmael and Dean James who gave me the strength to finish this work in the last few months.

I would like to thank the University of Oxford for funding my work with a Clarendon scholarship, and Lincoln College, Oxford, for financial support with their generous graduate research funds and senior scholarship award.

Contents

Page

1 Introduction **1**

1.1 The potential energy surface 1

1.2 Experimental methods 3

1.2.1 Molecular beams 4

1.2.2 The crossed beam experiment 11

1.2.3 Pump-probe spectroscopy 14

1.2.4 Universal and state selective ionization 23

1.2.5 Velocity-map imaging 27

1.2.6 Covariance imaging using the PImMS sensor 38

1.2.7 The pixel-imaging-mass-spectrometry sensor 42

1.3 Outline of the thesis 46

2 Photofragmentation of *d*-metal containing clusters and oxides **47**

2.1 Introduction 48

2.2 Experimental considerations 51

2.3 Analysis of velocity-map imaging data 57

2.4 Results and discussion 58

2.4.1 Photofragmentation dynamics of niobium oxide 58

2.4.2 Velocity-map imaging of photoelectrons 75

2.4.3 Photofragmentation dynamics of VCO_2^+ 85

2.5 Conclusion and outlook 89

3 Time-resolved imaging of the UV fragmentation dynamics in CH_2BrI 92

3.1 Introduction 93

3.2 Experimental considerations 95

3.3 Particularities of data analysis 101

3.3.1 Analysis of time-of-flight data 101

3.3.2 Analysis of velocity-map imaging data 103

3.3.3 Correction of pump-probe delay 105

3.3.4 Correction for XUV intensity fluctuations 109

3.4 Results and discussion 112

3.4.1 XUV-induced Coulomb explosion of CH_2BrI 112

3.4.2 Dissociative ionization of CH_2BrI with intense femtosecond UV laser pulses 126

3.4.3 UV dissociation dynamics probed with Coulomb explosion imaging 130

3.5 Conclusion and outlook 162

4 Velocity-map imaging of electron ionization products 165

4.1 Introduction 166

4.2 Experimental considerations 169

4.2.1 Modifications to the experimental set-up 171

4.3 Data analysis 176

4.3.1 Analysis of time-of-flight data 176

4.3.2 Analysis of velocity-map image data 178

4.4 Results and discussion 181

4.4.1 Partial ionization cross-sections 181

4.4.2 Velocity-map image data 184

4.4.3 Comparison to photoionization studies 199
4.5 Conclusion and outlook 203

5 Conclusion **206**

A Integration of the PImMS sensor at the FLASH1 beamline **223**

B Calculation of XUV photon numbers **228**

Chapter 1

Introduction

Understanding the fundamental molecular dynamics between reactants in chemical transformations is a major objective in the field of chemical reaction dynamics. Unfortunately, the detailed molecular processes behind many observations are too complex to grasp. It is therefore of interest to prepare reactants within a controlled environment, initiate a reaction, and study the products with as much detail as possible. The tools available to study such reaction products have been extended considerably by the recent development of multi-mass velocity-map imaging. This has proven a powerful tool to probe product angular and energy distributions and thus draw conclusion on the underlying potential energy surface upon which the dynamics proceed. The concept of the potential energy surface is described in the next section, followed by a detailed discussion of the experimental methods used in this work, and an outline of this thesis.

1.1 The potential energy surface

Chemical reactivity, *i.e.* the breaking and formation of internuclear bonds, is governed by the potential energy surface (PES). This is a multi-dimensional energy profile which describes the potential energy of a system at any given configuration of the molecule's nuclei [1]. Figure 1.1 shows a typical two-dimensional potential energy

surface, as a function of the internuclear distances R_1 and R_2. The reaction proceeds along the trajectory shown from the reactants **C** to the products **D** over the transition state **E**. Two stable configurations corresponding to local minima **A** and **B** are also shown.

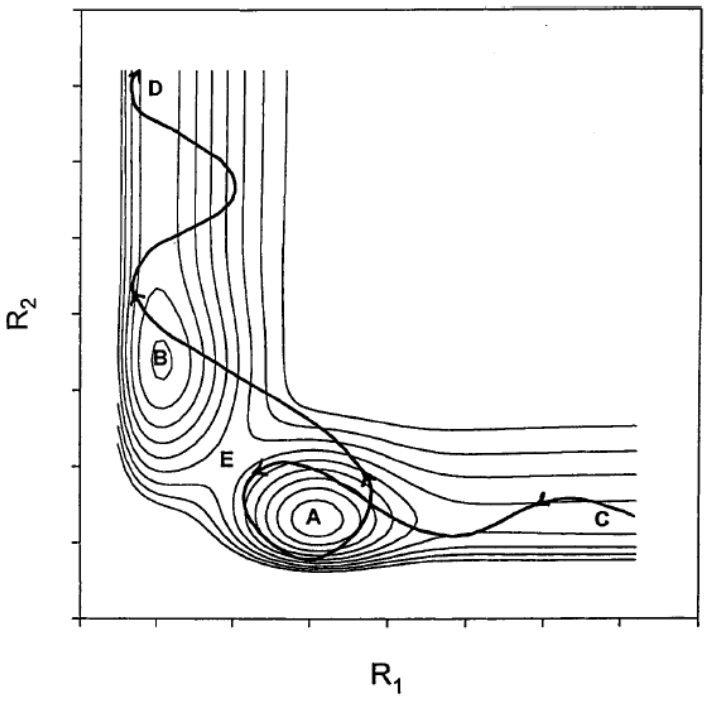


Figure 1.1: Typical two-dimensional representation of a multi-dimensional potential energy surface; R_1 and R_2 are bond distances which change along the shown reaction pathway from the starting material **C** to the product state **D** *via* the transition state **E** and local stable configurations **A** and **B**; reproduced from J.C. Tully, *Theor. Chem. Acc.* **2000**, 103, 173 with permission from Springer Nature.

The concept of the potential energy surface was first established to describe the $H_2 + H \longrightarrow H + H_2$ reaction as a concerted process forming a transient H_3 species, rather than stepwise breaking and forming of H-H bonds [1]. The idea is based on the Born-Oppenheimer Approximation [2] (BOA) which separates the electronic motion from the nuclear motion, and thus allows for an analytic solution of the Schrödinger equation for a many-electron, many-nuclei system. The BOA is based on the argu-

ment that the electron is much lighter than the molecule's nuclei and adjusts instantaneously to the nuclei motion. Thus, the potential energy surface is calculated for each electronic state of the molecule separately. When considering a photoinitiated reaction, following the excitation from the ground state surface, the reaction can be perceived to follow a classical trajectory on the excited potential energy surface. In this thesis it is shown how information on the excited state potential energy surface can be deduced experimentally by measuring the velocity distributions of the reaction products using velocity-map imaging.

1.2 Experimental methods

Recent developments of various experimental tools allow for the detailed study of fundamental molecular dynamics in the gas phase. Following a short summary, the experimental tools of relevance for this work will be discussed in detail.

The discovery of the molecular beam by L. Dunoyer and O. Stern in 1911 [3] gave rise to the preparation of cooled pulses of molecules in vacuum, where interactions with other particles, surfaces or photons can be studied. In many of these studies a key aim is to follow the characteristics and populations of quantum states during a reaction event [4–7]. Following the development of pulsed lasers [8], the population of vibrational, rotational, and electronic states could be probed with resonant ionization methods [9, 10], in which one photon is resonant with an intermediate state and the molecules are ionized *via* a multi-photon transition.

The underlying fragmentation dynamics of molecules was first studied using time-of-flight mass spectrometry, and was extended with the development of the ion imaging and velocity-map imaging techniques [11, 12]. Besides the particle mass, these

methods yield information on the velocities of the fragments formed in a reaction event. The fragment velocity distributions give wide insight into the dynamics of the fragmentation process. For the photodissociation of a diatomic molecule, as a consequence of conservation of momentum, velocity-map imaging of one fragment gives a detailed picture of the electronic states involved in the dissociation process. Velocity-map imaging has been applied successfully in photofragmentation [13], molecular scattering [14], and surface scattering studies [15, 16]. So far, in the majority of these studies, small molecules with a limited number of reaction pathways have been investigated. For larger molecules, the study of a single fragmentation product is often insufficient to deduce pathways which lead to individual fragments. In order to study multiple fragments along with their velocity distributions, universal ionization using electron beams and strong laser-fields can be used to ionize all molecules and fragmentation products irrespective of their electronic structure [17]. The development of multi-mass imaging techniques [18, 19] allows for simultaneous study of the velocity distributions of multiple reaction products. These new methods significantly reduce the acquisition time, and also allow correlations between the velocities of different reaction products to be revealed [19–23].

1.2.1 Molecular beams

In all experiments described in this work, the sample molecules are prepared in a molecular beam. A brief description of the production and applications of molecular beams will be given; a more detailed account can be found in Reference [24].

A molecular beam is an ensemble of internally cold molecules that move with constant velocity in a near-collision-free environment [24]. Continuous and pulsed molecular beams are prepared *via* a supersonic expansion of gas from a high pressure

source into a low pressure region. During the expansion, thermal translational and rotational energy are efficiently transferred into translational energy along the molecular beam axis. In comparison with a thermal distribution, this yields particles with a cold but fast translational distribution and little rotational excitation. In the context of the experiments presented here, this has four main advantages: i) The geometry of most spectroscopic experiments employing pulsed molecular beams largely eliminates inhomogeneous line broadening effects [24]; ii) The preparation of the sample in low-lying quantum states limits the possible number of pathways in a subsequent reaction event, and thus allows for a direct comparison with molecular dynamics simulations at the sample's temperature; iii) The preparation of a translationally cold molecular beam pulse is essential for successfully establishing a sharp velocity and time focus in the velocity-map imaging technique; iv) The preparation of sample molecules in a supersonic pulsed beam yields an improved signal-to-noise ratio, as the number density of molecules is increased at the peak of the pulse in comparison to a gas sample with a thermal velocity distribution.

Figure 1.2 (a) shows regions of different flow properties in a free-jet expansion. A sample gas or gas mixture with initial temperature T_{i} and molecular mass m is expanded *via* a small orifice from a container, at high pressure p_0, into the high-vacuum of the experiment. Three different regions are shown here: the high pressure stagnation region behind the nozzle; the supersonic zone of silence in front of the nozzle; and the surrounding subsonic zones separated from the zone of silence by the Barrel shock lines and the Mach shock disc. Optimum flow properties, *i.e.* maximum velocity and laminar flow with a Mach number $M >> 1$, are found in the zone of silence.

During the expansion, as the molecules pass through the orifice and in the region immediately beyond, they collide multiple times. In each collision, internal energy

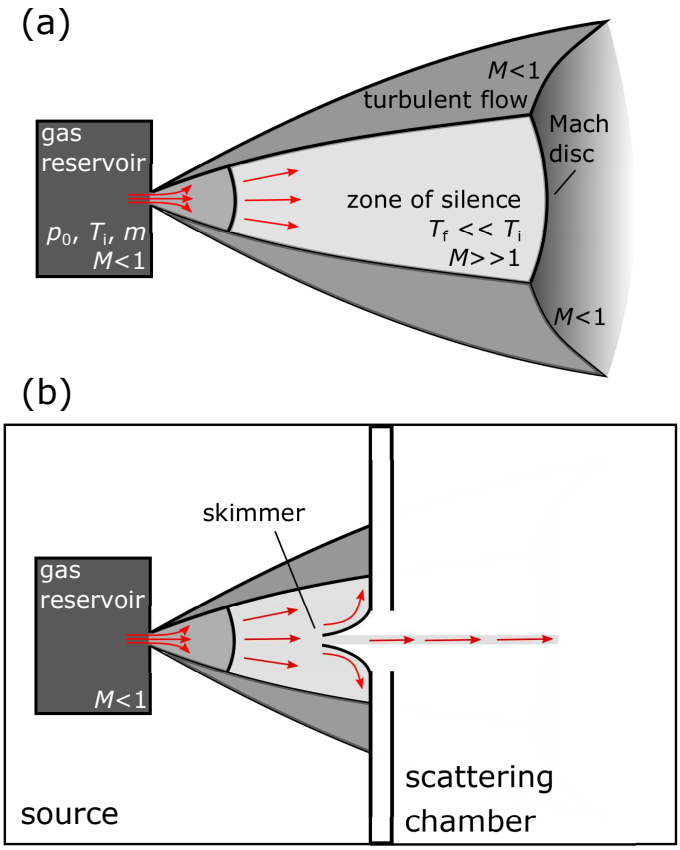


Figure 1.2: (a) Structure of a free-jet expansion from a high-pressure gas reservoir. Zones with different flow characteristics and Mach number M are shown; (b) The technical application of free-jet expansion in a two chamber experiment. Molecules in the "zone of silence" are extracted using a skimmer and differential pumping.

and undirected translational motion is converted into directed translation. To achieve a sufficient number of collisions to direct the flow in the expansion, the orifice size and gas pressure are chosen so that the mean-free path inside the source is much smaller than the nozzle diameter. Hence, the molecules undergo multiple collisions during the expansion. If the mean free path is larger than the nozzle diameter, molecules expand into the vacuum with only a few or no collisions. In this case the expansion is effusive. The speed distribution of an effusive beam is closely related to the thermal distribution inside the gas reservoir, but the distribution's maximum is shifted to slightly higher speeds as faster molecules have a larger probability of encountering and passing through the orifice.

While rotational and translation energy is efficiently converted into translation along the direction of molecular flow, vibrations are cooled less efficiently, due to the larger energy spacing involved [24]. Characteristic rotational and vibrational temperatures within a supersonic beam are 10 K and 100 K, respectively. An upper limit for the resulting translational velocity v can be derived by assuming that the thermal energy of molecules within the source is converted into translational kinetic energy of motion along the beam axis [24].

$$\frac{1}{2}mv^2 = -\int_{T_\mathrm{i}}^{T_\mathrm{f}} C_p \mathrm{d}T = \int_{T_\mathrm{f}}^{T_\mathrm{i}} C_p \mathrm{d}T \tag{1.1}$$

Here, T_i and T_f are the temperatures before and after the expansion, and C_p is the heat capacity at constant pressure in the sample container. With efficient cooling, T_f is much smaller than T_i, and can be approximated to zero. Equation (1.1) then becomes:

$$\frac{1}{2}mv^2 = C_p T_\mathrm{i} \tag{1.2}$$

$$v = \sqrt{\frac{2C_p T_\mathrm{i}}{m}} \tag{1.3}$$

From Equation (1.3) it can be seen that the final beam velocity is proportional to the square root of the heat capacity, and inversely proportional to the square root of the mass of the expanding molecule. Light molecules are therefore accelerated to much higher speeds than heavier molecules during a supersonic expansion. For example, based on tabulated thermodynamical values in Reference [25] and using Equation (1.3), the maximum beam speeds achievable in the expansion of a room temperature sample of helium and argon are calculated as $1760\,\mathrm{m\,s^{-1}}$ and $560\,\mathrm{m\,s^{-1}}$, respectively. A fast beam of heavy molecules can be produced by mixing the heavy sample molecule with a light carrier gas such as helium, typically in a ratio of 1:10 to 1:100. As long as the mass difference between the components in the gas mixture

is not too large, the carrier gas and the sample expand together to form a molecular beam with a velocity determined by the average mass.

To improve the beam quality a skimmer [26] can be employed in the experiment (see Figure 1.2 (b)). The tip of the conical shaped skimmer is positioned within the zone of silence. Molecules in laminar flow pass through an aperture in the tip of the skimmer, collimating the beam. The skimmer is shaped to reflect the barrel shock waves away from the beam axis.

During the expansion the pressure in the vacuum system containing the operating beam-valve typically rises by two to three orders of magnitude relative to the base pressure. Efficient pumping of the chamber is required in order to maintain a sufficiently good vacuum for gas-phase experiments. Differential pumping can be used to minimize the effect on the pressure of the background gas in the scattering chamber. In this scheme, the sample is expanded in a separate part of the experimental apparatus, commonly referred to as the "source chamber", which ends at the skimmer before the Mach disc, as shown in Figure 1.2 (b). The two regions are pumped separately, thus the gas load in the "scattering chamber" is significantly reduced. Within this regime an intense beam pulse of collinear flowing molecules can be prepared for further experiments while maintaining a low background pressure of $< 10^{-6}$ mbar in the experimental chamber. At this pressure, the mean free path of the fragmentation products and the sample molecules is much larger than the chamber dimensions, and it can be assumed that there are no collisions between parent molecules and their fragmentation products, between each other, or with background gas particles.

By rapidly opening and closing the expansion orifice a pulsed beam can be produced. Hence, a pulse of sample molecules can be prepared alongside other pulsed

sources of molecules, electrons, or laser radiation. In pulsed molecular beams, high number densities of molecules can be achieved while at the same time maintaining low background pressures and minimizing the sample consumption. Reduced number densities are found in continuous beams, which are used in the work described in Chapter 3. In the work described in this thesis, molecular beam pulse lengths on the order of a few hundreds of microseconds using solenoid valves (Parker Hannifin) have been used to perform the experiments in Chapters 2 and 4.

While the supersonic expansion is limited to gaseous sample molecules, a number of different methods have been developed to evaporate liquid or solid samples and to introduce them into the supersonic expansion. Liquid samples with a high enough vapour pressure at room temperature can be prepared in the gas phase using a bubbler, in which a carrier gas, *e.g.* helium or argon, is bubbled through the liquid sample to pick up molecules on its way to the beam source. The resulting mixture of carrier gas and sample is expanded into the vacuum. Solid samples can be evaporated by heating in a furnace or by laser ablation in a Smalley/Bondybey source [27, 28].

The Smalley/Bondybey source was used for sample preparation in Chapter 2. In this source, laser ablation of a metal or another solid material generates a plasma, which is then entrained into a molecular beam pulse. Hence, molecular beams of otherwise solid samples can be produced. Reactive gases can be mixed into the carrier gas to form covalently-bound species [29] and metal-ligand coordination clusters [30], or to mediate cluster growth [31] in the beam.

Figure 1.3 shows a laser ablation molecular beam source with a growth channel, used for preparing molecular beams of clusters. The pulsed valve is attached to a mounting plate behind a stainless steel block. Inside the block the ablation target is

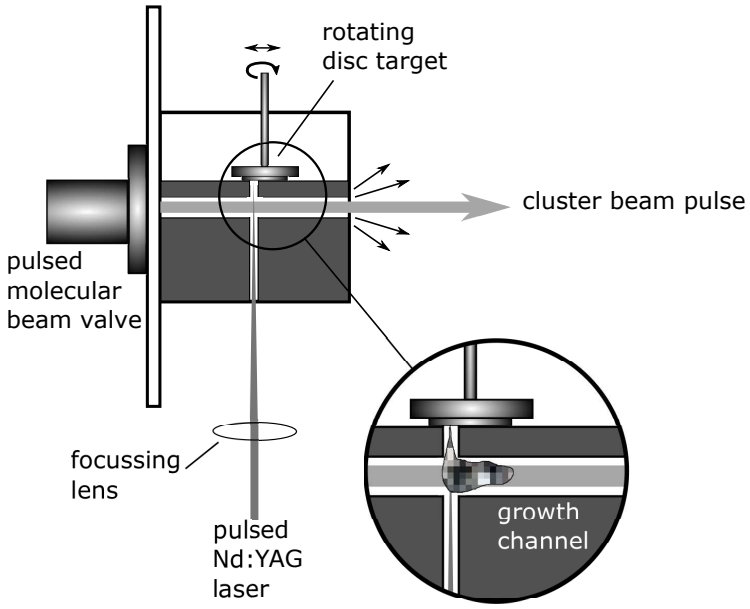


Figure 1.3: Laser vaporisation source [27, 28] with a linear growth channel and a disc-shaped ablation target. The inset shows a detailed view of the ablation region.

mounted facing a small hole to allow for the ablation laser to be introduced into the source. In order to provide a fresh surface at each laser shot, the disc-shaped target is translated and continuously rotated. In this type of ablation source the supersonic expansion of carrier gas is hindered; the gas fills a *ca.* 5 cm long channel before the laser pulse hits the ablation target and forms a plasma inside the channel. The ablation region is shown in detail in the inset to Figure 1.3. Through collisions with the carrier gas, excess internal energy introduced during the ablation is conducted away from the metal vapour towards the walls of the source. When the gas pulse exits the source channel, it expands and is cooled again. In this source covalently-bound species, such as metal oxides or carbides, and larger clusters, can be prepared.

Contrastly to the growth channel design, in the "cut-away" source the expansion is not hindered by the ablation block. In this design, the cluster source is opened up behind the point of ablation, allowing the carrier gas to expand into the plasma. Because of the short interaction time with the ablation plasma and the reduced density

of the carrier gas around the plasma, predominately single metal-centre complexes are formed. In spite of this, weakly-bound metal clusters such as $M^+(Ar)_n$ can be formed because of the more efficient cooling in the supersonic expansion [32].

The form of the ablation target is chosen according to the availability of the metal. In the work reported here, disc-shaped samples have been used. However, ablation of metal rods [27] or pressed pellets [33] has been reported in the literature. The stable formation and high abundance of the species of interest requires careful characterisation and optimisation of the carrier gas pressure, ablation laser power, source type, and source dimensions, all of which determine the interaction between the carrier gas and the plasma.

Pulsed molecular beams of sample molecules offer a versatile tool for use in crossed-beam experiments, as described in the following section.

1.2.2 The crossed beam experiment

Crossed-beam scattering experiments yield speed and angular distributions of reaction products. In the following, the analysis of data from a crossed-beam scattering experiment in the laboratory and centre-of-mass frame is briefly introduced, based on the treatment in References [34, 35] and [36]. A typical beam scattering experiment is shown in Figure 1.4 (a). The species A and B are prepared in two molecular beam pulses with velocities $\vec{v}_A, \vec{v}_B$. The two beams intersect at the collision point CP, where the reaction occurs. A detector is placed in the collision plane around CP to detect the collision products, which are scattered with velocities $\vec{v}_{A'}, \vec{v}_{B'}$ and at an angle Θ relative to one of the incident beam directions.

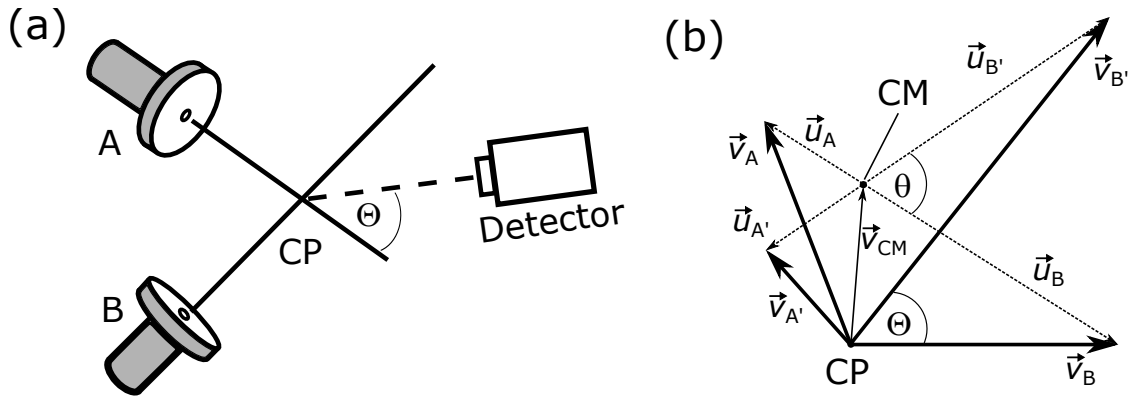


Figure 1.4: (a) Schematic crossed-beam scattering experiment in which two molecular beams A and B cross at the collision point CP; the intensity and speed of scattering products are detected as a function of the deflection angle Θ in the laboratory frame; (b) Geometric relationship between the initial and final velocity vectors of scattering partners A and B in the laboratory frame $\vec{v}_{\mathrm{A}}, \vec{v}_{\mathrm{B}}, \vec{v}_{\mathrm{A}'}, \vec{v}_{\mathrm{B}'}$ and in the centre-of-mass frame $\vec{u}_{\mathrm{A}}, \vec{u}_{\mathrm{B}}, \vec{u}_{\mathrm{A}'}, \vec{u}_{\mathrm{B}'}$; the centre-of-mass CM moves with the velocity $\vec{v}_{\mathrm{CM}}$. Scattering products are deflected by an angle Θ in the laboratory and θ in the centre-of-mass frame.

In the "laboratory frame", *i.e.* the reference frame in which the measurement is recorded, the intensity distribution as a function of the deflection angle Θ is dependent on the scattering angle between the two beams A and B. To make scattering experiments comparable to each other, it is convenient to convert angular distributions from the laboratory frame into a coordinate system independent of the experimental geometry.

Conventionally, the collision event is followed from the viewpoint of the centre-of-mass of species A and B. The relationship between the laboratory frame and the centre-of-mass frame is shown in Figure 1.4 (b). From the viewpoint of the centre-of-mass, A and B collide head on with velocities $\vec{u}_{\mathrm{A}}, \vec{u}_{\mathrm{B}}$, and the reaction products A′ and B′ scatter with velocities $\vec{u}_{\mathrm{A}'}, \vec{u}_{\mathrm{B}'}$ at the deflection angle θ. In three dimensional space, the relative velocity vectors of the products point towards the surface of a sphere around the centre-of-mass, the so called "Newton sphere". The complete scattering distribution of the reaction is a series of nested Newton spheres, with each

sphere corresponding to a combination of populated initial and final quantum states. The angular distribution of products on the surface of the Newton sphere is usually not isotropic, and contains information on the dynamics of the reaction under study.

In cases where the scattering partner A has much more momentum than B, the centre-of-mass proceeds approximately along the velocity vector of particle A, and the deflection angles in the laboratory and centre-of-mass frames Θ, θ are almost equal.

The concept of a Newton sphere, originally developed in the context of bimolecular crossed beam experiments, can also be applied to the electron-molecule colisions and photoinduced fragmentation processes studied in the present work. The fragmentation products form a series of nested Newton spheres around the interaction region of a molecular beam and a laser or electron beam. Zare and coworkers [37, 38] showed that the angular distribution of photodissociation products is given by,

$$F(R,\theta) \propto \sum_{l=0}^{l_{\max}} \beta_l(R) P_l(\cos\theta) \tag{1.4}$$

Here, θ is the product scattering angle with respect to the laser polarization axis, and R is the radial component of the sphere. P_l is the l-th order Legendre polynomial, and $\beta_l(R)$ is the corresponding anisotropy parameter. For linearly-polarized light the scattering distribution is described by components with even l in Equation (1.4) up to $l_{\max} = 2n$, where is n is the number of photons involved in the dissociation process. For a one-photon dissociation the parameter β_2 takes values from -1 to +2 for a fragmentation excited *via* a transition dipole oriented perpendicular and parallel to the breaking bond, respectively. The angular and speed distributions of the fragmentation products can be probed directly using velocity-map imaging, as discussed in Section 1.2.5.

1.2.3 Pump-probe spectroscopy

Understanding the dynamics of a system during a chemical reaction is crucial for the prediction of the properties and abundance of products. Pump-probe spectroscopy is a powerful tool for following a chemical reaction. The process of interest is initiated by a pump pulse, and the system is then probed spectroscopically at one or more times afterwards. Porter and Norrish [39] performed the first light-based pump-probe experiments. Free radicals were formed by irradiating CS_2 sample molecules with a two millisecond intense flash of light in a one meter long quartz tube. The absorption spectrum of the reaction products was measured using a second flash of light which was several milliseconds to minutes delayed relative to the first light flash.

The experiment by Porter and Norrish probed the products after the reaction took place. Similarly, dynamics between electronic states of molecules in a molecular beam can be probed using nanosecond laser pulses. Two pulsed laser-beams are overlapped with a molecular beam. The first laser pulse excites the molecules and the second laser pulse probes the reaction products, usually by resonant ionization or laser induced fluorescence [40].

The time resolution of pump-probe experiments is limited by the pulse lengths of the pump and probe pulses. In order to probe the reaction products and intermediates in real time, and to study the vibrational motion and fragmentation dynamics on and between electronic states, laser pulses with pulse lengths on the order of pico- to femtoseconds are required.

To initiate precisely a chemical reaction in the pump step and to detect spectroscopically products in the probe step, laser pulses with tunable wavelength and narrow bandwidth are required. Different laser sources supply various colours of out-

put radiation. Nd:YAG, Ti:Sapphire or other solid-state lasers generate laser pulses with a few Watts of output power in the near infrared region of the electromagnetic spectrum [41]. Higher harmonic generation in non-linear media extends this range towards shorter wavelengths into the extreme ultraviolet region [42], but is limited to multiples of the pump-laser frequency. In contrast, optical parametric oscillators and UV-pumped dye lasers are sources of tunable laser pulses in the IR, visible and UV regions of the spectrum. Large-scale facilities such as free-electron lasers can be used to obtain ultra-short laser pulses with high intensities from the X-Ray [43] to the IR [44] regions.

In Chapters 2 and 3, laser pulses of different spectral colours and with pulse lengths ranging from nanoseconds to femtoseconds are used to study the fragmentation dynamics of a range of different molecules. In Chapter 3, an ultraviolet pump extreme-ultraviolet probe scheme is used to study the UV dissociation dynamics of the CH_2BrI molecule.

In the following sections, experimental techniques for the generation of short and ultra-short laser pulses, higher harmonic generation, and basic principles of free-electron lasers are described.

1.2.3.1 Production of short and ultrashort laser pulses

This section describes techniques to produce short and ultrashort laser pulses which are employed throughout this thesis. Firstly, the application of the Q-switching technique for the production of nanosecond laser pulses is described, using the example of an Nd:YAG laser. Secondly, Kerr-lens mode locking and its application in the generation of femtosecond laser pulses is discussed.

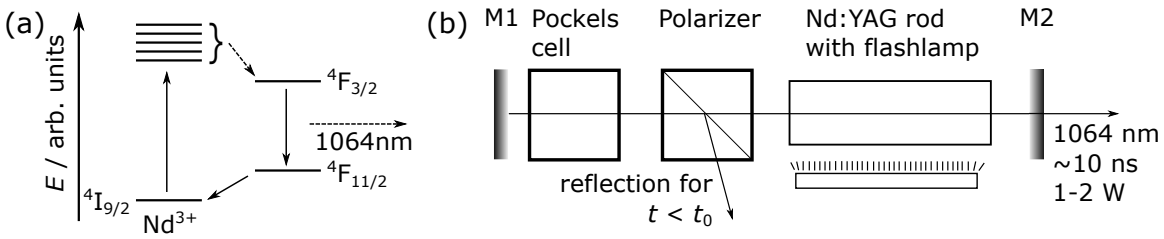


Figure 1.5: (a) Energy diagram summarizing the electronic states of Nd^{3+} involved in the lasing process in an yttrium-aluminium garnet crystal (Nd:YAG); (b) Technical application of the Nd:YAG medium in a Q-switched laser generating IR radiation pulses with a typical power of a few Watts and durations of a few nanoseconds; the combination of the polarizer, Pockels cell and mirror M1 introduces a loss into the laser cavity suppressing stimulated emission while a voltage is applied to the Pockels cell for $t < t_0$.

Figure 1.5 (a) shows the electronic states involved in the lasing process of triply ionized neodynium inside a doped yttrium aluminium garnet (Nd:YAG) crystal [41]. Ground state neodynium ions are pumped by broadband white light of one or multiple flash lamps to an array of excited states which quickly decay to the $^4F_{3/2}$ state. The lasing process occurs by stimulated emission between the $^4F_{3/2}$ and $^4F_{11/2}$ states, yielding photons in the near IR spectral region ($\lambda = 1064\,\mathrm{nm}$). Next, Nd^{3+} ions in the $^4F_{3/2}$ relax to the ground state and can be pumped again. The transition $^4F_{11/2} \nleftrightarrow ^4F_{3/2}$ is spin allowed but Laporte forbidden, which results in a long lifetime of the upper level. Thus, a large population of the $^4F_{3/2}$ state can build up when the medium is pumped inside a laser cavity.

The temporal profile of the laser pulse depends largely on the duration and intensity of the pump pulse, since the oscillation inside the laser cavity only takes place once a sufficient population inversion between the ground state and the upper $^4F_{3/2}$ state has been achieved. This generally leads to a large jitter in the pulse time and fluctuation in the pulse intensity and width. The application of the Q-switching technique allows for precise timing of the laser pulse.

Q-switching

Q-switching employs one or multiple optical elements placed inside the laser cavity to introduce losses of radiation and thus prevent the stimulated emission before a sufficient population has built up in the upper laser level $^4F_{3/2}$. An example of a Q-switch in a Nd:YAG laser is shown in Figure 1.5 (b). The Q-switch consists of a polarizer and a Pockels cell positioned in front of cavity mirror M1. The polarizer selects the vertical polarization component on the first pass, but will only transmit horizontally polarized light on the pass back towards the active medium. For any time $t < t_0$ before the desired population inversion is achieved, a voltage is applied to the Pockels cell and the polarization plane is turned from horizontal to vertical within the two passes through the cell. Thus the radiation wave inside the cavity is completely reflected and stimulated emission can not take place. At $t = t_0$, the voltage is pulsed down and the lasing process occurs, leading to an intense output pulse with a length of typically a few nanoseconds and power of a few Watts. As a consequence of the Q-switching technique, the output laser pulse can be precisely triggered together with other elements of an experiment such as molecular beam pulses, other lasers, or detectors.

Mode locking

Using mode-locking, laser pulse lengths below 1 ps can be achieved [45, 46]. This method is described in the following.

Typically, a number of different modes resonate in the laser cavity. All modes available from the lasing species which resonate with the cavity dimensions are present, but their phases are not aligned with each other. Mode-locking brings the intensity maxima of all those modes into phase, generating a single, short burst of coherent

radiation. With active mode-locking techniques, pulse lengths of as little as a few hundred picoseconds can be achieved [45]. In this approach, an acoustic phase modulator is placed inside the laser cavity, and the oscillating radiation waves are modulated until their phases coincide constructively.

Kerr-lens mode-locking generates laser pulses shorter than 10 fs, with pulse energies of around $1 - 10$ nJ [47]. This method is based on the Kerr-effect [48], which describes the observed increase in refractive index with laser intensity at high intensities. As a result of the Kerr effect, for a Gaussian beam profile, the refractive index has a maximum in the centre of the laser beam. This results in a self focussing of the beam within the Kerr medium, which strongly depends on the intensity. In a Ti:Sapphire laser the Kerr effect is introduced by the pumped medium itself [47]. An aperture is placed in the beam path behind the Kerr medium which cuts away all parts of the beam that are not sufficiently focused, *i.e.* only the most intense part of the beam both spatially and in time is allowed to resonate within the laser cavity. The resonator modes therefore align in phase, forming a single, highly intense laser pulse.

Both high spectral resolution and high time resolution are in principle desirable. A smaller bandwidth of the pump laser pulse allows for precise preparation of the system in an excited state, and, in addition, the dynamics can be followed in smaller and more precise steps using a shorter laser pulse.

The minimum pulse length and bandwidth are linked by the Fourier limit. For a Gaussian beam pulse this relationship is:

$$\Delta\tau\Delta\nu \geq 0.4 \tag{1.5}$$

Here, $\Delta\tau$ is the pulse length and $\Delta\nu$ is the spectral bandwidth of the laser. Hence, the production of shorter laser pulses is achieved at the expense of broad spectral width.

1.2.3.2 High harmonic generation

Coherent radiation obtainable from a dye-laser ranges from fundamental wavelengths of 311 nm using the laser dye DMT to 1040 nm operating with LDS-925 [49]. This range can be extended into the VUV and XUV region by generating higher harmonic frequencies in a medium of sufficiently large non-linear susceptibility. Non-interaction of light with material is used in Chapter 2 to generate the third harmonic of a Nd:YAG laser and visible output of an optical parametric oscillator. In Chapter 3, the third harmonic of a mode-locked Ti:Sapphire laser is generated in order to obtain laser radiation at a wavelength of 267 nm. Non-linear light-matter interaction has been well described in References [46] and [50], and will only be summarized here.

While passing through a medium with a sufficient susceptibility χ, the fundamental radiation field $\vec{E}$ temporarily displaces bonding electrons within the matter. Thus, an oscillating polarization $\vec{P}$ is induced according to Equation (1.6) [50].

$$\vec{P} = \varepsilon_0(\chi^{(1)}\vec{E} + \chi^{(2)}\vec{E}^2 + \chi^{(3)}\vec{E}^3 + ...) \tag{1.6}$$

Here, $\chi^{(m)}$ is the mth-order electric susceptibility of the medium, and ε_0 is the vacuum permittivity. The induced oscillating polarization generates a new electromagnetic wave. Elastic Rayleigh scattering in the non-linear medium is described by the linear term, whereas higher order non-linear mixing of the inducing radiation, *i.e.* generation of a linear combination of the electric field frequencies, is described by the later terms. The susceptibility decreases rapidly with higher orders in m, and higher order non-linear processes are therefore less efficient than lower order processes. For

efficient generation of high harmonics of the pump beam, high laser intensities are required. Thus, ultra-short laser pulses are suitable for high harmonic generation as all of the pulse energy is concentrated in a very short, highly intense pulse.

At each point in the medium, new waves with frequencies ω_1 and ω_2 are generated. Because energy is conserved in the process, the fundamental frequency ω_3 is given by:

$$\omega_3 = \omega_1 \pm \omega_2 \tag{1.7}$$

According to Equation (1.7) there are infinite pairs of frequencies $\omega_1 \pm \omega_2$ that can be generated. However, in order to conserve momentum, $\vec{p} = \hbar\vec{k}$, the wave vectors, $\vec{k}_i$, of the inducing electric field and the resulting pair of photons need to be matched according to:

$$\vec{k}_3 = \vec{k}_1 \pm \vec{k}_2 \tag{1.8}$$

Conditions satisfying Equations (1.7) and (1.8) are known as phase matching conditions. Two types of phase matching are defined. In type I phase matching the higher harmonic wave is polarized orthogonal to the fundamental wave. In type II phase matching the higher harmonic wave is not polarized in plane with the fundamental nor orthogonal to it. This case of phase matching often leads to less efficient higher harmonic generation [50]. The choice of the non-linear medium, the angle at which it is cut relative to the crystal lattice, ϕ, and the spectral range of the generated higher harmonic output define the type of phase matching. For example, a beta-barium borate (BBO) crystal cut at $\phi = 30°$ will allow for type I phase matching in a range from $\lambda = 410–3500\,\text{nm}$ and type II phase matching in the range $\lambda = 710–1500\,\text{nm}$ [50].

A special case of higher harmonic generation is frequency doubling, or second harmonic generation (SHG). Here, two photons of lower wavelength are up-converted in a non-linear crystal to generate a third photon with double the frequency of the

original photon. Thus, the output of a dye laser in the visible region of the spectrum can be converted into UV radiation.

Another technical application of the non-linear interaction of light with matter gives rise to the optical parametric oscillator (OPO). This is a widely tunable source for generating coherent radiation over a wide spectral range. While passing through a medium of sufficient high non-linear susceptibility, the incident pump photon generates two photons, called the signal and idler, which satisfy conservation of energy and momentum:

$$\omega_\mathrm{p} = \omega_\mathrm{s} + \omega_\mathrm{i} \tag{1.9}$$

$$\vec{k}_\mathrm{p} = \vec{k}_\mathrm{s} + \vec{k}_\mathrm{i} \tag{1.10}$$

Placed into a cavity, lasing takes place if the gain of the high harmonic generation process is larger than the losses within the cavity. Changing the orientation of the non-linear crystal relative to the pump beam propagation vector selects different pairs of signal and idler frequencies for which Equation (1.9) and (1.10) are satisfied. Thus, the output frequency ω_s is tuned by turning the crystal inside the cavity around its lattice vector. This process is most efficient for a collinear propagation of the pump, signal and idler beam. However, changing the crystal orientation changes the output propagation direction of the signal and idler beam. Thus, not only is the output laser power reduced for large orientation changes, but also an offset is introduced in the output laser beams. To ensure spatial stability of the output, a compensator crystal is placed behind the cavity, which introduces the opposite offset to that of the non-linear crystal, thereby compensating for the spatial offset of the laser beams.

The typical bandwidth of an optical parametric oscillator is about $5\,\mathrm{cm}^{-1}$, but can be reduced to as low as $0.01\,\mathrm{cm}^{-1}$ using a tilted etalon [50, 51] or injection seeding [52].

1.2.3.3 Free-electron lasers

A free-electron laser (FEL) [53] is a tunable light source that employs an electron pulse in a tailored magnetic field as an active medium. Bunches of electrons are accelerated in a linear accelerator and pass through a periodic magnetic field established either by an undulator, a periodic array of magnets in varying orientation, or by a helical superconducting magnet known as a "wiggler" [50]. The electron beam oscillates periodically under the influence of the magnetic field, and emits radiation with a wavelength that depends on the period of the magnetic field oscillation Λ_{w}.

The speed of light c is larger than the speed of the electron beam v_z. Therefore, the time-lag Δt between the electrons and light after one period of the magnetic field oscillation is given by [50],

$$\Delta t = \Lambda_{\mathrm{w}}\left(\frac{1}{v_z} - \frac{1}{c}\right) \tag{1.11}$$

Also, constructive interference of the radiation created at two different points inside the undulator can only be achieved for certain wavelengths that fulfil the phase matching condition that the time-lag between the electron beam and light wave is an integer multiple m of the light period T [50],

$$\begin{aligned} \Delta t &= m \cdot T = \frac{m \cdot \lambda_m}{c} \\ \lambda_m &= \frac{\Delta t \cdot c}{m}. \end{aligned} \tag{1.12}$$

Comparing Equation (1.11) and (1.12) yields,

$$\lambda_m = \frac{\Lambda_{\mathrm{w}}}{m}\left(\frac{c}{v_z} - 1\right). \tag{1.13}$$

Thus, the first order ($m = 1$) output of the FEL can be tuned by changing the electron velocity v_z. The output I_{total} of a free-electron laser is especially bright, and follows the relationship [50]:

$$I_{\mathrm{total}} \propto N^2 I_{\mathrm{el}} \tag{1.14}$$

where N is the number of electrons in the undulator and I_{el} is the light emitted by a single oscillating electron. Equation (1.14) describes the case in which all electrons inside the undulator emit radiation in phase. This can be achieved in practice by self-amplified spontaneous emission (SASE) [54, 55]. In the undulator, the accelerated electrons emit light that travels slightly faster than the electrons. Slightly faster and slightly slower electrons lose and gain kinetic energy in interaction with the emitted radiation and thus add to the population at the peak velocity v_c. The output intensity of a free-electron laser in the XUV to X-ray regime [43, 56, 57] is about 10^{12} to 10^{13} photons per pulse, nine orders of magnitude higher than radiation from a synchrotron or table-top HHG source with comparable photon energy [58]. Pulse durations as low as 39 fs were measured [59] at the free-electron laser in Hamburg (FLASH) [56] employed in this work.

The high output intensity and short pulse duration make XUV pulses from a FEL an ideal probe light source for a pump-probe experiment. The XUV pulse can ionize the molecule at any point along the reaction coordinate on an excited state potential energy surface and can overcome the excited molecule's ionization potential in a single step without the need for intermediate electronic states in resonant multi-photon ionization, as discussed in the following section. The disadvantage of a free-electron laser is the large expense and experimental effort associated with establishing and running such a facility.

1.2.4 Universal and state selective ionization

In the gas phase, electric fields can be used to accelerate, decelerate and manipulate the trajectories of charged particles. Ions can be detected with very high sensitivity using micro-channel plate (MCP) or channeltron detectors. However, many reac-

tions studied in the gas phase have neutral reactants, and yield neutral molecules or molecular fragments. Ionization of neutral reaction products and sample molecules facilitates their detection, and extends the available tools for the study of chemical processes in the gas phase. For example, fragmentation patterns and branching ratios can be studied using time-of-flight mass spectrometry and velocity-map imaging, as discussed in Section 1.2.5. Two general classes of ionization methods can be defined: universal and state-selective ionization. In the former, a low-energy electron beam or highly intense focussed pulsed laser beam is used to ionize molecules in the gas phase. In contrast, state-selective ionization methods ionize only molecules present in a specific selected quantum state. In the following, different laser-based approaches for both universal and state-selective ionization are discussed.

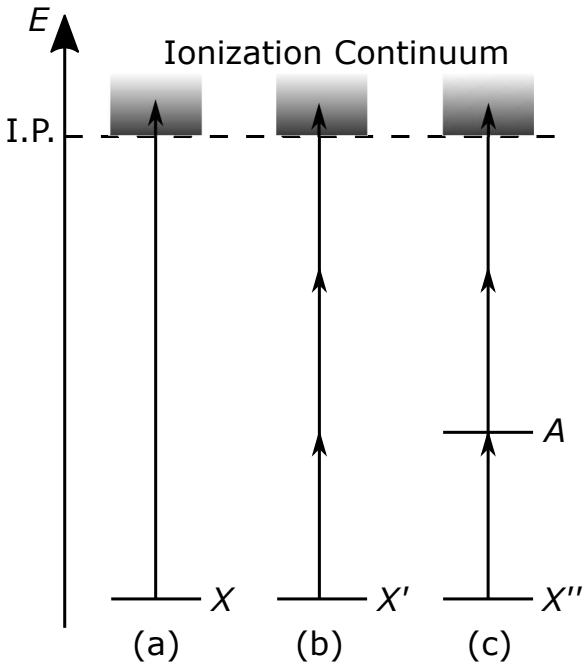


Figure 1.6: Schematic illustration of (a) one-photon, (b) non-resonant multi-photon and (c) resonance enhanced multi-photon ionization from the ground state X to the ionization potential (I.P.); A is an intermediate state between the ground state and the I.P.

Figure 1.6 shows three ways in which a molecule can be excited by one or more

photons to an energy above the ionization potential (I.P.). By interaction of the molecular transition dipole with the oscillating electric field of the laser pulse, the molecule may absorb a photon, promoting an electron from its ground state X. The molecule is ionized if the sum of the energy of the state X and the photon energy exceeds the ionization potential. For single-photon ionization, as shown in Figure 1.6 (a), the photon wavelength is usually in the extreme ultraviolet part of the electromagnetic spectrum. For example, the ionization potential of a carbon monoxide molecule is 14.013 eV [60], thus, one photon ionization would require a photon wavelength of 88.478 nm. Intense light sources in this spectral range are not yet readily available in a standard chemical physics laboratory, though can be accessed at synchrotron or FEL facilities.

If high enough light intensities are employed at longer wavelengths, corresponding to photon energies below the I.P., the molecule may undergo a multi-photon transition, absorbing two or more photons and promoting an electron over the ionization potential as shown in Figure 1.6 (b).

The efficiency of a multi-photon transition can be enhanced significantly by tuning the photon wavelength into resonance with a state intermediate between X and the I.P. So called resonance-enhanced multi-photon ionization (REMPI) can be achieved using multiple photons from one laser (one colour) or using two laser pulses of different wavelength (two colour). In the two-colour approach, one laser's wavelength is tuned to match the transition from the ground state to the intermediate state with one or more photons and another photon (or sometimes multiple photons) is tuned to overcome the ionization potential from the intermediate state. Figure 1.6 (c) shows a one-colour (1+2) REMPI transition using three photons of the same wavelength, where one photon is in resonance with an intermediate state A and two photons are

required to ionize from this state.

In combination with REMPI, the preparation of cooled molecules in a molecular beam pulse becomes a particular advantage. As REMPI is much more efficient than non-resonant multi-photon ionization, the intensity spectrum of photoions or photoelectrons as a function of wavelength shows the transitions from the populated ground to intermediate states. Starting from a few vibrational and rotational states in the molecular beam and scanning the REMPI laser wavelength yields an intensity spectrum, which describes the rotational and vibrational structure of the neutral excited state A.

Reducing the pulse length of the laser pulse often leads to an increased field strength E_0. For very high laser intensities, $I > 10^{13}\,\mathrm{W\,cm^{-2}}$, the electric field of the light pulse is of the same order of magnitude as the field arising from the Coulomb interaction between bound electrons and nuclei. The interaction of the electronic potential of the molecule with the applied electric field is shown in Figure 1.7. Panel (a) shows two electronic states A and B in the Coulomb potential of the molecule. If an external electric field (dashed line in Figure 1.7) is applied along the z axis, then the potential barrier towards ionization is lowered by the electric field as shown in Figure 1.7(b). The formerly neutral electronic state B' lies above the ionization limit and becomes ionized immediately, while state A' can undergo tunnel ionization through the ionization barrier. For very high laser intensities almost all electrons become ionized and field ionization becomes a universal ionization method [61]. For lower intensities, tunnel ionization competes with non-resonant multi-photon ionization according to the Keldysh parameter γ [62, 63], which compares the laser frequency ω_0 with the tunnelling frequency ω_t.

$$\gamma = \frac{\omega_0}{\omega_\mathrm{t}} = \omega_0 \sqrt{\frac{2 I_e m_e}{e E_0}} \tag{1.15}$$

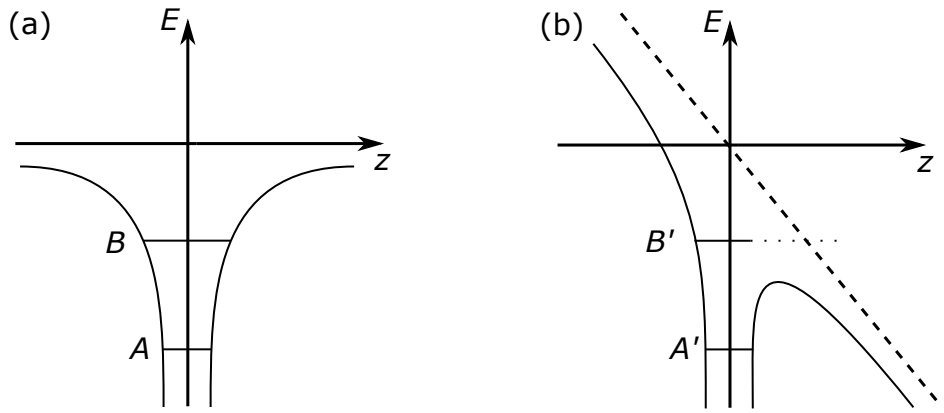


Figure 1.7: Illustration of the effect of an external electric field on two neutral electronic states A and B in (a); Upon application of an electric field along z, the ionization potential is lowered in (b); A' becomes ionized directly and B' undergoes tunnel ionization.

Here, m_e and e are the electron mass and elementary charge, respectively. The ionization energy I_e, the electric field strength E_0, and the laser frequency ω_0 determine whether $\gamma < 1$, in which case tunnelling ionization dominates or $\gamma > 1$, when multiphoton ionization dominates the mechanism.

1.2.5 Velocity-map imaging

The velocity-map ion imaging technique [12] is a variation of Wiley-McLaren time-of-flight mass spectrometry [64]. Particles with the same mass-to-charge ratio and velocity are mapped by a carefully tuned electric field to the same position on a two-dimensional position sensitive ion-detector. Thus, the scattering distribution of particles formed in the interaction region of a molecular beam and a laser or other beam can be recorded in the form of an image for each mass-to-charge ratio.

If the reaction yields ionic products, information on the branching ratio between different reaction channels can be gained from the time-of-flight mass spectrum. Figure 1.8 (a) shows the key features of a Wiley-McLaren mass spectrometer [64]. Ions

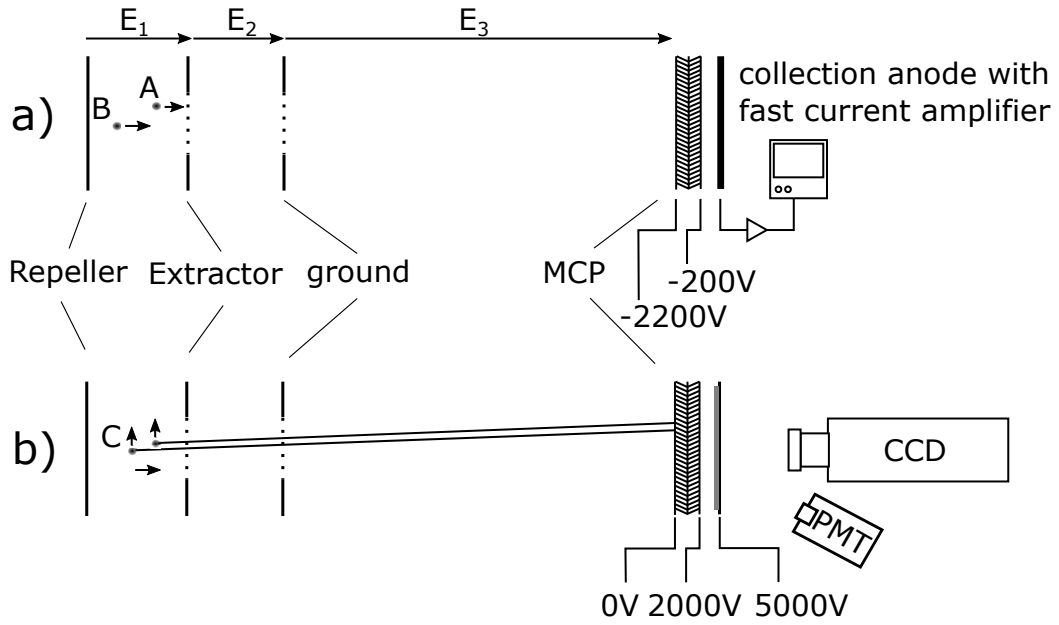


Figure 1.8: (a) Wiley McLaren time-of-flight mass spectrometer [64] in comparison with (b) ion imaging set-up by Chandler and Houston [11].

are created in the source region between the repeller and extractor lens, and are extracted using the electric field maintained within the Wiley-McLaren ion lens [64]. Each of the lens elements is a stainless steel ring with a high transmittance metal mesh in its centre to ensure a homogeneous electric field. Positive ions are accelerated by the field gradient between the first lens element held at a high positive potential, the repeller, and last grounded lens element. The second lens element, the extractor, is kept at an intermediate potential so that the overall acceleration field is the sum of the field gradient between repeller and extractor element, $\vec{E}_1$, and between extractor and ground element, $\vec{E}_2$. As the ions traverse the field-free region in between the ground lens element and the detector, they separate and arrive at different times on the detector according to their mass-to-charge ratio m/q.[64]

$$t \propto \sqrt{\frac{m}{qU}} \tag{1.16}$$

Here, U is the potential difference experienced by the extracted ion between the repeller and ground lenses. In an ideal experiment, maximum mass resolution is

achieved by creating all ions in a single plane parallel to the detector with no initial velocity component towards the detector. Thus, the mass resolution is limited by the initial distribution of ion velocities and origins within the source region. In the three lens set-up it is possible to focus two ions A and B (see Figure 1.8) with different points of origin in the spectrometer to arrive at the same time on the detector according to Equation (1.16). Particle A is created closer to the extractor plate, gains less velocity in the electric field $\vec{E}_1$ and will catch up with B in a focussing plane along the field-free region. The position of this plane can be made coincident with the detector by adjusting the ratio of the electric fields $\vec{E}_1/\vec{E}_2$. Ions are typically detected with a channeltron or multi-channel plate (MCP) in combination with a collection anode and current amplifier [65]. While this method is very powerful in determining absolute or relative ion yields of reactions in the gas phase, limited information on the fragments' kinetic energy release can only be retrieved by an analysis of the peak shape in the time-of-flight spectrum. High kinetic energy release into the reaction product of interest leads to a broadening of the peak, while low kinetic energy release channels yield narrower peaks.

In 1987, Chandler and Houston extended the time-of-flight mass spectrometry approach and collected information on the velocities of the 266 nm photolysis products of CH_3I [11]. The experimental set-up employed in these experiments is shown schematically in Figure 1.8 (b). A beam of sample molecules was introduced into a three-element Wiley-McLaren ion lens through a hole in the repeller plate, and was intersected with the frequency quadrupled output of a Nd:YAG laser in between the repeller and extractor lens. Photoproducts were then extracted along the flight tube to a position-sensitive ion detector. The detector consisted of a microchannel plate, which converted each incoming ion into a burst of electrons, and a P47 phosphor screen to visualize the electron bursts. The intensities of the visible flashes of light

were measured using a photomultiplier tube, and the spatial distribution was acquired using a charge coupled device (CCD) camera. While the camera acquired image data throughout the time-of-flight cycle, the front microchannel plate was held at ground for most of the experimental cycle and rapidly pulsed to −600 V for the arrival time of the ion of interest, activating ion detection. Thus, ion images of only one mass-to-charge ratio were recorded. As the extraction field was homogeneous, the position at which the ion arrives at the detector was governed by its momentum component perpendicular to the time-of-flight axis. Hence, the kinetic-energy distribution and angular distribution of photoproducts were recorded, highlighting that the dissociation excites both the umbrella bending and the symmetric C-H stretching mode of CH_3.

The ion imaging technique was picked up in a few studies [66–68], but suffered from low velocity resolution. Because of the homogeneous electric extraction field, the size of the interaction region between laser and molecular beams is projected onto each point of the ion image, leading to a significant blurring of the image. This is illustrated in Figure 1.8, in which two particles C both have the same off axis momentum, but are projected onto two different positions within the detector because their trajectories start at two different points in the source region. Moreover, the accelerated ions scatter off the mesh in the ion optics, leading to a further reduction in the velocity resolution, image quality and ion transmission.

In an attempt to avoid the distortion induced by the mesh, Eppink and Parker performed an imaging experiment with an open, meshless ion optic design [12, 13], shown in Figure 1.9. Serendipitously, in addition to eliminating distortions caused by the mesh, a ratio of the potentials applied to the extractor and repeller lenses could be found which focussed velocities onto the detector plane regardless of the parti-

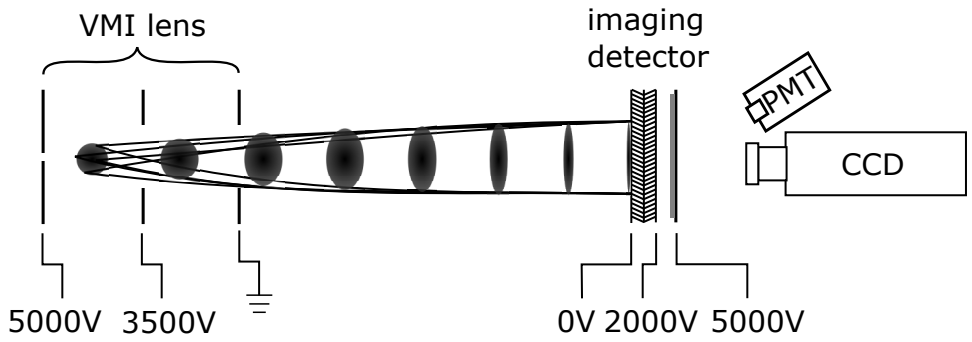


Figure 1.9: Velocity-map imaging spectrometer [12] with typical voltages applied to the VMI lens and imaging detector.

cles' position of origin within the interaction region. Thus, the main disadvantage of the original ion imaging approach of Chandler and Houston - the projection of the spatial distribution of ions in the source region onto the recorded image - had been overcome. The optimized velocity-mapping potentials were identified using the ion image of the parent, in this case O_2^+, which yields a small spot corresponding to the transverse velocity distribution of the molecular beam. The refocussing of the velocities is a result of the cylindrically inhomogeneous electric field generated within the velocity-mapping lens. In practice, VMI can achieve satisfactory velocity focussing for interaction volumes of up to a few cubic millimetres.

In their original VMI paper, Eppink and Parker studied the photolysis of molecular oxygen, and describe the two principal pathways in the three photon dissociative ionization. Following excitation to the $3d\pi(^3\Sigma_{1g}^-)$ Rydberg state, velocity-map images of photoions and photoelectrons distinguish the formation of O^+ ions by dissociation of O_2 into two neutral atoms and subsequent ionization of the atoms, from ionization to form an O_2^+ cation which subsequently dissociates. Furthermore, the O^+ and electron scattering distributions clearly elucidated the populations of the $O_2^+(v{=}2,3,6,20,23)$ vibrational states and the $O^*(^3P, ^5P, ^3S, ^5S)$ electronic states.

Closely related to VMI is spatial-map imaging (SMI), in which the lens potentials are tuned so that the positions of the ions at their point of formation, rather than their velocities, are mapped onto the detector. Eppink and Parker [12] used SMI to image the path of the laser beam through the molecular beam, thereby mapping out the spatial cross-section of the molecular beam in the interaction region. The drastic improvement of velocity resolution relative to the original ion imaging approach has made velocity-map imaging a powerful tool for dynamics studies. Some of these studies are summarized in References [69] and [70].

In the conventional approach to velocity-map imaging, the three-dimensional sphere of nascent particles is focused along the ToF axis and is acquired as a two-dimensional projection at the detector. Several analytical strategies have been developed to recover the speed and angular distributions from the two-dimensional projection. The polar basis function expansion [71] (pBASEX) method has been developed for velocity-map imaging of photoelectrons and photofragments, and is discussed in the following.

For a sufficiently large extraction field [72] and as long as cylindrical symmetry about an axis parallel to the detector is conserved, the Abel integral [73] in Equation (1.17) describes the relation between the central slice of the scattering distribution $F(R,\theta)$ and the two-dimensional projection on the detector $P(R',\theta')$.

$$\begin{aligned} P(R',\theta') &= 2\int_{|x|}^{\infty} \frac{rF(R,\theta)}{\sqrt{r^2-x^2}}\mathrm{d}r, \\ x &= R'\sin\theta', \\ r &= R\sin\theta \end{aligned} \tag{1.17}$$

Usually, there is no analytical solution of Equation (1.17) for a general velocity-map image $P(R',\theta')$, and the integral is solved numerically. In the pBASEX approach the

central slice of the three-dimensional scattering distribution is described using a set of basis functions with an analytical solution for Equation (1.17). Typically, Gaussian basis functions $f_{k,l}(R,\theta)$ with width σ and centre R_k are used.

$$F(R,\theta) = \sum_{k=0}^{k=k_{\max}} \sum_{l=0}^{l=l_{\max}} c_{k,l} f_{k,l}(R,\theta) \tag{1.18}$$

$$f_{k,l}(R,\theta) = e^{-(R-R_k)^2/\sigma^2} P_l(\cos\theta) \tag{1.19}$$

Each Gaussian is weighted with the factor $c_{k,l}$ and $P_l(\cos\theta)$ is the l-th order Legendre polynomial describing the angular distribution of the nested Newton sphere within the scattering distribution (see Section 1.2.2 for more details). As there is an analytical solution of Equation (1.17) for a Gaussian function, each Gaussian basis function $f_{k,l}(R,\theta)$ can be expressed as its two-dimensional projection in the velocity-map image $g_{k,l}(R',\theta')$.

$$g_{k,l}(R',\theta') = 2\int_{|x|}^{\infty} \frac{r f_{k,l}(R,\theta)}{\sqrt{r^2-x^2}} \mathrm{d}r \tag{1.20}$$

The recorded scattering distribution $P(R',\theta')$ is now fitted with a set of projected Gaussian basis functions.

$$P(R',\theta') = \sum_{k=0}^{k=k_{\max}} \sum_{l=0}^{l=l_{\max}} c_{k,l} g_{k,l}(R',\theta') \tag{1.21}$$

The resulting weighting coefficients c_{kl} for each radial element k and angular element l are used to describe the central slice of the original three dimensional scattering distribution in Equation (1.19).

$$I(R) = \frac{1}{I_{\max}} \int_0^{\pi} F(r,\theta) R^2 \sin\theta \mathrm{d}\theta \tag{1.22}$$

$$I(R) = \frac{R^2}{I_{\max}} \sum_k c_{k,0} f_{k,0} \tag{1.23}$$

As the fitted basis function in Equation (1.19) corresponds to the analytical description of the Newton sphere by Zare *et al.* [37, 38], the l-order angular anisotropy

parameters $\beta_l(R)$ can be retrieved directly from the weighting coefficients $c_{k,l}$.

$$\beta_l(R) = \frac{\sum_k c_{k,l} f_{k,0}(R)}{\sum_k c_{k,0} f_{k,0}(R)}$$
$$\beta_l(R) = \frac{R^2}{I(R) I_{\max}} \sum_k c_{k,l} f_{k,0}(R) \tag{1.24}$$

The Abel inversion has been implemented in a number of other algorithms, which are discussed in detail in Reference [74]. All of these methods share the feature that they invert the recorded two-dimensional image and return the central slice through the resulting three-dimensional product sphere. Examples of different approaches include onion-peeling [72], BASEX [75] and the maximum entropy approach [76]. For an ideal noise-free image, all of these methods should give comparable results. However, different inversion methods are known to handle experimental noise in the recorded image differently. The maximum entropy approach is known to be favourable for a low experimental count rate [70]. The experimental noise from the recorded image is projected onto the centre of symmetry in the image and appears as a line of noise in the inverted image. The polar-onion-peeling (POP) and pBASEX approaches invert the images in a spherical coordinate system, which in certain cases reflects the underlying distribution of photodissociation products better. In these algorithms the experimental noise is not projected onto the symmetry axis of the image, but into the centre of the inverted image. This is advantageous as the noise obscures a much smaller region of the inverted image.

Another approach to retrieving information on the three dimensional product scattering distribution directly is "time slicing" first introduced by Gebhardt *et al.* [77]. The authors allowed the nascent product sphere to expand under field-free conditions for a short time before applying an extraction pulse to the VMI optics. A homogeneous field was used to extract the expanded Newton spheres from the interaction region, which was followed by an Einzel lens to recover velocity-mapping in the image

plane. Having stretched the arrival time distribution at the detector to several hundred nanoseconds *via* the initial Newton sphere expansion, time-gating the detector so that it only detects ions within a ~ 40 ns time window allowed the central slice of the scattering distribution to be recorded directly.

Following this work, Townsend *et al.* [78] used "direct current slice imaging" ion optics to stretch the product scattering distribution along the ToF axis, rather than compressing it as in conventional VMI. The direct current slice imaging set-up was developed starting with the open three-lens-element design by Eppink and Parker [12]. By reducing the extraction voltage the sphere is expanded across the detector plane and along the time-of-flight axis until the image becomes too large to fit onto the detector or the particles' momentum is insufficient to be detected on the MCP [79]. To overcome these limitations, two additional lenses are introduced between the extractor and ground lens to accelerate the ion cloud towards the detector and recompress the product sphere in the plane parallel to the detector. Based on this approach, velocity resolutions as high as 0.19% have been achieved for the photodissociation products of CD_3I [80].

Another noteworthy experimental approach for retrieving the central slice of the product scattering distribution directly has been presented by Tonokura and Suzuki [81]. Using a two-laser pump-probe scheme, the authors modified the beam profile of the probe laser to ionize only the central slice of the product scattering distribution after allowing the neutral product Newton sphere to expand for a short period of time.

Following inversion or slice imaging, the speed distribution of the products in pixel units is retrieved by integrating the image over the angular coordinate. Eppink and Parker [12] showed that the image radius must be corrected to account for a

magnification factor N introduced by the ion optics in order to relate the radial coordinate r of the image to the fragment speed v.

$$r = Nvt \tag{1.25}$$

For a homogeneous extraction field $N = 1.0$. As stated by Eppink and Parker [12], the inhomogeneous extraction field introduces only a minor distortion into the focussing of ions with the same mass-to-charge ratio onto the same arrival time at the detector, and the relationship between the ion's mass-to-charge ratio m/q and its time-of-flight t in Equation (1.16) is still approximately valid. Hence, comparing of Equation (1.25) with Equation (1.16) yields:

$$r \propto Nv\sqrt{\frac{m}{qU}} \tag{1.26}$$

$$r \propto N\sqrt{\frac{E_{\mathrm{kin}}}{qU}} \tag{1.27}$$

Here, $E_{\mathrm{kin}} = \frac{1}{2}mv^2$ is the kinetic energy of a detected product moving parallel to the detector. Conversion from the linear velocity into a quadratic energy scale requires a Jacobian transformation in order to ensure that the integral over both distribution remains unchanged during the conversion [65].

$$\int I(E)\mathrm{d}E = \int I(v)\mathrm{d}v \tag{1.28}$$

For small changes in v and E, *i.e.* a small bin size on the velocity axis, Equation (1.28) can be written as,

$$I(E)\mathrm{d}E = I(v)\mathrm{d}v \tag{1.29}$$

$$I(E) = I(v)\frac{\mathrm{d}v}{\mathrm{d}E} \tag{1.30}$$

The Jacobian in (1.30) can be expressed as,

$$E = \frac{1}{2}mv^2 \tag{1.31}$$

$$\frac{\mathrm{d}E}{\mathrm{d}v} = mv \tag{1.32}$$

$$\frac{\mathrm{d}v}{\mathrm{d}E} = \frac{1}{mv}. \tag{1.33}$$

Therefore, it follows that,

$$I(E) = I(v)\frac{1}{mv} \tag{1.34}$$

$$I(E) \propto \frac{I(v)}{v}. \tag{1.35}$$

The velocity distribution is divided by the velocity before being plotted on the energy scale.

The kinetic energy E_{kin} retrieved in this manner is the kinetic energy of the recorded fragment A. The total kinetic energy release, $E_{\mathrm{kin,tot}}$, is the sum of the reaction products' kinetic energy,

$$E_{\mathrm{kin,tot}} = E_{\mathrm{A}} + E_{\mathrm{B}} \tag{1.36}$$

$$E_{\mathrm{kin,tot}} = \frac{1}{2}m_{\mathrm{A}}v_{\mathrm{A}}^2 + \frac{1}{2}m_{\mathrm{B}}v_{\mathrm{B}}^2. \tag{1.37}$$

If the second fragment B of a two-body fragmentation is undetected but known, the total kinetic energy release in the fragmentation can be derived using the conservation of momentum,

$$m_{\mathrm{A}}v_{\mathrm{A}} = m_{\mathrm{B}}v_{\mathrm{B}} \tag{1.38}$$

$$v_{\mathrm{A}} = v_{\mathrm{B}}\frac{m_{\mathrm{B}}}{m_{\mathrm{A}}}. \tag{1.39}$$

Hence, this expression for the unknown velocity of B, v_B, can be used in Equation (1.37) to derive the total kinetic energy release according to,

$$E_{\mathrm{kin,tot}} = (1 + \frac{m_{\mathrm{A}}}{m_{\mathrm{B}}})E_{\mathrm{A}}. \tag{1.40}$$

Because the magnification factor N in Equation (1.27) depends on the design of the velocity-mapping lens and dimensions of the spectrometer, a calibration of the particle's momentum mv or kinetic energy has to be performed using a system of known total kinetic energy release. Alternatively, a simulation of particle trajectories

in a computer model of the spectrometer can be used to determine the magnification factor N.

Velocity-map imaging is a powerful tool for investigating the fragmentation or reaction dynamics of a simple diatomic molecule. However, the application of the method to larger, more complicated molecular systems present some challenges. Firstly, with increasing number of atoms the molecule can follow multiple reaction pathways potentially leading to a large number of fragments. Recording velocity-map images for each of these fragments can be time consuming. This can be a particular problem if expensive sample molecules are required or the experiments demand advanced light sources with limited available experimental time. Secondly, multiple reaction pathways can lead to the same product fragment with identical or very similar kinetic energy release. Multi-mass velocity-map imaging can overcome both of these difficulties. By imaging the scattering distribution of all fragments simultaneously, experimental time is saved, and correlated velocity distributions between pairs of reaction products can be retrieved in the form of covariances, as further described in the following section.

1.2.6 Covariance imaging using the PImMS sensor

The relative yield of a reaction product together with its angular and kinetic energy distribution, provide detailed insights into the reaction mechanism that leads to its production. With increasing complexity of the parent molecule's electronic structure and higher numbers of constituent atoms, it becomes more difficult to deduce a specific reaction pathway from observations made for an individual fragment ion, since a specific fragment can often be formed *via* a number of different pathways. If reactions products from these pathways have similar kinetic energy and angular distributions,

it might not be possible to distinguish them solely from the individual velocity-map image data.

Information on the correlation between the velocity of individual ion pairs, *i.e.* the relative detection time and position on the detector, can potential decipher different reaction pathways. This correlation between detected reaction products is in principle preserved in a velocity-map imaging experiment as product ions from a single reaction event arrive together at the detector of the velocity-map imaging or time-of-flight spectrometer in each experimental cycle.

For very low count rates, in a limit where only particles from a single reaction event are detected, the correlation between both fragment ions can be obtained by measuring the products' arrival times and relative angular and radial positions and assigning them to one coincidence event. For direct imaging of coincidence events, delay-line anodes are used [82].

For higher count rates, the coincidences cannot be measured directly as products from multiple reaction pathways are detected at the same time, averaging correlated ions with products from different reaction events. While in some experiments the count rate can be reduced, *e.g.* by diluting the sample in a molecular beam or by decreasing the intensity of a probe laser, in other experiments using high intensity laser pulses such as those at free-electron laser facilities, reducing the count-rate into the limits of coincidence imaging is difficult. In such count rate regimes, the correlation between reaction products can be obtained by covariance analysis [83, 84].

The covariance describes the statistical relationship between two variables X and

Y according to,

$$\mathrm{cov}(X,Y) = \langle XY \rangle - \langle X \rangle \langle Y \rangle \tag{1.41}$$

Here, $\langle i \rangle$ is the expectation value of i. For the covariance analysis of reaction products in a time-of-flight spectrometer, X, in Equation (1.41), becomes the time-of-flight spectrum and $Y = X^{\mathrm{T}}$ is its transposed form. Figure 1.10 shows a simple representation of time-of-flight covariance between two particles A and B with times-of-flight t_{A} and t_{B}. The obtained time-of-flight covariance is a two-dimensional matrix, in which positive elements describe correlation between two arrival times and non-correlated regions are zero as they are subtracted by the second term in Equation (1.41). The covariance matrix is symmetric along the diagonal elements, which represent the variance of the variable X as,

$$var(X) = \langle X^2 \rangle - \langle X \rangle^2 \tag{1.42}$$

The intensities of elements off-axis to the variance line gives information on the relative yield of reaction channels forming the respective ion pair.

In general, successful covariance analysis requires one to measure and store acquired data for each experimental cycle individually, as signal averaging over many experimental cycles will average out the fluctuations in X and Y which are picked up as covariance. The quality of the covariance results depends strongly on the detection efficiency of the employed imaging detector. The signal-to-noise ratio of off-axis covariance events is proportional to $\sqrt{Np\alpha\beta}$, where N is the number of experimental cycles, p is the number of ion pairs produced in each experimental cycle, and α and β are the detection efficiencies of the two correlated ions [85].

As the covariance analysis obtains the fragments' correlation based on common fluctuations in the yield of products arising from the same reaction event, all fluctuations in the experiment that vary the overall ion yield induce false covariances.

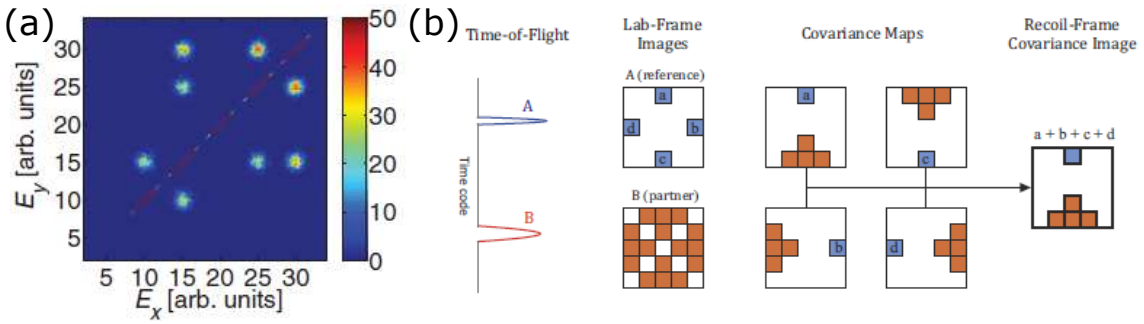


Figure 1.10: (a) Simulated time-of-flight covariance map, adapted from Reference [86], (b) Schematic of the covariance analysis applied in this work to retrieve the recoil-frame covariance image on the right-hand side from the velocity-map images of the fragments A and B on the left-hand side; reproduction from Reference [87] with permission of the American Physical Society.

Examples for such experimental fluctuations are varying output intensity of a laser, and varying molecular beam density. If the fluctuating parameters are precisely monitored, the covariance that such fluctuations would induce can in principle be corrected for using partial covariance techniques [88, 89].

Because of the multi-mass imaging capabilities of the PImMS2 sensor, the covariance expression in Equation (1.41) can be applied to the recorded (x, y, t)-data and extended to correlations between the relative positions of the detected ion on the imaging detector. Thus, relative velocity vectors of multiple detected products are revealed. The covariance analysis algorithm applied throughout this thesis has been developed by Jason W.L. Lee and Craig S. Slater [87, 90, 91]. To simplify the presentation of the resulting covariance matrix, the covariance between the pixel coordinates in two ions is presented in a common recoil frame. The analysis steps involved in converting velocity-map imaging data in the laboratory frame into recoil-frame covariance maps are shown in Figure 1.10 (b). For each ion mass-to-charge ratio, the PImMS data-set is integrated over the time bins corresponding to its arrival time distribution, yielding (x, y)-datasets. One ion is identified as the reference ion, and the covariance of each pixel in the reference image with each pixel in the

partner ion's image is calculated, yielding a covariance map for each pixel in the reference image. Next, each of these covariance maps is rotated to align each pixel in the reference image onto the same vector and the maps are summed together. Thus, the covariance map depicts the relative recoil direction between the species A and B.

Multi-mass imaging using the PImMS sensor and recoil frame covariance analysis has been successfully applied to determine the structure of pre-aligned substituted benzenes [19, 87] and to quantify components in a mixture of structural isomers thereof [21]. Three-fold covariance, elucidating the covariance between three partner ions in a common recoil frame, has also been reported [20].

The following section describes the pixel-imaging mass-spectrometry sensor, which is employed throughout this work for multi-mass and covariance imaging.

1.2.7 The pixel-imaging-mass-spectrometry sensor

The charge-coupled device (CCD) camera [92] used by Eppink and Parker [12] in their early VMI work is a reliable tool for acquiring the velocity-map image of a single fragment. The camera consists of an array of pixels which accumulate charge upon exposure to light. The acquired image corresponds to a map of accumulated charge across the detector, and is read out pixel-by-pixel at the end of each experimental cycle. Since the first application of this device in the early 1970s, CCD cameras have been continuously improved in order to achieve higher resolution and better signal to noise ratio. In an ion imaging experiment the velocity resolution is often limited by the arraysize of the CCD camera. However, the read-out is inherently slow and, at the time of this work, a typical readout time is 5 ms [93] for a commercially available CCD sensor with approximately 1 megapixel resolution. This readout time is

much larger than the ion time-of-flight in a typical velocity-map imaging spectrometer, which is on the order of microseconds. Therefore, a CCD sensor is too slow to capture velocity-map images of multiple fragment ions within the same time-of-flight cycle.

One approach to overcoming the slow read-out time is to employ a "fast framing" CCD sensor, in which each pixel contains a light sensitive element and a number of memory registers to store multiple exposures before the chip is read-out. This allows images to be recorded for a number of different ions on each time-of-flight cycle, which are all read out together at the end of the experimental cycle.

First proof-of-principle experiments [94] showed that fast framing CCD sensors can in principle be used for multi-mass velocity-map imaging. However, increasing the number of memory registers comes at the cost of reducing the light-sensitive area within each pixel. Also, the amount of data quickly becomes too great to transfer off the chip in the available time. Because of the limited number of images that can be stored on the fast framing CCD chip, it also does not provide a general solution to the acquisition of the full time-of-flight spectrum.

The number of required memory registers can be decreased significantly if each pixel only registers an event when it detects light. This task is, however, beyond the abilities of the CCD chip architecture. To achieve this, sensors based on CMOS technology have been developed, incorporating logic circuitry into each pixel. The TimePix/MediPix sensor [95] can be used for direct particle detection in vacuum or in combination with an MCP [18]. The Pixel Imaging Mass Spectrometry (PImMS) sensor [96], employed throughout this work, detects light, and can be used for velocity map imaging with a standard MCP/scintillator screen set-up.

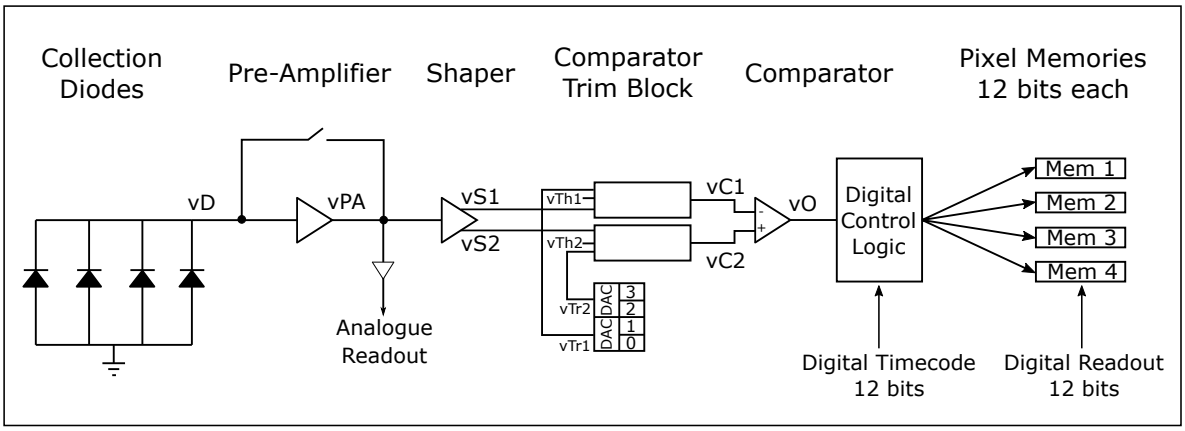


Figure 1.11: Schematic of the operation of an individual pixel in the Pixel-Imaging Mass Spectrometry sensor.

The PImMS sensor has been described in detail before [97]. The first version of the PImMS sensor (PImMS1) [98] consists of a 72x72 pixel array, while the second-generation (PImMS2) sensor is considerably larger, with a 324x324 pixel array. The functionality within an individual pixel is shown schematically in Figure 1.11. Following a global trigger, four in-pixel memory registers allow for sequential particle detection within each pixel during an experimental acquisition cycle. At the beginning of the experimental cycle an internal clock starts in each pixel. When an ion signal from the phosphor screen of the imaging detector is registered, the corresponding time is stored on-chip in one of the memory registers. The time resolution can be as high as 12.5 ns. The combination of a trim register for each pixel, which allows the sensitivity of individual pixels to be tuned, and a global intensity threshold is used to define the number of photons necessary to register an event. Because only active pixels are registered, the number of image "slices" that can be acquired throughout the time-of-flight spectrum is only limited by the memory depth of the 12 bit memory register ($2^{12} = 4096$). This allows for the application of the PImMS sensor in time-of-flight imaging experiments.

The PImMS sensor is controlled using custom software. Data is written out as a list of events of the form (x,y,t,n,r) defining the spatial coordinates (x,y) of the active pixel, the time-code t of the event, the number n of the experimental cycle and the pixel timing register r the event was stored in ($r = 0, 1, 2, 3$). The sensor also has an analogue mode, which yields a conventional image for use when focussing the camera lens and setting-up the camera system.

An ion event detected by an ion imaging detector results in a flash of light detected by the camera system. The flash of light has a sharp rising edge, but a long falling edge determined by the emission lifetime of the scintillator. As the PImMS camera pixels are triggered when the signal exceeds a pre-programmed threshold, the ion event is registered at its rising edge. Each flash of light from the scintillator screen has approximately a Gaussian spatial profile, with highest intensity towards its centre, and illuminates multiple pixels on the camera sensor. Furthermore, a single ion event might stretch over multiple time-codes as higher intensity parts of the profile overcome the signal threshold early and are registered at shorter time. Single event counting and centroiding is used to reduce the cluster of pixels triggered by each event to a single pixel. In an approach by Slater *et al.* [19], the cluster is reduced to the earliest time-code, and to the centre-of-mass of the pixel area. Following the centroiding procedure, the time-of-flight resolution of the processed data is primarily determined by the 12.5 ns pixel clock of the PImMS sensor, and not by the lifetime of the scintillator material. However, while the event is triggered from the rising edge of the light flash on the screen, a second ion event within the decay-time of the preceding flash might not be recorded depending on the light intensity. Furthermore, dead-times of the MCP-channels, which vary strongly with signal load, have to be taken into account.

1.3 Outline of the thesis

In this chapter, it has been shown how the multi-mass imaging technique using the PImMS2 sensor complements and widens the available experimental methods for the investigation of chemical reaction dynamics in the gas phase. In the following three chapters, the application of this technique is showcased on experiments investigating three distinct research topics. In Chapter 2, velocity-map imaging is applied to investigate the dissociation dynamics of the niobium oxide molecule and further applications of multi-mass imaging for the study of *d*-metal containing neutral and charged cluster are outlined. In Chapter 3, the application of the PImMS2 sensor at the free-electron laser FLASH and the dissociation dynamics of the CH_2BrI molecule are explored in a UV-pump XUV-probe experiment. In Chapter 4, the scope of multi-mass imaging is further extended, investigating the fragmentation dynamics of the CF_3I molecule upon electron ionization. This thesis is concluded with a summary of the presented work and an outlook into future developments of the multi-mass imaging technique.

Chapter 2

Photofragmentation of *d*-metal containing clusters and oxides

In this chapter, the fragmentation and ionization dynamics of *d*-metal containing molecules is probed using velocity-map imaging of photoions and photoelectrons. Upon analysis of the photofragments velocity-map images a refined value of the NbO and NbO^+ dissociation energy has been determined as $60,650 \pm 124$ cm^{-1} and $57,414 \pm 124$ cm^{-1}, respectively. Moreover, a photoionization study of NbO, using photoelectron velocity-map imaging, yields a vibrational constant of 1002 ± 11 cm^{-1} for the $X^3\Sigma^-$ state of the NbO^+ ion. Recent modifications to the experimental set-up designed to permit velocity-map imaging studies of charged cluster fragmentation are outlined and the current state of the experiment is discussed. This chapter showcases velocity-map imaging as a powerful experimental tool to elucidate electronic states of the photofragmenation products.

2.1 Introduction

The partially filled d-orbitals in transition metal atoms give rise to a rich electronic structure such that molecules and clusters containing these atoms may fragment on many potential energy surfaces *via* a large number of possible reaction trajectories. These molecules and clusters are not only challenging and exciting to study, but the electronic structure often leads to catalytic reactivity, *e.g.* in biochemical reactions, where d-metals form the active center of most enzymes, and heterogeneous catalysis in the industrial-scale synthesis of chemicals. In both of these examples, the metal mediates a reaction by lowering the activation barrier from the reactant to the product.

Neutral metal oxides are of further interest to the astrochemistry community as these species are often identified in the spectra of stars. For example, niobium oxide (NbO), the subject of this chapter, has been tentatively identified in the S-type star R. Cygni [99, 100].

One objective of this work is the determination of the dissociation energy of neutral NbO. The dissociation energies of the neutral and cationic metal-oxide, $D_0(\mathrm{NbO})$ and $D_0(\mathrm{NbO^+})$, and the oxide and metal atom adiabatic ionization energies, $E_\mathrm{i}(\mathrm{NbO})$ and $E_\mathrm{i}(\mathrm{Nb})$, are state properties and independent of the ionization or dissociation pathway. The properties are linked to each other in a thermodynamic cycle shown in Figure 2.1 (a) and more specifically in the molecular potentials of the neutral and charged molecules shown in (b).

Ionization and dissociation energies of NbO have been determined in several studies employing Knudsen cell mass-spectrometry [101], ion beam mass-spectrometry [102] and photoelectron spectroscopy [103]. Knowledge of the neutral dissociation energy

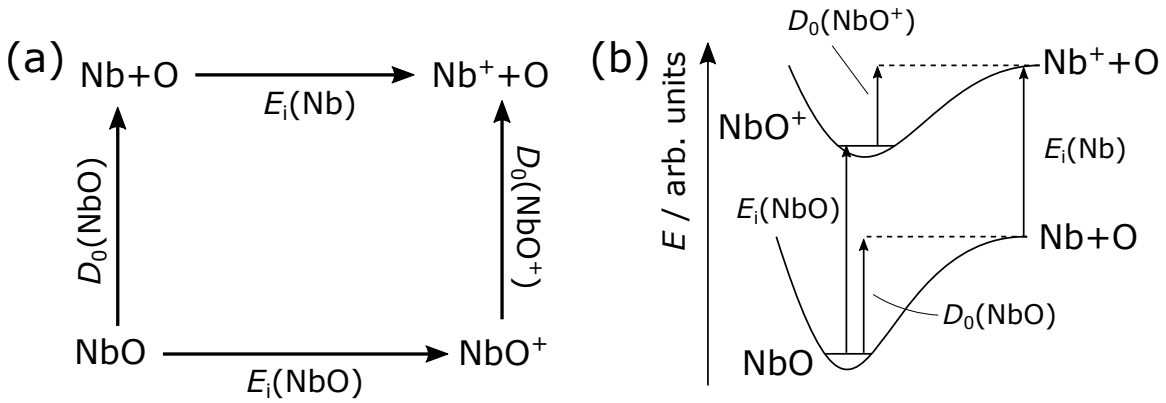


Figure 2.1: (a) Thermodynamic cycle linking the ionization energies of the niobium atom, E_i(Nb), and oxide, E_i(NbO), with the dissociation energies of the neutral, D_0(NbO), and charged niobium oxide, $D_0(NbO^+)$; (b) description of the thermodynamical cycle in the molecular potentials of NbO and NbO^+.

together with the ionization energies of the molecule and the metal atom allow for the determination of the dissociation energy of the NbO^+ ion as shown in Figure 2.1 and according to,

$$D_0(NbO^+) = D_0(NbO) + E_i(Nb) - E_i(NbO). \tag{2.1}$$

While the values for the ionization energy of NbO and Nb are readily available with high precision, values of the neutral oxide dissociation energy are mostly measured indirectly using the Knudsen cell method [101]. Given the reviewed literature to date, the most precise value of the dissociation energy is 7.53 ± 0.11 eV [104] derived by measuring the ionization energy of NbO as 7.160 ± 0.004 eV and employing the thermodynamic cycle in Equation (2.1) together with the ionization energy of metal atom, 6.75885 ± 0.00004 eV [105], and dissociation energy of the NbO^+ ion, 7.13 ± 0.11 eV [102], determined in a guided ion beam mass-spectrometry experiment. In this approach, however, the precision of the result is always limited by the precision of the least well-determined value of the thermodynamic cycle.

In order to complement the available data on NbO, an improved value of the neutral oxide dissociation energy is reported. In the approach employed in this chapter,

neutral niobium oxide molecules are dissociated with multiple photons and the resulting neutral niobium atom is ionized in the same laser pulse. The internal energy of the niobium oxide, $E_{\mathrm{int,NbO}}$, and photofragments, $E_{\mathrm{int,Nb}}$ and $E_{\mathrm{int,O}}$, are related to the energy of n photons, $nh\nu$, the dissociation energy, $D_0(\mathrm{NbO})$, and the total-kinetic energy release of both neutral fragments, $E_{\mathrm{kin,tot}}$, as,

$$E_{\mathrm{int,NbO}} + nh\nu = D_0(\mathrm{NbO}) + E_{\mathrm{int,Nb}} + E_{\mathrm{int,O}} + E_{\mathrm{kin,tot}}. \tag{2.2}$$

The internal energy of NbO prepared in a molecular beam is negligible. With knowledge of the photon energy and product state energies, the dissociation energy is determined by measuring the fragment kinetic energy for dissociation at different photon energies across the visible spectrum. Based on this strategy, the dissociation energy of CuO and Cu_2 [106], AgO and Ag-RG (RG=Ar, Kr, Xe) [107], MoO and CrO [108] and, most recently, VO [109] have been determined successfully.

It is of further interest to expand our experimental set-up to allow for the study of charged metal compounds. This not only complements the dissociation energy of neutral species in the above thermodynamic cycle but would allow for the investigation of a large number of charged ligand metal complexes, which are of great importance in homogeneous catalysis. The preparation and velocity-map imaging of charged parent species is an ongoing challenge in this experimental set-up, but several approaches are known to date, for example in work from Maner *et al.* [110] and Johnston *et al.* [111]. Based on the two experimental approaches published to date, a small number of charged metal compounds have been studied recently [112–114]. The first steps to improve our experimental set-up towards the investigation of charge species' fragmentation dynamics have been taken and the well known photofragmentation of VCO_2^+ [115–117] has been investigated to illustrate the experiment in its present stage.

The remainder of this chapter is structured as follows. Firstly, the experimental set-up is described for the study of neutral and charged species of interest. Next, the specific analysis procedure of VMI data in this chapter is described based on the more general description in Section 1.2.5. Results for photofragment imaging of NbO is presented concluding in the determination of the dissociation energy of NbO. Next, recent application of photoelectron velocity-map imaging to the experiment is described on the example of photoionization of atomic vanadium and the technique is further used to study the ionization of niobium oxide. Following this, a preliminary photofragmentation study of VCO_2^+ is presented show-casing the recent experimental modification. The chapter is concluded with a summary of the findings and outlook into future studies.

2.2 Experimental considerations

Figure 2.2 gives an overview on the experimental set-up used in this study. The set-up consists of four vacuum chambers and a typical base pressure on the order of 10^{-9} mbar is maintained with three turbo pumps on the source (Edwards, STP A1603C), first differential (Edwards, EXT75DX) and scattering chamber (Oerlikon, Turbovac TMP151). The experiment can be operated in two modes to study fragmentation dynamics of either neutral or charged metal clusters, and it is operated in six steps, labelled 1-6 in Figure 2.2.

The source chamber contains a laser ablation source [27, 28] forming a molecular beam pulse of both neutral and charged metal containing molecules. This process is described in more detail in Section 1.2.1. In brief, a beam pulse of carrier gas (He, 3 bar) is formed by supersonic expansion *via* a pulsed valve (step 1) and picks up metal compounds which are formed by laser ablation of a rotating metal disc (step 2)

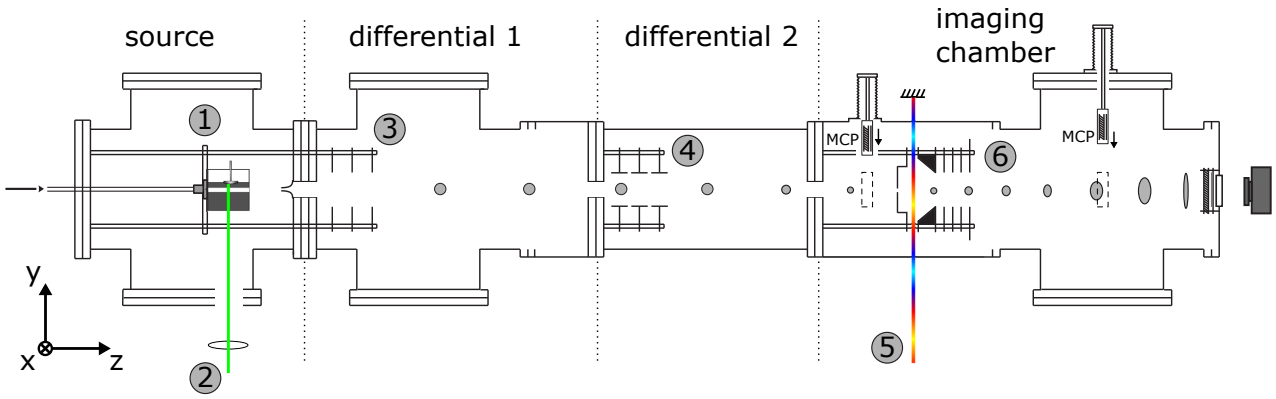


Figure 2.2: Experimental set-up of the metal cluster velocity-map imaging spectrometer containing of 4 vacuum chambers: source, differential 1 and 2 and imaging chamber.

using the second harmonic of a Nd:YAG laser (532 nm, Continuum Minilite). The molecular beam is collimated with a skimmer (1 mm diameter, Beam Dynamics, type 2) and passes two differential stages containing a homebuilt Wiley McLaren lens [64] in differential chamber 1 and a homebuilt Einzel lens [26, p.363] in differential chamber two. A pulsed field applied to the Wiley McLaren lens extracts charged species from the beam and separates them according to their mass-to-charge ratio along the flight-path between the first and second differential chamber (step 3). In the second differential chamber a pulsed Einzel lens is used to focus charged components into the scattering chamber (step 4). A retractable multi-channel plate (MCP) detector (Kore Technology Ltd.) is used to monitor the ion arrival time at the entrance to the scattering chamber. For the investigation of neutral species the Wiley McLaren and Einzel lens elements are held at ground potential and the beam pulse passes freely into the scattering chamber. In either of the two modes the beam enters the velocity-map imaging lens through a 2 mm hole in the back of the repeller element.

Neutral or charged species in the molecular beam are dissociated in the interaction region between the repeller and extractor elements (step 5) by the focussed output of an optical-parametric oscillator (OPO, Continuum Panther) or a dye laser (Sirah

Cobra Sketch) in the visible part of the spectrum, each pumped with the third harmonic output of Nd:YAG laser (355 nm, Continuum Surelite). Neutral species are also ionized by the focussed dissociation laser. The product Newton sphere is velocity-mapped onto an imaging detector (step 6) consisting of an MCP (chevron stack) and scintillator screen (P46). A second retractable MCP detector (Kore Technology Ltd.) can be placed into the flight path to study the intensity spectrum of photoproducts as a function of the OPO- or dye-laser wavelength. The velocity-map imaging lens is designed after Wrede *et al.* [118] employing a conical extractor which produces a nearly uniform extraction field minimizing the aberrations from curved field lines in the original velocity-map imaging lens design [12]. Typical extraction voltages are 2500 V and 1500 V on the repeller and extractor element, respectively. In charge cluster mode, the velocity-map imaging lens is kept at ground potential while the parent species enters the interaction region and is pulsed up to typical velocity-map imaging potentials carefully timed with the photodissociation laser using a pair of fast voltage switches (Behlke). The visual response of the imaging detector is captured using a camera based on either a CCD (Photek, VID240) or PImMS2 sensor.

The experiment is operated at a repetition rate of 10 Hz and one experimental cycle is sketched out in Figure 2.3. To begin the experimental cycle, the pulsed nozzle is opened at t_{MB} and the molecular beam pulse is partially expanded into the ablation block. Shortly afterwards, the ablation laser is fired and the expanding molecular beam pulse picks-up and cools the plasma created on the rotating metal target. For the investigation of neutral species (dashed line), the Wiley McLaren and Einzel lenses are kept at ground potential and the neutral species traverse the experiment and are both fragmented and ionized at t'_{PDL}. The charged photoproducts are extracted and velocity-mapped with a constant extraction potential to the VMI lens.

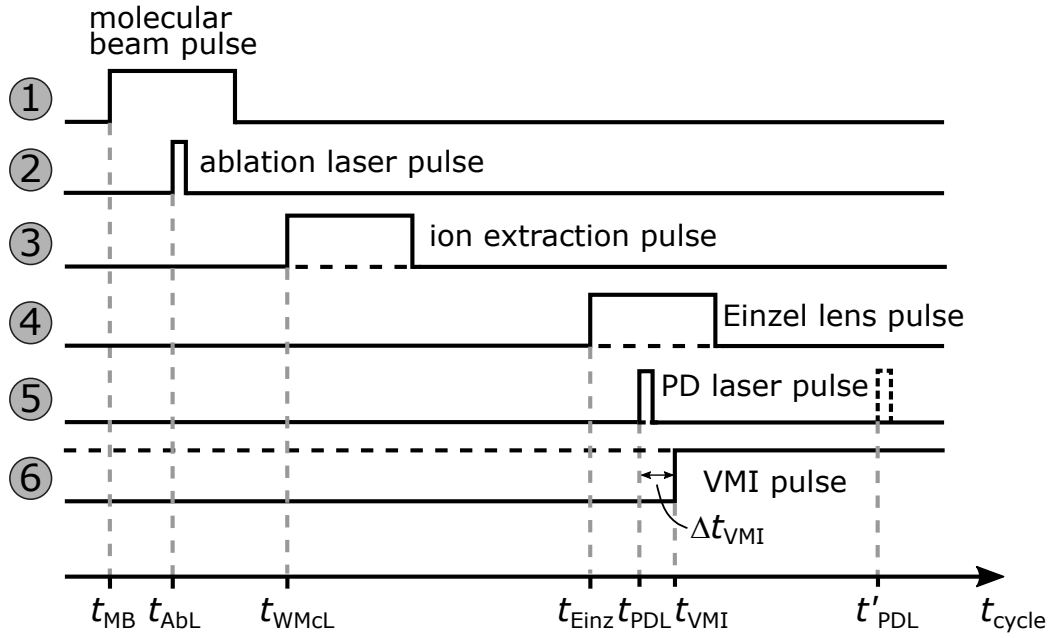


Figure 2.3: Schematic overview of one experimental cycle investigating the photofragmentation of charged metal cluster (solid line) and neutral species (dashed line); the labels 1-6 are consistent with the labelled experimental elements in Figure 2.2; for the investigation of charged metal clusters: The molecular beam valve, ablation laser, Wiley McLaren lens, Einzel lens, photodissociation laser and VMI lens are pulsed at t_{MB}, t_{WMcL}, t_{Einz}, t_{PDL} and t_{VMI} along the time of the experimental cycle t_{cycle}; for the investigation of neutral species, the Wiley McLaren and Einzel lens are kept at ground potential and a constant extraction voltage is applied to the VMI lens.

To study charged metal clusters, these species are extracted from the molecular beam with the Wiley McLaren lens behind the skimmer at the entrance to the first differential chamber at t_{WMcL} (step 3). The Einzel lens is pulsed up at t_{Einz} shortly before the species of interest has arrived in the second differential chamber focussing ions with this mass-to-charge ratio and heavier species into the scattering chamber (step 4). This largely discriminates against lighter ions as these will not reach the scattering chamber on their original flight path. After the species of interest has entered the velocity-map imaging lens, the extraction potential is rapidly pulsed up at t_{VMI} preventing heavier species from entering the interaction region with the photodissociation laser (step 6) and extracting photoproducts which are formed in the interaction with the photodissociation laser at t_{PDL}. Typically, the photodissociation

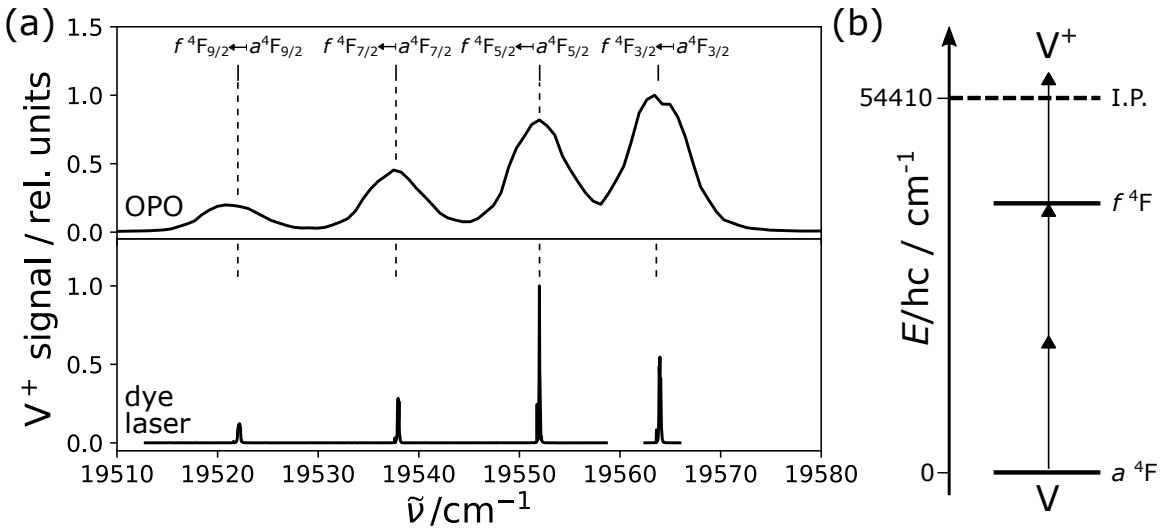


Figure 2.4: (a) (2+1)-REMPI spectrum of atomic vanadium, recorded as the V^+ ion signal for different wavenumbers of an optical parametric oscillator (top) and dye laser (bottom); in this spectral region vanadium atoms are ionized in a three-photon transition as shown in (b); the photon energy of the ionization laser is on resonance with the $f^4\mathrm{F} \leftarrow a^4\mathrm{F}$ two-photon transition from the ground state; a third photon is used to overcome the ionization potential, I.P., from the f-state.

laser is fired earlier for the fragmentation of charged species compared to the investigation of neutral species as the neutral molecules travel with the speed from the supersonic expansion which is smaller than the speed of the extracted charged species.

The output wavelengths of the OPO and dye laser were calibrated on the previously observed $f^4\mathrm{F}_J \leftarrow a^4\mathrm{F}_J$ transition of atomic vanadium. The output of a dye laser is selected and the wavelength is changed by varying the angle of a diffraction grating inside the dye laser resonator cavity [50, pp.346]. The wavelength of the OPO output is set by varying the lattice orientation of the non-linear medium relative to the wavevector of the pump pulse as described in Section 1.2.3.2. The output wavelength of both lasers is scanned over the $f^4\mathrm{F}_J \leftarrow a^4\mathrm{F}_J$ two photon transition and vanadium atoms in the molecular beam pulse, prepared from laser ablation of a vanadium disc (Goodfellow, 99.98%), are ionized. The V^+ yield is recorded as the (2+1)-REMPI spectrum with the OPO and dye laser, and the spectra are shown in Figure 2.4 (a)

on the top and bottom, respectively. The (2+1)-REMPI transition is schematically shown in Figure 2.4 (b). Three photons in the green part of the spectrum are required to overcome the ionization potential of the vanadium atom at 54410 cm^{-1} [119] *via* the $f^4\mathrm{F}_J$ state manifold.

J	$E_\mathrm{V}(a^4\mathrm{F}_J)$ / cm^{-1}	$E_\mathrm{V}(f^4\mathrm{F}_J)$ / cm^{-1}
3/2	0.000	39,127.228
5/2	137.383	39,241.384
7/2	323.432	39,398.893
9/2	552.955	39,596.988

Table 2.1: energy levels of the $a^4\mathrm{F}_J$ and $f^4\mathrm{F}_J$ manifold for J =3/2, 5/2, 7/2, 9/2; taken from Reference [120] and [121].

The (2+1)-REMPI spectrum of atomic vanadium is compared to known energy levels, E_V, of the $a^4\mathrm{F}_J$ ground state and $f^4\mathrm{F}_J$-state manifold from Reference [120] and [121], which are listed in Table 2.1. Four transitions for ΔJ = 0 are observed in the REMPI spectrum in Figure 2.4, and in the following data analysis the wavelength of OPO and dye laser is corrected so that the observed lines match the tabulated values of the vanadium energy levels. The observed peak-width is consistent with the factory specified linewidths of the OPO, $< 6\,\mathrm{cm}^{-1}$ [122], and dye laser, $0.08\,\mathrm{cm}^{-1}$[123].

2.3 Analysis of velocity-map imaging data

Following the determination of the image center, the recorded image is rotated by six degrees counter-clockwise to align the observed anisotropy with the image axis. The image is symmetrized along both image axes and then Abel inverted, and kinetic energy and angular distributions are retrieved using the pBASEX algorithm [71]. Basis functions employed in the inversion consist of one Gaussian function per radial element with a full-width-at-half-maximum of 0.7 pixel and Legendre polynomials up to $l = 6$, as outlined in Section 1.2.5. The energy axis, E_{Nb^+}, of the retrieved kinetic energy distributions is defined as:

$$E_{Nb^+} = \frac{1}{2} m_{Nb} v_{Nb^+}^2 \tag{2.3}$$

where $m_{Nb} = 92.906\,\text{amu}$ is the mass of a Nb atom and the velocity of the Nb^+ fragment ion is given according to Equation (1.25) as,

$$v_{Nb} = \frac{r}{N t_{Nb^+}}. \tag{2.4}$$

Here, N is the spectrometer-magnification factor which was previously determined as 1.055 [109, 124], and t_{Nb+} is the Nb^+ time-of-flight. r is the radial distance from the image centre of the recorded ion event in units of meter. In the set-up of the camera a typical calibration factor for conversion from camera pixel units to distance on the detector has been determined as $3.673 \cdot 10^{-5}\,\text{m/pixel}$. This value varies slightly when the camera is replaced or the camera focus is changed and needs to be redetermined when the camera configuration changes. The ion time-of-flight was determined in advance of every image acquisition and typical time-of-flights of Nb^+ ions in this study were $5.335\,\mu\text{s}$, $7.350\,\mu\text{s}$ and $10.2410\,\mu\text{s}$ for extraction voltages of 5000 V, 2500 V and 1250 V, respectively.

2.4 Results and discussion

2.4.1 Photofragmentation dynamics of niobium oxide

The fragmentation of niobium oxide (NbO) has been investigated in the vicinity of the $C^4\Sigma^- \leftarrow\!\shortmid X^4\Sigma^-(v',0)$ transitions in the blue part of the spectrum. In this energy range at least three photons are required to overcome the dissociation energy which was previously determined as 7.53 ± 0.11 eV [104] ($60,734 \pm 887$ cm^{-1}). The non-resonant multi-photon dissociation is inefficient but its efficiency is greatly enhanced if one photon is on resonance with an intermediate state according to,

$$\mathrm{NbO}(X^4\Sigma^-) \xrightarrow{\mathrm{h}\nu} \mathrm{NbO}(C^4\Sigma^-) \xrightarrow{\geq 2\mathrm{h}\nu} \mathrm{Nb}^* + \mathrm{O} \tag{2.5}$$

The niobium atom produced in Reaction (2.5) can be ionized by additional photons in the same laser pulse, and velocity-map images of the Nb^+ product ions are recorded.

While some NbO molecules are dissociated, some are ionized resonantly. The yield of NbO^+ ions is recorded across the spectrum and the resulting (1+n)-REMPI spectrum is shown in Figure 2.5 (a). n is the number of photons required to overcome the ionization potential from the intermediate state, and in this spectral region at least three photons are required to overcome the first ionization potential of NbO, 7.160 ± 0.004 eV [104] ($57,749 \pm 33$ cm^{-1}), from the ground state. See Section 1.2.4 for more detail on REMPI. By assigning the transitions observed in the REMPI spectrum, the nature and spectral position of the intermediate state available for the multi-photon fragmentation of NbO can be identified.

The NbO ground state has been described by Brom *et al.* [127] as $X^4\Sigma^-$, and the ground state electron configuration is shown in Figure 2.6 (a). The three unpaired electrons occupy the non-bonding 2δ and 12σ orbitals formed from the Nb $4d$ and $5s$ atomic orbitals. The spectrum of niobium oxide (NbO) was first studied by Rao [130]

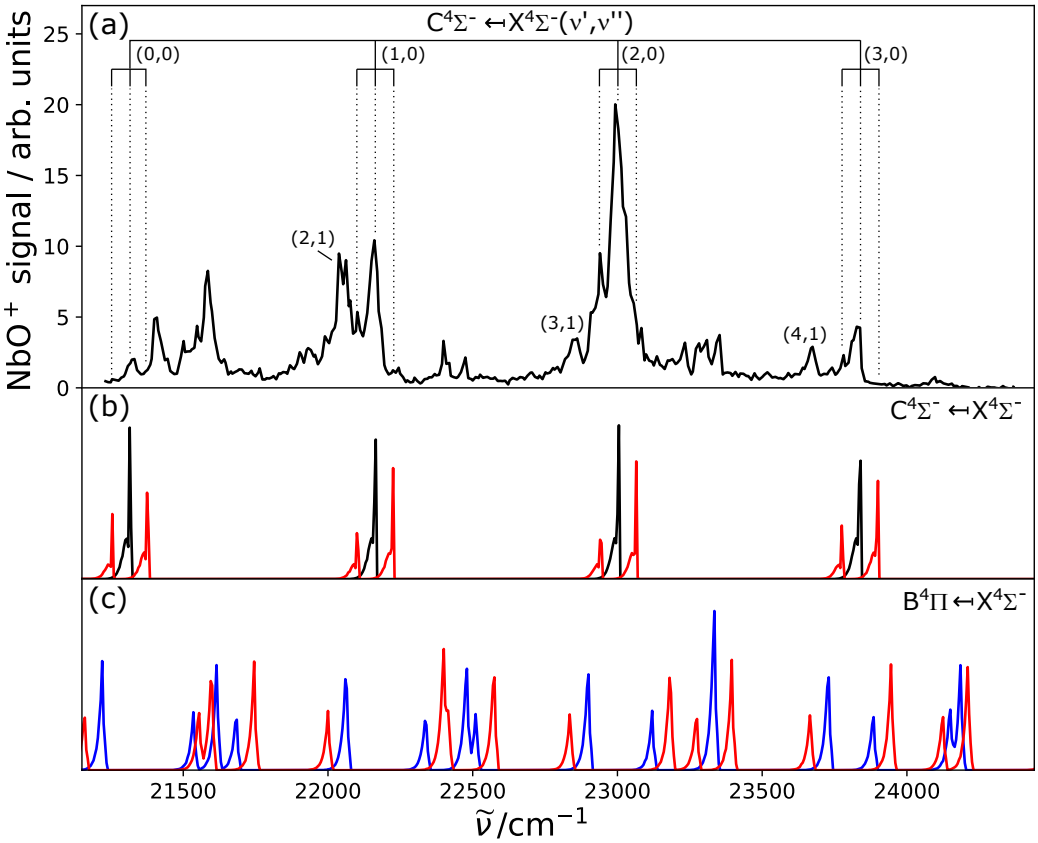


Figure 2.5: (a) (1+2)-REMPI spectrum of the NbO molecule in the vicinity of the $C^4\Sigma^- \leftarrow\!\!\!\shortmid\; X^4\Sigma^-(v',0)$ transitions for $v' = 0, 1, 2, 3$; the hot band transitions (2,1), (3,1) and (4,1) are also assigned; unassigned bands can mostly be attributed to resonant ionization *via* the B-state show in (c); (b) simulation of the $C^4\Sigma^- \leftarrow\!\!\!\shortmid\; X^4\Sigma^-$ transition based on spectroscopic values in Reference [125]; red bands correspond to transitions which are forbidden in Hund's case (a); (c) simulation of the $B^4\Pi \leftarrow\!\!\!\shortmid\; X^4\Sigma^-$ transition based on spectroscopic values in Reference [126].

observing three band-systems in the visible part of the spectrum. These were later attributed to the $C^4\Sigma^- \leftarrow\!\!\!\shortmid\; X^4\Sigma^-$ [104, 125, 128, 131, 132] and $B^4\Pi \leftarrow\!\!\!\shortmid\; X^4\Sigma^-$ [126, 128, 133] transitions in the blue and red part of the visible spectrum, respectively. The energies of the quartet states in the visible region of the spectrum are summarized in Figure 2.6. The B-state splits into four spin-orbit levels with total electronic angular momenta $\Omega = -1/2, 1/2, 3/2, 5/2$. Both the ground and C-state, show evidence for Hund's case (a) coupling [128]. This is rather uncommon for $^4\Sigma$ states because the electronic spin is usually not coupled to the internuclear axis for $L = 0$ and such

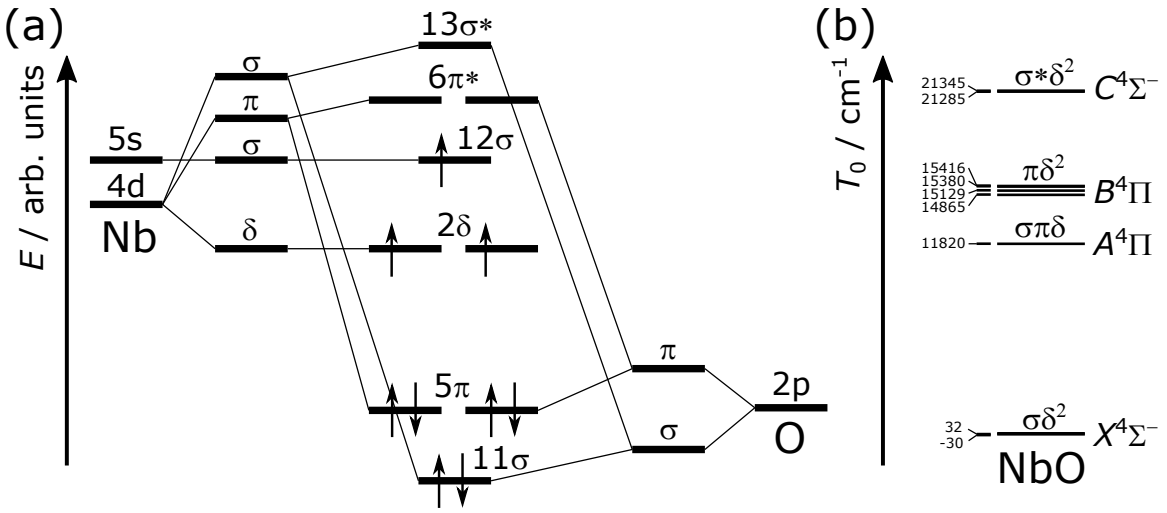


Figure 2.6: (a) Electron configuration of the $X^4\Sigma^-$ ground state of NbO [127]; the three unpaired electrons occupy non-bonding orbitals 2δ and 12σ; (b) energies of the low-lying quartet electronic states, T_0 [125, 128]; six states with doublet multiplicity are also known in the same spectral range [129].

molecules are typically better described within Hund's case (b) [134]. However, the assignment is consistent with the relatively large second order spin-orbit splitting of $62\,\mathrm{cm}^{-1}$ in the ground and $60\,\mathrm{cm}^{-1}$ in the C-state [128] which confines the electronic spin to the internuclear axis for low rotational levels. Similar second order spin-orbit interactions were observed before in SnH [135], GeF [136] and MoN [137]. Cheval *et al.* [125] attributed the observed large second order spin-orbit splitting in NbO to interaction of the $^4\Sigma^-$ state with a $^2\Sigma^+$ state which the authors predicted at approximately 10,000 cm^{-1} above the ground state.

Figure 2.5 (b) and (c) show simulations of the $C^4\Sigma^- \leftarrow\!\!\shortmid\; X^4\Sigma^-$ and $B^4\Pi \leftarrow\!\!\shortmid\; X^4\Sigma^-$ transitions, respectively. The transitions are simulated with the PGOPHER software suite [138] using spectroscopic values from Cheval *et al.* [125] for the X-state and C-state and from Kingston *et al.* [126] for the B-state. The linewidth of the fragmentation laser of 6 cm^{-1} and an internal temperature of the sample of 150 K are considered in the simulation. Transitions shown in black and blue are allowed

according to the selection rule, $\Delta\Sigma = 0$, for for electronic transitions within Hund's case(a) molecules, and forbidden transitions are shown in red.

A comparison of the simulated spectra in (b) and (c) to the REMPI spectrum in (a) shows that this spectral region is dominated by transitions *via* the $C^4\Sigma^-$ state which has its origin band at 21346.002 cm^{-1} [125]. Transitions from the ground state *via* the vibrational excited levels, $v' = 1, 2, 3$, are observed and assigned in (a). Each vibrational branch is split into three components of the $C^4\Sigma^-_{|\Sigma'|} \leftarrow\!\!\shortmid X^4\Sigma^-_{|\Sigma''|}$ for transitions between the different fine structure components of the C- and X-state. The $\Sigma = 1/2$ and $3/2$ components are split by 62 cm^{-1} [128] in the ground and 60 cm^{-1} [125] in the excited C-state and previous studies [125, 128] showed that both states are best described in Hund's case (a) for low rotational level. The central component of the observed triplet can be attributed to transitions $\Delta\Sigma = 0$ which are allowed in Hund's case (a). Hund's case (a) forbidden transitions $\Sigma' = 1/2 \leftarrow\!\!\shortmid \Sigma'' = 3/2$ and $\Sigma' = 3/2 \leftarrow\!\!\shortmid \Sigma'' = 1/2$ can also be observed due to the uncoupling of the spin from the nuclear axis into Hund's case (b) for higher rotational states [128]. Transitions observed at $22,040$, $22,850$ and $22,670$ cm^{-1} are assigned to hot-band transitions from the vibrational excited level, $v'' = 1$, in the ground state which is populated in the molecular beam due to the inefficient cooling of the vibrations in the supersonic expansion. Observed transitions at $21,500$, $22,400$, $23,300$, and $23,900$ cm^{-1}, are tentatively attributed to transitions *via* the vibrational excited levels, $v' = 7, 8, 9, 10$, of the $B^4\Pi$ state.

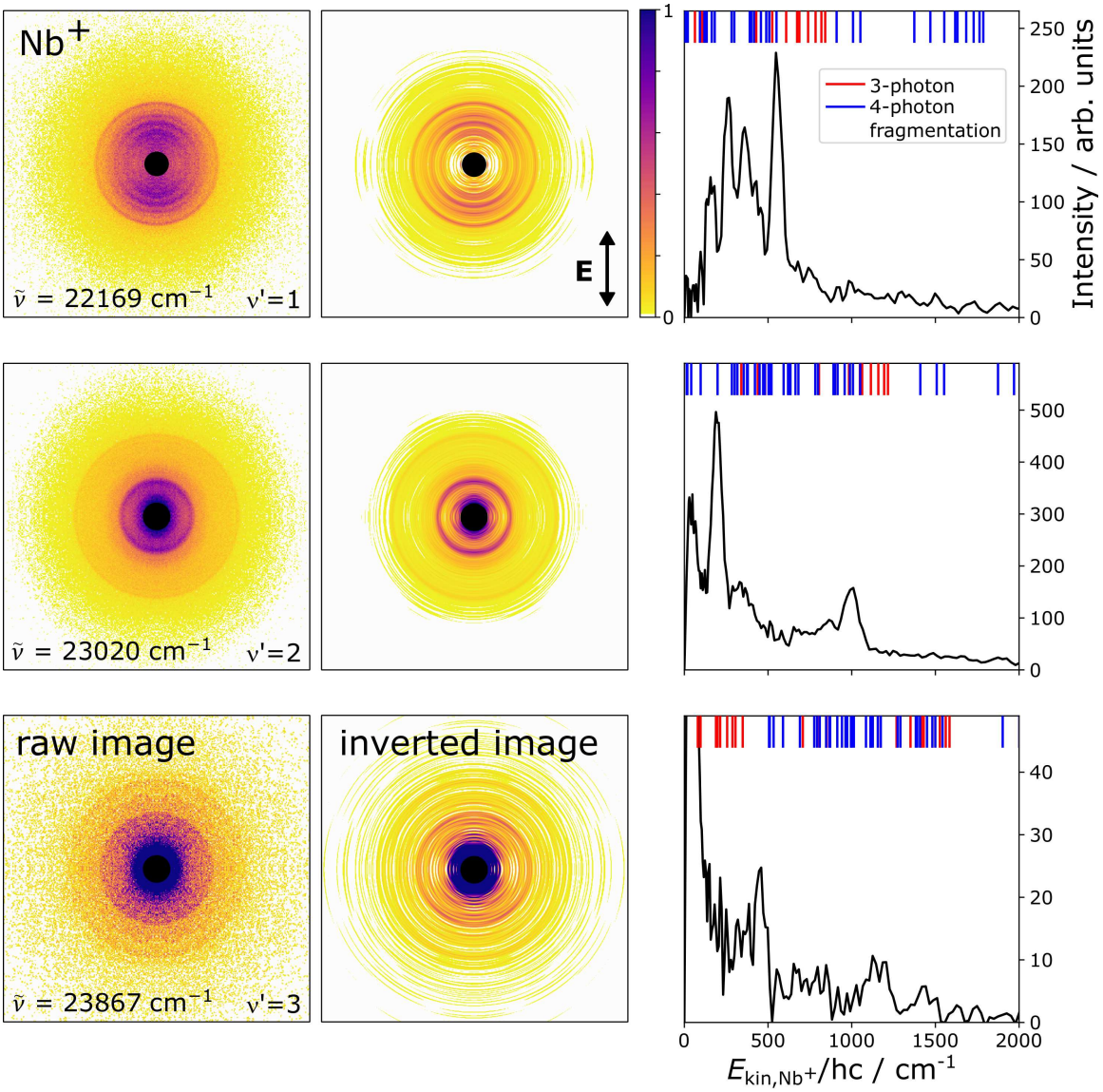


Figure 2.7: Velocity-map images of Nb^+ fragment ions produced on resonance with the $C^4\Sigma^- \leftarrow X^4\Sigma^-(v',0)$ transition for $v' = 1, 2$ and 3 from top to bottom; the symmetrized velocity-map image is shown on the left, Abel-inverted images in the centre and the Nb^+ kinetic energy, $E_{\mathrm{kin,Nb^+}}$, distributions are shown in the right-hand side column; the kinetic energy distributions are compared to kinetic energies of Nb atoms formed in a resonant three-photon (red ticks) and four-photon (blue ticks) fragmentation for different combinations of product states in the niobium and oxygen atom.

Figure 2.7 shows velocity-map images of the Nb^+ photoproducts produced on resonance with the vibrational excited levels, $v' = 1, 2, 3$, of the $C^4\Sigma^- \leftarrow X^4\Sigma^-(v',0)$ transition. Symmetrized velocity-map images are shown on the left-hand side, pBASEX [71] inverted images are shown in the middle and resulting Nb^+ kinetic energy

distributions are shown on the right-hand side. The photofragmentation laser is polarized along the vertical image axis.

Fragment kinetic energy, $E_{\mathrm{kin,Nb}}$, observed in Figure 2.7 is a fraction of the total kinetic energy release, $E_{\mathrm{kin,tot}}$, from the dissociation of the NbO molecule in Reaction (2.5). The total kinetic energy release can be derived from the fragment kinetic energy release as described in Section 1.2.5 according to,

$$E_{\mathrm{kin,tot}} = \left(1 + \frac{m_{\mathrm{Nb}}}{m_{\mathrm{O}}}\right) \cdot E_{\mathrm{kin,Nb}}. \tag{2.6}$$

The total kinetic energy release derived in Equation (2.6), the internal energy of the NbO reactant, $E_{\mathrm{int,NbO}}$, and the photoproducts, $E_{\mathrm{int,Nb}} + E_{\mathrm{int,O}}$, dissociation energy of the NbO molecule, $D_0(\mathrm{NbO})$, and the energy of the n photons involved in the photofragmentation, $nh\nu$, are related according to conservation of energy:

$$E_{\mathrm{int,NbO}} + nh\nu = D_0(\mathrm{NbO}) + E_{\mathrm{Nb}} + E_{\mathrm{O}} + E_{\mathrm{kin,tot}}. \tag{2.7}$$

Using Equation (2.7), the fragment kinetic energy is derived for different niobium and oxygen product state combinations, for the dissociation energy, $D_0 = 60,850 \pm 165$ cm^{-1}, and for the number of photons, $n = 3$ and $n = 4$, determined in this work in Section 2.4.1.1.

Figure 2.8 summarizes the electronic states of niobium and oxygen which can be populated in the three-photon or four-photon dissociation of NbO. There is a large number of low-lying electronic states of niobium with a total spin angular momentum quantum numbers, $S = 5/2, 3/2$ and $1/2$. In the same energy range, the oxygen atom has only one electronic excited state, $^1\mathrm{D}_2$, at 15,867.862 cm^{-1}, above the spin-orbit manifold of the $^3\mathrm{P}_J$ ground state.

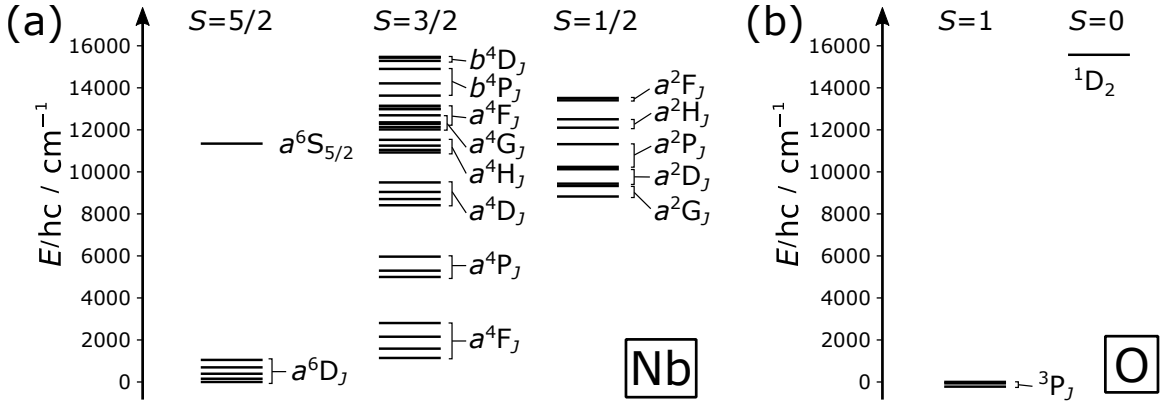


Figure 2.8: Electronic states of (a) niobium [139] and (b) oxygen atoms [140] accessible in the three and four-photon dissociation of niobium oxide.

In Figure 2.9, the energy of the product electronic states is compared to the NbO states involved in the fragmentation, $X^4\Sigma^-$ and $C^4\Sigma^-$ illustrating the complexity of the photodissociation dynamics in this region. The potential energy curve of the NbO $X^4\Sigma^-$ ground state is shown alongside with the product states at energies $D_0+E_\mathrm{O}+E_\mathrm{Nb}$. Multi-photon fragmentation *via* different vibrational level of the molecular C-state excites the molecule to different energies in the product state manifold shown as dashed lines. Product states are shown as black, blue and red lines fragmentation channel producing niobium atoms in sextet, quartet and doublet states, respectively.

The three-photon dissociation can only produce ground-state oxygen atoms, and most of the excess energy of the fragmentation is transferred in electronic excitation of the niobium atom. In a four-photon fragmentation, enough energy is available to produce electronically excited oxygen atoms in the $^1\mathrm{D}_2$ state.

In total, 44 different niobium electronic states can be accessed either in combination with three different spin-orbit levels of the oxygen ground state in a three-photon dissociation or in combination with the oxygen $^1\mathrm{D}_2$ state. This yields 176 exit chan-

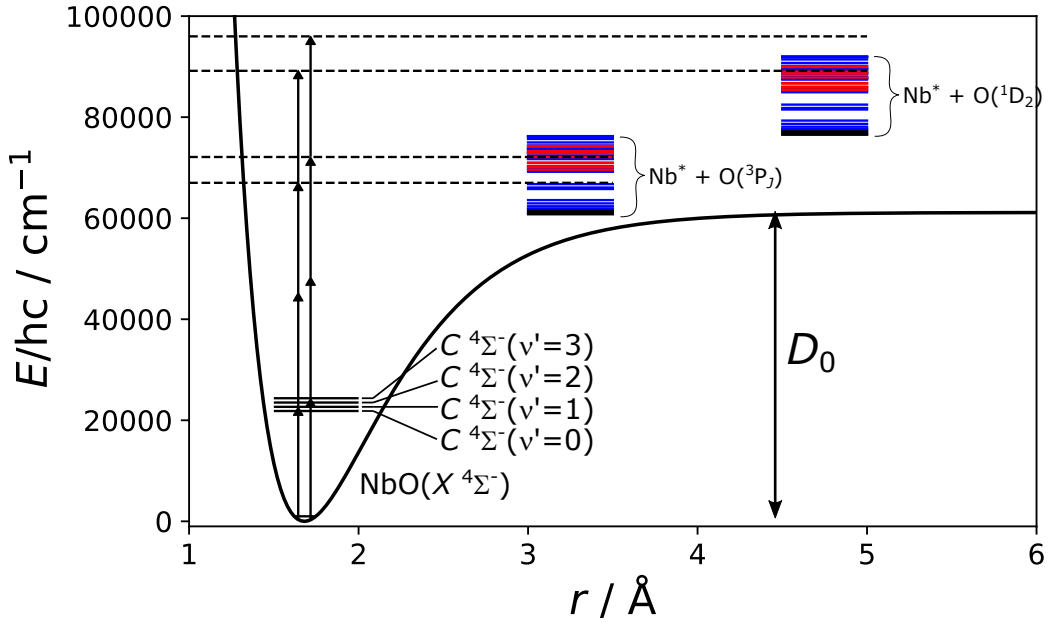


Figure 2.9: Potential energy curve of the NbO($X^4\Sigma^-$) ground state and energies of different Nb+O product state combinations; black, blue and red product states correspond to niobium atoms produced in sextet, quartet and doublet states, respectively; fragmentation *via* different vibrational level in the C-state access different product channels shown for $v' = 1, 3$; three-photon fragmentation can only produce oxygen atoms in the ^3P_J ground state while oxygen atoms in the $^1D_2$ state can be produced in a four-photon fragmentation, for the photon energies considered here.

nels, each of which could potentially be observed with varying branching ratios in the recorded velocity-map imaging data.

Despite the high number of possible product state combinations, the velocity-map images presented in Figure 2.7 show distinct sets of features. These features are not fully assigned yet and additional effort with higher kinetic energy resolution will be necessary to distinguish the underlying product channels. The changing branching ratio and number of features observed at different photon energies is, however, qualitatively consistent with the range of different states accessed in the resonant multi-photon fragmentation *via* different vibrational levels of the C-state.

2.4.1.1 Determination of the niobium oxide dissociation energy

To determine the dissociation energy of the niobium oxide molecule, velocity-map images of the Nb^+ photoproducts were recorded at 50 different photon energies in the vicinity of the $C^4\Sigma^-(v') \leftarrow\!\!\!\shortmid\; X^4\Sigma^-(v''=0)$, $v' = 1, 2, 3$, transitions. In the first step, the number of photons involved in the photodissociation is determined and the identity of the fragmentation partner is confirmed. Then, the dissociation energy is derived by extrapolating the change in total kinetic energy release with the photon energy of the n-photon fragmentation.

The number of photons involved in the photofragmentation process and the identity of the parent species are determined in the vicinity of the $C^4\Sigma^-(v'=1) \leftarrow\!\!\!\shortmid\; X^4\Sigma^-(v''=0)$ transition. Velocity-map images of Nb^+ ions are recorded at 39 photon energies, four of which are shown in Figure 2.10 for four different photon wavenumbers. The symmetrized image, the Abel-inverted images, and kinetic energy distributions are shown on the left-hand side, in the centre, and on the right-hand side.

In the four presented kinetic energy distributions the same main features with changing branching ratio can be found. Because the overall energy is conserved during the fragmentation, the fragment kinetic energy increases with increasing photon energy which can be observed in four series which are highlighted in Figure 2.10 (black, blue, red and green dashed lines).

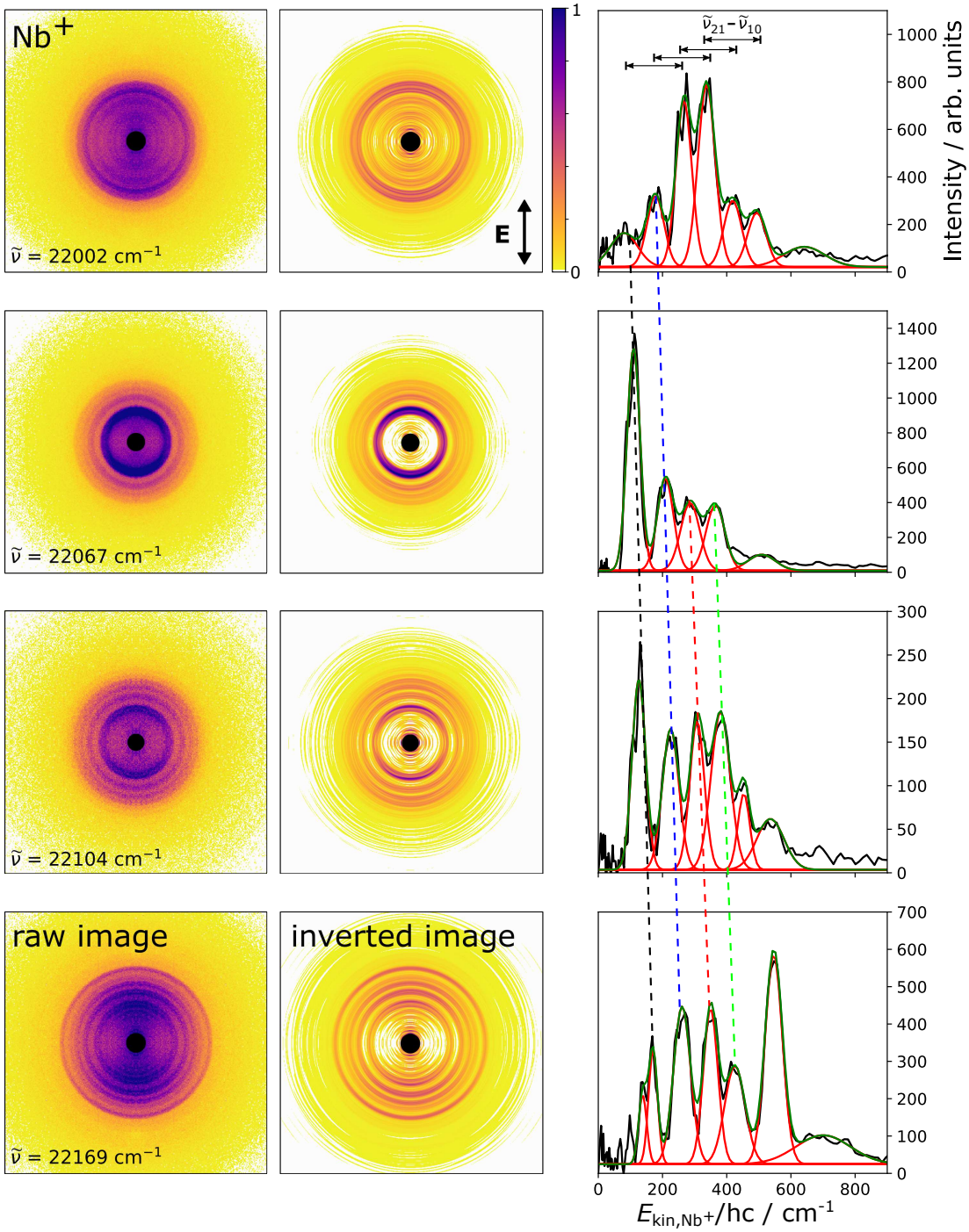


Figure 2.10: Nb^+ velocity-map images and kinetic energy, E_{kin,Nb^+}, distributions recorded at four photon energies in vicinity of the $B^4\Pi \leftarrow X^4\Sigma^-(8,0)$ and $C^4\Sigma^- \leftarrow X^4\Sigma^-(1,0)$ transitions; the kinetic energy distributions are fitted with Gaussian functions in Equation (2.8) (red line); the kinetic energy of the observed features increases with increasing photon energy and four such series are assigned with black, blue, red and green dashed lines; velocity-map image data shown in the top row is recorded at a photon wavenumber 22,002 cm^{-1} on resonance with the $C \leftarrow X(2,1)$ hot-band transition and the additional quantum of vibrational energy shifts the observed features to higher kinetic energies by 144 cm^{-1} as indicated by the horizontal arrows.

Velocity-map image data recorded at a photon wavenumber of 22,002 cm^{-1} is resonant with the $C^4\Sigma^- \leftarrow\!\shortmid X^4\Sigma^-$ (2,1) hot-band transition (see REMPI spectrum in Figure 2.5). The total kinetic energy release of photofragments produced *via* this transition is increased by a vibrational quantum of the NbO ground state which was reported as 981 cm^{-1} [126]. According to Equation (2.6), this corresponds to an additional 144 cm^{-1} fragment kinetic energy of the Nb fragment. Consequently, the features in the Nb^+ kinetic energy distribution are shifted by 144 cm^{-1} to higher kinetic energy as indicated by the horizontal arrows in Figure 2.10. The less intense features remaining at lower kinetic energies can be attributed to vibrationally cold NbO molecules which are fragmented non-resonantly or *via* the $B^4\Pi \leftarrow\!\shortmid X^4\Sigma^-$(8,0) transition which overlaps with the C-state in this spectral region.

To quantify the peak centre and width of the observed features in Figure 2.10, the peaks are fitted with Gaussian functions, P, of the form,

$$P(E_{\mathrm{kin}}; E_{\mathrm{kin,c}}, \sigma) \propto e^{-\frac{(E_{\mathrm{kin}}-E_{\mathrm{kin,c}})^2}{2\sigma^2}}. \tag{2.8}$$

Here, E_{kin} is the Nb^+ fragment ion kinetic energy, $E_{\mathrm{kin,c}}$ is the central energy of the Gaussian and the full-width-at-half-maximum (FWHM) of the fitted feature is given as $FWHM = 2\sqrt{2\ln 2}\sigma$.

Comparing the central position of the observed features shows that the fragment kinetic energy increases with increasing photon energy. Substituting the expression for the total kinetic energy release in Equation (2.6) into Equation (2.7) yields an expression for the fragment kinetic energy, $E_{\mathrm{kin,Nb}}$, as:

$$E_{\mathrm{int,NbX}} + nh\nu = D_0(\mathrm{NbX}) + E_{\mathrm{Nb}} + E_{\mathrm{X}} + \left(1 + \frac{m_{\mathrm{Nb}}}{m_{\mathrm{O}}}\right) \cdot E_{\mathrm{kin,Nb}}$$

$$E_{\mathrm{kin,Nb}} = \frac{E_{\mathrm{int,NbX}} + nh\nu - D_0(\mathrm{NbX}) - E_{\mathrm{Nb}} - E_{\mathrm{X}}}{1 + m_{\mathrm{Nb}}/m_{\mathrm{X}}} \tag{2.9}$$

$$E_{\mathrm{kin,Nb}} = h\nu \frac{n}{1 + m_{\mathrm{Nb}}/m_{\mathrm{X}}} - k \tag{2.10}$$

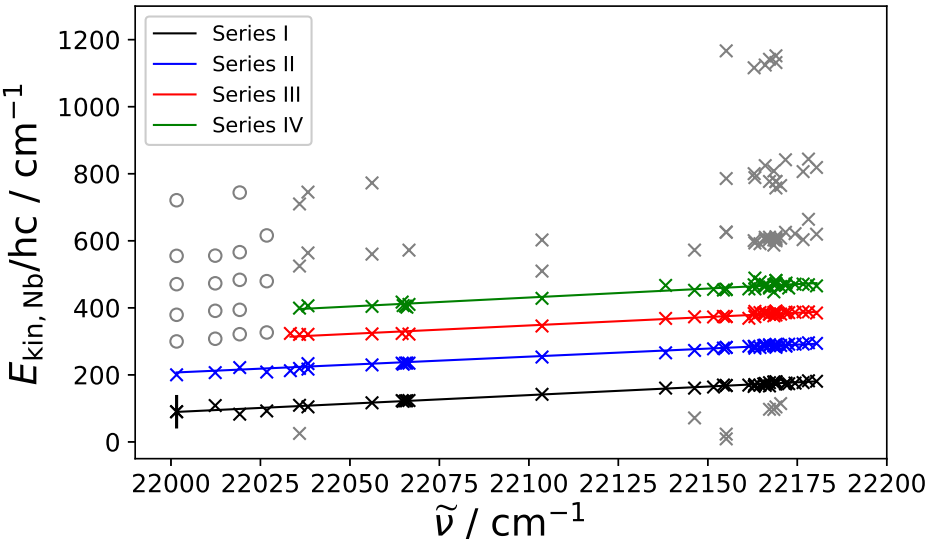


Figure 2.11: Central kinetic energy of Gaussian fits to features observed in 39 velocity-map images recorded in vicinity of the $C^4\Sigma^- \leftarrow\!\shortmid\; X^4\Sigma^-(1,0)$ transition centred at $22,160$ cm^{-1}; the distinct Series I to IV are fitted linearly according to Equation (2.10) and the slopes are listed in Table 2.2; Nb atoms dissociated *via* the (2,1)-hot band at about $22,000$-$22,025$ cm^{-1} gain an additional vibrational quantum of the ground state energy and their kinetic energy features overlap with dissociation products of the $B^4\Pi^- \leftarrow\!\shortmid\; X^4\Sigma^-(8,0)$ transition (see overview spectrum in Figure 2.5); affected kinetic energy features (grey circles) are excluded from the fit.

with,

$$k = \frac{E_{\mathrm{int,NbX}} - D_0(\mathrm{NbX}) - E_{\mathrm{Nb}} - E_{\mathrm{X}}}{1 + m_{\mathrm{Nb}}/m_{\mathrm{X}}}. \tag{2.11}$$

According to Equation (2.10), the fragment kinetic energy depends linearly on the photon energy. The centre kinetic energy of the Gaussian fits to features observed in the 39 velocity-map images observed in this region are plotted as a function of the photon wavenumber, $\widetilde{\nu}$, in Figure 2.11. The series I, II, III and IV identified in Figure 2.10 are fitted linearly. Comparing to Equation (2.10) the slopes of the linear fits, m, are given by:

$$m = \frac{n}{(1 + \frac{m_{\mathrm{Nb}}}{m_{\mathrm{X}}})} \tag{2.12}$$

Here, n is the number of photons involved in the photofragmentation process, $m_{\mathrm{Nb}} = 92.9$ amu is the mass of a niobium atom and m_{X} is the mass of the partner fragment.

Series	m	n(Nb-C)	n(Nb-N)	n(Nb-O)	n(Nb-Nb)	n(Nb-Nb_2)
I	0.50 ± 0.07	4.4 ± 0.6	3.9 ± 0.6	3.4 ± 0.5	1.0 ± 0.1	0.8 ± 0.1
II	0.48 ± 0.05	4.2 ± 0.6	3.6 ± 0.4	3.2 ± 0.4	1.0 ± 0.1	0.7 ± 0.1
III	0.50 ± 0.09	4.4 ± 0.9	3.8 ± 0.8	3.4 ± 0.7	1.0 ± 0.2	0.8 ± 0.1
IV	0.54 ± 0.09	4.7 ± 0.8	4.1 ± 0.7	3.7 ± 0.7	1.1 ± 0.2	0.8 ± 0.1

Table 2.2: Slope, m, of linear fits to Series I to IV in Figure 2.11 and derived number of photons, $n_{(\mathrm{Nb–X})}$, involved in the photodissociation of Nb-X for X=C, N, O, Nb, Nb_2.

The detected Nb^+ fragments could, in principle, originate from a number of different parent species, Nb-X, which are produced in the ablation source. Using slopes observed in Figure 2.11, a photon number, $n_{(\mathrm{Nb–X})}$, can be derived for each possible partner fragment, X. The slopes and number of photons assuming different fragmentation partners are summarized in Table 2.2.

The photon numbers in Table 2.2 are compared to known values of the dissociation energy and plausible combinations of $n_{(\mathrm{Nb–X})}$ and X are discussed. Assuming niobium carbide as the parent species, the observed slopes are consistent with a four or five photon dissociation. This would supply sufficient energy to overcome the dissociation energy of niobium carbide which has been reported as 5.62 eV (45328 cm^{-1}) [141]. Similarly, dissociation energies of NbN (8.08 eV; $65,200\ \mathrm{cm}^{-1}$) [142] and NbO (7.53 eV; $60,734\ \mathrm{cm}^{-1}$) [104] are consistent with the photon numbers obtained from the fit as four photons for NbN and three or four photons for NbO. The identification of Nb_2 or Nb_3 as parent species would be consistent with a one photon dissociation which is insufficient to overcome the dissociation energy of 5.48 eV [119] (44190 cm^{-1}) and 4.3 eV [143] (34680 cm^{-1}), respectively. This excludes Nb_2 and Nb_3 as parent species for the observed Series I to IV.

In principle, niobium carbide, nitride and oxide could be the parent species. However, strong evidence for niobium oxide as the parent species is the spectral position

of the fragmentation laser close to the $C^4\Sigma^- \leftarrow\!\!\!| X^4\Sigma^-(1,0)$ transition which has been assigned using the well-known position of the origin band and vibrational constant of the C-state [125]. Furthermore, nitride and carbide species are usually only produced in this experiment if a low percentage of nitrogen or carbon containing reactive gas is added to the carrier gas in the ablation source. In the data presented here, pure helium was used as a carrier gas and it is therefore concluded that niobium oxide is the most likely parent species. Within the uncertainty of the slope of the fits, Series I to IV are consistent with both a three and four-photon dissociation of niobium oxide.

Having some knowledge of the photon number of the dissociation process, conservation of energy in Equation (2.7) can now be used to determine the dissociation energy of niobium oxide. The total kinetic energy of the dissociation and $n = 3, 4$ is given as,

$$E_{\mathrm{kin,tot}} = nh\nu - \big(D_0(\mathrm{NbO}) + E_{\mathrm{Nb}} + E_{\mathrm{O}}\big). \tag{2.13}$$

Figure 2.12 shows the total kinetic energy release of the fragmentation, $E_{\mathrm{kin,tot}}$, as a function of the three-photon wavenumber, $3\widetilde{\nu}$, in (a) and four-photon wavenumber, $4\widetilde{\nu}$, in (b). The total kinetic energy release is derived from the fragment kinetic energy of features in velocity-map images recorded in vicinity of the $C\big(v' = 1\big) \leftarrow\!\!\!| X\big(v'' = 0\big)$ and $C\big(v' = 2\big) \leftarrow\!\!\!| X\big(v'' = 0\big)$ bands centred at $22,160$ cm^{-1} and $23,006$ cm^{-1}, respectively.

The observed data-points are compared to the expected energy for different combinations of niobium and oxygen electronic states in a three-photon and four-photon fragmentation. Hereby, a dissociation energy of 7.53 eV ($60,734$ cm^{-1}) has been taken as a reasonable first guess to construct a set of product channels shown as lines in Figure 2.12. This value was determined by Loock *et al.* [104] as 7.53 ± 0.11 eV ($60734 \pm$

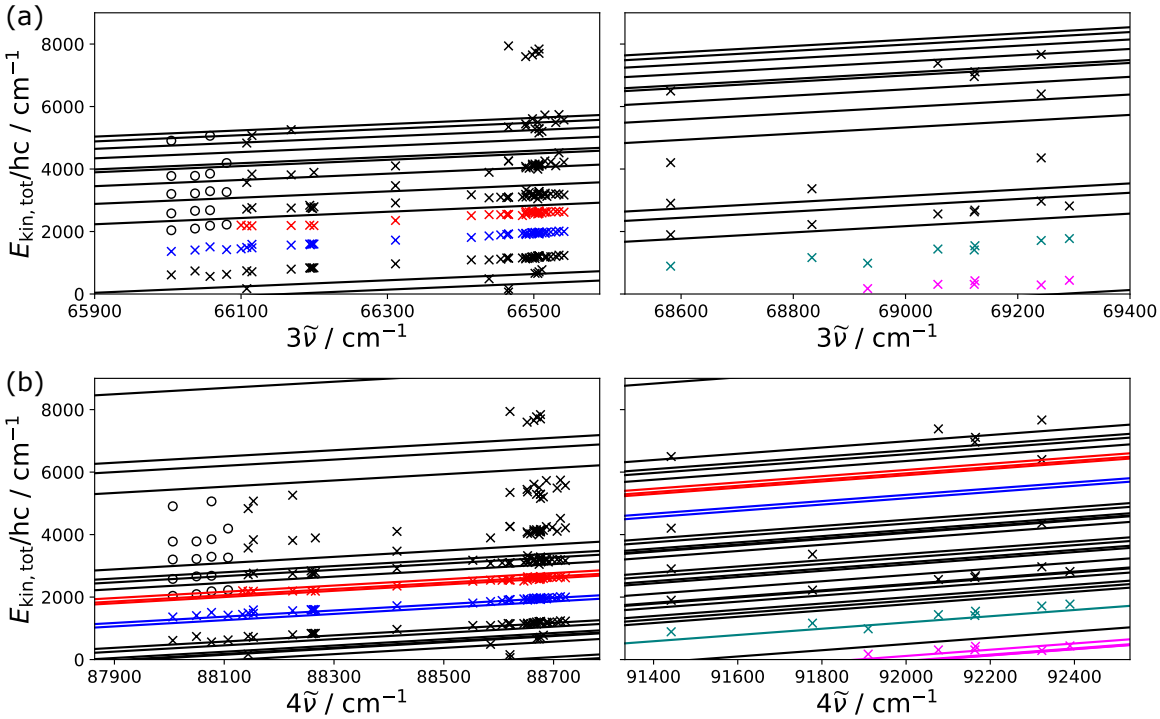


Figure 2.12: Total kinetic energy release, $E_{\mathrm{kin,tot}}$, for the three-photon dissociation in (a) and four-photon dissociation in (b) of niobium oxide; the black lines indicate the expected kinetic energies of the shown series for population of electronic states in the oxygen and niobium atom and assuming a dissociation energy of 7.53 eV (60734 cm^{-1}) [104]; for the four-photon dissociation the $^1D_2$ state can be populated in the oxygen atom.

887 cm^{-1}). The authors measured the NbO ionization energy as 7.160 ± 0.004 eV derived the NbO dissociation energy based on the previously reported values of the Nb ionization energy, 6.75885 ± 0.00004 eV [105], and dissociation energy of NbO^+, 7.13 ± 0.11 eV [102].

Despite the high complexity of the electronic structure and the large number of possible product states, several consecutive series of data-points can be identified, for which the observed kinetic energy increases linearly with the photon energy, $3\widetilde{\nu}$ and $4\widetilde{\nu}$. Given the ambiguity of the number of photons involved in the fragmentation process, in most cases it is not clear which combination of product electronic states describe the observed data-points best, because most series are described both by

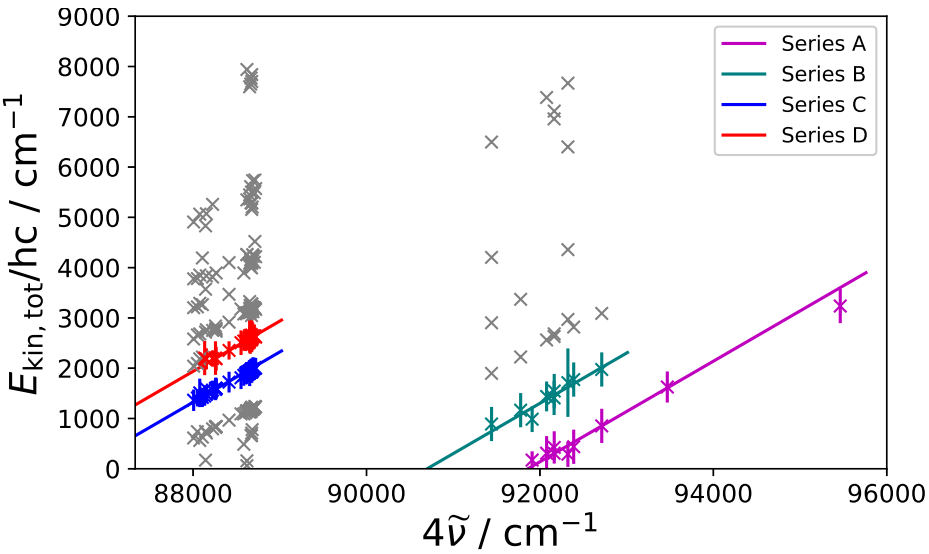


Figure 2.13: Total kinetic energy release, $E_{\mathrm{kin,tot}}$, of observed kinetic energy features as a function of the four-photon wavenumber, $4\tilde{\nu}$; data-points shown in purple, turquoise, blue and red are assigned to sets of product states accessed in a four-photon fragmentation; the series are fitted linearly with constraint slopes, $m = 1$, to determine the NbO dissociation energy from the extrapolated y-intercepts of the fits; unassigned kinetic energy features are shown as grey markers.

combination of states on the four-photon level and are, at the same time, described by a combination of states on the three-photon level. There are, however, four series of data-points which appear to be best described with a four-photon process. Series A to D are here shown in purple, turquoise, blue and red markers.

Comparing these assigned series of data-points to the energy of the combinations of oxygen and niobium product states yields a refined value of the dissociation energy based on the value by Loock *et al.* [104]. For this purpose, all available data for these series are plotted as a function of the four-photon wavenumber in Figure 2.13 and the identified series are fitted linear with a constrained slope, $m = 1$. According to Equation (2.13) the extrapolated y-axis intercept, k, of each assigned series yields a

dissociation energy:

$$k = -(D_0 + E_{\mathrm{Nb}} + E_{\mathrm{O}})$$
$$D_0 = -k - E_{\mathrm{Nb}} - E_{\mathrm{O}} \tag{2.14}$$

Table 2.3 summarizes the extrapolated y-intercepts of Series A to D, their assignment to niobium and oxygen product states with energies $E_{\mathrm{Nb}} + E_{\mathrm{O}}$, and the resulting dissociation energy, $D_0(\mathrm{NbO})$.

Series	k	product states	$E_{\mathrm{Nb}} + E_{\mathrm{O}}$	$D_0(NbO)$
A	$-91,861 \pm 135$	$\mathrm{Nb}(b^4\mathrm{D}_{7/2}) + \mathrm{O}(^1\mathrm{D}_2)$ $\mathrm{Nb}(b^4\mathrm{D}_{3/2}) + \mathrm{O}(^1\mathrm{D}_2)$ $\mathrm{Nb}(b^4\mathrm{D}_{1/2}) + \mathrm{O}(^1\mathrm{D}_2)$ $\mathrm{Nb}(b^4\mathrm{D}_{5/2}) + \mathrm{O}(^1\mathrm{D}_2)$	$15,412 \pm 65$	60580 ± 150
B	$-90,698 \pm 189$	$\mathrm{Nb}(b^4\mathrm{P}_{3/2}) + \mathrm{O}(^1\mathrm{D}_2)$	14,211.30	$60,619 \pm 189$
C	$-86,676 \pm 47$	$\mathrm{Nb}(a^2\mathrm{D}_{5/2}) + \mathrm{O}(^1\mathrm{D}_2)$ $\mathrm{Nb}(a^2\mathrm{P}_{1/2}) + \mathrm{O}(^1\mathrm{D}_2)$	$10,181 \pm 55$	$60,627 \pm 72$
D	$-86,063 \pm 55$	$\mathrm{Nb}(a^4\mathrm{D}_{7/2}) + \mathrm{O}(^1\mathrm{D}_2)$ $\mathrm{Nb}(a^2\mathrm{G}_{9/2}) + \mathrm{O}(^1\mathrm{D}_2)$ $\mathrm{Nb}(a^2\mathrm{D}_{3/2}) + \mathrm{O}(^1\mathrm{D}_2)$	$9,422 \pm 62$	$60,773 \pm 83$

Table 2.3: y-intercept of linear fits to Series A, B, C and D in Figure 2.13; the dissociation energy $D_0(\mathrm{NbO})$ is determined for each series using Equation 2.14 and based on the average value of the assigned product state energies.

The average dissociation energy over the values given in Table 2.3 is then $60,650 \pm 124$ cm^{-1}. This value is within the uncertainty interval of the reported dissociation energy by Loock *et al.* [104] from their mass-analyzed threshold ionization (MATI) study.

The refined value of the dissociation energy of neutral NbO can now be used in combination with reported ionization energies to calculate the dissociation energy of NbO^+, using the thermodynamic cycle in Equation (2.1):

$$D_0(\mathrm{NbO}^+) = D_0(\mathrm{NbO}) + E_{\mathrm{i}}(\mathrm{Nb} - E_{\mathrm{i}}(\mathrm{NbO}). \tag{2.15}$$

With the reported values of the NbO and Nb ionization energy, 7.160 ± 0.004 eV [104] ($57,749 \pm 33$ cm^{-1}) and 6.75885 ± 0.00004 eV [105] ($54,513.8 \pm 0.3$ cm^{-1}), respectively, a refined value of the NbO^+ dissociation energy is derived as $57,414 \pm 124$ cm^{-1}. This value is within the uncertainty interval of the previously reported value of 7.13 ± 0.11 eV [102] ($57,507 \pm 887$ cm^{-1}).

2.4.2 Velocity-map imaging of photoelectrons

The photoionization of niobium oxide and niobium atoms produces both ions and electrons. In the first velocity-map imaging studies, Eppink and Parker [12] showed that both ions and electrons can be recorded in a velocity-map imaging spectrometer by changing the polarity of the velocity-mapping field. While past experiments on the present spectrometer were solely focussed on the study of fragment ions, this is the first velocity-map imaging experiment detecting photoelectrons in this set-up. The kinetic energy and angular distribution of the detected electrons gives insight on the orbital the electron is emitted from and on the electronic structure of the product ion.

One challenge in velocity-map imaging of photoelectrons is the low mass and, thus, small momentum of low kinetic energy electrons. Because electrons are at least three orders of magnitude lighter than ion products, their trajectories in the velocity-map imaging spectrometer are more easily perturbed by electric and magnetic fields than those of ions. These fields can originate from equipment inside and outside the experiment. Initially distorted velocity-map images have been greatly improved by identifying and eliminating sources of such fields in this experimental set-up. In the following, the velocity calibration of the spectrometer for photoelectrons is described and initial experiments imaging photoelectrons from the ionization of vanadium atoms are presented. This section is concluded with a photoionization study of NbO.

2.4.2.1 Velocity calibration for imaging of photoelectrons

Because of the large mass difference between ions and electrons, the magnification factor, N_{ele}, for velocity-map imaging of photoelectrons was redetermined simulating the electron trajectories in a model of the spectrometer using the SIMION [144] software package. To this purpose, trajectories of ten groups of 1000 electrons with kinetic energies ranging from 0.5 eV to 5.0 eV are simulated for an extraction potential of 5000 V. Thus, a simulated velocity-map image of electrons in the model spectrometer was produced and is shown in Figure 2.14. The electron time-of-flight inside the spectrometer, t_{ele} = 11.9 ns, was also retrieved from the simulation.

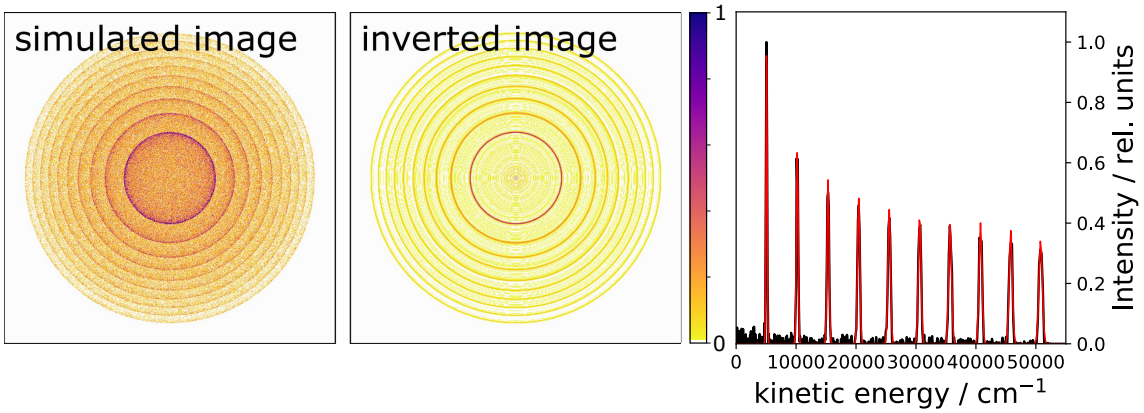


Figure 2.14: Left: simulated velocity-map image of ten groups of electrons with kinetic energies ranging from 0.5 eV to 5.0 eV; centre: Abel-inversion of the simulated image using the pBASEX [71] and the l = 0 Legendre polynomial; right: kinetic energy distributions of simulated electrons for a magnification factor, N = 1; the ten kinetic energy features are fitted with Gaussian functions (red line).

The simulated velocity-map image in Figure 2.14 is Abel-inverted using the pBASEX algorithm [71]. The kinetic energy distributions were produced as outlined in Section 2.3. To determine the magnification factor the kinetic energy axis is initially constructed using N = 1. The kinetic energy distribution of the simulated electrons (black line) and Abel-inverted image are shown in Figure 2.14. The ten features in the

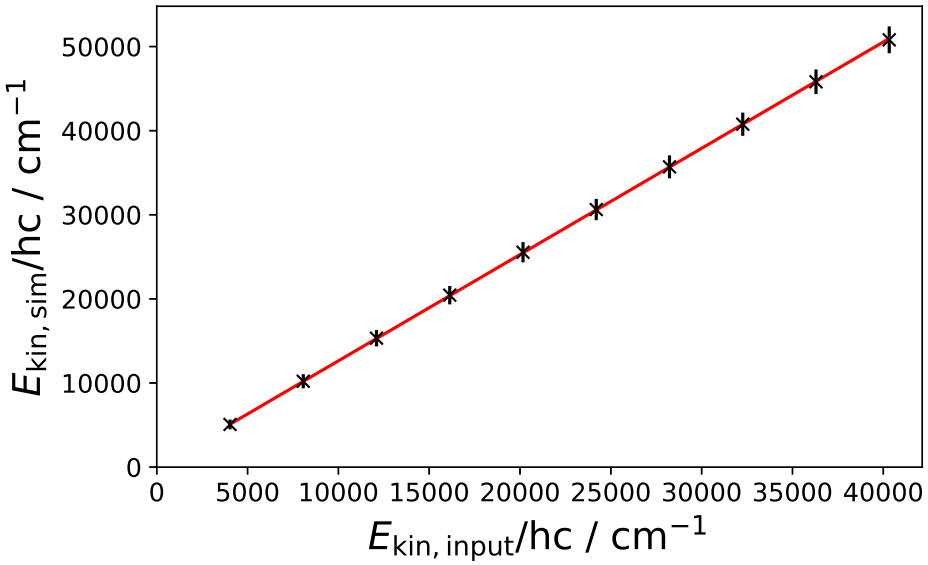


Figure 2.15: Relation between the kinetic energy extracted from the simulated velocity-map image, $E_{\mathrm{kin,sim}}$, and kinetic energy of the simulated electrons, $E_{\mathrm{kin,input}}$; the magnification factor of the velocity-map imaging spectrometer is determined from the slope of a linear fit to the data, $N_{\mathrm{ele}}^2 = 1.26 \pm 0.02$, according to Equation (2.18).

kinetic energy distribution are fitted with Gaussian functions (red line) to determine their width and central position.

According to Eppink and Parker [12], the radius of a feature in the velocity-map image and the particle velocity, v, is given by,

$$r = N\,v\,t \tag{2.16}$$

$$v = \frac{r}{t} = N\,v_{N=1}. \tag{2.17}$$

Here, $v_{\mathrm{N=1}}$ is the velocity assuming a homogeneous extraction field. The kinetic energy, $E_{\mathrm{kin}} = 1/2\,m\,v^2$, extracted from the simulated velocity-map image, $E_{\mathrm{kin,sim}}$, and the kinetic energy which is put into the simulation, $E_{\mathrm{kin,input}}$, are then given by,

$$E_{\mathrm{kin,input}} = N_{\mathrm{ele}}^2\,E_{\mathrm{kin,sim}}. \tag{2.18}$$

Figure 2.15 shows a plot of the electron kinetic energies retrieved from the simulation in Figure 2.14 as a function of the input kinetic energies of the simulated electrons.

According to Equation (2.18), the square of the magnification factor, N_{ele}^2, is retrieved as the slope of a linear fit to the data, and the magnification factor for velocity-map imaging of photoelectrons is therefore obtained as $N_{\mathrm{ele}} = 1.12 \pm 0.01$.

The errorbars in Figure 2.15 represent the full-width-at-half-maximum of Gaussian fits to the electron kinetic energy distribution. These can be used to estimate the energy resolution of the spectrometer which is 0.1 eV in the image centre and 0.4 eV at the detector edge.

2.4.2.2 Photoionization of vanadium atoms

To illustrate the newly established electron imaging capabilities, velocity-map images of photoelectrons born in the (2+1)-REMPI ionization of vanadium atoms *via* the $f^4\mathrm{F}_{J'}$ state are recorded. In Section 2.2, the V^+ ion signal observed at these transitions was used to calibrate the photon energy of the employed dye laser and optical-parametric oscillator.

Figure 2.16 shows velocity-map images of photoelectrons recorded in vicinity of the $f^4\mathrm{F}_{J'} \leftarrow\!\shortmid\, a^4\mathrm{F}_{J''}$ for $\Delta J = 0$ and J'' =3/2, 5/2, 7/2, 9/2. The recorded velocity-map image is shown in the left-hand column, the Abel-inverted image is shown in the centre column and the retrieved kinetic energy distribution (black line) is shown in the right-hand side column. Velocity-map image data are analyzed and the kinetic energy distribution are produced as described in Section 2.3 and using the magnification factor determined for velocity-map imaging of electrons above. The ionization laser is polarized along the vertical figure axis.

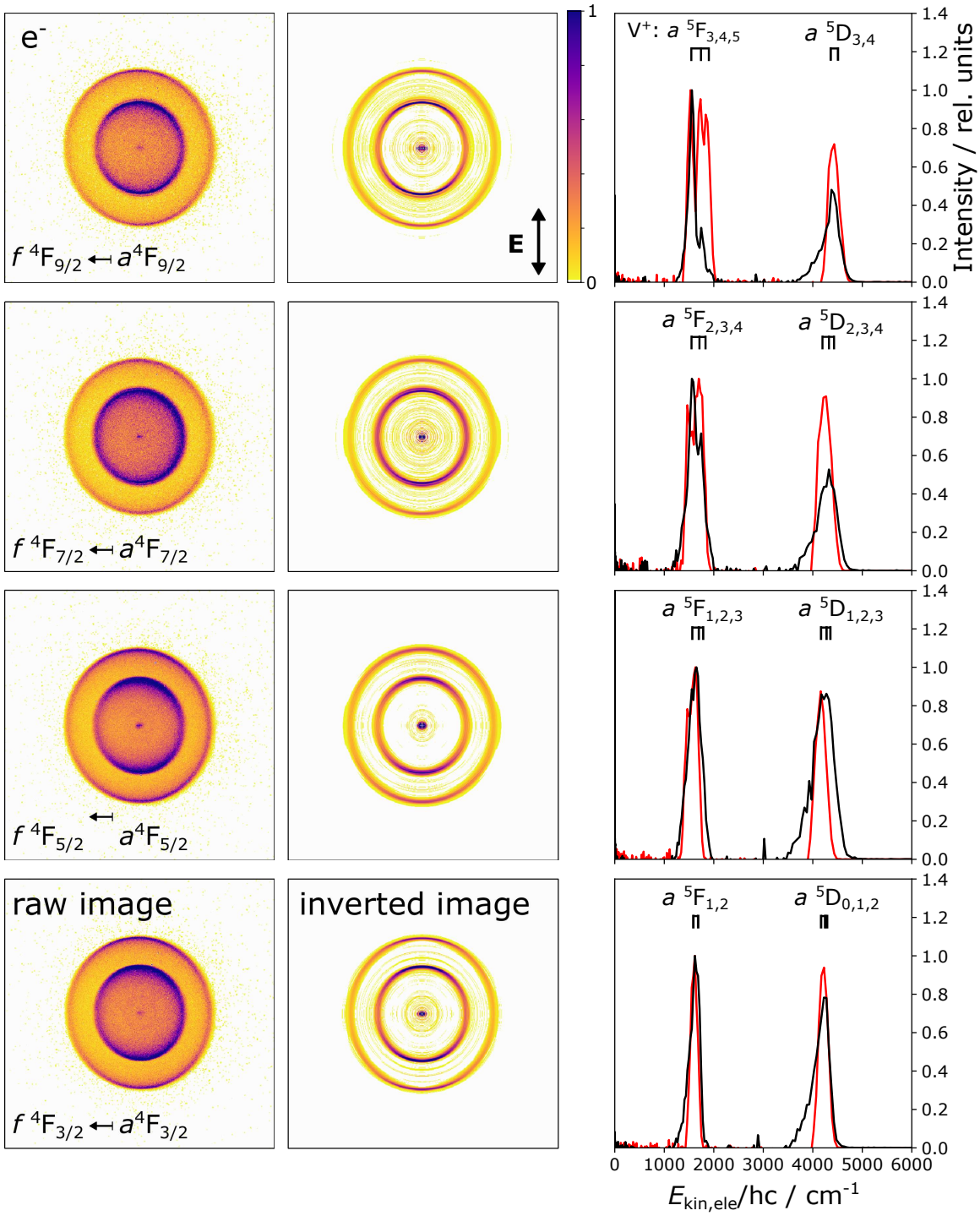


Figure 2.16: Photoelectron velocity-map images of the (2+1)-REMPI *via* the $f^4F_{J'}$ state for $J' = 3/2, 5/2, 7/2, 9/2$ from the top to bottom row; the recorded velocity-map image is shown in the left-hand side column, the Abel-inverted image is shown in the central column and the electron kinetic energy distribution is shown in the right-hand side column; the electron kinetic energy distributions (black line) are compared to kinetic energies of photoelectrons according to Equation (2.19) for different accessible V^+ electronic states and to simulated kinetic energy distributions in a model of the spectrometer.

The electron kinetic energy distributions are compared to kinetic energies expected for a three photon ionization of the vanadium atom from the respective spin-orbit level in the electronic ground state to the $a^5\mathrm{F}_{J^+}$ and $a^5\mathrm{D}_{J^+}$ state of the V^+ ion. The energies of the photoionization products, the photon energy and the atom internal energy is given according to conservation of energy as,

$$E_{\mathrm{kin,ele}} = E_{\mathrm{V}} + 3h\nu - E_{\mathrm{V}^+} - E_{\mathrm{i}}. \tag{2.19}$$

Here, E_{i} is the ionization energy which has been determined previously as 6.7461 eV (54411 cm^{-1}) [119]. The energies of the spin-orbit levels of the electron ground state $a^4\mathrm{F}_{J''}$ in the vanadium atom and the energies of the $a^5\mathrm{F}_{J^+}$ and $a^5\mathrm{D}_{J^+}$ in the V^+ ion is given in Table 2.4.

J	$E_{\mathrm{V}}(a^4\mathrm{F}_{J''})$ / cm^{-1}	$E_{\mathrm{V}^+}(a^5\mathrm{D}_{J^+})$ / cm^{-1}	$E_{\mathrm{V}^+}(a^5\mathrm{F}_{J^+})$ / cm^{-1}
0	-	0.000	-
1	-	36.1017	2605.0400
3/2	0.000	-	-
2	-	106.6421	2687.2090
5/2	137.383	-	-
3	-	208.7901	2808.9590
7/2	323.432	-	-
4	-	339.1256	2968.3883
9/2	552.955	-	-
5	-	-	3162.9673

Table 2.4: Energy levels of the $a^4\mathrm{F}''_J$ manifold for $J'' = 3/2, 5/2, 7/2, 9/2$ taken from Reference [120] and [121]; energy levels of the $a^5\mathrm{D}_J$ and $a^5\mathrm{F}_J$ manifold for $J = 0, 1, 2, 3, 4, 5$ taken from Reference [145].

Applying conservation of angular momentum, transitions between neutral $f^4\mathrm{F}_{J'}$ and ionic electronic states need to satisfy the selection rule:

$$\Delta L = 0, \pm 1 \tag{2.20}$$

The system gains one quantum of angular momentum upon absorption of a photon in the f-state and the photoelectron carries $L = 1$ as it leaves the atom as a p-wave.

Thus, electronic states with $L = 2, 3, 4$ can be accessed in the V^+ ion. In the observed energy range, the $a^5D_{J^+}$ and $a^5F_{J^+}$ states can be populated in the photoionization step.

Conservation of total angular momentum furthermore yields that only transition between spin-orbit levels are allowed which satisfy the selection rule:

$$\Delta J = 0, \pm 1. \tag{2.21}$$

As the photoelectron carries $S = 1/2$ of spin, those transitions between the neutral f^4F_J state and ionic state are allowed which satisfy:

$$\Delta J = \frac{1}{2}, -\frac{1}{2}, -\frac{3}{2} \tag{2.22}$$

For example, from the $a^4F_{9/2}$ ground state and *via* the $f^4F_{9/2}$ excited state, transition to the $J^+ = 3, 4, 5$ spin-orbit levels in the $a^5F_{J^+}$ and $J^+ = 3, 4$ levels in the $a^5D_{J^+}$ of the V^+ ion are allowed.

Using Equation (2.19), the electron kinetic energies are derived for the accessible spin-orbit levels and electronic states of the V^+ ion, and the electron kinetic energies are compared to the velocity-map imaging results in Figure 2.16. The experimental determined electron kinetic energy (black line) is compared to kinetic energies retrieved from a simulation of the velocity-map image using the derived kinetic energies employing the SIMION [144] software package (red line). The simulated and experimental kinetic energy distribution are in very good agreement and illustrate that VMI studies of photoelectrons can be performed with this experimental set-up. The width of the features in the experimental data and the simulated kinetic energy distributions is similar which indicates that the kinetic energy resolution is mainly limited by the kinetic energy resolution of the VMI spectrometer.

The successful assignment of V^+ product states to the features in the photoelectron velocity-map images shows that photoelectron spectroscopy using the present experimental set-up probes the photoion product state and also indirectly the electronic state of the neutral species in a photoionization.

2.4.2.3 Photoionization of niobium oxide

Having tested the capabilities of the experimental set-up to velocity-map photoelectrons from the photoionization of vanadium atoms, the photoionization of niobium oxide is studied in this section.

Figure 2.17 shows a photoelectron velocity-map image recorded at a photon energy of $22,152\ \mathrm{cm}^{-1}$, on resonance with the NbO $C^4\Sigma^-(v' = 1) \leftarrow\!\!\shortmid\ X^4\Sigma^-(v'' = 0)$ transition. The symmetrized velocity-map image is shown on the left, and the Abel-inverted image and electron kinetic energy distribution are shown in the centre and right-hand side. The features observed in the electron kinetic energy distribution are fitted with Gaussian functions (red line).

The kinetic energy distribution of the recorded photoelectrons shows a series of 12 features below a kinetic energy of $10,000\ \mathrm{cm}^{-1}$. Hereby, the highest kinetic energy feature matches closely with the maximum kinetic energy for a three-photon ionization of a ground state niobium oxide molecule, $3\widetilde{\nu} - E_\mathrm{i}$ (NbO), indicated with a downward pointing arrow in Figure 2.17. The adiabatic ionization energy of niobium oxide was previously reported as 7.160 ± 0.004 eV [104] ($54,513.8 \pm 0.3\mathrm{cm}^{-1}$). Consequently, the observed kinetic energy features are assigned to vibrational levels of the $X^3\Sigma^-$ state of the NbO^+ ion, accessed in the photoionization.

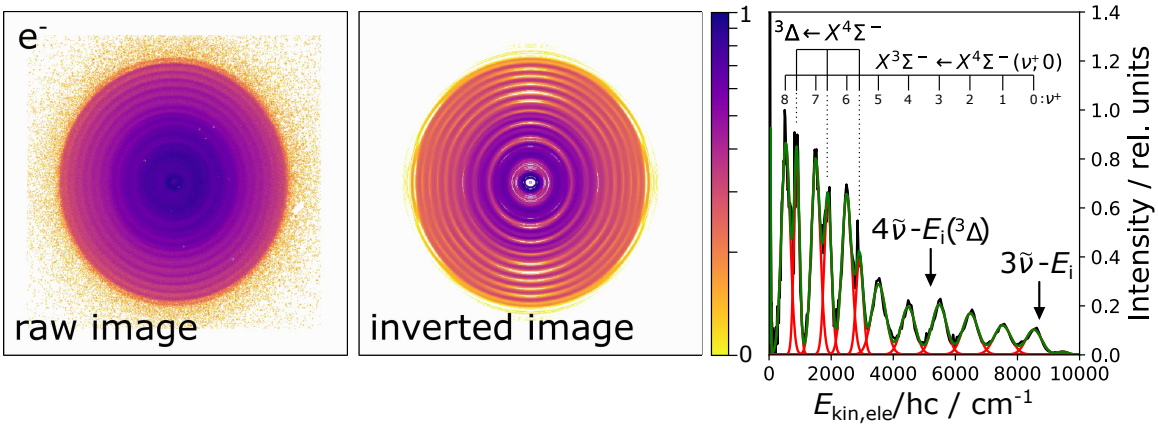


Figure 2.17: Photoelectron velocity-map image recorded at a photon energy of 22,152 cm^{-1}; left: symmetrized image, centre: Abel-inverted image, right: kinetic energy distribution; features in the kinetic energy distribution are fitted with Gaussian functions (red line), sum of the Gaussians is also shown (green line); the observed features are assigned with the series of vibrational levels of the $X^3\Sigma^-$ and $^3\Delta$ state accessed in a three and four-photon transition from the neutral ground state, respectively; the adiabatic ionization energy, E_i, for both states is indicated with two downward pointing arrows.

The electronic states of the NbO molecule and NbO^+ ion involved in the photoionization process are summarized in Figure 2.18 (a). Niobium oxide in the vibrational and electronic ground state $X^4\Sigma^-(v'' = 0)$ is resonantly ionized in a three-photon transition *via* the $C^4\Sigma^-(v' = 1)$ state and produce NbO^+ ions in its $X^3\Sigma^-$ ground state. The energy of the recorded photoelectron is then given by the difference between photon energy and the vibrational energy in the ion, so that the highest energy feature corresponds to the lowest accessed vibrational state, $v = 0$.

The $X^3\Sigma^-$ state of the NbO^+ ion has been observed together with three higher lying states in a photoelectron study by Dyke *et al.* [103]. The authors reported a vertical ionization energy of 10.34 eV (83,398 cm^{-1}) to the $^3\Delta$ excited state which could be accessed in a four-photon ionization. The expected electron energy of such a process, $4\tilde{\nu} - E_i(^3\Delta) = 5200$ cm^{-1}, is also indicated with a downward pointing arrow in Figure 2.17. Three features observed in the present study at kinetic energies below

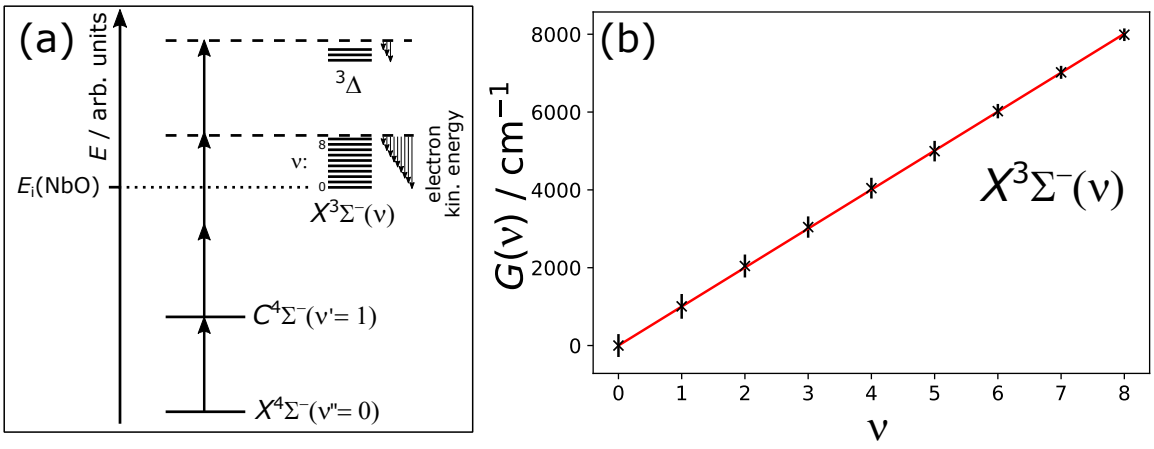


Figure 2.18: (a) Schematic diagram of the electronic and vibrational states involved in the three-photon and four-photon ionization (see text for more details on the photonionzation process); (b) observed energy spacings of the vibrational level in the $X^3\Sigma^-$ state of NbO^+; the progression is fitted to an expression of a harmonic oscillator in Equation (2.24) to obtain a vibrational constant of $\omega_e = 1002 \pm 11$ cm^{-1}.

3000 cm^{-1} are tentatively assigned to vibrational levels of the $^3\Delta$ state accessed in a four-photon ionization.

Observing a series of vibrational levels of the $X^3\Sigma^-$ state allows for the determination of the vibrational constant $\widetilde{\omega}_e(X^3\Sigma^-)$ assuming a harmonic oscillator for the $X^3\Sigma^-$ state. The central kinetic energy of the Gaussian fits is plotted as a function of the quantum number of the $X^3\Sigma^-$ vibrational levels, v, in Figure 2.18 (b). The dissociation energy of NbO^+ determined in Section 2.4.1.1, $57,615$ cm^{-1}, is much larger than the range of vibrational energy in Figure 2.18 and it is concluded that the potential of the $X^3\Sigma^-$ resembles to a reasonable approximation a harmonic oscillator. The wavenumber of the vibrational levels is then given approximately as,

$$G(v) = \widetilde{\omega}_e(v + \frac{1}{2}). \tag{2.23}$$

The spacings of the vibrational levels are described by the vibrational constant $\widetilde{\omega}_e$ and are given by,

$$\Delta G(v) = \widetilde{\omega}_e\, v. \tag{2.24}$$

Fitting Equation (2.24) to the data-points in Figure 2.18 (b), yields a vibrational constant $\widetilde{\omega}_e = 1002 \pm 11$ cm^{-1}.

Given the reviewed literature published to date, this is the first experimental determination of the vibrational constant of the $\widetilde{\omega}_e(X^3\Sigma^-)$ state in NbO^+. Dyke *et al.* [103] have performed *ab initio* calculations on a Hartree-Fock level of theory and derived a vibrational constant of 1067 cm^{-1} which is in reasonable agreement with the value reported here.

2.4.3 Photofragmentation dynamics of VCO_2^+

To test the recently adapted experimental set-up for the fragmentation of charged metal clusters, a proof of principle study of the dissociation dynamics of the VCO_2^+ complex was performed.

The photofragmentation of VCO_2^+ is one example for the mode-selective chemistry of the reactant on the pathway along the systems' potential energy surfaces. Here, the CO_2 ligand is bound linearly to the metal center *via* the O-atom, and a reactive and non-reactive fragmentation pathway have been described in Reference [115], [116] and [117].

$$VCO_2{}^+ \xrightarrow{h\nu} V^+(^5D) + CO_2(^1\Sigma^+) \tag{2.25}$$

$$\xrightarrow{h\nu} VO^+(^3\Sigma) + CO(^1\Sigma^-) \tag{2.26}$$

Figure 2.19 (a) shows the two fragmentation pathways of the VCO_2^+ cluster. Citir and Metz [117] have calculated energies of the VCO_2^+ complex for its configuration in local minima and determined transition states along the potential energy surfaces with quintet (red) and triplet multiplicity (blue). The ground state of the reactant

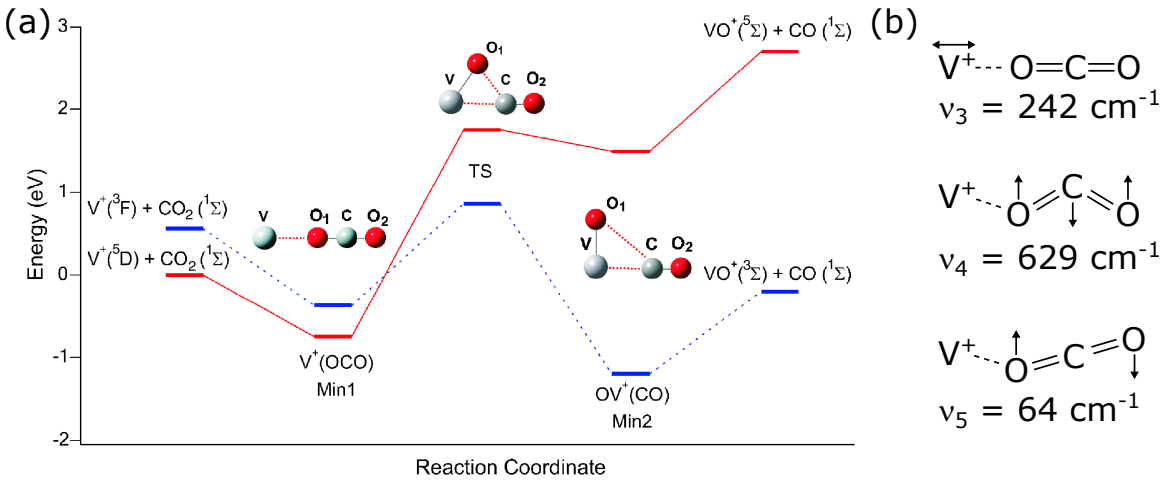


Figure 2.19: (a) Calculated potential energy surface with triplet (blue) and quintet spin multiplicity (red) on the CCSD(T) level of theory using a 6-311+G(3*df*) basis-set; the reaction starts in the local minimum of the quintet surface, Min1, and progresses along a non-reactive and reactive trajectory on the quintet and triplet potential energy surface, respectively; reproduction from M. Citir and R. B. Metz, *J. Chem. Phys.* **2008**, 128, 024307 with permission from AIP publishing; (b) low-energy vibrational modes of the $^5\Sigma$ ground state from Reference [116].

is found to be either $^5\Sigma$ or $^5\Delta$ [116, 146]. The reaction starts after absorption of a visible photon in the potential well, Min1, and excitation into a pre-dissociative electronic excited state. The reactive pathway proceeds to the right-hand side of the reaction coordinate while the non-reactive CO_2 loss proceeds to the left-hand site. In order to proceed *via* the reactive pathway, the system needs to follow a crossing from the quintet to the triplet surface. This spin-forbidden crossing is mediated by the rocking mode, v_5, such that electronic transitions exciting this vibration can proceed along the reactive channel [115, 117].

The photofragmentation spectrum of VCO_2^+ recorded in the present study is shown in Figure 2.20. The species is produced by laser ablation of vanadium and adding 1% of CO_2 to the carrier gas mixture. VCO_2^+ ions are prepared inside the velocity-map imaging spectrometer as outlined in Section 2.2 and the ions are photofragmented with photons in the red part of the spectrum. The ion yield of the V^+ and VO^+

fragmentation products are presented in (a) and (b), respectively. The non-reactive channel in Reaction (2.25) is observed in the V^+ ion yield in Figure 2.20 (a) and the reactive channel is observed in (b). The observations made here are consistent with the previous work [115–117].

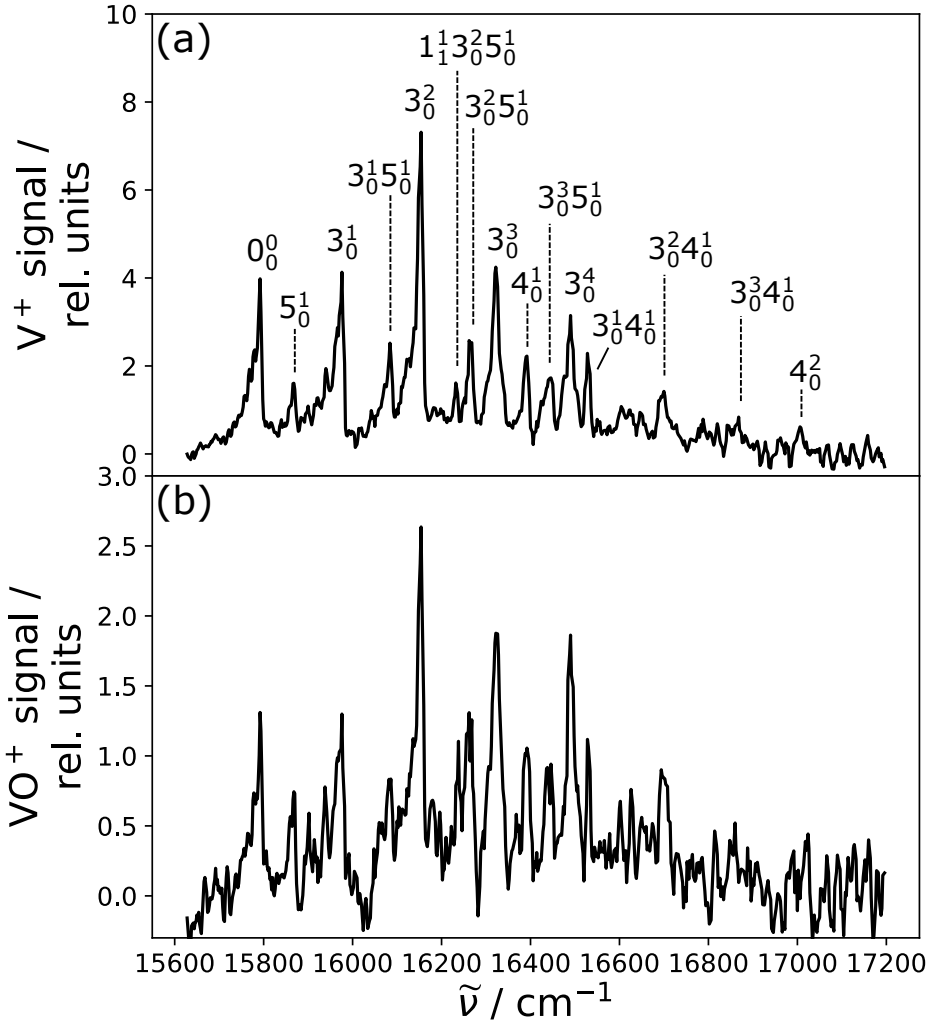


Figure 2.20: Photofragmentation spectrum of the VCO_2^+ complex; (a) observed V^+ ion yield in the non-reactive fragmentation channel in Reaction (2.25); vibrational bands are assigned according to Reference [117] (b) shows the VO^+ ion yield from the reactive channel (2.26); the spectra were smoothed using a two-point moving average.

Lessen *et al.* [115] and later Citir and Metz [117] recorded the photodissociation spectrum of VCO_2^+ in the red part of the visible spectrum. Here, the ion yields of both V^+ and VO^+ ions have been measured. In both studies, a rich vibrational structure is observed which is successfully assigned to excitation of the V^+-(OCO) stretching mode, v_3, bending mode, v_4, and CO_2 rocking mode, v_5. The observed vibrational structure was found both in the V^+ and VO^+ product channel, but it was found that the products' branching ratio varies with the vibrational mode in the photofragmentation spectrum.

Based on this observation and with the assignment of the vibrational bands, the authors concluded that the reactive pathway starts on the same electronic excited state and the reaction is mediated along the reactive trajectory (2.26) by the rock vibration, v_5, and along the non-reactive pathway (2.25) for excitation of the V^+-(OCO) stretch. This was further supported by Citir and Metz who excited the anti-symmetric CO_2 stretch in the VCO_2^+ cluster, and successfully suppressed the reactive pathway.

The vibrational bands observed in the present study for the non-reactive channel are shown in Figure 2.20(a) and were successfully assigned to previously reported transitions [117] from the ground to the excited electronic state surface. In agreement with previous studies products of both the reactive and non-reactive pathways, V^+ and VO^+, are observed at these transitions.

Comparing the strength of the 5_0^1 transition at approximately $15,850\,\mathrm{cm}^{-1}$ to the adjacent fundamental 0_0^0 and 3_0^1 transitions shows that the relative strength of the electronic transition involving the excitation of one vibrational quantum in the v_5 mode, is larger in the reactive compared to the non-reactive channel. This is evidence for the population of the triplet potential energy surface *via* the rock-vibration, v_5, me-

diating the reactive channel (2.26). However, the signal-to-noise ratio in the present study is too low to retrieve any more quantitative information from the data.

The VCO_2^+ complex was successfully mass-selected and a photofragmentation study is in good agreement with previous studies on this system. This shows that the recently adapted set-up can be used to study the photofragmentation dynamics of charged metal-containing molecules and this is the first step towards velocity-map imaging studies in the present set-up. Using the velocity-map imaging technique would yield the kinetic energy and angular distributions of the photoproducts and should in principle give additional information on the final potential energy surfaces of the fragmentation products. For successful velocity-mapping of the fragmentation products several challenges are yet to be overcome. One of these challenges is the control of the parent species kinetic energy distribution. A narrow distribution of slow parent ions is required to achieve a sufficient velocity focus of the spectrometer.

2.5 Conclusion and outlook

Results presented in this chapter highlighted the velocity-map imaging technique as a powerful tool to elucidate the photofragmentation dynamics of *d*-metal containing molecules.

The photofragmentation dynamics of the niobium oxide molecule in the visible part of the spectrum have been studied. Velocity-map image data elucidated the product channels of resonant three-photon and four-photon fragmentation *via* the $C^4\Sigma^- \leftarrow\!\!\!\shortmid\; X^4\Sigma^-$ transition. The branching ratio of observed product states was found to be dependent on the vibrational level of the intermediate C-state in the multi-photon fragmentation.

Analysis of Nb^+ fragment kinetic energy distributions at different photon energies yielded a refined value of the NbO dissociation energy of $60,650 \pm 124$ cm^{-1}. There remains some ambiguity in the determination of this value as it largely depends on a previously reported value of the dissociation energy, $60,734 \pm 887$ cm^{-1} [104], which is used to assign the observed kinetic energy features to product electronic states. Further work is needed to achieve an independent assignment of the product states. One possible approach for such an experiment could be the application of a two-colour multi-photon fragmentation of NbO. The niobium oxide molecule would be resonantly fragmented by one colour photons, the other colour photons are used to resonantly and state-selectively ionize the Nb product fragment. Thus, a specific niobium product channel can be experimentally probed and identified.

Based on the refined NbO dissociation energy and the ionization energies of Nb [105] and NbO [104], the dissociation energy of the NbO^+ ion was determined as $57,414 \pm 124$ cm^{-1}. This value is in excellent agreement with a previously determined value of the NbO^+ dissociation energy by Sievers *et al.* [102].

The capabilities of the experimental set-up were extended by application of photoelectron velocity-map imaging for the first time on this instrument. The performance of the technique in the present experiment was illustrated on a (2+1)-REMPI study of vanadium atoms *via* the $f^4\mathrm{F}_{J'} \leftarrow\!\shortmid\; a^4\mathrm{F}_{J''}$ transition, and the technique was further used to study the photoionization of niobium oxide. The photoelectron kinetic energy distribution shows features assigned to a series of vibrational states accessed in the $X^3\Sigma^-$ state of the NbO^+ ion. An analysis of the spacing of the observed vibrational levels yielded a vibrational constant of the $X^3\Sigma^-$ state, $\omega_e = 1002 \pm 11$ cm^{-1}, which, upon review of the literature published to date, appears to be the first experimentally

determination of this value.

First steps towards velocity-map imaging of fragmentation products from charged *d*-metal containing molecules were showcased on the example of the VCO_2^+ photofragmentation dynamics. In the present state of the experimental set-up, the parent species is successfully prepared and fragmented inside the velocity-mapping lens.

The multi-mass velocity-map imaging technique is expected to be of particular advantage in the study of charged cluster fragmentation dynamics. These species often produce a large number of fragmentation products *via* different fragmentation channels and it would be of particular interest to record velocity-map images of all products simultaneously to save experimental time.

Multi-mass imaging is most likely of limited use to study the photofragmentation of small *d*-metal oxides as the limited velocity and kinetic energy resolution of the available multi-mass imaging devices is too low to distinguish overlapping product channels in the fragments' velocity-map images. However, the simultaneous detection of charged particles in the same experimental cycle could be used to study correlations between photoelectrons and photoions using covariance analysis outlined in Section 1.2.6. In such an experiment, which has previously been conducted [90, 147, 148], photoelectrons are extracted from the interaction region of the molecular and laser beam in the beginning of the experimental cycle before the polarity of the extraction field is rapidly switched and photoions are extracted. Both charged particles are recorded on a single imaging detector and images can be captured using the pixel-imaging mass spectrometry (PImMS) sensor which recently became available to this experimental apparatus.

Chapter 3

Time-resolved imaging of the UV fragmentation dynamics in CH_2BrI

In this chapter, the dissociation dynamics of the CH_2BrI molecule upon absorption of a photon in the A-band is discussed. The ultra-violet (UV) dissociation dynamics of the CH_2BrI molecule is of special interest in a number of studies [7, 149–154] because of its selective dissociation along either the C-Br or C-I bond in two different regions of the UV spectrum. Here, it is shown how the dissociation along the C-I bond can be followed in a UV-pump extreme-ultraviolet (XUV) probe scheme. The XUV pulse ionizes the fragmentation product at an inner-shell orbital and rapid Auger relaxation leads to further ionization. The UV fragmentation is followed using three different probe wavelengths 18.6, 17.7 and 8.9 nm, ionizing at an inner shell electron of the iodine atom for the two longer wavelengths and at inner-shell electrons of the iodine and bromine for 8.9 nm. Time-dependent kinetic energy distributions of the product ions give insight into the charge transfer dynamics between the highly charged halogen ion and the neutral co-fragment. Throughout this chapter, multi-mass imaging with the PImMS2 sensor was utilized and was of great benefit to the experiment. The ionization of UV fragmentation products and of the parent molecule yields a large number of fragment ions for which velocity-map images were recorded simultaneously, saving valuable experimental time at the free-electron laser facility.

3.1 Introduction

The photon wavelength of 271.6 nm, used in the present study, lies in the A absorption band of the CH_2BrI molecule. This feature ranges from approximately 240 to 300 nm and is attributed to the transition of a non-bonding electron at the iodine atom to the C-I anti-bonding orbital, $\sigma^*(C-I) \leftarrow n(I)$ [7, 149].

The dissociation energies of the C-I and C-Br bond are 2.39 eV and 3.25 eV [7]. 271.6 nm corresponds to 4.56 eV of available energy, and absorption of a single photon at this wavelength can dissociate either carbon-halogen bonds but a three body dissociation, during which both bonds are broken, is not energetically feasible. The C-Br dissociation energy of the CH_2Br radical has been reported as 3.84 eV [155] and a secondary dissociation upon absorption of a second photon is possible and has been observed [7, 152]. Isomerisation of the CH_2BrI molecule and elimination of a BrI fragment has not been observed for absorption in the A-band at a wavelength of 248.5 nm [7], but for shorter wavelengths in the B-band at 193 and 210 nm. The elimination is attributed to long living molecular Rydberg states [7].

Following absorption in the A-band, several authors [7, 149, 153] have reported preferential dissociation along the C-I bond with minor contributions of C-Br fission. The C-I fragmentation is believed to occur on the 5A' state potential energy surface, on which an impulsive dissociation produces spin ground state iodine atoms $I(^2P_{3/2})$ [153]. Spin-orbit excited iodine atoms $I^*(^2P_{1/2})$ are believed to be produced on the 4A' and 4A" states which are accessed *via* an avoided crossing from the 5A' state. A minor contribution of C-Br dissociation producing both $Br(^2P_{3/2})$ and $Br^*(^2P_{1/2})$ was also reported [153] for absorption in the A-band. While the 5A' state is believed to be bound along the C-Br bond coordinate [151, 153], the dissociation has been

suggested [153] to progress on the 9A' state potential energy surface following population transfer at a crossing between the 5A' and 9A' state. This is in agreement with reaction times observed by Attar *et al.* [156] with ultra-fast transient absorption spectroscopy at a photo-dissociation wavelength of 266 nm. The authors reported appearance times of 48 ± 12 fs for the $I(^2P_{3/2})$ atom, 44 ± 4 fs for the $I^*(^2P_{1/2})$ atom and 114 ± 17 fs for the $Br(^2P_{3/2})$ atom.

Both C-Br and C-I fragmentation pathways are found to excite ro-vibrational states in the radical co-fragment. Murillo-Sanchez *et al.* [154] reported for the fragmentation yielding ground state $I(^2P_{3/2})$ atoms that 69% of the available energy is transferred into internal degrees of freedom of the CH_2Br co-fragment. In the same work, adiabatic classical trajectory calculations on the MS-CASPT2 level of theory were performed and predicted that most of the transferred energy is channelled into rotational excitation. The rotational excitation is found to be more prominent for dihalomethanes compared to iodomethane due to the "anchor" [154] effect of the second halogen atom, which shifts the centre-of-mass off the C-I bond axis and, thus, induces a torque of the co-fragment in the C-I bond dissociation.

In this work, highly intense extreme-ultraviolet (XUV) laser pulses are employed as a probe in a time-dependent UV-pump XUV-probe experiment. It will be discussed how XUV ionization can be used, similar to the REMPI approach by Murillo-Sanchez *et al.* [154] and Poullain *et al.* [153], as an element-specific probe of the product halogen atom. It will, furthermore, be shown how the XUV inner-shell ionization allows to follow charge-transfer processes between the highly charged halogen ion and its neutral co-fragment, similar to previous studies investigating charge transfer dynamics during the dissociation of CH_3I [157–159] and (2,5)-difluoroiodobenzene [159].

In the following, the experiment and data analysis procedure are introduced. Next, the fragmentation dynamics of the CH_2BrI molecule after XUV ionization at different wavelengths, and after UV ionization for different UV intensities is described. Finally, results from UV-pump XUV-probe experiments are presented for the three different probe wavelengths, and conclusions and new findings are discussed.

3.2 Experimental considerations

The experimental data discussed in this chapter has been recorded with the CFEL-ASG Multi-Purpose instrument (CAMP) [160] at beam-line 1 of the free-electron laser in Hamburg (FLASH1) [56].

Figure 3.1 shows a schematic overview of the CAMP instrument. The experiment is run at a repetition rate of 10 Hz while one experimental cycle proceeds as follows. A continuous beam of pure CH_2BrI is prepared *via* supersonic expansion. In the centre of a double-sided velocity-map imaging (VMI) [11, 12] spectrometer, the sample beam is intersected perpendicularly by a pulsed ultra-violet (UV, 271.6 nm) and extreme ultra-violet (XUV) beam of varying wavelength (8.9 nm, 17.7 nm, 18.6 nm). The FEL beam passes through a hole in the incouple mirror of the UV beam, and both beams travers the vacuum chamber nearly colinear with an angle of 6° to each other. In the interaction region with the molecular beam, the FEL beam and UV laser beam are focussed down to approximately 6 μm and 50 μm diameter, respectively.

Product ions and electrons formed in the photo-reaction are detected simultaneously on either side of the spectrometer. Here, the ions are extracted upwards in the experiment and perpendicular to the molecular beam, and their scattering distributions are recorded on a two-dimensional ion-imaging detector (chevron stack MCP,

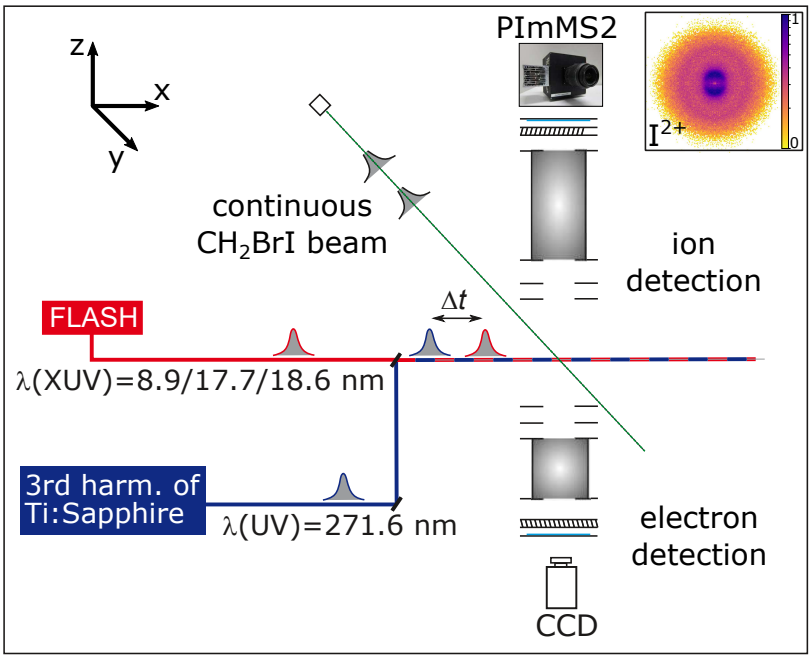


Figure 3.1: Schematic overview of the CAMP instrument at the free-electron laser in Hamburg (FLASH); a continuous molecular beam of CH_2BrI molecules (along y-axis) is intersected by UV and XUV pulses (along x-axis) with a controllable delay Δt; the momentum distribution of all photoions and photoelectrons is recorded in a double-sided velocity-map imaging spectrometer; an exemplary velocity-map image in the top-right corner shows I^{2+} ions produced in the UV-pump XUV-probe experiment; the spatial overlap of both laser beams is frequently adjusted in between data acquisitions to optimise the contrast of the UV photofragments in the image centre over the XUV-fragmentation products in the outer feature.

P47 scintillator). Details on the spectrometer can be found in reference [160], and in this work, typical potential differences of 3000 V for ion extraction and 1600 V for electron extraction have been applied. The PImMS2 sensor [94, 96] was used to image the scattering distribution of all fragment ions simultaneously. The energy resolution of the velocity-map imaging spectrometer is approximately 5%, and the resolution of the detection system is limited, for a singly charged ion, by the pixel size of the PImMS2 sensor to 0.010 eV in the image centre, and to 0.28 eV on the edge of the detector. Photoelectrons are extracted downwards from the interaction region and are detected in the same experimental cycle on a second position-sensitive detector (chevron MCP, P42 scintillator). Electron VMI images are recorded using a charge-

coupled device (CCD) camera but will not be discussed in the context of this work.

While some of the experimental parameters, such as molecular-beam density are consistently stable during the acquisition time of one dataset and are closely monitored, the output and characteristics of the free-electron laser fluctuates throughout the experiment and these fluctuations need to be accounted for. Among other parameters, the FEL pulse intensity fluctuates because of varying efficiencies of the self-amplified spontaneous emission (SASE) process leading to varying ionization efficiencies of target molecules in the experiment. Information on parameters such as the spatial position of the FEL beam, the timing of each XUV pulse and the pulse intensity are measured by diagnostic experiments in the beam-line of the free-electron laser. To synchronize data acquired at CAMP with the corresponding beam-line meta-data, each free-electron laser shot and experimental cycle is identified by a 32-bit integer ID called shot ID.

Fluctuations and drifts in the UV laser beam position reduce the overlap of both FEL and laser beam. To ensure a controlled experiment, the overlap of both laser beams and the molecular beam is checked before and after each data-acquisition by monitoring the pump-probe signal in the centre of the I^{2+} ion image (see inset in Figure 3.1).

Figure 3.2 depicts the integration of the CAMP instrument together with the free-electron laser FLASH and a Ti:Sapphire laser system. XUV laser pulses are delivered by FLASH in single-bunch mode with intensities ranging from 60 to 100 μJ per pulse. An electron bunch is generated by an injection laser and is accelerated to a few GeV kinetic energy by a linear accelerator. XUV laser pulses are generated by self-amplified spontaneous emission (SASE) of the electron pulse inside the undu-

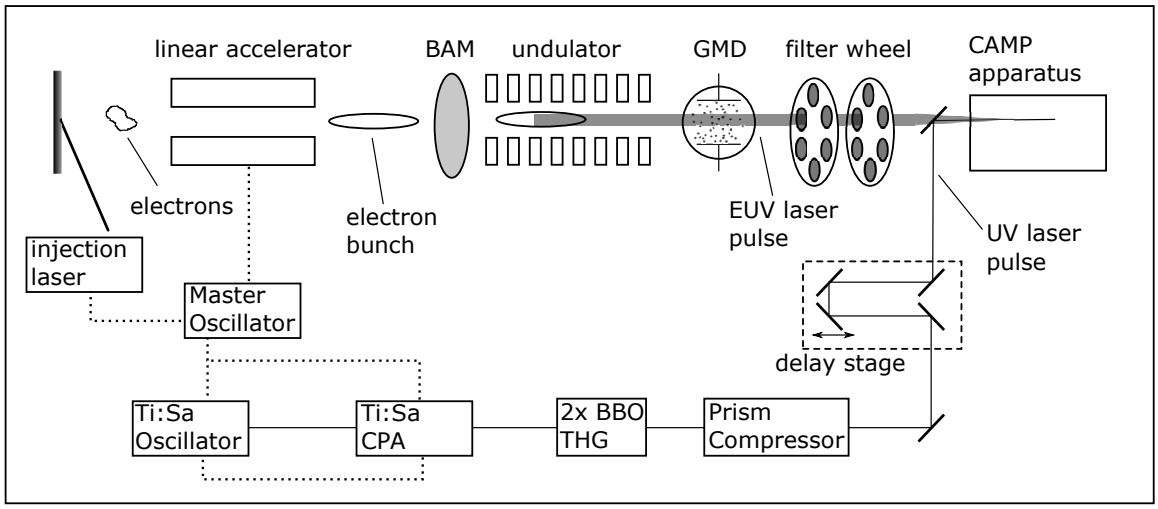


Figure 3.2: Schematic overview of CAMP integrated with FLASH and the pump-probe laser system at beamline 1; the free-electron laser and Ti:Sapphire (Ti:Sa) laser are synchronized *via* the master oscillator; the output of the Ti:Sa oscillator is amplified using a chirped-pulse amplifier (CPA) and the third harmonic of the fundamental pulse is recompressed in time to yield a UV laser pulse that can be delayed using a motorised delay stage; the free-electron laser pulse is formed in the undulator and is attenuated using a set of transmission filters before both laser are focussed and overlapped in CAMP; the bunch-arrival time monitor (BAM) and gas monitor detector (GMD) measure the timing jitter and shot-to-shot power of the free-electron laser pulse, respectively; not drawn to scale and based on Reference [161].

lator. Before entering the undulator, the timing of the electron bunch is registered at the beam-arrival monitor (BAM). The production of XUV radiation pulses using a free-electron laser and the SASE process has been described in Section 1.2.3.3. A gas-monitor detector (GMD) [162] is used to measure the intensity of each XUV laser shot as delivered from the undulator.

The GMD consists of a chamber filled with a rare gas (at low pressure of 10^{-8} mbar) which gets ionized by radiation pulses in the XUV range of the electronmagnetic spectrum. The photoelectrons and photoions are extracted simultaneously by a homogeneous electric field and are registered on a set of electrodes. The fast detection of photoelectrons allows for a shot-to-shot measurement of the intensity. Hence, the

device can track intensity fluctuations of the FEL pulse with an uncertainty of less then 10% [162]. Because of the low gas pressure inside the GMD, the device is almost transparent for the XUV radiation and can be placed into the beam-line in front of the experiment.

The XUV output of FLASH can be attenuated by transmission filters. These are a few nanometer thick films with well-known transmissions in the XUV part of the spectrum. Filters with different transmissions are mounted in two wheels and can easily be changed.

For each transmission filter setting and wavelength, and taking into account the transmission of the beamline, absolute photon numbers per FEL shot have been derived based on the shot-to-shot intensity measurements of the GMD. This calculation is described in detail in Appendix B, and the results are summarized in Figure 3.3. Here distributions of FEL powers are shown in numbers of photons per shot for photon energies of 66.7 eV (red), 70.1 eV (green) and 138.5 eV (blue). Different filter settings are shown in different colour-gradients and with different scatter symbols. The sample size is 1000 FEL shots per combination of filter and photon energy.

The near-infrared output of the Kerr lens mode-locked Ti:Sapphire oscillator is amplified using a chirped-pulse amplifier (CPA). Higher harmonic generation in two BBO crystals is used to obtain a UV laser pulse with a measured central wavelength of 271.6 nm (nominal 267 nm). The UV output is compressed to obtain a pulse length of about 100 fs using a prism compressor. The Ti:Sapphire oscillator and CPA are synchronized with the injection laser and linear accelerator of FLASH using the Master oscillator and Master Laser Oscillator [161, 163]. The delay between the UV and XUV laser pulses is altered by changing the path-length of the UV laser pulse using a

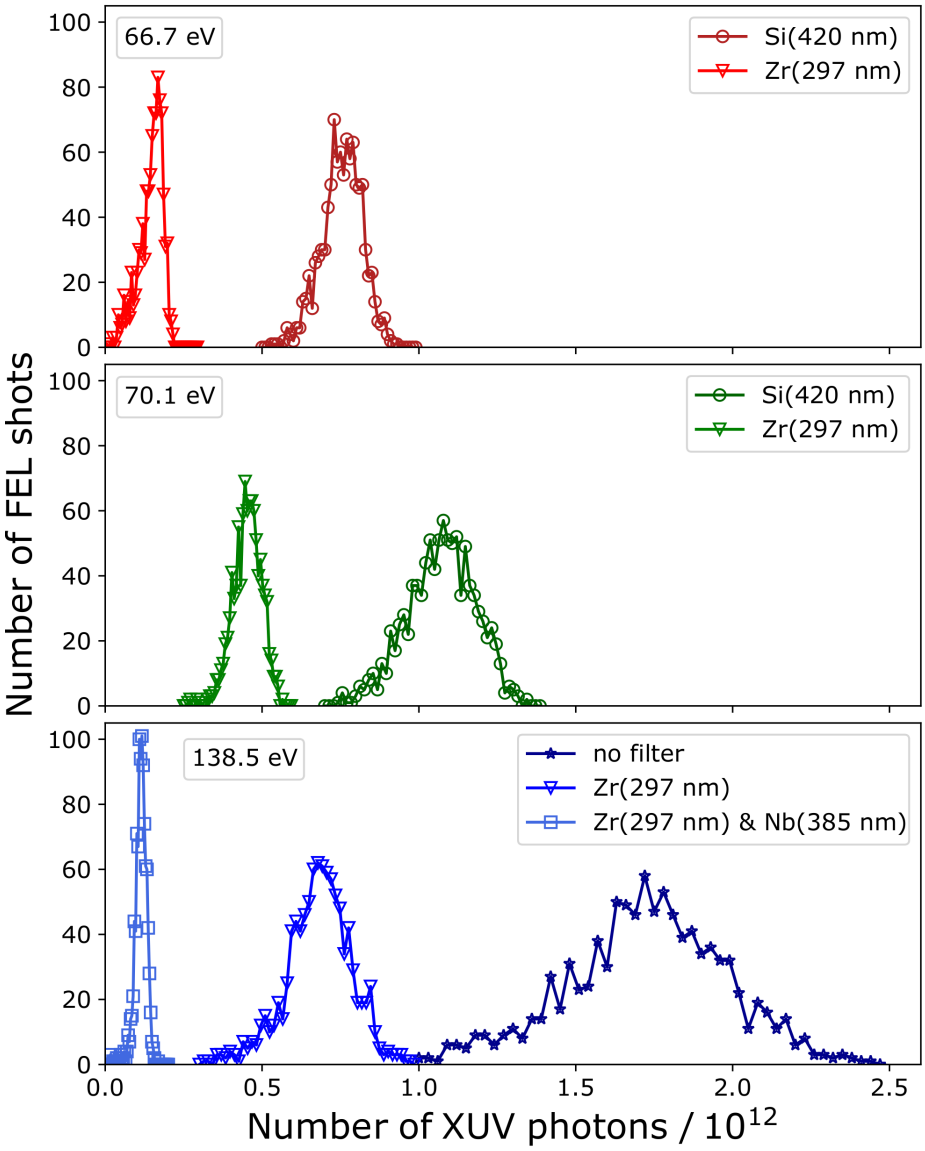


Figure 3.3: Distributions of FEL shot intensities in absolute photon numbers arriving in the interaction region for a sample size of 1000 FEL shots per filter and photon energy combination; Photon energies of 66.7 eV (red), 70.1 eV (green) and 138.5 eV (blue) are shown from the top to bottom panel; distributions of different attenuation filters are shown with different scatter markers; thicknesses of the used filters are given in parentheses.

motorised delay-stage. Section 3.3.3 describes how the jitter of the UV/XUV delay is corrected with the shot-to-shot measurement of the electron bunch at the undulator using the bunch-arrival monitor (BAM).

Varying response times of the beamline diagnostics system and time of data-transfer from the PImMS sensor to the acquisition PC lead to a poor correlation between the acquired data and the FEL shot ID. The reconstruction of this correlation and improvements of the PImMS sensor integration for future experiments are described in Appendix A.

3.3 Particularities of data analysis

Following the correction procedure on the FEL shot ID, time-of-flight and velocity-map image data recorded with the PImMS2 sensor were analyzed based on the procedure outlined in Section 1.2.5. In this section, details of the data analysis, the jitter correction of the pump-probe delay, and the correction methods for the FEL intensity fluctuations are discussed.

3.3.1 Analysis of time-of-flight data

In the data-sets recorded for this chapter, the detection system of the spectrometer was saturated in the centre of the detector by intense background ions, such as H_2O^+, N_2^+ and O_2^+ from residual air, leading to reduced intensities in the central part of the images recorded for heavier ions arriving at the detector at later time-of-flights. In the following, strategies to avoid this saturation artefact are described for an example dataset at low UV intensities and an XUV photon energy of 66.7 eV. In this experiment, the FEL beam was attenuated to moderate intensities using the 420 nm thick silicon filter.

Figure 3.4 shows a two-dimensional histogram of the three dimensional PImMS data-set (x- and y-axis and the time-of-flight axis): y-axis coordinate *vs.* the flight

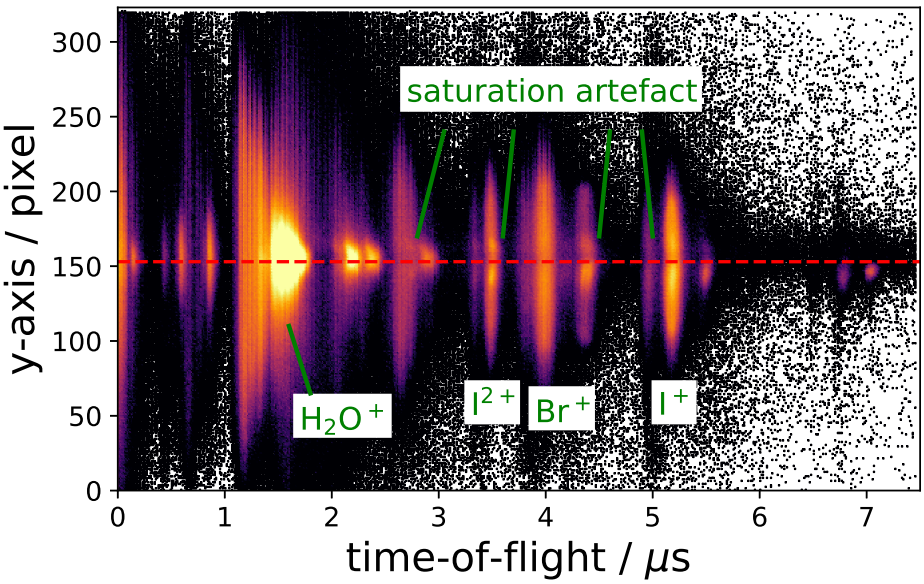


Figure 3.4: Two-dimensional histogram of experimental data recorded with the PImMS2 sensor over the vertical image and time-of-flight axes; shown here are photo-products of the CH_2BrI photo-fragmentation by the UV laser at low intensity and an XUV photon energy of 66.7 eV; the intense background ion signal, especially from H_2O^+ at a time-of-flight of 1.5 μs, saturates the detection system in the centre of the image; the dashed red line represents the image-centre of the CH_2BrI photoproducts.

time. The intense signal of the H_2O^+ ion at a time-of-flight of about 1.5 μs leads to saturation of the detector and reduced intensity for the heavier ions at this (x,y)-position. The green arrows indicate the resulting artefacts in the Br^{2+}/I^{3+} signal at around 2.7 μs up to the I^+ signal at about 5.2 μs. Because background ions are formed along the FEL beam path through the vacuum chamber and CH_2BrI fragmentation products are only formed in the region where the two laser beams and the molecular beam overlap, the most intense background signal is not precisely in the CH_2BrI photo-product image centre but projected slightly higher on the vertical image axis (y-axis in the laboratory frame). Hence, it is possible to discriminate against this saturation artefact by avoiding the top part of the vertical image axis in the following data-analysis. By doing so, time-of-flight mass spectra are produced by integrating the distribution shown in Figure 3.4 over the bottom part of the vertical image axis below the red dashed line, which indicates the centre of the photo-products image.

3.3.2 Analysis of velocity-map imaging data

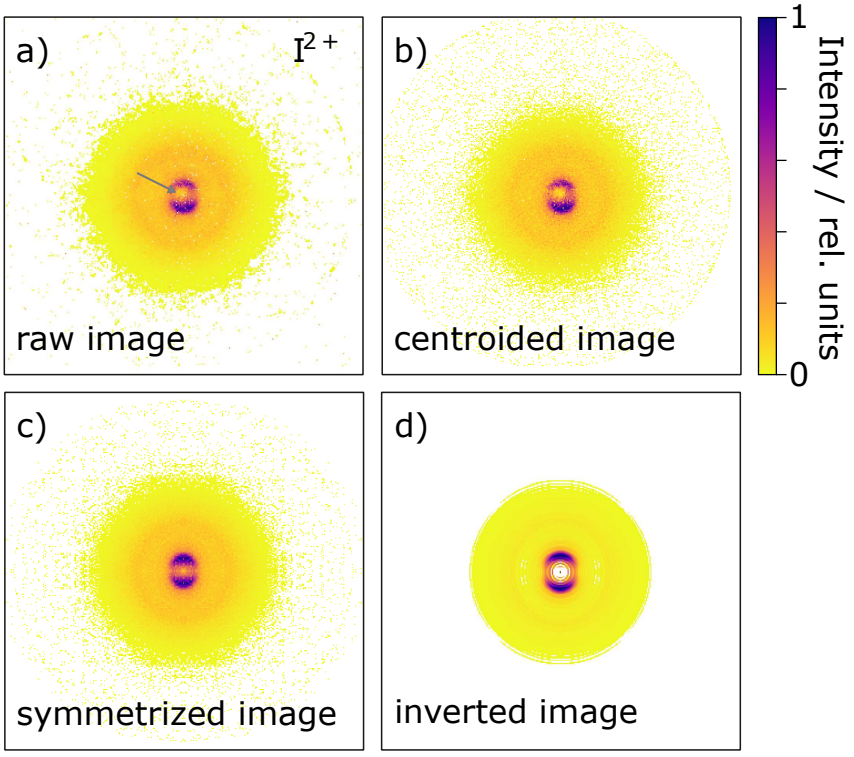


Figure 3.5: Steps for the analysis of the I^{2+} fragment ion recorded with low UV intensity and an XUV photon intensity of 66.7 eV; ion events in the raw image a) are centroided to a single pixel event to yield b), the bottom half of the image in b) is symmetrized over both image axes to yield c) and the pBASEX algorithm yields the Abel inverted image in d); saturation of the detection ensemble in the image centre is indicated by the grey arrow in a).

The analysis steps for velocity-map images are summarized in Figure 3.5 on the example of the I^{2+} fragment. The image is integrated over all UV/XUV delays recorded in this data-set. The hit-finding algorithm described in Section 1.2.7 is applied to the raw image in (a) to yield the "centroided" image in (b). On average, ion events triggered about seven pixel, and were reduced to single-pixel events. Strong background signal, shown and discussed in Figure 3.4, saturates the detection system in the centre of the image where the background signal is most intense. The saturation can clearly

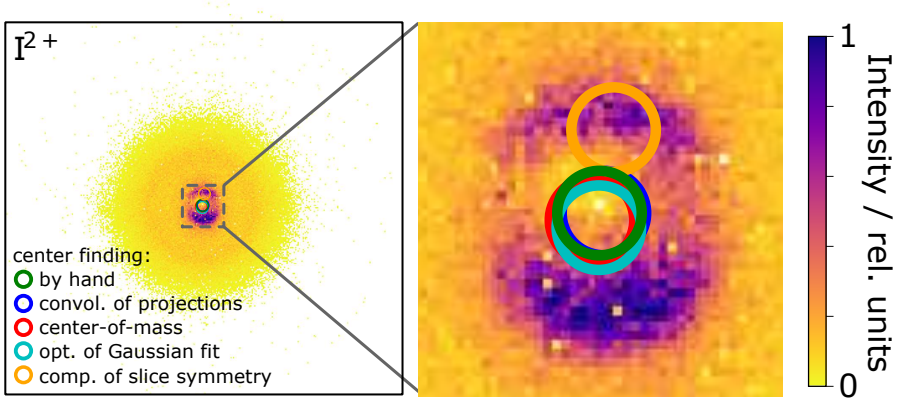


Figure 3.6: Comparison of centre-finding algorithms on a velocity-map image of the I^{2+} photo-product; the saturation artefact prevents algorithms based on the image symmetry from finding the true centre of the image.

be seen above the centre of the image in (a) and (b). The image is symmetrized along both image axes, by folding the bottom two image quadrants on top of each other and reforming the full symmetrized image, shown in (c). Thus, by avoiding the top half of the image, the saturation artefact is successfully eliminated from the data.

To retrieve kinetic energy distributions from the velocity-map images, the pBASEX algorithm [71] was applied. The employed basis functions consist of one Gaussian function per radial element with a full-width-at-half-maximum of 0.7 pixel and Legendre polynomials up to $l = 2$. A discussion of Abel inversion techniques for the reconstruction of the three-dimensional scattering distribution from the two-dimensional projection in a velocity-map image can also be found in Section 1.2.5.

An important analysis step for the symmetrization and Abel inversion of the velocity-map image is the definition of the centre of the scattering distribution's projection in the image. Powerful algorithms, which determine the image centre analytically, can be found in the literature; some of these are illustrated in Figure 3.6.

The influence of the saturation artefact on the centre finding is compared for dif-

ferent centre-finding methods and a careful manual determination of the image centre (green). On the right-hand side of the figure, a magnification of the central image feature is shown. The centre is determined by the convolution of two projections along each image axis (blue), by forming the centre-of-mass of the image (red), by minimizing the residual of a three-dimensional Gaussian fit to the intensity contour of the image (cyan), and by comparison of the symmetry of slices along both image axes (orange). All methods are implemented within the PyAbel software package [164].

The comparison of the determined image centres clearly shows that the comparison of slice symmetries, the centre-of-mass and the optimization of a Gaussian fit do not yield reliable image centres for further analysis. The centre determined by the comparison of symmetries is clearly off but even the slight error of the other two methods can have drastic influences on the symmetrization and inversion of the image and will yield incorrect speed and angular distribution. The convolution of different image projections determines the centre very close to the manually determined image centre. In the data analysis, the image centre was first determined using the convolution method (dark blue) and was then confirmed and adjusted manually for each dataset.

3.3.3 Correction of pump-probe delay

This section describes corrections applied to the pump-probe delay in order to account for temporal jitter of the free-electron laser pulse.

The free-electron laser, the Ti:Sapphire oscillator and chirped pulse amplifier are synchronized *via* the master oscillator and master laser oscillator [163]. If the synchronization between both lasers is working well, the remaining jitter in the pump-probe

delay should mostly originate from fluctuations in the electron bunch's arrival time at the undulator. The correction procedure for jitter in the UV/XUV-delay at the free-electron laser FLASH has been described before in references [165] and [161].

The arrival time of the electron bunch at the undulator is measured with the bunch-arrival monitor (BAM). The BAM is transparent for the electron bunch and measures the electrical transient signal from the electron bunch passing it towards the undulator. This device can measure the bunch-arrival time across a dynamic range of 4 ps.

As opposed to conventional approaches measuring the fluctuation of a laser delay directly using a cross-correlator [166, 167], the measurement of the electron-bunch arrival time is not a direct measurement of the delay between free-electron and optical laser. To confirm that the electron bunch timing is in fact a good measure for the UV/XUV delay, a streak-camera is used to measure the relative timing between the UV-laser pulse and the electron bunch directly. Figure 3.7 shows the fluctuations around the mean value of the electron bunch arrival time measured by the BAM (black line) and the delay between UV laser pulse and accelerated electron bunch measured by the streak-camera (red line). It can be seen that the fluctuations picked up by the streak-camera closely trace the 0.42 ps wide timing fluctuations measured by the beam-arrival monitor. Hence, it is assumed that the fluctuations in the UV/XUV delay are dominated by the arrival time jitter of the electron bunch at the undulator and that both the optical laser and FEL are synchronized successfully *via* the master oscillator and master laser oscillator.

Thus, the UV/XUV delay time deduced from the synchronization of the laser and the relative path-lengths, Δt, is corrected by the arrival time t_{BAM} to yield the

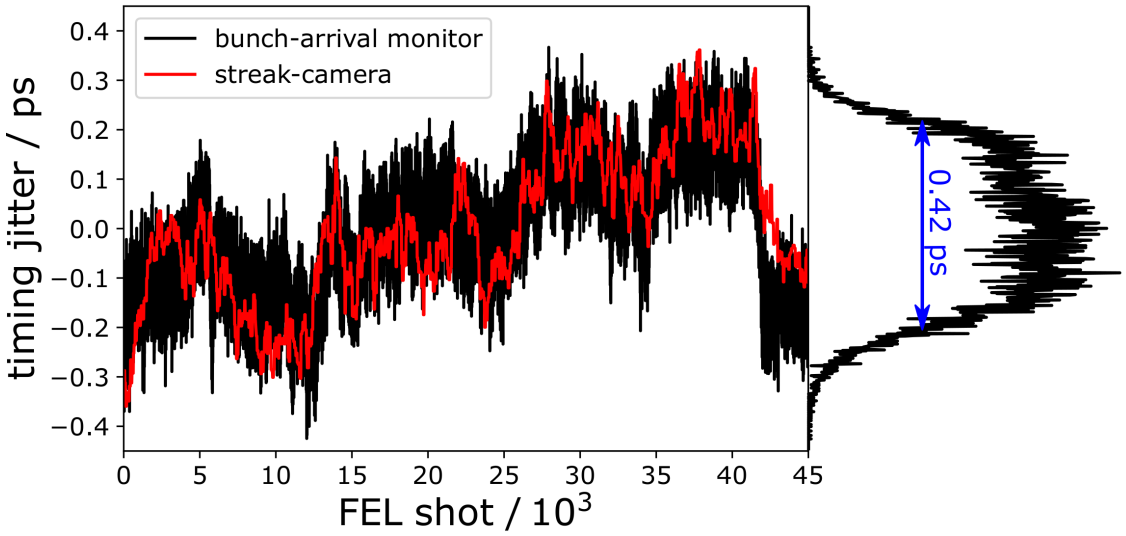


Figure 3.7: Fluctuation across the mean of the electron bunch arrival time measured by the bunch-arrival time monitor (black line) and the UV/XUV delay as measured by the streak-camera (red line). On the right-hand side of the plot the 0.42 ps wide distribution of electron-bunch arrival times is shown.

corrected delay-time Δt_{cor}. The delay is corrected for each individual PImMS camera frame before re-binning of the data across the UV/XUV delay axis:

$$\Delta t_{\mathrm{cor}} = \Delta t - t_{\mathrm{BAM}} \tag{3.1}$$

Figure 3.8 compares the time-dependence of the pump-probe signal in the centre of the I^{2+} ion image before and after the correction in Equation (3.1). This feature is further discussed in Section 3.4.3. Before the correction, the onset of the feature shows an apparent increase in signal at about 0.8 ps which is significant within the statistical error bars. Moreover, there are bins with very small statistics and large error bars. These are due to missing beam-line meta-data and exclusion of the corresponding laser shots from the dataset. However, it can be seen that the correction largely improves the resolution of the step function and evens out the number of laser shots per delay, because the correction in Equation (3.1) shifts data into the segments of missing metadata from adjacent delay bins.

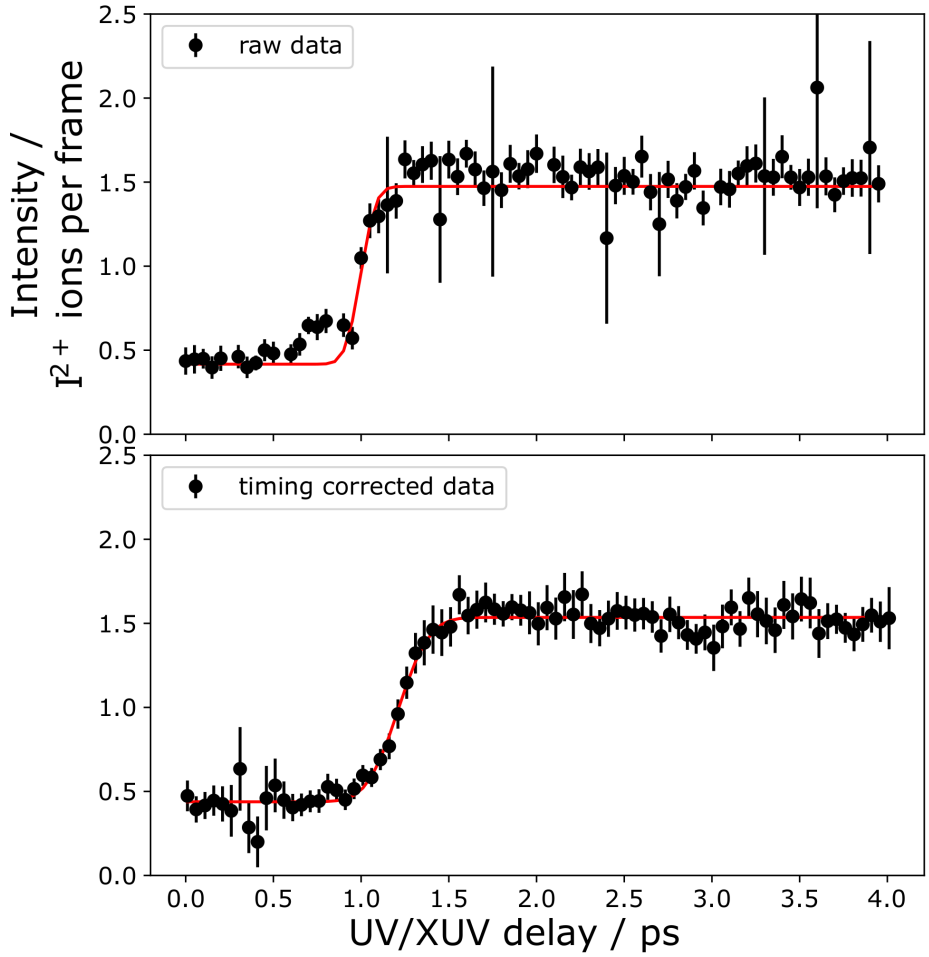


Figure 3.8: Dependence of the central feature in the I^{2+} ion image for an UV pump XUV(λ = 18.6 nm) probe experiment before and after correction for the FEL pulse temporal jitter in Equation (3.1); shown error bars correspond to two standard deviations of the mean bin value; the red line is a Gaussian cumulative distribution function fit to the data.

In Figure 3.8, the UV/XUV delay is arbitrarily defined with respect to the beginning of the dataset. However, the value of zero pump-probe delay corresponds to the temporal overlap of both laser pulses. The UV/XUV delay is defined relative to well known time-dependent features in Section 3.4.3.

The time-resolution of the pump-probe ensemble is limited by the timing fluctuations of the optical laser pulse, which is not accounted for, and the lengths of the XUV- (90 fs FWHM [160]) and UV-laser pulse (150 fs FWHM [159, 160]). Therefore

an effective time-resolution of 250 fs is estimated for this experiment.

3.3.4 Correction for XUV intensity fluctuations

The source of the XUV generation in the free-electron laser, the self-amplified spontaneous emission (SASE, see Chapter 1.2.3.3 for more details), is an inherently stochastic process and leads to fluctuations in the pulse energy of the output FEL pulse.

There are different approaches to correct artefacts in the data from the intensity fluctuation in the free-electron laser pulse. Amini *et al.* [159, 165] and Braußе *et al.* [168] used X-ray laser pulses from FLASH and found a linear correlation between the ion signal and the laser pulse intensity. Based on this, the authors divided the ion-yield for each delay-time interval by the sum of the interval intensities. A different approach has been applied by Erk *et al.* [157] and Boll *et al.* [158] using X-ray laser pulses from the Linac Coherent Light Source (LCLS) [169]. To eliminate the effect of intensity fluctuations from the data, the authors applied a filter in their analysis and only included data for laser shots that yielded pulse intensities with deviations below 2% of the mean. While both methods correct for the intensity fluctuations, the first approach assumes a specific power dependence, which may not be linear for all experimental conditions and different ionic species. Therefore, in cases where the intensity dependence changes with the pump-probe delay or is different for ions with different final kinetic energies, the second approach is favourable.

Figure 3.9 shows the delay dependent feature in the I^{2+} velocity-map image discussed in the previous section and here compares the two different correction approaches for the intensity fluctuations of the FEL. The uncorrected data is shown in the top panel. The approach assuming a linear power dependence is shown in the

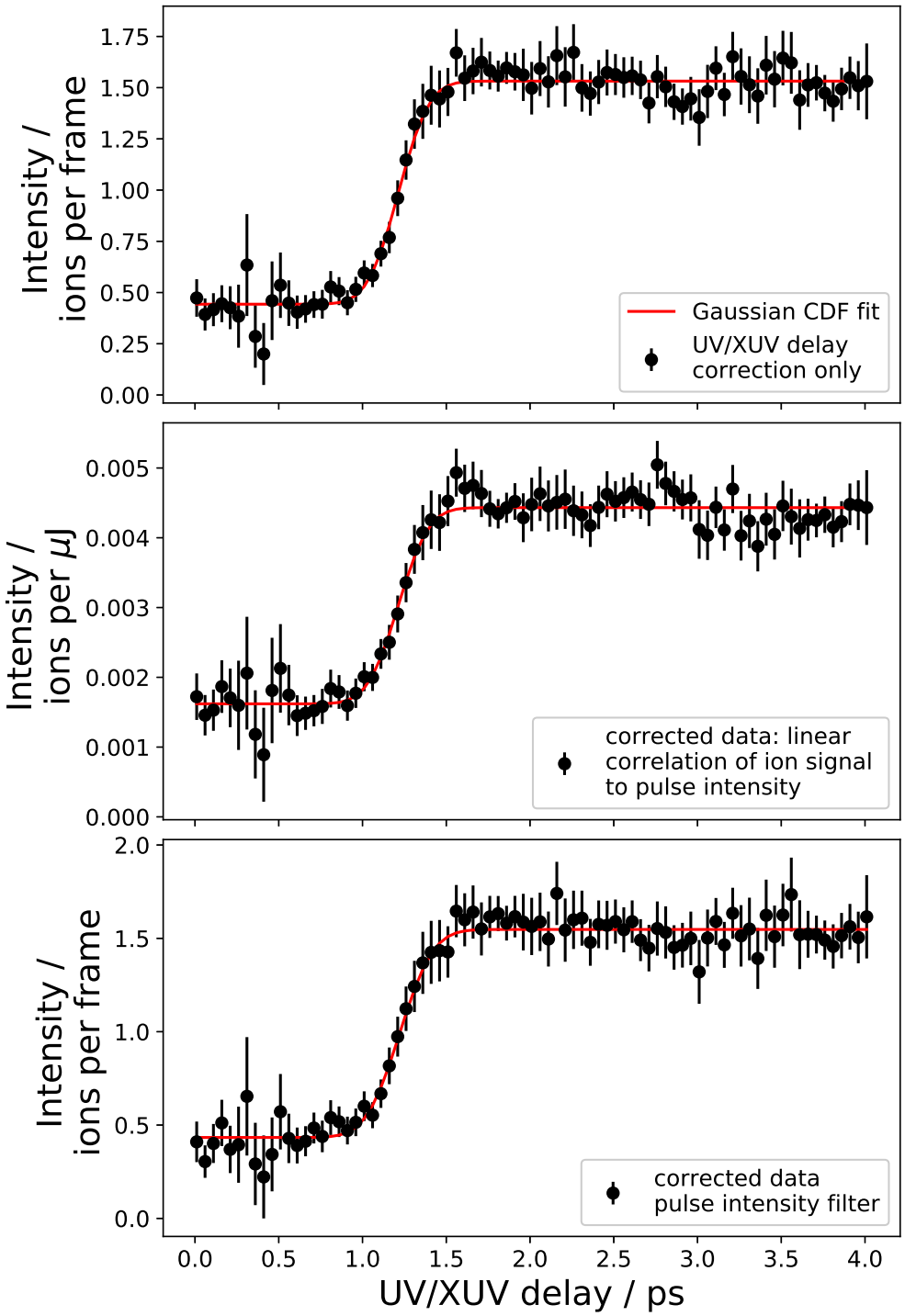


Figure 3.9: Comparison of two different approaches to correct for the XUV power fluctuations: *top*: uncorrected data, *middle*: linear power correction, *bottom*: intensity filter in data analysis; the red line is a Gaussian cumulative distribution function fit to the data; the shown error bars correspond to two standard deviations of the mean bin value.

middle panel, and the correction applying a filter is shown in the bottom panel. All results are similar in this case.

Figure 3.10 shows the pulse-energy as measured by the GMD over the example dataset and the applied filter of one standard deviation above and below the average value. In Figure 3.9, it can be seen that the contour of the step function improved largely by the applied filter, but decreasing statistics lead to larger error bars of the delay bins. This method has, however, the advantage that it does not imply a specific dependence of the signal intensity on the FEL pulse energy. Therefore, this method was applied in the following data analysis and discussion.

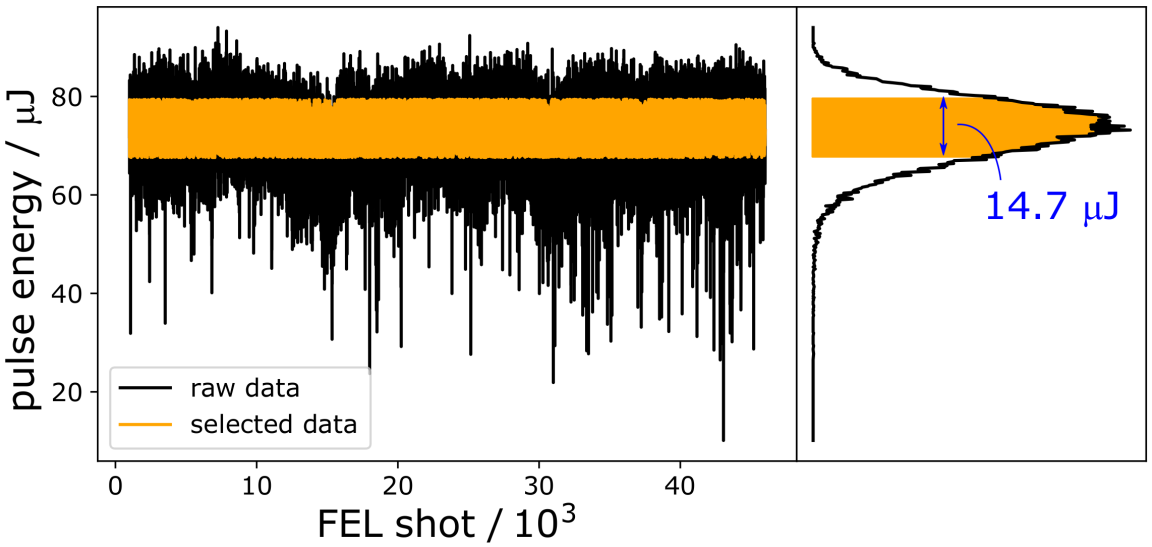


Figure 3.10: Shot-to-shot pulse energy of the free-electron laser as measured by the gas-monitor detector (GMD, black line) for the example dataset: 42500 shots of UV-pump XUV(λ = 18.6 nm) probe, over different pump-probe delays. The distribution of pulse energies throughout the data-set is shown on the right-hand side of the plot. One standard deviation of the mean (yellow) has been chosen to correct the shot-to-shot variations and produce the time-dependent feature shown in Figure 3.9.

3.4 Results and discussion

This section presents the UV dissociation dynamics of the CH_2BrI molecule at a wavelength of 271.6 nm. The dissociation products are probed *via* inner-shell ionization of the fragmentation products by an intense XUV pulse. For high UV laser intensity, dissociative multi-photon ionization becomes a significant fragmentation channel of the neutral parent molecule. This section is structured in three subsections. Firstly, the interaction of the sample molecules with the XUV light is described. In the second subsection the dissociative ionization of the CH_2BrI molecule in intense UV laser pulses is investigated. Finally, results of the time-resolved UV-pump, XUV-probe experiment for three XUV energies and different UV intensities are discussed.

3.4.1 XUV-induced Coulomb explosion of CH_2BrI

Here, the fragmentation of the CH_2BrI molecule by intense XUV pulses is discussed for three different XUV photon energies (66.7 eV, 70.1 eV, 138.5 eV). Mass spectra and kinetic energy distributions of the fragmentation products are discussed separately, followed by a summary of the conclusions on the fragmentation mechanism.

3.4.1.1 Mass spectra

Time-of-flight spectra of the fragmentation products are measured using the PImMS2 sensor and converted into mass spectra as described in Section 3.3.1. In order to compare the yield of fragment ions for different photon energies, the intensities have been normalized by dividing each time-of-flight spectrum by the sum of photons irradiating the sample in each dataset. FEL shot-to-shot photon numbers are derived as described in Appendix B.

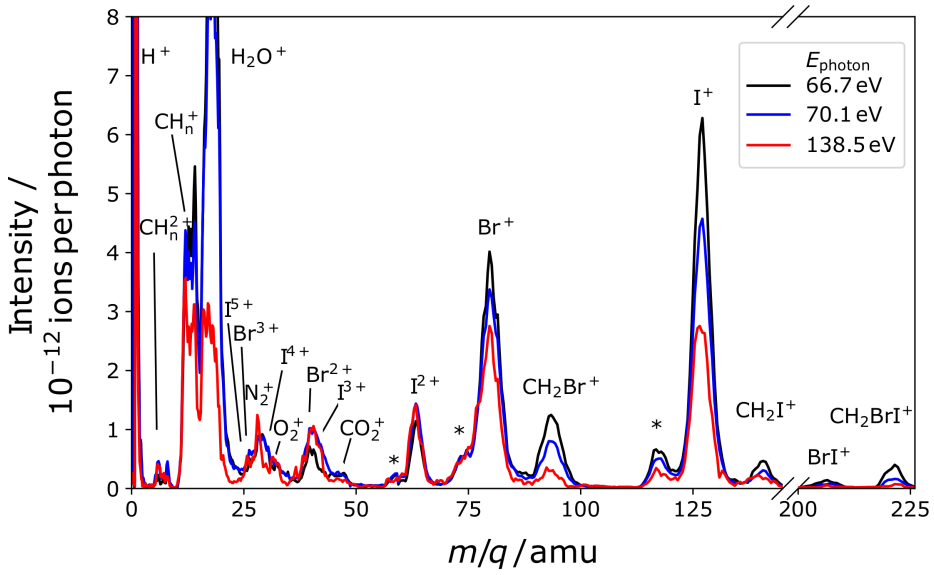


Figure 3.11: Mass spectra of fragmentation products of CH_2BrI molecules in XUV pulses of different photon energies: 66.7 eV (black line), 70.1 eV (blue line) and 138.5 eV (red line); the XUV intensity has been limited to $5 \cdot 10^{11}$ photons per FEL shot; the intensity is normalized by dividing each spectrum by the absolute photon number of the dataset; the mass spectra are smoothed using a two-point wide moving average.

Figure 3.11 shows the mass spectra of XUV fragmentation products at three photon energies: 66.7 eV (black line), 70.1 eV (blue line) and 138.5 eV (red line). The dominant fragment ions in all three spectra are the singly charged hydrocarbon-moiety, bromine and iodine ions. The CH_2Br^+ and CH_2I^+ fragment ions are also present in the spectrum. Compared to the lowest photon energy, the relative yields of higher charged ions is observed to be higher for the to higher photon energies. For the CH_x^+ fragment ion ($x = 0, 1, 2$), the loss of single hydrogen atoms is not resolved within the experimental resolution of about 2 amu at m/q = 12 amu. At mass-to-charge ratios of 18 amu, 28 amu, and 32 amu, contributions of background ions dominate the spectrum. The peaks labelled with an asterisk at mass-to-charge ratios 59, 75 and 118 amu originate from electrons, generated when an ion hits the mesh at the end of the drift tube of the spectrometer.

The fragmentation products are mainly formed *via* two different mechanisms. Fragmentation of a singly charged parent ion which can be formed in valence shell ionization of the neutral CH_2BrI molecule and fragmentation of a multiply charged ion. Muliply charged parent ions can be formed by ionization at an inner-shell electron of the neutral CH_2BrI molecule forming a highly excited parent ion which can relax losing a secondary Auger electron and producing a doubly or higher charged parent ion. The multiply charged ion may then fragment into charged and neutral fragments. The high intensity of the FEL output radiation further facilitates sequential multi-photon ionization [170–172], a process where ionization and Auger relaxation of the sample molecule successively occur multiply times in a single XUV pulse, producing highly charged parent and fragment ions. The difference in ion yield observed in the mass spectra is discussed in the following, on the one hand, in the context of different absorption cross sections of the molecule for the three photon energies. On the other hand, higher photon energies can ionize a stronger bound electron in the molecule leading to different relaxation dynamics of the inner-shell electron vacancy.

Attar *et al.* [156] have measured the XUV absorption spectrum of CH_2BrI in the range from 46 eV to 73 eV and reported a 65 % increase in the absorption cross section at 70.1 eV compared to 66.7 eV. The authors assigned most of the contributions at higher photon energy to inner-shell ionization at the iodine $4d$ electron into the ionization continuum, features at 70.5 eV and 71.5 eV were assigned to core-to-valence transitions of the bromine $3d_{5/2}$ and $3d_{3/2}$ electron into the anti-bonding σ^* orbital. The photon energy used in the present work, 70.1 ± 0.5 eV, coincides with the reported $\sigma^*(\mathrm{C-Br}) \leftarrow\!\shortmid 3d_{5/2}(\mathrm{Br})$ transition.

No absorption spectra of CH_2BrI could be found for photon energies above 73 eV, but absolute absorption cross sections of CH_3Br [173] and CH_3I [174] have been re-

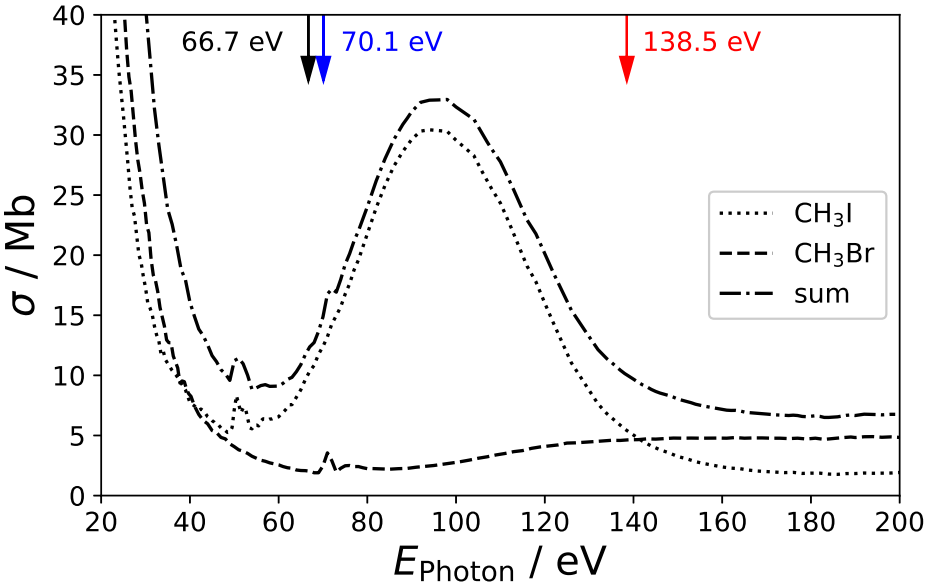


Figure 3.12: Absolute absorption cross sections of CH_3I (dotted line) [174] and CH_3Br (dashed line) [173], and sum of both spectra (dotted and dashed line); downwards pointing arrows show the photon energies used in this work.

ported in the literature, with a resolution of 1 eV, from 6 eV to 450 eV and 4.5 eV to 488 eV, respectively. Figure 3.12 summarizes the data from both studies for photon-energies of interest to this work.

An intense feature centred at about 94 eV was assigned to the ionization of an electron at the iodine $4d$ shell [174]. Two main features were found at 50.6 eV and 52.3 eV for CH_3I, and 70.6 eV and 75.5 eV for CH_3Br. These features correspond to core-to-valence transitions of the iodine $4d_{5/2,3/2}$ and bromine $3d_{5/2,3/2}$ electrons, respectively. These transitions are in close agreement with the energies reported for CH_2BrI by Attar *et al.* [156]. Valence ionization dominates the spectrum from the molecular ionization potential to the binding energy of the lowest energy valence electron at 23.2 eV for CH_3I and 24.9 eV for CH_3Br, and the contribution of valence ionization decreases quickly for higher photon energies.

Similar to the absorption of CH_2BrI observed by Attar *et al.* [156], the sum of ab-

sorption cross-section from CH_3I and CH_3Br (dashed and dotted line in Figure 3.12) shows an increase of absorption cross section by 20% for 70.1 eV, and a decrease by 20% is observed for 138.5 eV compared to 66.7 eV. The absorption cross section determines the relative yield of the parent ion species before fragmentation occurs. The ionization at different photon energies potentially leads to different parent ion charge states and different fragmentation pathways. Therefore, no quantitative information on the absorption cross-section can be drawn from the fragment ion yield observed in the present study. The decreasing yield of the CH_x^+ moiety following ionization at 138.5 eV over 66.7 eV is maybe to some extend a result of the reduced absorption cross section at a photon energy of 138.5 eV.

Olney *et al.* reported the appearence potentials of XUV photo-products for dissociative ionization of CH_3Br [173] and CH_3I [174]. In this study, low flux synchrotron radiation with a typical power of 10^{11} photons per second was employed. Singly charged fragments were mostly found at the binding energies of valence electrons, formed together with one or several neutral co-fragments. Doubly charged halogen ion species were found to appear around the ionization potential of the inner-shell electrons for photon-energies above 50 ± 2 eV for I^{2+} and 71 ± 2 eV for Br^{2+}. Alongside the appearance of doubly charged halogen ions, an increase of fragmentation into singly charged fragments was observed for both CH_3I and CH_3Br. These observations can be explained by the relaxation processes of an inner-shell ionized parent molecule. Upon ionization at an inner-shell electron the molecule undergoes rapid Auger-relaxation processes involving at least two higher energetic electrons. The doubly charged parent ion might undergo fragmentation into multiple singly charged fragments or fragmentation into a doubly charged ion and a neutral charged co-fragment. Both neutral and charged fragments may undergo secondary dissociation.

The inner-shell ionization and core-to-valence transitions observed by Olney *et al.* [173, 174] and Attar *et al.* [156] agree well with calculated binding energies of inner-shell electrons [175] as 61.5041 and 134.737 eV at the $4d$ and $4p$ shell of atomic iodine, and 80.6137 eV and 185.193 eV at the $3d$ and $3p$ shell of atomic bromine. While 66.7 eV and 70.1 eV photons can only ionize the electrons from the iodine $4d$ shell, 138.5 eV photons can additionally ionize the CH_2BrI molecule at the iodine $4p$ and bromine $3d$ shell.

The increasing yield of doubly charged bromine ions for a photon energy of 138.5 eV and 70.1 eV, observed in the present study, is consistent with an appearance potential of Br^{2+} at 71 ± 2 eV, reported by Olney *et al.* [173, 174], and it is therefore concluded that the Br^{2+} ions observed in Figure 3.11 are formed in the Auger decay of the bromine inner-shell vacancy following ionization at the bromine $3d$ electron by a photon with an energy of 138.5 eV or core-to-valence excitation at 70.1 eV. The sequence of single photon absorption, inner-shell ionization and Auger decay of the inner-shell vacancy can occur multiple times within the duration of a single intense FEL pulse, leading to multiple ionization of the parent molecule and formation of highly charged fragment ions [170–172]. This explains the observed triply and higher charged halogen ions observed in the present study. While the Br^{2+}, I^{2+} and I^{3+} ion yields increase for higher photon energies, the ion yield of the singly charged fragment ions decreases. This is consistent with the production of higher parent ion charge states and subsequent fragmentation into higher charged ions upon ionization at the iodine $4d$ and $4p$ and the bromine $3d$ shell.

More information on the fragmentation mechanism is gained from the ion kinetic energy distributions which is discussed in the following section.

3.4.1.2 Kinetic energy distributions

Figures 3.13, 3.15 and 3.16 present the velocity-map imaging data which are analyzed as described in Section 3.3.2. All data are taken with an XUV power up to $1 \cdot 10^{12}$ photons per pulse. Each row shows data for a different fragmentation product. In the left-hand side and central column crushed and inverted image data for a photon energy of 66.7 eV are shown. In the right-hand side column the kinetic energy distribution for 66.7 eV (black line) is compared to the two data-sets acquired with higher photon energy: 70.1 eV (blue line) and 138.5 eV (red line). The kinetic energy distributions are normalized by dividing each distribution by its sum.

Figure 3.13 shows velocity-map image data for the I^+, I^{2+} and I^{3+} ion. The kinetic energy distribution of the I^+ shows two main features, one in the image centre and one centred around 1.7 eV, and two minor contributions at around 3.5 eV and 5.9 eV, respectively. The low kinetic energy ions most likely originate from fragmentation with a neutral co-fragment following ionization at the CH_2BrI valence shell. The higher kinetic energy contributions can be attributed to "Coulomb explosion" products. The Coulomb explosion describes the loss of valence electrons and chemical binding force which results in a partial or complete fragmentation of the molecule governed by the Coulomb repulsion forces between the charged and unbound ions.

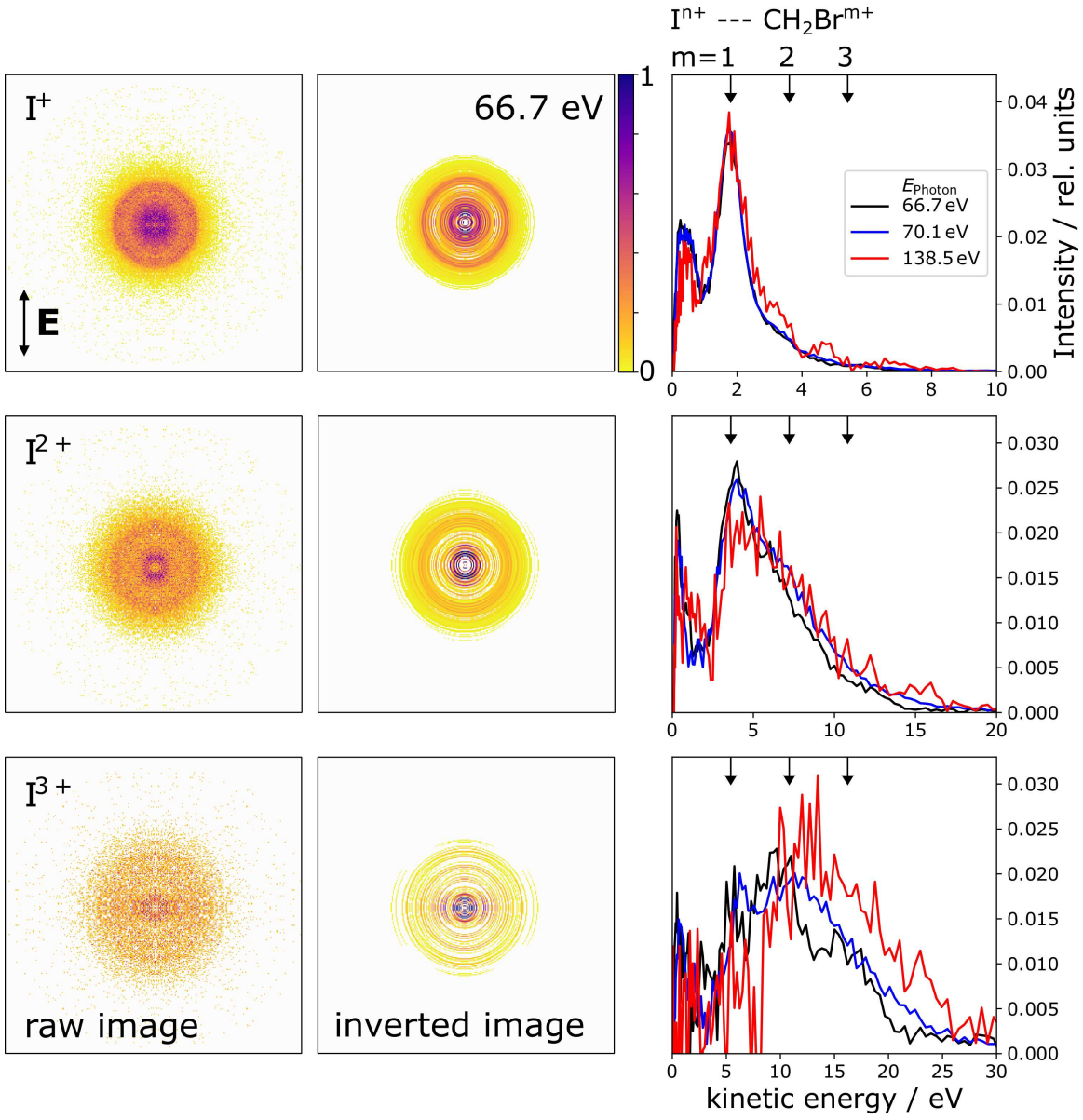


Figure 3.13: Velocity-map images of singly, doubly and triply charged iodine fragments from top to bottom; the symmetrized raw image is shown on the left-hand side and the pBASEX inverted image is shown in the middle column for a photon energy of 66.7 eV; on the right-hand side kinetic energy distributions for all three photon energies are compared to the energies for a singly, doubly, and triply charged co-fragment predicted by a Coulomb repulsion model (see text for details); m and n denote the charges localized on the iodine and bromine atom of the CH_2BrI molecule as shown in Figure 3.14.

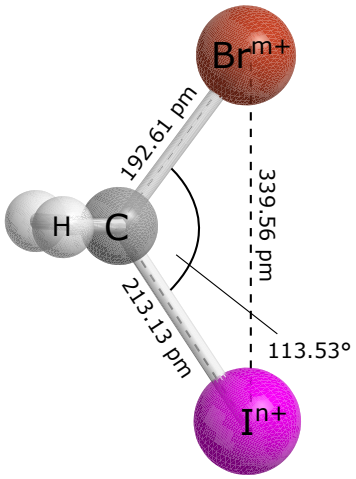


Figure 3.14: Summary of bond-lengths and angles in the CH_2BrI molecule as determined in reference [178]; the I-Br bond distance is derived according to Equation (3.3).

The kinetic energy distributions in Figure 3.13 are compared to a Coulomb repulsion. It is assumed that the fragment kinetic energy results solely from Coulomb interaction of charges placed on the structure of the neutral CH_2BrI molecule. The total kinetic energy $E_{\mathrm{kin,total}}$ of two particles repelling from each other with like charges q_1 and q_2, and separated by a distance r, is given by Coulomb's law [176, p. 13]:

$$E_{\mathrm{kin,total}} = \frac{1}{4\pi\epsilon_0} \cdot \frac{q_1 q_2}{r}. \tag{3.2}$$

The vacuum permittivity is $\epsilon_0 = 8.8541 \cdot 10^{-12}\,\mathrm{F\,m^{-1}}$ [177]. The bond lengths and angles of the CH_2BrI molecule in its vibrational ground state have been determined using microwave and millimeter-wave spectroscopy [178] and are illustrated in Figure 3.14.

The distance between the two halogen atoms r_{BrI} has been derived from the C-I and C-Br bond lengths r_{CI} and r_{CBr}, and the Br-C-I bond angle α_{BrCI} using the law of cosine [179, p. 28]:

$$r_{\mathrm{BrI}} = \sqrt{r_{\mathrm{CI}}^2 + r_{\mathrm{CBr}}^2 - 2 r_{\mathrm{CBr}} r_{\mathrm{CI}} \cos(\alpha_{\mathrm{BrCI}})} \tag{3.3}$$

The total kinetic energy release in the fragmentation of a molecule AB into fragments

A and B, $E_{\mathrm{kin,total}}$, given by Equation (3.2) is distributed over the two fragmentation partners as described in Section 1.2.5 according to,

$$E_{\mathrm{kin,total}} = (1 + \frac{m_{\mathrm{A}}}{m_{\mathrm{B}}}) \cdot E_{\mathrm{A}}$$
$$E_{\mathrm{A}} = E_{\mathrm{kin,total}}/(1 + \frac{m_{\mathrm{A}}}{m_{\mathrm{B}}}). \tag{3.4}$$

Here, E_{A} is the measured kinetic energy of fragment A and m_{A} and m_{B} are the masses of A and B, respectively. The calculated kinetic energies for singly, doubly and triply charged partner fragments are indicated by arrows above the measured kinetic energy distributions in Figures 3.13, 3.15 and 3.16.

The contributions of higher kinetic energy I^+ ions closely match energies expected for a repulsion of the I^+ ion from a singly charged partner fragment at 1.80 eV. Repulsion from a doubly and triply charged rest at kinetic energies of 3.61 eV and 5.41 eV, respectively, are also indicated with downward-pointing arrows in Figure 3.13. The kinetic energy distributions of I^{2+} and I^{3+} fragments compare similarly to the Coulomb explosion model, which predicts twice and three times the kinetic energies for fragmentation against a singly, doubly and triply charged partner fragment. As explained above, the model assumes that the charges are localized on the iodine and bromine atoms in the neutral CH_2BrI geometry, however, the real position of both repelling charges is better described on the potential energy surface of the respective parent ion accessed in the ionization of the molecule and, because the bond length starts increasing upon the first sequential ionization step, the effective distance between both charges in the final charge state tend to be larger than in the neutral geometry [180]. Therefore, the model applied here tends to overestimate fragment kinetic energies and this should become more significant for higher charge states on both fragments [171].

Comparison of the ion yield in the different fragmentation channels assigned based on the Coulomb model show that higher charged fragment ions appear to dissociate

predominately with a higher charged co-fragment. While the I^+ fragment is mostly found to fragment with a singly charged co-fragment, the kinetic energy distribution of I^{3+} fragments is found to be best described by fragmentation against a doubly or triply charged species. This is consistent with the production of a range of different charge states of the parent ion. The parent ions fragment and the charge is found to be distributed between the fragmentation products. Thus, kinetic energy distributions of higher charged ions show evidence for higher charged co-fragments. A comparison between the I^{2+} kinetic energy distributions for the different photon energies shows that the co-fragment charge state appears to be higher for a photon energy of 138.5 eV compared to the two lower energies. One explanation for this is the production of higher charged parent ions upon additional ionization at the bromine $3d$ and iodine $4p$ shell for 138.5 eV.

The observations made of the iodine ions can similarly be found in the velocity-map image data of the bromine fragment ions. For all three bromine ion charge states, there is a central component in the images at low kinetic energies up to 1.5, 3.0 and 5.0 eV, for Br^+, Br^{2+}, and Br^{3+}, respectively. Higher kinetic energy ions are found approximately in three regions, in agreement with Equation (3.2) for repulsion from a singly, doubly and triply ionized molecular partner fragment. The strong central feature in the velocity-map image of the Br^{3+} fragment is due to residual N_2^+ background ions whose arrival time on the detector overlaps with the one for the Br^{3+} ions (see Figure 3.11).

As for the iodine fragment ions the ratio between the intensities of lower and higher kinetic energy ions seems to be slightly shifted towards higher kinetic energies for higher photon energies. Compared to the iodine fragments, the kinetic energy distributions of bromine ions are showing evidence for a higher charge state of the

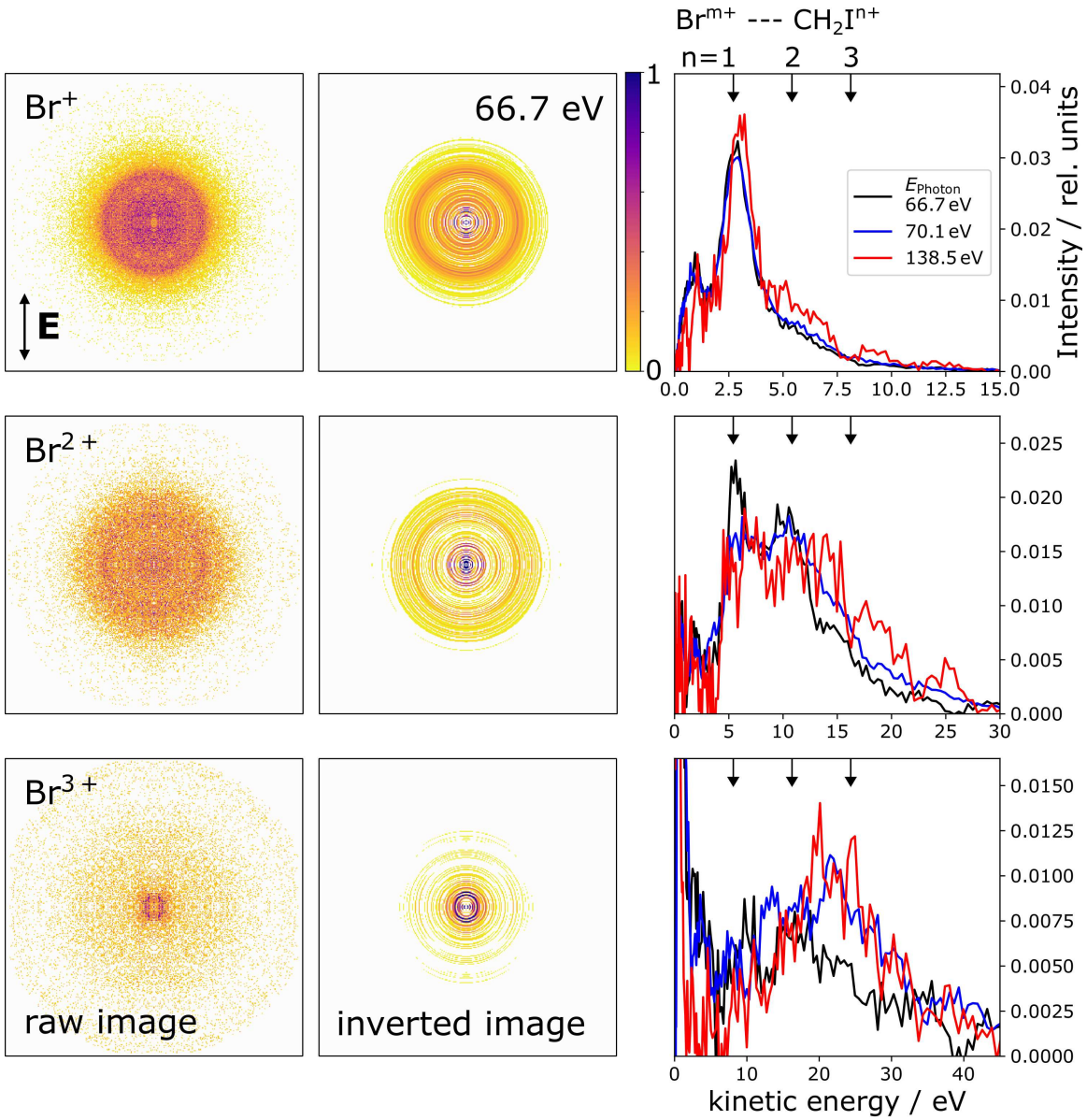


Figure 3.15: Velocity-map images of singly, doubly and triply charged bromine fragments from top to bottom; the symmetrized raw image is shown on the left-hand side and the pBASEX inverted image is shown in the middle column for a photon energy of 66.7 eV; on the right-hand side kinetic energy distributions for all three photon energies are compared to a Coulomb repulsion model described in the text; kinetic energy distributions are compared to the energies for a singly, doubly, and triply charged co-fragment predicted by a Coulomb repulsion model (see text for details); m and n denote the charges localized on the iodine and bromine atom of the CH_2BrI molecule as shown in Figure 3.14.

respective co-fragment. For example in case of the Br^{2+}, the intensities of the components at approximately 5 eV and 10 eV are, for the lowest photon energy of 66.7 eV,

much more similar than in the kinetic energy distribution of the I^{2+} fragment, which is dominated by a single component at approximately 4 eV. This is consistent with the charge remaining mostly on the atom on which the initial ionization step has occurred and at the two lower photon energies the molecule is predominately ionized at an electron localized at the iodine atom.

Figure 3.16 shows velocity-map imaging data for the CH_2Br^+, CH_2I^+ and CH_x^+ fragment ions. The kinetic energy distributions of the CH_2Br^+ are CH_2I^+ fragments consist of two main features, one low kinetic energy component up to kinetic energies of approximately 1 eV and a single higher kinetic energy component centred at 2.4 eV for CH_2Br^+ and 1.6 eV for CH_2I^+. While the low kinetic energy components can be attributed to fragmentation with a neutral halogen co-fragment, the higher kinetic energy components closely match kinetic energies predicted by the Coulomb model for fragmentation of the CH_2Br^+ fragment with a singly charged iodine ion at 2.43 eV and for fragmentation of the CH_2I^+ fragment with a singly charged bromine ion at 1.53 eV. Higher kinetic energy ions indicating fragmentation of CH_2Br^+ and CH_2I^+ with higher charged halogen ions are not observed. This suggest that only singly or doubly charged parent ions undergo two-body fragmentation while higher charged parent ions either undergo a concerted multi-body fragmentation or form unstable higher charged CH_2Br and CH_2I fragments which further dissociate. Further fragmentation yields CH_x^+ fragments and the kinetic energy distribution for these ions is also shown in Figure 3.16. Because of the large number of reaction pathways yielding CH_x^+ fragments, their kinetic energy distribution is broad and almost featureless and further information on the fragmentation mechanism cannot be drawn from these fragments. The intense feature in the image centre originates most likely from background water ions whose arrival time on the detector overlaps with parts of the CH_x ions.

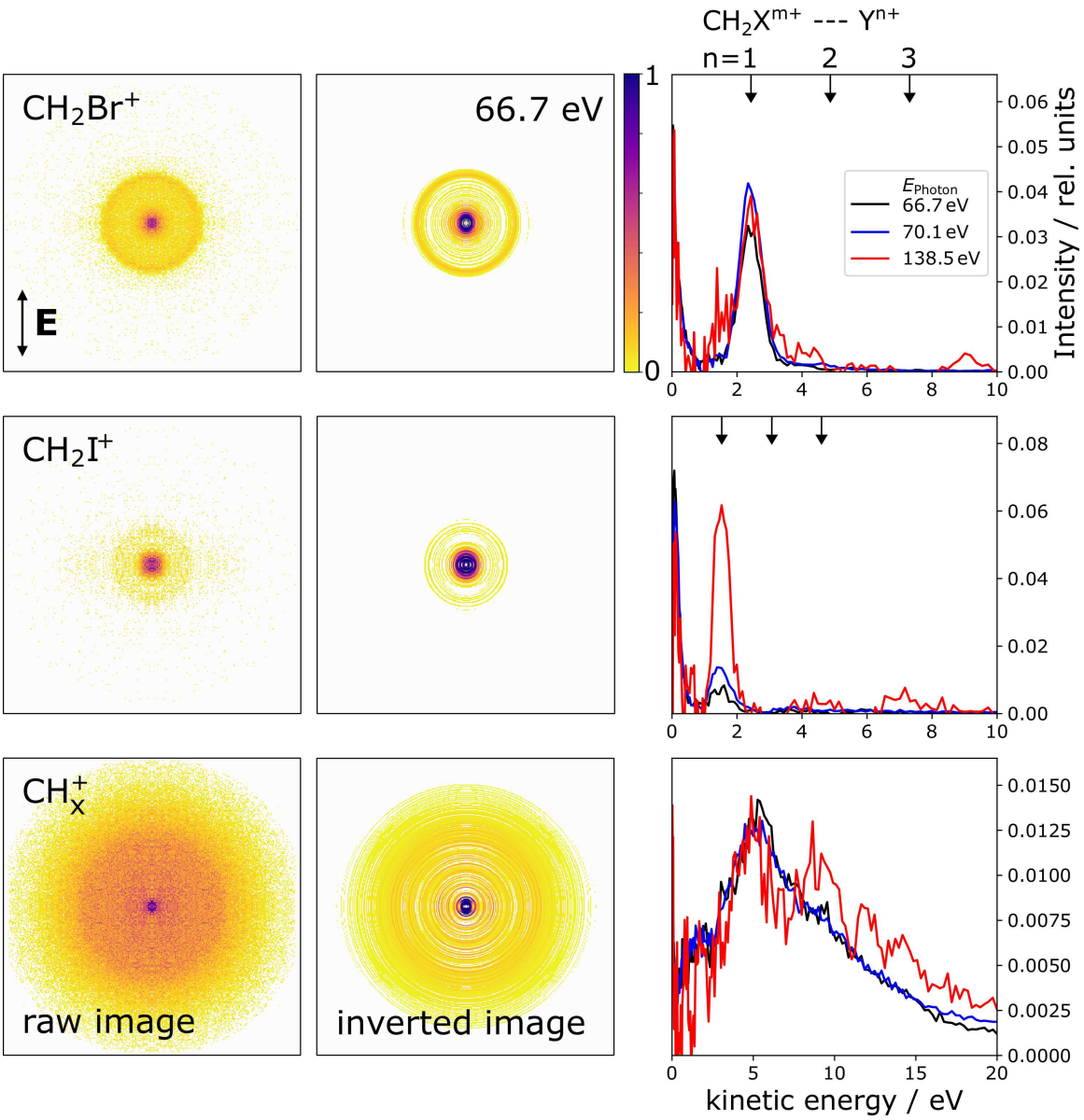


Figure 3.16: Velocity-map images of the CH_2Br^+, CH_2I^+, CH_n^+ fragments from top to bottom; the symmetrized raw image is shown on the left-hand side and the pBASEX inverted image is shown in the middle column for a photon energy of 66.7 eV; on the right-hand side kinetic energy distributions for all three photon energies are compared to a Coulomb repulsion model described in the text; kinetic energy distributions are compared to the energies for a singly, doubly, and triply charged co-fragment predicted by a Coulomb repulsion model (see text for details); m and n denote the charges localized on the halide atoms of the CH_2BrI molecule as shown in Figure 3.14.

In conclusion, the available data suggests that following ionization from an inner-shell electron of the CH_2BrI molecule, fragmentation occurs in a similar manner along both the C-I and C-Br bonds. The observed kinetic energy distributions of singly, doubly and triply charged halogen ions are in accordance with a simple Coulomb repulsion model. Singly charged halogen ions seem to be predominately paired with singly charged fragmentation partners, while higher charged halogen ions are observed to have higher kinetic energies indicative of an on average higher charged partner fragments. While this suggests that the original charge state of the parent ion might be different for the formation of different halogen ion charge states, no definite conclusions on individual parent charge states can be drawn here. Additional fragmentation processes or multi-body fragmentation involving the loss of hydrogen atoms can not be traced within the available statistics and the kinetic energy resolution.

3.4.2 Dissociative ionization of CH_2BrI with intense femtosecond UV laser pulses

The principal goal of the UV-pump XUV-probe study presented in Section 3.4.3 is to investigate the neutral dissociation of the CH_2BrI molecule upon single-photon absorption in the A-band. The third harmonic of the Ti:Sapphire oscillator provides photons of a wavelength of 271.6 nm which corresponds to a photon energy of 4.56 eV. These photons are used to initiate the photo-dissociation of CH_2BrI. In addition, multi-photon ionization of the CH_2BrI molecule may take place, in particular at higher laser intensities. The vertical ionization potential from the CH_2BrI ground state has been reported as 9.5944 ± 0.0006 eV [181], and thus it takes three photons to ionize the molecule. In this subsection the fragmentation dynamics of the CH_2BrI molecule following multi-photon ionization for three different UV intensities is discussed to compare the influence of the UV-pump pulse for different UV intensities. Low (15 μJ/pulse), medium (60 μJ/pulse) and high UV pulse powers (90 μJ/pulse) are

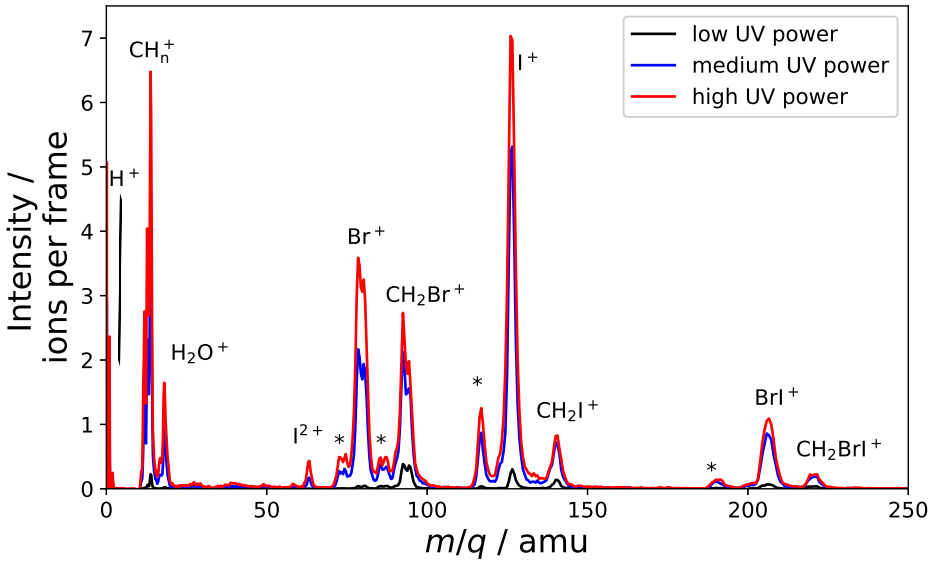


Figure 3.17: Time-of-flight mass spectra of UV fragmentation products of CH_2BrI for three different UV intensities; peaks labelled with an asterisk originate from electrons generated when an ion hits the mesh at the end of the drift tube of the spectrometer.

employed. The discussion is based on mass spectra and velocity-map images recorded with only the UV laser interacting with the molecular sample and this subsection is focussed on I^+, I^{2+} and Br^+ fragment ions which are of significance in the discussion of the UV-pump XUV-probe experiment.

Figure 3.17 shows the mass spectrum of ionic fragmentation products from CH_2BrI interacting with the UV laser at three different laser intensities. As expected, higher laser intensities result in stronger ionization and a higher degree of fragmentation yielding smaller m/q fragments. The most prominent fragment ions are I^+, CH_2Br^+, Br^+ and CH_x^+, while CH_2I^+ and IBr^+ are also observed but have lower signal levels. The parent ion at a mass of 220.84 amu is observed to be much less intense than the most prominent fragmentation product, the I^+ ion.

Upon single ionization, the CH_2BrI molecule may fragment along the C-I and C-Br bonds forming neutral and charged fragments. Larger fragmentation products can

undergo secondary fragmentation into smaller fragments. For low UV intensities the CH_2Br^+ and I^+ fragments have a higher abundance compared to the CH_x^+ fragment. CH_2I^+, Br^+ and BrI^+ fragments are also observed as minor products. With higher UV intensities the ion yield increases drastically.

Figure 3.18 shows the velocity-map images and kinetic energy distributions of the fragmentation products I^+, I^{2+} and Br^+. Velocity-map images are only shown for the highest UV intensity with the highest ion count, and kinetic distributions are shown for all three UV intensities if sufficient signal was recorded for the ion of interest.

Fragmentation into a charged and a neutral fragment yields relatively low kinetic energy ions and is observed as a single feature below 1 eV for each of these halogen ions. This fragmentation channel appears to be dominant but there is also a minor channel which becomes more prominent for higher UV intensities centred at about 1.5 eV, 3.5 eV and 2.0 eV for I^+, I^{2+} and Br^+, respectively. One possible explanation for these higher-energy ions is ionization to a multiply charged parent ion and a subsequent Coulombic fragmentation of the parent ion into multiple charged fragment ions. The observed fragment kinetic energies are compared to the energies derived in the Coulomb repulsion model described in Section 3.4.1.2. Predicted fragment kinetic energies compare well the features observed in the data. The observation of the charged halogen ion repelling from another charged co-fragment implies the initial formation of a doubly charged parent ion to produce Br^+ and I^+ and a triply charged parent ion for I^{2+}.

The presented data is consistent with a major contribution of dissociative ionization into one charged and neutral fragments. Furthermore, there is evidence for the formation and subsequent fragmentation of a multiply charged parent ion as a

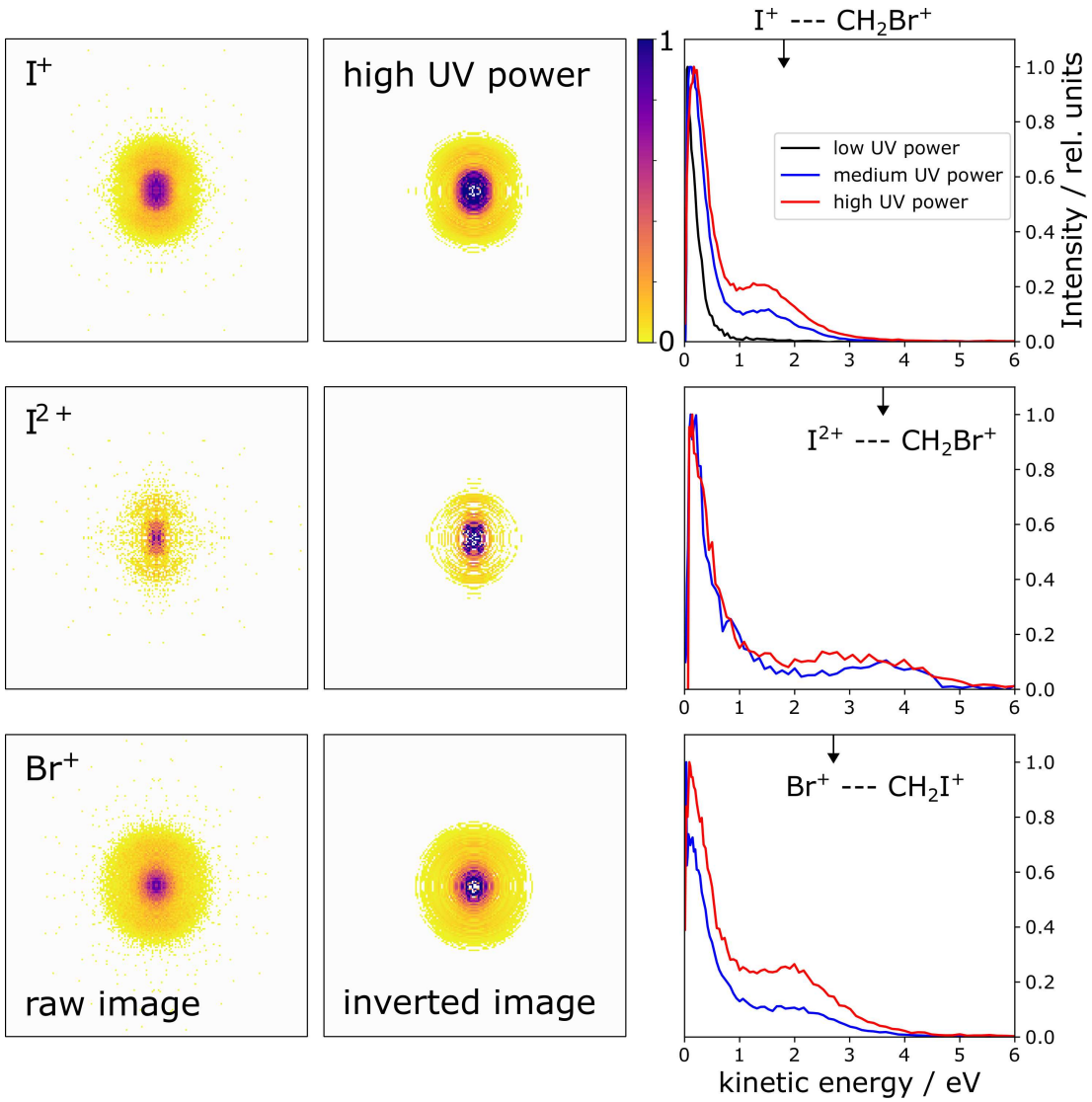


Figure 3.18: Velocity-map image data of the I^+, I^{2+}, Br^+ ions from the top to bottom; Abel-inverted data using pBASEX with even order Legendre polynomials up to $l = 4$ are shown in the central column; kinetic energy distributions of the fragmentation products are shown in the right-hand side column at the highest (red), medium (blue) and lowest UV intensity (black); the kinetic energy distributions at the lowest UV intensity are only shown for fragments with sufficient ion yield; the downward pointing arrows indicate energies predicted with the Coulomb repulsion model in subsection 3.4.1.2.

minor channel. The observed ion yield is much larger for higher UV power which is consistent with a non-linear dependence of the ion yield on UV power, as expected for a UV multi-photon ionization of CH_2BrI.

3.4.3 UV dissociation dynamics probed with Coulomb explosion imaging

In this section, the neutral dissociation dynamics of the CH_2BrI molecule is investigated in a UV-pump XUV-probe experiment. XUV pulses with three different photon energies, 66.7 eV, 70.1 eV and 138.5 eV, and FEL powers of $(0.75 \pm 0.1) \cdot 10^{12}$ photons per pulse for 66.7 eV, $(0.45 \pm 0.1) \cdot 10^{12}$ photons per pulse for 70.1 eV and $(1.7 \pm 0.3) \cdot 10^{12}$ photons per pulse for 138.5 eV are employed to ionize the neutral fragmentation products.

Figure 3.19 shows the combined results from UV fragmentation of the CH_2BrI molecule probed time-dependently with intense XUV pulses. On the bottom of the figure, the difference between mass spectra integrated over the "UV early", with the UV laser preceding the XUV pulse, and "UV late" regimes, with the XUV pulse preceding the UV laser pulse, is shown for the three different XUV probe photon energies 66.7 eV, 70.1 eV and 138.5 eV. Data for an experiment employing high intensity UV pump pulses and an XUV photon energy of 138.5 eV is also shown (green line). A positive difference signal corresponds to fragmentation products due to the UV laser pulse, followed by ionization by the XUV pulse. Singly charged fragment ions H^+, CH_x^+, Br^+ and I^+ generally show a decreased yield for the "UV early" relative to the "UV late" regime. The CH_2I^+ yield is approximately constant at all probe energies and the CH_2Br^+ yield is approximately constant for probe energies of 70.1 eV and 138.5 eV but decreases at high UV intensities and an increase is observed at 66.7 eV, as shown in the inset. An increase of ion yield is observed for doubly and higher charged halogen ions. For the two lower photon energies, an increase in the I^{2+} and I^{3+} can be observed while for 138.5 eV the higher charged halogen ions I^{4+} and I^{5+} increase in yield. Even higher charged halogen ions such as I^{6+} or Br^{4+} at $m/q = 21.1$ and 19.9 amu coincide with the intense water signal and are not analyzed here.

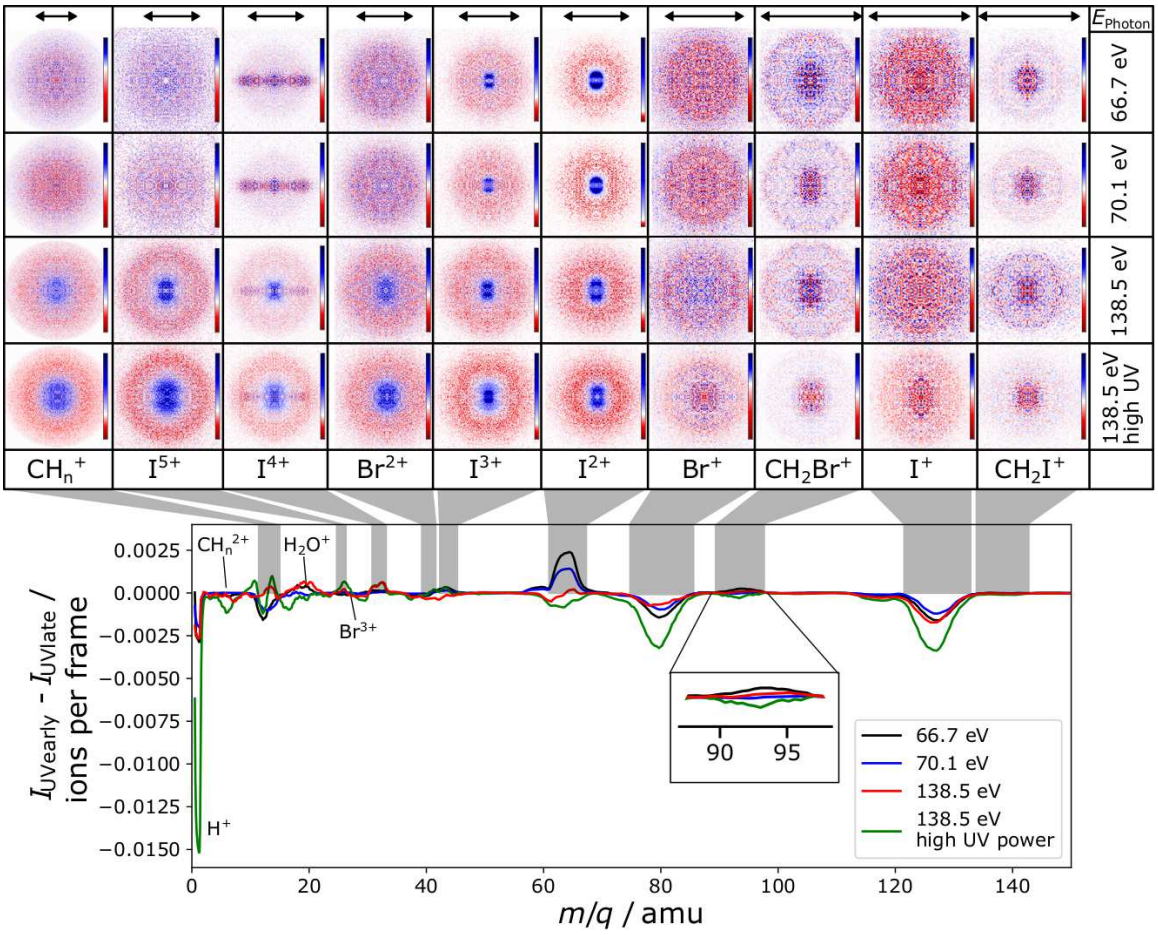


Figure 3.19: *Bottom*: difference mass spectrum of CH_2BrI fragmentation products for three different XUV probe photon energies: 66.7 eV (black), 70.1 eV (blue), 138.5 eV (red) and 138.5 eV with high UV pump intensity (green); the ion yield is derived as the difference between the ion yields of the "UV early" and "UV late" regime; *top*: difference velocity-map images for all four experimental conditions; blue image regions represent an increased ion yield for "UV early" compared to "UV late", red image regions correspond to a decrease in the ion yield; the image size is adjusted to zoom-in on the image region of interest, the original image sizes are compared with the size of the smallest image (CH_2I^+) given as an arrow in the top row; both laser beams are polarized along the vertical figure axis.

In the top part of Figure 3.19, difference velocity-map images show how the ion yield changes across the velocity distributions of a respective fragment ion for different XUV energies. While for I^+ and Br^+, the yield decreases uniformly across the distribution, higher charged halogen ions comprise two components. For all four experimental

conditions, the scattering distribution of I^{2+} and I^{3+} ions show an increased yield for low kinetic energy ions in the image centre, and a decreasing ion yield for higher energy components at larger image radii. Notably, an increased yield in the distribution's centre can also be observed for the Br^{2+}, I^{4+} and I^{5+} fragments for a photon energy of 138.5 eV while it is much less pronounced for the lower photon energies. Finally, the CH_x^+ also shows an increasing ion yield in the image centre which may originate from I^{9+} and I^{10+} ions overlapping with the CH_x^+ fragment at m/q = 14.1 and 12.7 amu.

The observations made in Figure 3.19 can be explained in the context of two main processes which compete with each other: fragmentation of the CH_2BrI molecule following inner-shell ionization by the XUV laser; and UV fragmentation of the target molecule forming neutral iodine and bromine atoms which are subsequently ionized in the XUV pulse. The former process is described in detail in Section 3.4.1, and it was found that the CH_2BrI molecule loses multiple electrons after inner-shell ionization and Auger-relaxation and that the highly charged parent ion undergoes a Coulomb explosion into multiple charged particles. Although ions with smaller kinetic energy are also observed and attributed to valence ionization processes, the majority of XUV fragmentation products are observed with larger kinetic energy ranging up to 20 eV for a triply charged iodine ions.

Absorption of one UV photon in the A-band leads to fragmentation along the C-I bond as a major dissociation channel according to,

$$CH_2BrI \longrightarrow CH_2Br + I/I^*. \tag{3.5}$$

A smaller contribution of sample molecules fragments along the C-Br bond and *via* secondary dissociation of the CH_2Br intermediate following C-I dissociation according to,

$$CH_2BrI \longrightarrow CH_2I + Br/Br^* \tag{3.6}$$

$$CH_2Br \longrightarrow CH_2 + Br/Br^*. \tag{3.7}$$

Reactions (3.5) to (3.7) reduce the amount of molecules in the shared interaction region of the FEL and UV laser beams which are available to be inner-shell ionized by the FEL. Hence, the yield of molecular XUV fragmentation products with predominately larger kinetic energies decreases for the "UV early" compared to the "UV late" regime.

Isolated iodine and bromine atoms formed in Reactions (3.5) to (3.7) can be ionized in the XUV pulse either at an inner-shell or valence shell electron. The kinetic energy of the halogen ion is then gained in the UV fragmentation and is much smaller than the kinetic energies of XUV fragmentation products. These ions form the low kinetic energy contribution of the higher charged halogen ions, appearing in the centre of the velocity-map images. In accordance with previous UV photo-fragmentation studies of CH_2BrI in the A-band [7, 153], these low kinetic energy components show a clear anisotropy parallel to the polarization axis of the UV laser beam which is polarized along the vertical axis of Figure 3.19.

Given the high intensity of the XUV probe pulse from the free-electron laser, the halogen atom is ionized multiple times at inner-shell electrons in a single XUV pulse [170], and each ionization step is followed by Auger decay processes of the ion-hole state. Thus, a highly charged halogen ion is produced. The binding energies of halogen inner-shell electrons were calculated [175] as 61.5051 and 137.737 eV at the

$4d$ and $4p$ shell of the iodine atom, and 80.6137 and 185.193 eV at the $3d$ and $3p$ shell of the bromine atom. Therefore, iodine atoms can be ionized at an $4d$ electron with a probe photon energies of 66.7 eV and 70.1 eV, and at the $4d$, $4p$ for the highest photon energy of 138.5 eV. Bromine atoms can only be ionized at the inner-shell $3d$ electron with the highest XUV photon energy.

The halogen can also be ionized at the valence shell. According to calculated atomic ionization cross sections [175] for an XUV photon energy of 66.7 eV, valence shell ionization of the bromine atom is about 42 times less probable than at the iodine $3d$ shell for the same photon energy. Bromine and iodine atoms ionized at the valence shell would yield singly charged ions and the ionized UV photo-products would appear in the centre of the velocity-map image. Consistent with the low ionization cross-section of the bromine atom, no significant UV photo-products are observed in the Br^+ difference image in Figure 3.19, but the ion yield decreases uniformly for all kinetic energies from the "UV early" compared to "UV late" regime.

The calculated binding energies of the inner-shell electrons at both halogen atoms are consistent with observation of I^{2+} ions as the main halogen ionization products of XUV probe photons at energies of 66.7 eV and 70.1 eV. Photons of these energies cannot ionize bromine atoms formed in Reaction (3.7) at inner-shell electrons and, thus, present a site-selective probe for the iodine photo-dissociation products from Reaction (3.5). In contrast to this, probe photons with a higher energy of 138.5 eV can ionize a bromine atom at the $3d$ shell and an iodine atom at the $4d$ and $4p$ shell. Thus, bromine photo-products from the UV fragmentation are detected at this XUV photon energy. While ionization from a deeper shell on the iodine can lead in principle to multiple losses of Auger electrons [182], and could produce I^{3+} ions observed in the present study, these and higher charged halogen ions are more likely a result

of sequential multi-photon ionization, given the XUV probe intensity employed here.

In the following three sections, the UV dissociation processes along the C-I and C-Br bonds and the observed depletion of the XUV fragmentation channels is discussed in more detail.

3.4.3.1 C-I bond dissociation

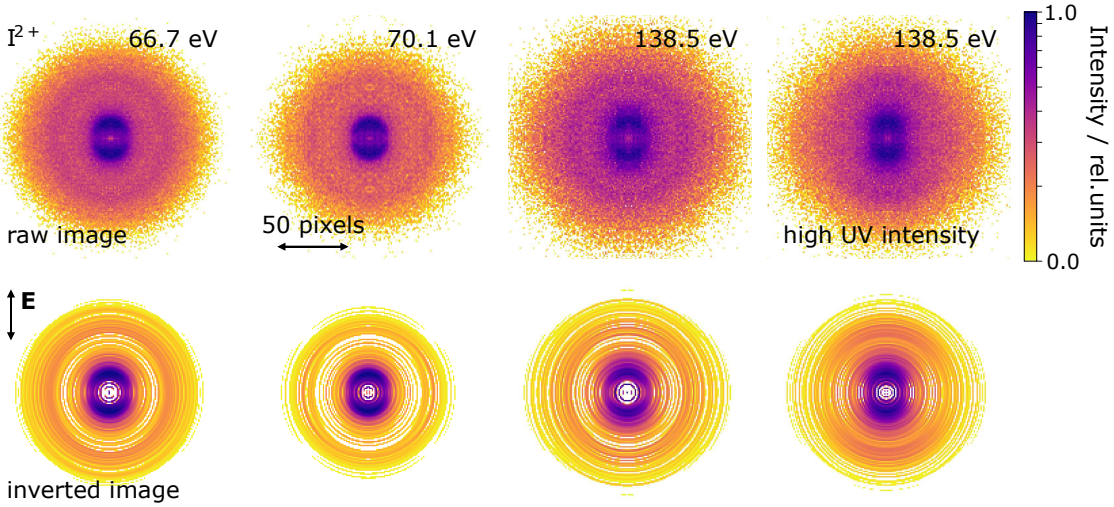


Figure 3.20: I^{2+} velocity-map images for XUV probe times $t > 1.5$ ps after the UV-laser pulse; symmetrized raw images are shown in the top and pBASEX inverted images are shown in the bottom row; three different XUV probe photon energies 66.7 eV, 70.1 eV, 138.5 eV for low UV pulse intensities are shown from the left to right; high intensity UV pump and 138.5 eV probe data is shown on the right-hand side.

Figure 3.20 shows velocity-map images of the I^{2+} fragment integrated for a UV/XUV delay, $t > 1.5$ ps ("UV early"), and for the three different XUV probe photon energies 66.7 eV, 70.1 eV and 138.5 eV, left to right. Data for a high UV pump intensity and a probe photon energy of 138.5 eV is shown on the right-hand side of the figure. The symmetrized images are shown in top row and the pBASEX inverted images are shown in the bottom row. The resulting kinetic energy distributions and

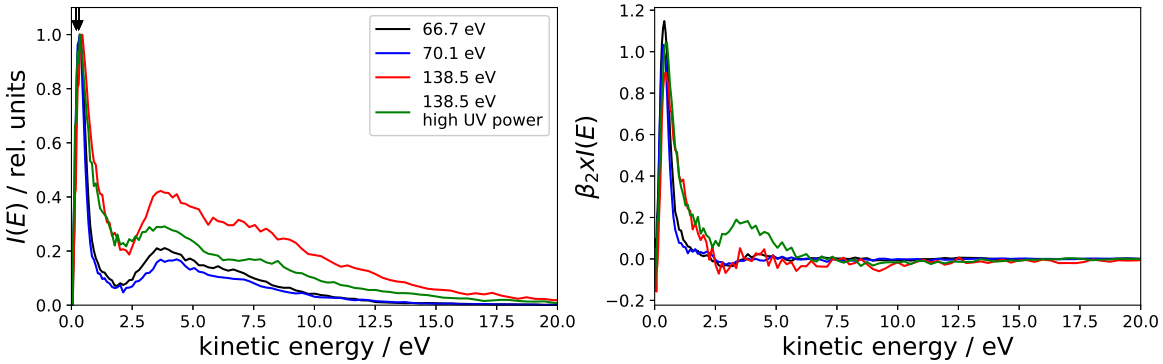


Figure 3.21: Kinetic energy distributions, $I(E)$, (left) and angular anisotropy parameters, β_2, (right) extracted from velocity-map images presented in Figure 3.20 of the I^{2+} fragment for times $t > 1.5$ ps after the start of the dissociation; the downward pointing arrows indicate iodine atoms kinetic energies observed in the photodissociation of CH_2BrI [153].

angular anisotropy parameter, β_2, are shown in Figure 3.21.

The low kinetic energy component of I^{2+} ions peaks at about 0.3 eV, close to the kinetic energy reported [153] for ground-state iodine atoms $I(^2P_{3/2})$ at 0.2 eV and excited-state $I^*(^2P_{1/2})$ at 0.3 eV (indicated by downward pointing arrows in the left-hand side panel of Figure 3.21) produced in Reaction (3.5). In the present study, iodine atoms are ionized irrespective of their spin-orbit state and the measured velocity-map images contain both spin-orbit excited and ground state photoproducts. Poullain *et al.* [153] used time-resolved resonance-enhance multi-photon ionization (REMPI) to probe the iodine atom fragmentation product and concluded from comparison with electron structure calculations that the C-I dissociation occurs on the 5A' potential energy surface, which is strongly repulsive in the Franck-Condon region of the ground electronic state, and excitation to this state leads to impulsive dissociation producing spin ground state iodine atoms, $I(^2P_{3/2})$. In the same study, spin-orbit excited iodine atoms $I^*(^2P_{1/2})$ were also observed to be produced along the 4A' and 4A" states following an avoided crossing [150, 151, 153, 154] from the 5A' state. The high kinetic energy ion in an energy range from 2.5 eV to 15 eV are XUV

fragmentation products of molecular CH_2BrI.

On the right-hand side of Figure 3.21, the angular anisotropy parameter β_2 is shown for the different kinetic energy components in the image. In the peak of the low kinetic energy channel the anisotropy parameter, β_2, is found ranging from 0.9 to 1.1 for different XUV probe photon energies. This is consistent with findings from Poullain *et al.* [153], who reported the angular anisotropy parameter β_2 as 1.38 for ground state $I(^2P_{3/2})$ atoms, indicating a predominantly parallel transition similar to findings of Butler *et al.* [7]. The angular anisotropy parameter is smaller than expected for a parallel dissociation in the axial recoil approximation, $\beta_2 = 2$. The authors [153] attribute this to the orientation of the transition dipole moment in the CH_2BrI molecule which lies approximately 33° towards the C-I bond axis. The formation of $I^*(^2P_{1/2})$ products from vibrationally excited CH_2BrI molecules leads to a slightly distorted geometry of the parent molecule [153], and this is observed in a smaller but still positive angular anisotropy parameter for the I^* atoms, $\beta_2 = 1.08$. The angular anisotropy parameter of high-kinetic energy I^{2+} ions observed in Figure 3.20 is approximately zero, except at the high UV intensity, for which the anisotropy parameter is positive. This is consistent with contributions to the total ion signal from dissociative multi-photon ionization by the UV laser, as described in Section 3.4.2.

To time-dependently follow the C-I dissociation and formation of halogen ion products during the fragmentation process, the kinetic energy distributions of iodine ions is plotted for different UV/XUV delay times in Figure 3.22, yielding contour plots of ion intensity as a function of kinetic energy and UV/XUV delay of I^{2+} (left) and I^{3+} (right), and for 66.7 eV (top) and 70.1 eV (bottom).

The contour plots of the time-dependent I^{2+} kinetic energy distribution in Fig-

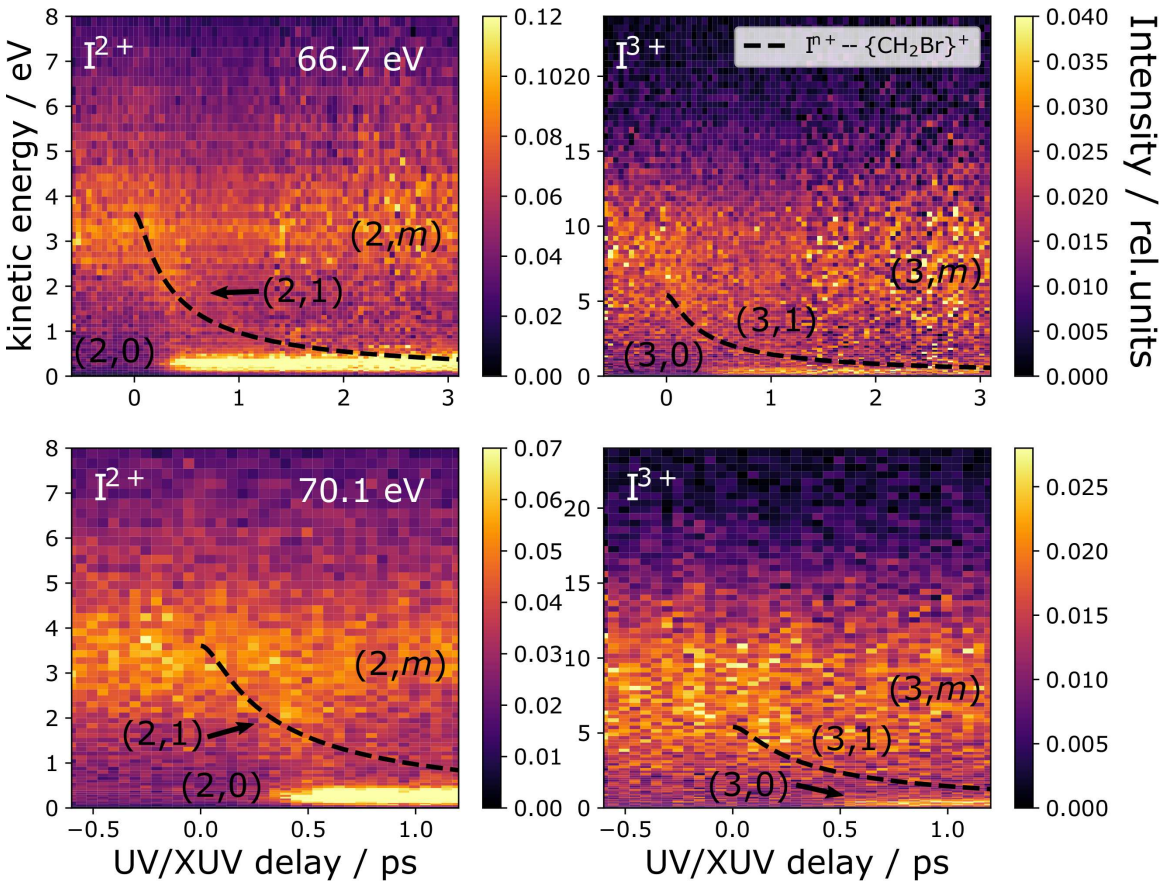


Figure 3.22: UV/XUV delay dependent kinetic energy distributions of the I^{2+} (left) and I^{3+} (right) fragment ions for a photon energy of 66.7 eV (top) and 70.1 eV (bottom).

ure 3.22 elucidate the depletion of the molecular XUV fragmentation channel in a feature above 2 eV, labelled as (2,m) indicating the charges of the doubly charged halogen ions and the m-charged co-fragment. The emerging photo-products from Reaction (3.5) below approximately 0.5 eV, labelled as (2,0), can also be followed here. At an UV/XUV delay of about 0.2 to 0.5 ps, there is an additional feature just below the (2,m) fragmentation channel between a kinetic energy of 1 and 2 eV. This feature, labelled (2,1), has previously been observed when probing dissociation products from carbo-halogen species such as iodomethane and (2,5)-difluoroiodobenzene [159], and it has been attributed to an electron transfer to a halogen ion photo-product from

the neutral co-fragment, according to:

$$CH_2Br + I \xrightarrow{XUV} CH_2Br + I^{3+} \xrightarrow[\text{transfer}]{\text{charge}} CH_2Br^+ + I^{2+} \tag{3.8}$$

The charge transfer process described in Equation (3.8) takes place shortly after the onset of the dissociation, while the particles are still in close proximity. While the kinetic energy of the neutral dissociation (2,0) channel is given by the final kinetic energy of the photo-dissociation process, products of the charge transfer reaction experience a Coulomb repulsion force between each other and, thus, I^{2+} fragment ions in the (2,1)-channel are detected with larger kinetic energy compared to the neutral (2,0) channel. The dashed line in Figure 3.22 indicates the kinetic energy of the iodine ion in this channel according to the Coulomb repulsion model described in Section 3.4.1.

Following the C-I bond dissociation, the two products, I and CH_2Br, move apart and the final velocity of the iodine is observed in the (2,0) channel in Figure 3.21 as 0.3 eV. Based on the work by Poullain *et al.* [153] the C-I bond dissociates repulsively after UV excitation with 266 nm in the Franck-Condon region of the ground state. Therefore, the fragment velocity can be assumed to increase approximately exponentially until it reaches its final velocities, $v_{CH_2Br,\,final}$ and $v_{I,\,final}$, according to:

$$v(t) = \left(v_{CH_2Br,\,final} + v_{I,\,final}\right) \cdot \left(1 - e^{-t/\tau}\right) \tag{3.9}$$

Therefore, the time-dependent inter-fragment distance is given under the axial-recoil approximation as:

$$R(t) = \int v(t)dt = \left(v_{CH_2Br,\,final} + v_{I,\,final}\right) \cdot \left(t/\tau + e^{-t/\tau} - 1\right) + R_{eq} \tag{3.10}$$

Here, R_{eq} is the equilibrium distance in the neutral molecule which has been determined by microwave spectrscopy [178] as discussed in Section 3.4.1. τ is the dissociation time of the C-I bond which has been determined by Attar *et al.* [156] as

48 ± 12 fs and 44 ± 4 fs for the production of spin-orbit ground state I($^2P_{3/2}$) and excited state I*($^2P_{1/2}$) atoms, respectively. Because iodine product atoms are detected irrespective of the product spin-orbit state, an average value of 46 fs is used in the following analysis. Evaluating the Coulomb repulsion energy for inter-fragment distances at times t yields a time-dependent expression for the total Coulomb repulsion energy while the particles move apart from each other. The kinetic energy of one fragmentation partner is then derived according to conservation of momentum, as described in Section 3.4.1, and shown as a dashed line in Figure 3.22. The UV/XUV delay time t = 0 ps is defined so that the fragmentation model coincides with the well-known charge transfer signature (2,1) yielding I^{2+} ions. It can also be seen that the (2,1) feature does not follow the model to its asymptotic value but vanishes at an UV/XUV delay of approximately 0.4 ps. At this time, both particles have reached a critical distance beyond which charge transfer is no longer possible and reaction channel (3.8) is closed off.

Observations made in the delay-dependent kinetic energy distributions of the I^{2+} and I^{3+} ions in Figure 3.22 are very similar for the two probe photon energies 66.7 and 70.1 eV below the bromine $3d$ and iodine $4p$ edge. At these photon energies the probe pulse ionizes the halogen atom photo-product but does not seem to significantly ionize the CH_2Br co-fragment. For the higher probe photon energy 138.5 eV, the delay-dependent kinetic energy distributions look qualitatively different, these are shown in Figure 3.23 for the I^{2+}, I^{3+}, I^{4+} and I^{5+} fragment ions. The data shown here have been measured with a higher UV pump intensity, which looks qualitatively very similar to data taken with the low UV intensity at this photon wavelength. However, the lower intensity data was measured with much less statistics and shows poorer resolved features. Consequently, data with a higher UV pump intensity is shown here for a probe photon energy of 138.5 eV.

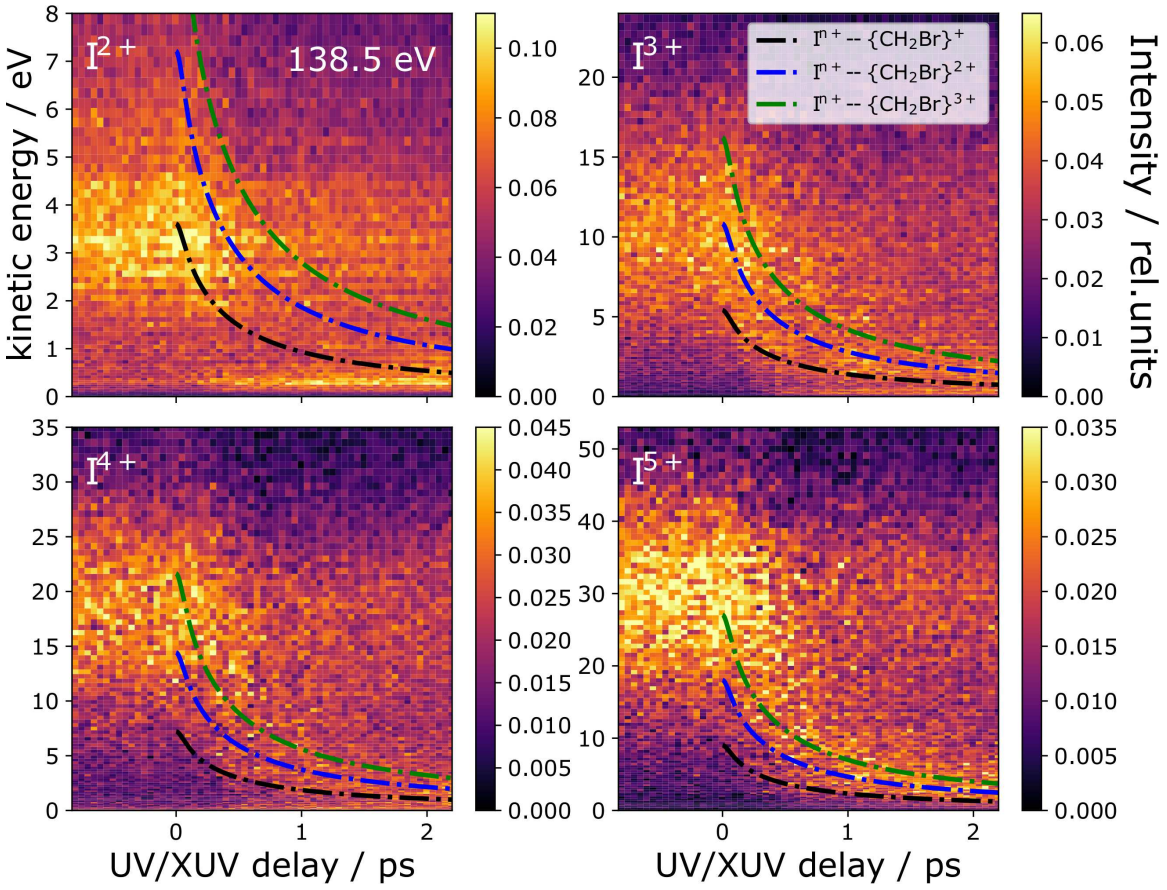


Figure 3.23: UV/XUV delay-dependent kinetic energy distributions of the I^{2+} (top-left), I^{3+} (top-right), I^{4+} (bottom-left) and I^{5+} (bottom-right) fragment ions for a photon energy of 138.5 eV.

The UV/XUV delay-dependent kinetic energy distributions in Figure 3.23 show the same two features for the high photon energy above the bromine $3d$ and iodine $4p$ shell as observed for the I^{2+} and I^{3+} fragment ions at the two lower probe photon energies: the depletion of the high kinetic energy molecular XUV fragmentation feature and an emerging $(n,0)$ channel, where $n = 2, 3, 4, 5$ is the charge of the measured halogen ion. In contrast to the two lower photon energies, there is an additional broad (n,m) feature with delay-dependent kinetic energy, following the time-dependent Coulomb repulsion model introduced in context of Figure 3.22 down to its asymptotic value in the $(n,0)$ channel. At this probe-photon energy of 138.5 eV

the co-fragment can be ionized at the bromine $3d$ electron, which, in turn, leads to further ionization *via* relaxation of the bromine inner-shell hole state, producing higher charged co-fragments. The dashed and dotted lines in Figure 3.23 describe the repulsion of the I^{n+} fragment from a singly charged CH_2Br^{m+} co-fragment with a dissociation time of 46 fs. The ionized co-fragment can dissociate further and broadens the observed (n,m) feature, if the fragmentation occurs in the Coulomb field of the I^{n+} fragment. This feature is further broadened by rotational excitation of the CH_2Br fragment [154], which, however, has not been accounted for in the present model.

The observed feature (n,m) is approximately described by the Coulomb repulsion of initally neutral dissociation products. In the same set of experiments as the present study, Burt *et al.* [152] used a UV-pump IR-probe scheme, where the CH_2BrI molecule is dissociated by the UV pulse and the fragments are strong-field ionized by the IR-probe pulse. The observed delay-dependent kinetic energy release of the dissociating fragments was only about 0.2 eV wide and closely followed the kinetic energy predicted for repulsion of singly charged iodine ions with a singly charged co-fragment, so that information on the photo-dissociation process could be drawn from a fit of the Coulomb repulsion model to the observed (1,1) feature. In the present study, the spread of charge states on and secondary fragmentation of the CH_2Br co-fragment significantly broadens the observed (n,m) feature and masks further information on the photo-dissociation process, precluding, for example, insight into the rotational and vibrational dynamics of the CH_2Br fragment after the UV dissociation.

There appears to be a general correlation between the charge state of the iodine, n, and the charge state of the co-fragment, m. Higher charged iodines are observed to repel from higher charged co-fragments. This correlation is still visible at UV/XUV-delay times of 1.5 ps, at which point the two fragments are 17.5 Å apart given a total

kinetic energy release of 0.62 eV in the probed UV dissociation. One possible explanation for the observed correlation is that the higher charged fragments are ionized together in regions of higher intensity of the free-electron laser beam. Both UV and FEL beam are focussed and overlapped with the molecular beam with the FEL focus being about ten times tighter then the UV focus. Assuming a Gaussian beam shape, the FEL beam is most intense in its centre were both halogen atom and co-fragment are ionized to higher charge states, and less intense on the edges where smaller charge states n and m are formed.

The time-dependence of the (n,0) channel in the I^{n+} fragment ion kinetic energy distributions is analyzed in more detail in Figure 3.24. In this figure, the integral of the (n,0) channel is shown for halogen ion charge states $n = 2, 3, 4, 5$ (from top to bottom row) and the three probe-photon energies 66.7 eV, 70.1 eV and 138.5 eV (left to right). Each channel is integrated from 0 upto 0.55 eV to include the full (2,0)-channel which has its maximum at a kinetic energy of 0.3 eV as shown in Figure 3.21. The data shown has been recorded at low UV pump power for all three probe-photon energies.

As discussed above, the product iodine atom is ionized to produce I^{2+} and I^{3+} ions for the two probe-photon energies below the iodine $4p$ shell but to higher charge states for ionization above the $4p$ edge for a probe photon energy of 138.5 eV. The small increase of ion yield in the (4,0) and (5,0) channel for photon energies of 66.7 and 70.1 eV is barely significant within the error bars, and this could be indicative of a minor contribution from multi-electron relaxation of the iodine $4d$ hole state or a sequential multi-photon ionization of the iodine atom within one FEL pulse as discussed above. For the channels where a significant ion yield increase is observed, the onset of I^{n+} fragment ions is fitted with a Gaussian cumulative distribution function [179,

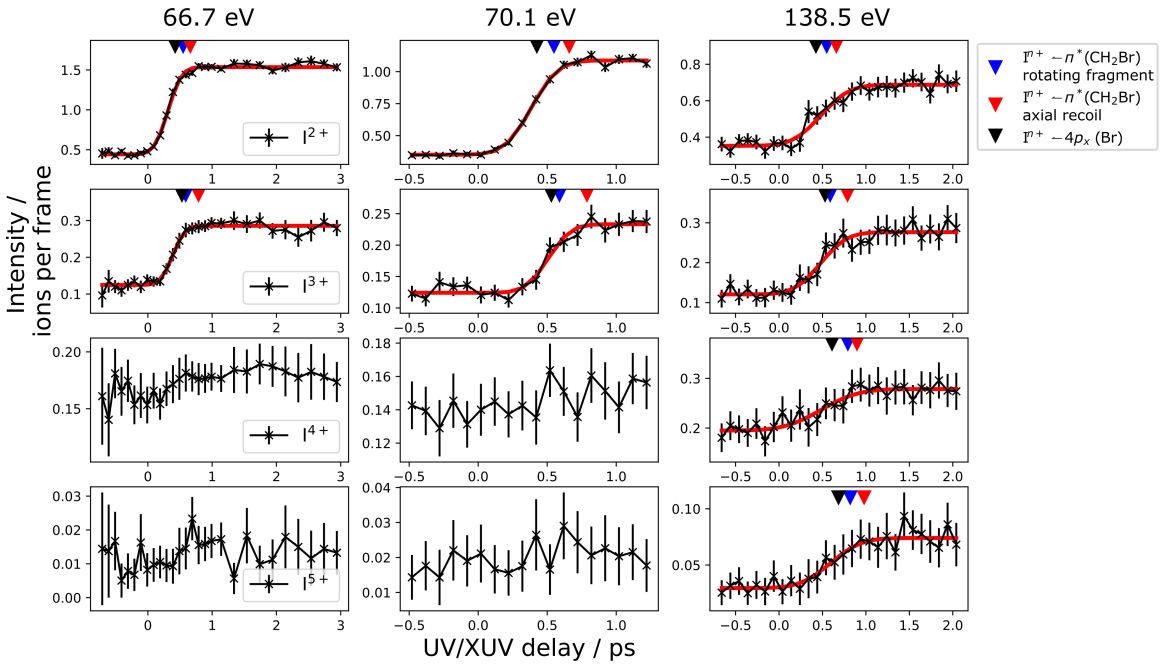


Figure 3.24: Integral of the (n,0)-channel in the I^{n+} fragment ion kinetic energy distributions as a function of UV/XUV delay time for the three probe photon energies 66.7 eV, 70.1 eV and 138.5 eV and low UV intensity; a Gaussian cumulative distribution function (red line) in Equation (3.11) are fitted to the data; the downward pointing triangles describe maximum UV/XUV delays for which charge transfer is expected in the over-the-barrier model between the I^{n+} ion and the neutral co-fragment (see text for more details).

p. 419] according to,

$$\Phi(x|\sigma,\mu) = \frac{1}{2}[1 + \mathrm{erf}(\frac{x-\mu}{\sigma\sqrt{2}})]. \tag{3.11}$$

Here, σ is the width and μ is the time of the turning point in the step-function.

The onset of the (n,0)-channel is clearly delayed by about 500 fs relative to the start of the dissociation for $n = 2$ and this onset becomes larger for higher iodine ion charge states. This observation is qualitatively consistent with previous experiments on CH_3I [157–159] and (2,5)-difluoroiodo-benzene [159]. In those experiments, this onset was attributed to charge transfer of an electron from the neutral co-fragment onto the isolated I^{n+} ion. The (n,0) channel is quenched as long as the neutral co-fragment is in close enough proximity to transfer a charge. After the start of the

dissociation, the two charge transfer partners drift apart and the critical distance at which charge transfer is no longer possible, and the (n,0) channel appears in the kinetic energy distribution, was well described by an over-the-barrier charge transfer model [183, 184]. This model describes the charge transfer as a classical process over the Coulomb barrier between the charged and neutral particle. The critical distance corresponds to the internuclear distance at which the barrier equals the energy of the transferred electron, and for larger internuclear distances, the barrier exceeds the electron energy and charge transfer is not longer feasible. The critical distance, R_{crit}, is given as:

$$R_{\mathrm{crit}}(n) = \frac{(m+1) + 2\sqrt{(m+1)n}}{E_{\mathrm{i}}} \tag{3.12}$$

Here, n is the charge state of the electron receptor and $m = 0$ is the charge-state of the co-fragment. E_{i} is the first ionization energy of the co-fragment. Comparing the critical distance in Equation (3.12) with a time-dependent expression of the internuclear distance yields a UV/XUV delay at which the critical distance is expected to be reached and coincide with the appearance of the (n,0) channel in the delay-dependent kinetic energy distribution of the I^{n+} fragment ion.

Figure 3.25 shows a schematic of the molecular orbital energies of the CH_2Br radical formed in the C-I dissociation of the CH_2BrI molecule. As in other halomethyl radicals a C-X π-bond is formed upon interaction of the $4p_y$ orbital with the $2p_y$-orbital on the carbon atom, while the $4p_x$ orbital forms a non-bonding lone-pair on the bromine atom [185–187]. In the present study, electron transfer to the iodine ion is considered for the unpaired electron in the π^*(C-Br) HOMO and an electron in the $4p_x$ bromine lone pair. The former is localized on the carbon atom in accordance with electronic structure calculations [188] and experimental studies employing hyperfine resolved microwave spectroscopy [189]. Charge density distributions of the π^*(C-Br) and $4p_x$ orbitals, calculated at the density functional level of theory using the B3LYP

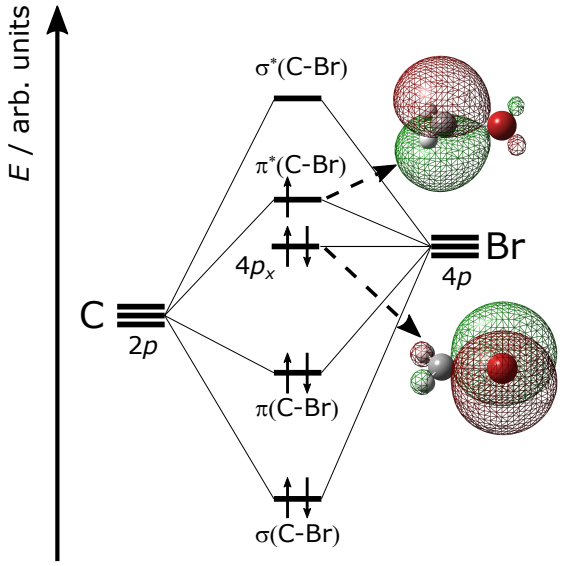


Figure 3.25: Schematic of the molecular orbitals in the CH_2Br radical; the HOMO is the π^* anti-bonding orbital formed by interaction of the $4p$ and $2p$ atomic orbitals on the bromine and carbon atoms, respectively; charge density distributions calculated on the DFT level of theory using an aug-cc-pVTZ basis set are also shown for the HOMO and bromine $4p_x$ lone pair; in accordance with previous studies [188, 189], the HOMO is localized on the carbon atom.

functional and an aug-cc-pVTZ basis set [190–192], are shown in Figure 3.25.

The downward pointing triangles in Figure 3.24 describe the maximum UV/XUV delay for the charge transfer to occur, assuming an over-the-barrier model. Here, three different charge transfer processes are described: transfer of the weakest bound electron from the π^*(C-Br) highest occupied molecular orbital (HOMO) localized at the carbon atom (red triangle) during the C-I dissociation under the axial recoil approximation; transfer of the same electron but under consideration of the rotational excitation of the CH_2Br co-fragment [154]; and transfer of the stronger bound electron from the $4p_x$ orbital localized on the bromine atom. For all three experiments and different iodine ion charge states it can be seen that the onset of the (n,0) channel is largely overestimated assuming a transfer of an electron from the HOMO under the C-I axial recoil approximation. The experimental data agrees best with a transfer of

an electron from the $4p_x$(Br) orbital, although the transfer of the weakest bound electron under consideration of the molecular rotation also shows reasonable agreement with the experiment. The three charge transfer cases in the over-the-barrier model are discussed in more detail in the following.

The vertical ionization energy of the CH_2Br radical has been reported as E_i = 8.72 eV [193] and the ionization energy for an electron in the $4p_x$ bromine lone pair has been determined in the present study by calculating the zero-point corrected energy of the CH_2Br radical in its singlet ground electronic state and the energy of the singly charged CH_2Br^+ ion in its triplet configuration and neutral geometry on the CCSD(T) level of theory with the aug-cc-pVTZ basis set [190–192]. The calculations have been performed using the Gaussian 09 software suite [194]. The difference between the two zero-point corrected energies is the vertical ionization energy of the CH_2Br radical from the $4p_x$ orbital, E_i = 10.974 eV. Based on the reported and derived ionization energies, critical charge transfer distances are calculated with Equation (3.12) and listed in Table 3.1 for an electron transfer from the HOMO and $4p_x$ orbital to the iodine ion.

n	$R_{crit}(I^{n+} \leftarrow\!\shortmid\, \pi^*)$ / Å	$R_{crit}(I^{n+} \leftarrow\!\shortmid\, 4p_x)$ / Å
2	11.9	9.5
3	13.9	11.1
4	15.6	12.4
5	17.1	13.6

Table 3.1: Critical distances limiting the transfer process of an electron from the π^*(C-Br) HOMO and $4p_x$(Br) lone pair on the CH_2Br fragment to the n-charged iodine ion derived using the over-the-barrier model in Equation (3.12)

The critical charge transfer distances in Table 3.1 can be compared to an expression of the internuclear distance between the iodine ion and carbon or bromine atom in the CH_2Br co-fragment. Here, electron transfer from the π^* HOMO is compared to the iodine carbon distance, R_{CI}, and electron transfer from the $4p_x$ non-bonding

orbital is compared the iodine bromine distance, R_{BrI}.

In the simplest case, the axial recoil approximation, the dissociation occurs along the axis of the broken bond and the C-I distance is then given, as discussed above:

$$R(t) = \int v(t)dt = \left(v_{\mathrm{CH_2Br,\,final}} + v_{\mathrm{I,\,final}}\right) \cdot \left(t/\tau + \mathrm{e}^{-t/\tau} - 1\right) + R_{\mathrm{eq}} \tag{3.13}$$

The axial recoil approximation is valid as long as the centre-of-mass of both particles progresses along the bond axis during the dissociation. However, in the A-band dissociation of CH_2BrI the centre-of-mass of the CH_2Br fragment is located close to the bromine atom. This induces a torque around the centre-of-mass and significant rotational excitation of the CH_2Br fragment during the dissociation. Murillo-Sanchez *et al.* [154] studied the C-I dissociation of the CH_2BrI molecule and performed full-dimensional on-the-fly trajectory calculations under consideration of surface hopping, to investigate the rotational dynamics of the CH_2Br fragment. Their calculations yielded time-dependent C-I distances, Br-I distances, C-Br distances and I-Br-C angles, γ. The individual results of 24 trajectories (grey lines) [195], and the averaged bond lengths and angles (black lines) are shown in Figure 3.26 (a). In (b), three snapshots of the molecular geometry at times, $t = 0, 40, 110\,\mathrm{fs}$, after the start of the dissociation are shown. It can be seen that the CH_2Br fragment revolves approximately around the bromine atom. The bromine atom which originally points away from the carbon iodine bond axis is located between the carbon and iodine atoms at approximately 110 fs.

The rotational motion of the CH_2Br fragment is extrapolated to reaction times observed in the present study. Under the assumption that the CH_2Br fragment rotates around the bromine atom, the time-dependent C-I distance can be derived using the time-dependent Br-I distance, $R_{\mathrm{BrI}}(t)$, C-Br distance, $R_{\mathrm{CBr}}(t)$, and the angle $\gamma(t)$

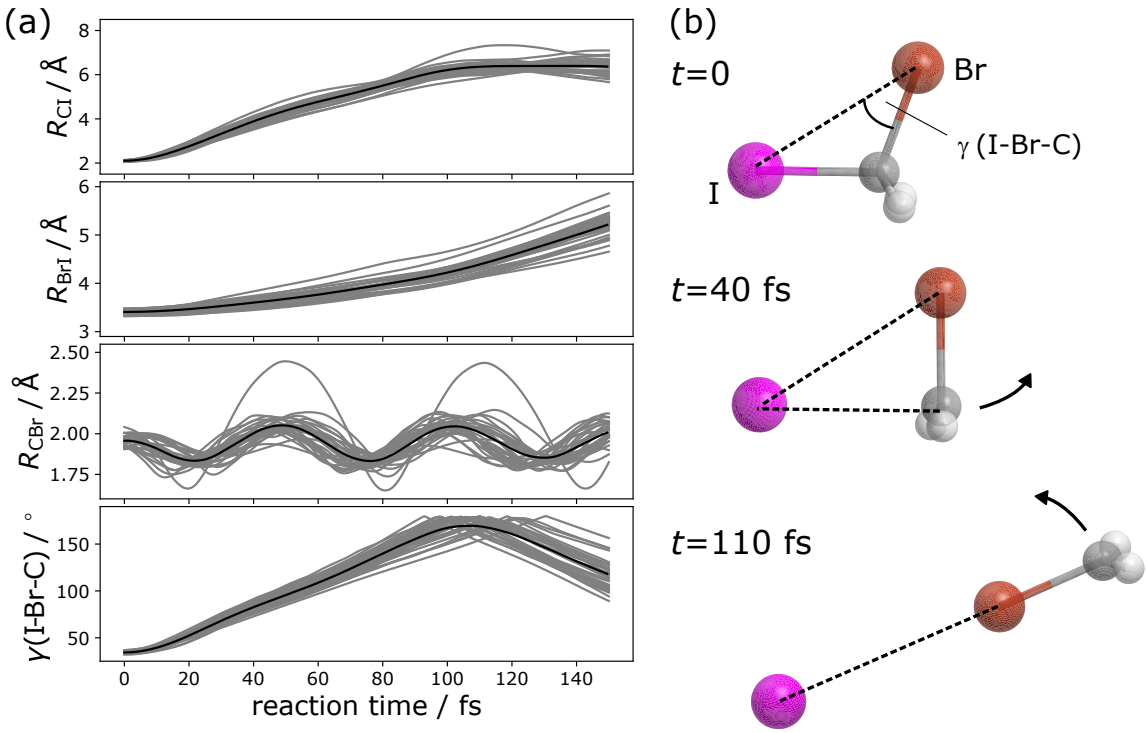


Figure 3.26: Results from full-dimensional on-the-fly trajectory calculations [154, 195]: (a) time-dependent C-I distance, R_{CI}, Br-I distance, R_{BrI}, C-Br distance, R_{CBr}, and I-Br-C angle, γ; results from individual trajectories are shown in grey, while the average time-dependent geometry is shown as a black line; (b) snap-shots of the geometry of the fragmenting CH_2BrI molecule at time $t = 0, 40, 110$ fs after the start of the dissociation.

according to,

$$R_{CI}(t) = \sqrt{R_{CBr}(t)^2 + R_{BrI}(t)^2 - 2\,R_{CBr}(t)\,R_{IBr}(t)\,\cos(\gamma(t))} \tag{3.14}$$

The centre-of-mass of the CH_2Br fragment recoils from the iodine atom and assuming that the centre-of-mass is approximately on the bromine atom, the Br-I distance is derived as an accelerated motion starting from equilibrium distance in the molecule, $R_{BrI,eq} = 339.56$ pm, according to:

$$R_{BrI}(t) = (v_{CH_2Br,\,final} + v_{I,\,final}) \cdot (t/\tau + e^{-t/\tau} - 1) + R_{IBr,eq} \tag{3.15}$$

Similar to the derivation of the C-I distance under the axial recoil approximation, a dissociation lifetime, $\tau = 46$ fs, corresponding to the average of the lifetimes for the two

different spin-orbit states, as determined by Attar *et al.* [156], was used. The time-dependent C-Br distance is approximated as a harmonic oscillator with a vibrational period, ω = 54 fs, and amplitude, A = 0.109 Å, estimated from the oscillation of the C-Br distance illustrated in Figure 3.26 (a). The time-dependent angle $\gamma(t)$ is derived according to,

$$\gamma(t) = \omega_\gamma \tau_\gamma \left(t/\tau_\gamma + \mathrm{e}^{-t/\tau_\gamma} - 1\right) + \gamma(t = 0) \tag{3.16}$$

The angle at the beginning of the fragmentation, $\gamma(t = 0) = 35.13°$, the angular speed, $\omega_\gamma = 1.45° \, \mathrm{fs}^{-1}$, and the dissociation lifetime have been estimated from the time-dependent angle derived for the first 140 fs of the fragmentation in Figure 3.26 (a).

The extrapolated C-I distances (blue line) from Equation (3.14) and Br-I distances (black line) from Equation (3.15) are shown in Figure 3.27 (a) and (b), respectively. The C-I distance under the axial recoil approximation (red line), in Equation (3.13), is also shown in Figure 3.27 (a). The results from Murillo-Sanchez *et al.* [154, 195] are shown in black and cyan for the C-I and Br-I distance, respectively.

The critical charge transfer distances in Table 3.1 are compared to the C-I distance for an electron transfer from the π^*(C-Br) (dashed yellow line), and to the Br-I distance for an electron transfer from the $4p_x$(Br) orbital (dashed orange line). The intersection between the critical distances and the time-dependent internuclear distances yield the UV/XUV delay times which are compared to the integral of the (n,0)-channels in Figure 3.24. This comparison yields two main results. Firstly, the observed onset is clearly overestimated by the model assuming charge-transfer from the π^*(C-Br) electron and a C-I fragmentation under the axial recoil approximation, but the agreement between the over-the-barrier model and the data is improved, at least for some iodine ion charge states, when considering the rotational dynamics of

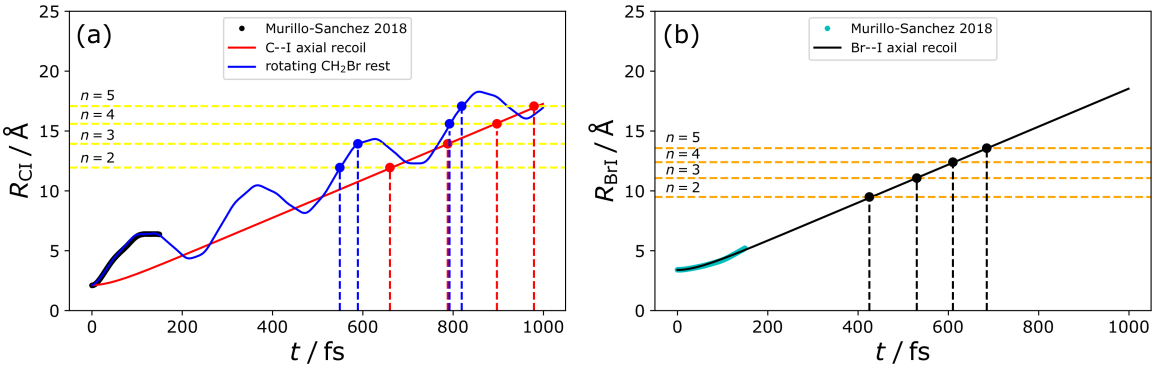


Figure 3.27: Internuclear C-I and Br-I distances, in (a) and (b), respectively, at different times after the start of the UV fragmentation of CH_2BrI: (a) C-I distances derived under the axial recoil approximation in Equation (3.13) (red line) and under consideration of the co-fragment's rotational dynamics by extrapolating trajectory calculations from Murillo-Sanchez *et al.* [154, 195] (black line); (b) Br-I distance derived using Equation (3.15) (black line) compared to the results from Murillo-Sanchez *et al.* [154, 195](cyan line); the internuclear distances are compared to critical distances of electron transfer from the π^*(C-Br) orbital (yellow lines) and $4p_x$ orbital (orange lines) onto the n-charged iodine ion, the intersections between the three different expressions for the C-I and Br-I internuclear distances and the two critical charge transfer distances yields UV/XUV delay times which are compared to the (n,0) channel in Figure 3.24 and 3.28 as blue, red and black triangles, respectively.

the CH_2Br co-fragment. Secondly, the onset of the (n,0)-channel appears to be best described considering charge transfer of an electron from the stronger bound $4p_x$ orbital, localized on the bromine atom.

The weaker bound π^*(C-Br) electron should be transferred over a longer distance than the stronger bound $4p_x$ electron. One explanation for the good agreement between a model assuming charge transfer from the bromine centred $4p_x$ electron and the observed onset of the (n,0)-channel could be de-phasing of the rotational motion of the CH_2Br fragment. This effect can be observed in the geometries of the fragmenting molecule in Figure 3.26 (a). While in the first few tens of femtoseconds, the 24 shown trajectories produce geometries that closely follow their average values, the individual trajectories start deviating from the average value during the fragmentation. At a reaction time of t = 150 fs a deviation from the mean value of 4% is found for the

C-I distance compared to a deviation 0.8% at the start of the fragmentation. Given a long enough fragmentation time, a significant portion of the observed ensemble will have de-phased and some molecules will always be found in a geometric configuration where the bromine atom is placed in between the iodine ion and the carbon atom. Thus, charge transfer for these molecules is only feasible for an electron from the $4p_x$ orbital at the bromine, giving an effective lower limit on the observed UV/XUV delay of the (n,0) onset.

The observation made from the comparison of the model to the data in Figure 3.24 is qualitatively consistent with observations made for a probe photon energy of 138.5 eV and higher UV pump intensity. This is shown in Figure 3.28.

On the left-hand side of Figure 3.28, magnifications of the delay-dependent kinetic energy distribution of the (n,0) channel are shown for different iodine ion charge states, $n = 2, 3, 4, 5$, from top to bottom. The integrals up to fragment kinetic energies of 0.55 eV (white dashed line) are shown on the right-hand side of the figure. The Gaussian cumulative distribution function fit in Equation (3.11) (red curve) is also shown. Similar to the step functions for low UV intensity in Figure 3.24 a delayed onset of the I^{n+} halogen ion can be observed.

The onset of the (n,0) channel compares similarly to the over-the-barrier model assuming electron transfer from two different orbitals on the CH_2Br co-fragment under axial-recoil approximation and consideration of the rotational dynamics of the CH_2Br co-fragment. In contrast to the data shown in Figure 3.24, the integral of the (4,0) channel appears to consist of two components, one emerging at an approximate UV/XUV delay of 400 fs and another one at approximately 700 fs. This could be evidence for the de-phasing of rotational motion within the observed ensemble. Under

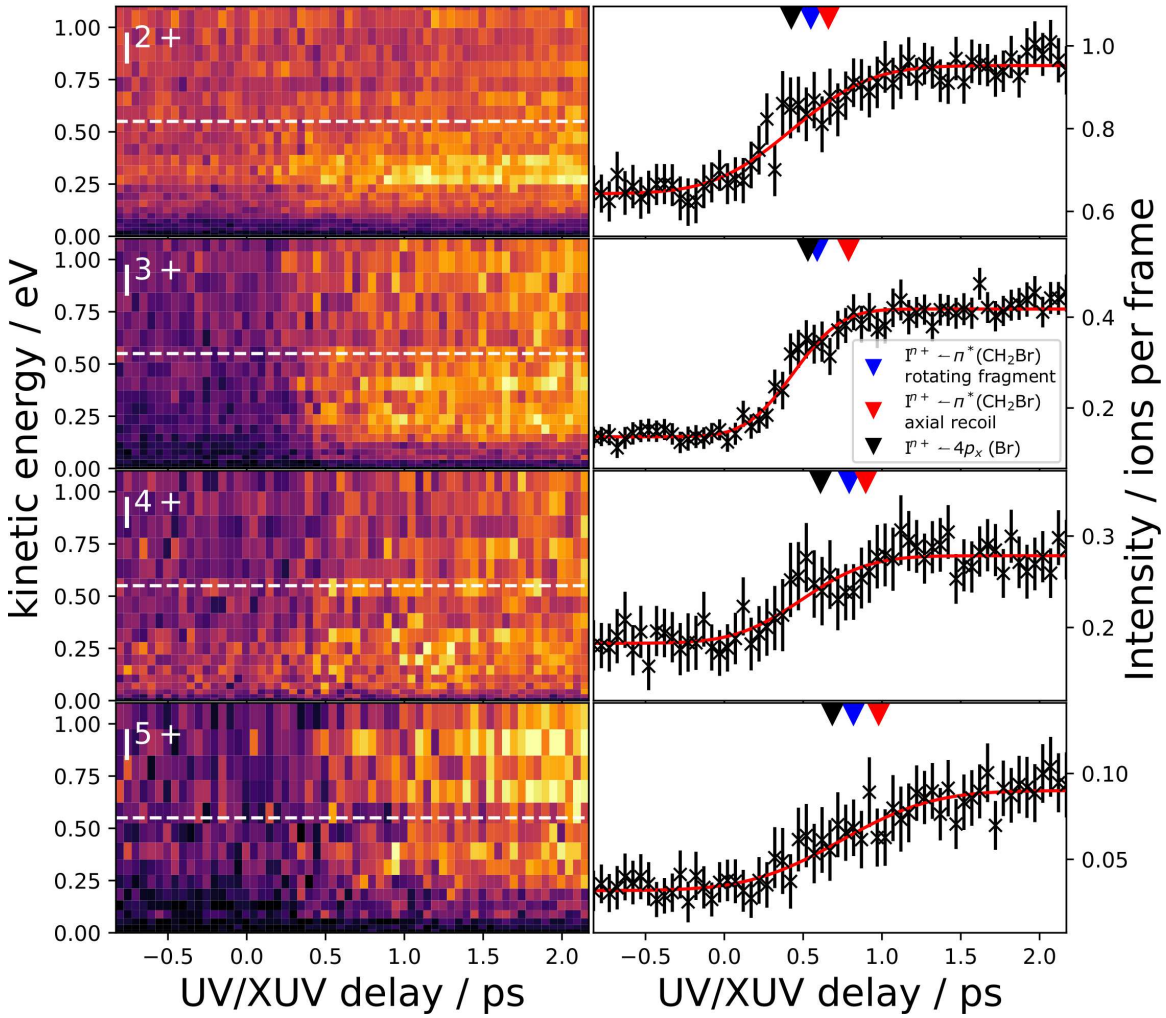


Figure 3.28: Zoom-in on the (n,0)-channel of I^{n+} fragment ions; right: integral of fragment ions up to a kinetic energy of 0.55 eV corresponding to the white dashed line on the left; error bars correspond to two standard deviations of the average integral value of each delay bin; a Gaussian cumulative distribution function fit according to Equation (3.11) (red line) to the data is also shown.

this assumption, some molecules are in a geometric configuration at a reaction time, t = 400 fs where the carbon atom has moved behind the bromine atom and transfer of a stronger bound electron from the $4p_x$ orbital forms a lower limit on the distance the charge transfer can occur across.

3.4.3.2 C-Br dissociation

Bromine atoms are produced upon absorption of a single UV photon and direct fragmentation of the C-Br bond, and secondary fragmentation of the CH_2Br intermediate following absorption of a second photon.

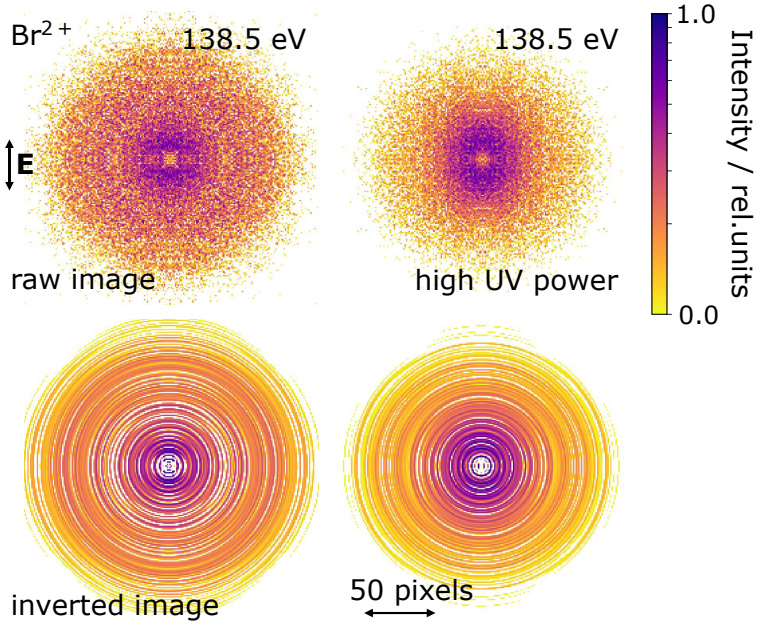


Figure 3.29: Br^{2+} velocity-map images for delay times $t > 1.5$ ps after the start of the dissociation; symmetrized raw images are shown in the top and pBASEX inverted images are shown in the bottom row; data for an XUV probe photon energy of 138.5 eV are shown with low and high UV pump power on the left- and right-hand side, respectively.

Figure 3.29 shows velocity-map image data for the Br^{2+} and the "UV early" regime, and Figure 3.30 shows the corresponding kinetic energy distributions for a probe photon energy of 138.5 eV for low (red line) and high UV pump power (green line), respectively. At this photon energy, the bromine atom is ionized from a $3d$ inner-shell electron and the ion in its excited inner-shell hole state undergoes Auger relaxation forming a Br^{2+} ion.

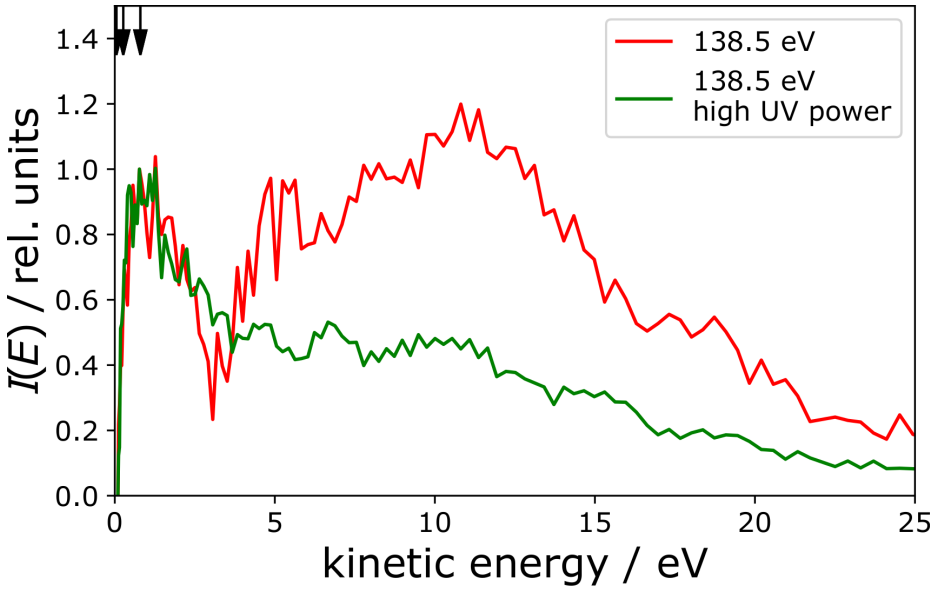


Figure 3.30: Kinetic energy distributions of the Br^{2+} fragment extracted from the velocity-map images presented in Figure 3.29 for times $t > 1.5$ ps after the start of the reaction; bromine kinetic energies for primary and secondary fragmentation of CH_2Br are indicated with arrows at 0.05, 0.265 and 0.8 eV [153].

The velocity-map images and kinetic energy distributions of Br^{2+} ions show two components: ionized bromine atoms from the UV fragmentation of CH_2BrI in the image centre for kinetic energies below approximately 2 eV; and bromine ions formed in the inner-shell ionization and fragmentation of the CH_2BrI molecule by the XUV pulse forming a broad feature from 4 to 15 eV as discussed in Section 3.4.1. The relative intensity of the low kinetic energy feature compared to the high-energy feature is dominant in the high pump power data, while the two features are roughly equal at the lower UV pump power. This indicates that more bromine atoms are formed in the fragmentation of the molecule in the more intense UV laser pulse. This is consistent with secondary fragmentation of the CH_2Br fragment in the production of bromine atoms upon absorption of photons in the A absorption band [153]. While there is a minor channel of direct C-Br dissociation following a single photon absorption at the A-band, the majority of CH_2BrI molecules is found to dissociate along the C-I bond. The energy of a single photon would be insufficient for C-I bond fission and secondary

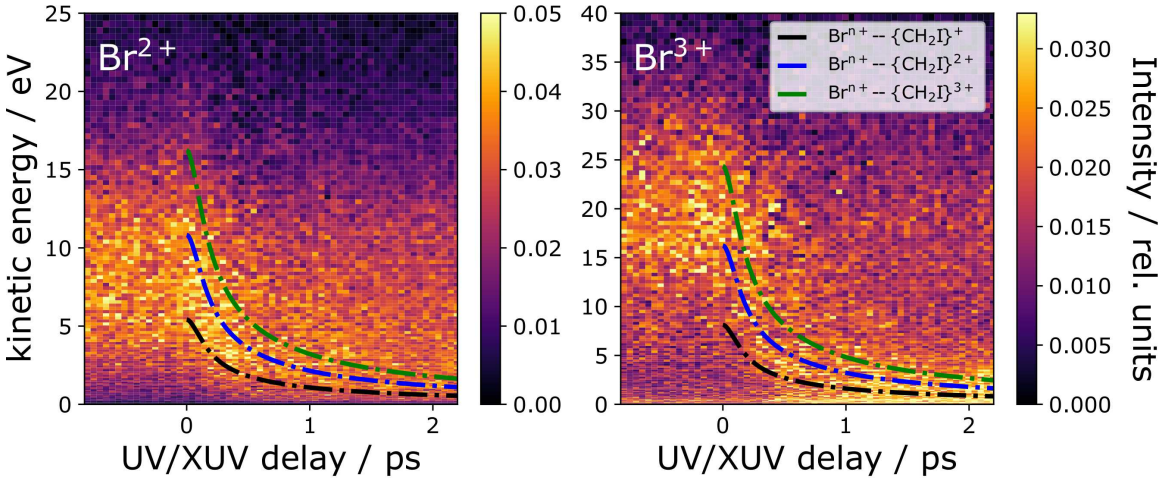


Figure 3.31: UV/XUV delay dependent kinetic energy distributions of the Br^{2+} (left) and Br^{3+} (right) fragment ions for a photon energy of 138.5 eV and high UV pump intensity.

fragmentation of the CH_2Br co-fragment, but dissociation of the co-fragment following the absorption of a second photon is found to produce Br atoms with a kinetic energy of about 0.8 eV [153]. This is consistent with the increased production of Br^{2+} ions at about 1 eV for the high UV intensity data (green line) compared to the low UV intensity data. The reported kinetic energy of bromine atoms formed in the direct and secondary dissociation channels are shown as downward pointing arrows in Figure 3.30.

Similar to the discussion of the iodine fragment ions, the Br^{2+} and Br^{3+} fragment kinetic energy distribution is plotted as a function of the UV/XUV delay in Figure 3.31. Here, data for high UV pump power and a probe photon energy of 138.5 eV is shown. The black, blue and green dashed and dotted lines describe the kinetic energy of the bromine ion repelling from a singly, doubly and triply charged CH_2I^+ co-fragment following neutral dissociation of the C-Br bond. As described in Section 3.4.3.1, the fragment kinetic energy is derived from the Coulomb repulsion of both fragment ions and the time-dependent internuclear distance is described by an accelerated motion of both fragmentation partners up to the final bromine atom

kinetic energy of 0.5 eV and a dissociation lifetime, τ = 114 fs, as determined by Attar *et al.* [156] in time-dependent transient absorption experiments. The broad delay-dependent kinetic energy feature is approximately described by the model for repulsion of a CH_2I^{m+} fragment ion in different charge states, m. Bromine atoms from the primary dissociation pathway are formed with a CH_2I co-fragment, while secondary fragmentation products fragment with a CH_2 co-fragment. Because of the much smaller mass of the CH_2 fragment, repulsion of a charged CH_2^+ co-fragment following secondary dissociation of the CH_2BrI molecule is expected to follow a much steeper curve than the model shown in Figure 3.31 predicts. The agreement of the primary dissociation model with the experimental data is consistent with the four times larger ionization cross section [175] of a 138.5 eV photon at the iodine atom of the CH_2I co-fragment compared to the CH_2 valence shell electron.

The integrated intensities of the (2,0)- and (3,0)-channel of Br^{2+} and Br^{3+} ions are shown in Figure 3.32 for all three photon energies, 66.7, 70.1 and 138.5 eV, and low UV pump power. A significant production of Br^{2+} ions for positive UV/XUV delays can only be observed at a photon energy of 138.5 eV. There is, however, a small increase in Br^{2+} ions for the two lower photon energies which is indicative of a potential minor channel of valence ionization at the bromine atom or a concerted multi-photon ionization of a bromine inner-shell electron. The Br^{3+} ion yield is not observed to increase for the two lower photon energies for "UV early" compared to "UV late", but a small increase in Br^{3+} yield is observed for 138.5 eV. This is consistent with a sequential multi-photon ionization mechanism for the higher probe photon energy at the $3d$ inner-shell electron, producing Br^{2+} ions in one and Br^{3+} ions in two ionization steps.

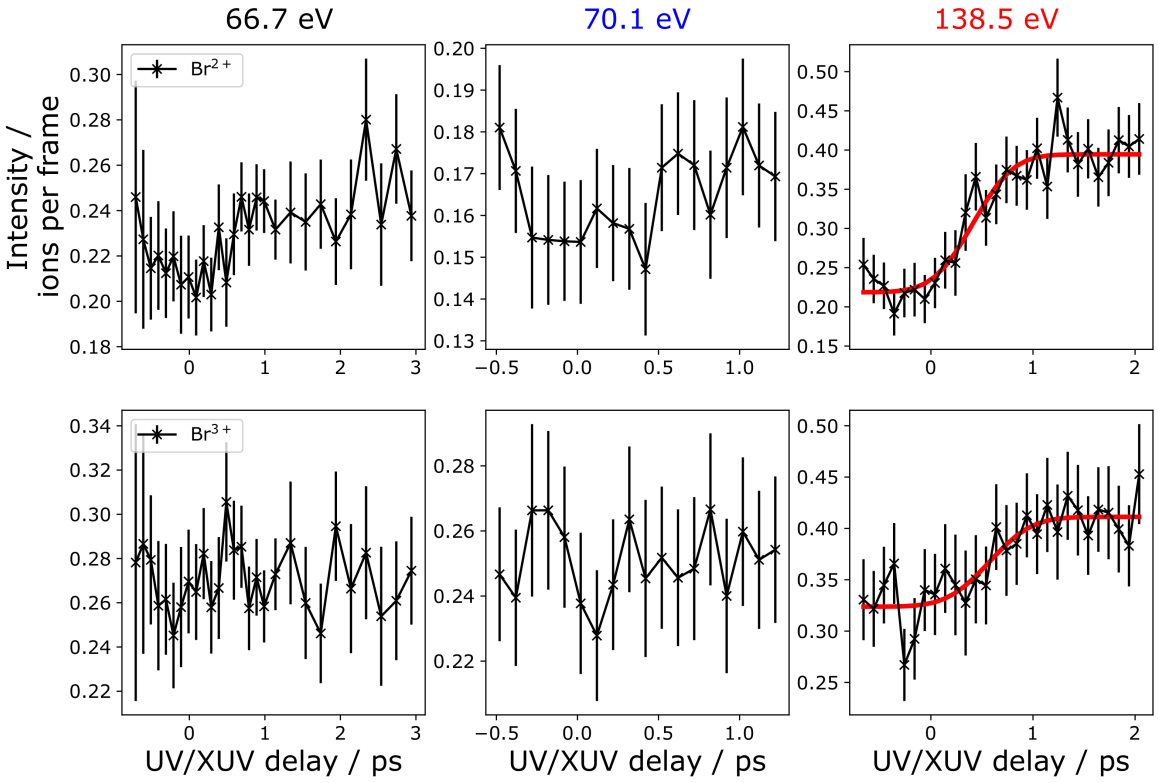


Figure 3.32: Integrated intensities of the (n,0)-channels in the Br^{n+} fragment kinetic energy distributions as a function of UV/XUV delay time for the three probe photon energies 66.7, 70.1 and 138.5 eV and low UV intensity; the red curve is a Gaussian cumulative distribution function fit according to Equation (3.11).

3.4.3.3 Depletion of molecular fragmentation channels

The time-dependent ion yield of molecular XUV fragmentation channels for all four pump/probe conditions are summarized in Figure 3.33. The presented error bars correspond to two standard deviations of the mean delay-bin value and the grey dashed lines indicates the time $t = 0$ ps throughout the figure.

The neutral dissociation and dissociative ionization by the UV laser pulse reduces the amount of CH_2BrI molecules available for XUV fragmentation. Thus, the yield in fragmentation channels with kinetic energies attributed to XUV fragmentation of the CH_2BrI molecule in Section 3.4.1 is reduced if the UV laser precedes the free-electron laser. This can be seen in the total ion yield for the CH_x^{2+}, Br^+, CH_2Br^+, I^+ and CH_2I^+

fragments for all four experimental conditions shown in Figure 3.33. In case of the CH_x^+ fragment the intensities are only integrated over the high kinetic energy feature for 138.5 eV to avoid the overlap with halogen ions in the centre (see Figure 3.19) and over all CH_x^+ fragments for the two lower photon energies. While for the multiply charged halogen ions the integrals over the high kinetic energies excluding the tail of the (n,m)- and $(n,0)$-channels are shown, the depletion of XUV fragmentation products is observed similarly to the singly charged fragments. For the Br^{3+}, I^{4+} and I^{5+} fragments the depletion are only observed for a photon energy of 138.5 eV. At the lower XUV probe photon energies, these species are not produced in sufficient amounts to observe a time-dependent effect within the experimental uncertainty. At the high UV intensity the depletion can also be observed in the CH_x^{2+} fragment and the CH_2Br^+ ion yield because more CH_2BrI molecules fragment compared to the low pulse intensity.

Around the UV/XUV delay, $t = 0$, there is a signal maximum in all multiply charged fragments which arises from the (n, m)-channel merging with the XUV fragmentation channel. This can be best seen for the highest UV intensity and XUV photon energy in the right-hand side column but is also visible in the I^{2+} fragment ion for a photon energy of 66.7 eV.

Generally, the midpoint of the depletion feature is shifted to slightly later timings compared to the temporal overlap of the two laser beams. This is another indication of the charge transfer process following the neutral UV dissociation and multiple ionization of the produced halogen atom. For example an n-charged iodine ion receives an electron from the neutral co-fragment yielding an $n-1$ charged iodine ion which is now repelling with the charged co-fragment forming an $(n-1, 1)$-channel in the delay-dependent kinetic energy plot as shown in Figure 3.22. This channel will over-

lap with the XUV fragmentation products of the $n-1$ charged iodine ion leading to the observed shift of the depletion to later UV-pump XUV-probe delay times.

Further evidence for the electron transfer to the highly charged halogen ion from the neutral co-fragment is observed in the CH_2Br^+ fragment, especially for probe photon energies of 66.7 eV and 70.1 eV. There is a slight increase of CH_2Br^+ ion yield for delay times where is charge transfer is observed in the onsets of the $(0,n)$-channels discussed in the context of Figures 3.24 and 3.28 up to approximately $t = 0.5\,\mathrm{ps}$. The increased CH_2Br^+ yield could be interpreted as ions produced in the electron transfer, according to,

$$CH_2BrI \longrightarrow CH_2Br + I \longrightarrow CH_2Br + I^{n+} \xrightarrow{\text{charge transfer}} CH_2Br^+ + I^{n-1}. \qquad (3.17)$$

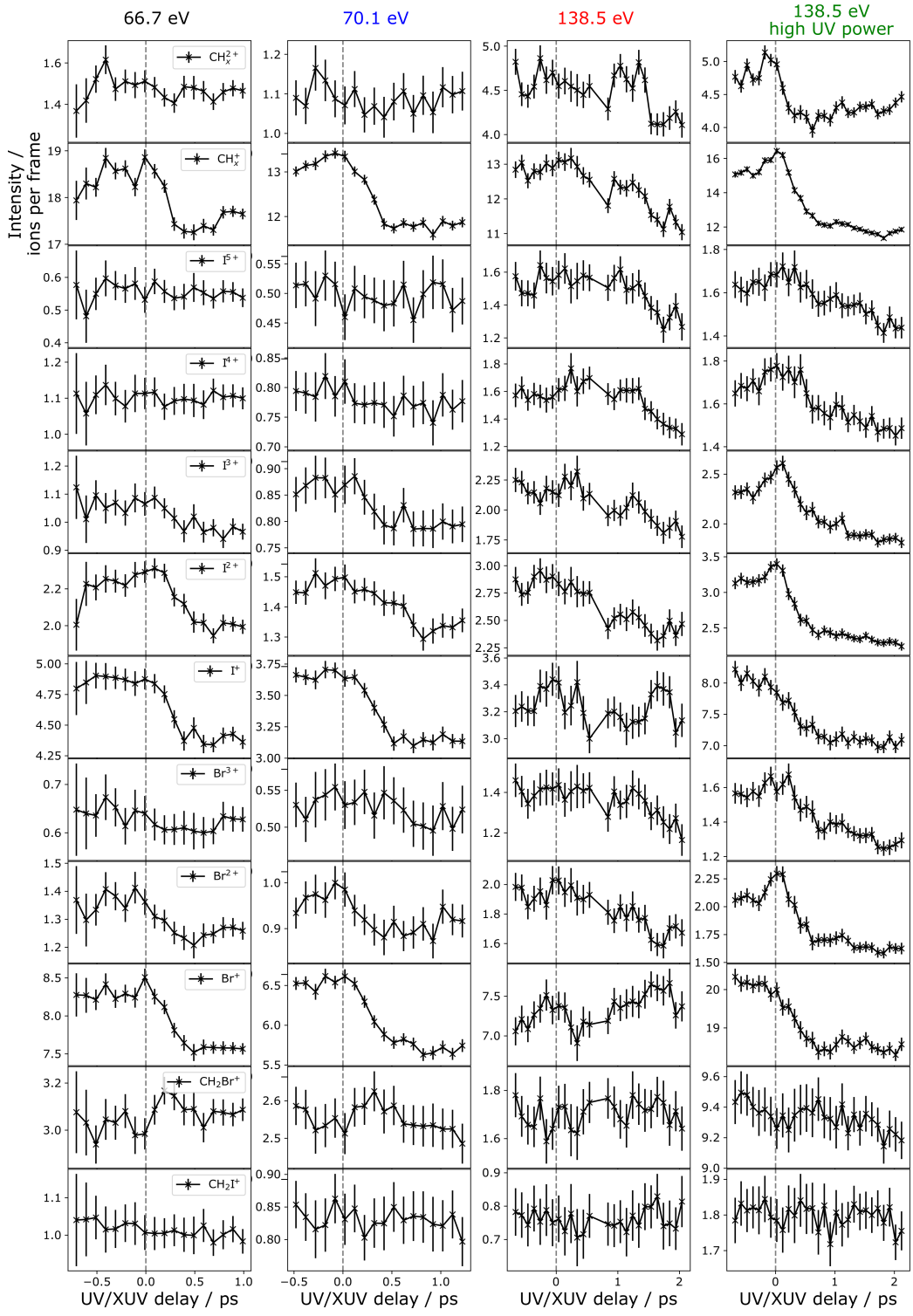


Figure 3.33: Time dependence of molecular fragmentation channels for the three photon energies 66.7, 70.1, 138.5 eV, and 138.5 eV with high UV pump intensity from left to right; from top to bottom the different fragment ions are shown: CH_x^{2+}, CH_x^{+}, I^{5+}, I^{4+}, I^{3+}, I^{2+}, I^{+}, Br^{3+}, Br^{2+}, Br^{+}, CH_2Br^{+} and CH_2I^{+}.

3.5 Conclusion and outlook

Velocity-map images of ions created in a UV-pump XUV-probe experiment have been analyzed. Pump-probe delay dependent data illustrated how neutral photo-fragmentation products are probed with the XUV-probe pulse at three different probe photon energies. The observations are consistent with previous experimental [7, 149, 152–154] and theoretical studies [150, 151] on the UV photo-dissociation dynamics following absorption of an UV photon in the A-band of CH_2BrI.

In accordance with previous studies on (2,5)-difluoroiodobenzene [159], the intense XUV-probe pulse of a probe photon energy of 66.7 eV was found to be an element-specific probe predominately ionizing a $4d$ inner-shell electron in the neutral iodine photo-dissociation product. For higher photon-energies, above the bromine $3d$ edge, additional ionization of the bromine atom and CH_2Br fragments from C-Br and C-I bond fission, respectively, were observed. The ionization of the CH_2Br and CH_2I co-fragment at the higher photon energy is believed to lead to the observed delay-dependent changes in the halogen ion kinetic energy. In previous studies, using highly intense IR pulses as a probe, it was shown how "time-dependent Coulomb explosion imaging" can be used to follow the structural changes in the UV dissociation of I_2 [196], CH_2BrI [152], CH_2ClI and CH_3I [22]. In contrast to these studies, the delay-dependent kinetic energy distributions observed of the present study gave only little insight into the UV-fragmentation mechanism but were consistent with the production of different charge states at the co-fragment producing features of similar kinetic energy which are indistinguishable within the kinetic energy and delay-time resolution of this experiment. Further improving the spectrometers and detectors kinetic energy resolution, and conducting the experiments with higher delay-time resolution might give further insight into the rotational dynamics of the CH_2Br co-fragment.

Charge transfer between the highly charged product halogen ions and the neutral co-fragments were observed, similar to previous studies of CH_3I [157, 158] and (2,5)-difluoroiodobenzene [159]. While in the cases of CH_3I and (2,5)-difluoroiodobenzene the charge transfer process was observed along the dissociating bond axis, in the present investigation of the CH_2BrI fragmentation, the CH_2Br co-fragment is produced highly rotationally excited and does not follow the axial recoil approximation. Within the over-the-barrier charge transfer model, the observations made here clearly show that the rotational dynamics of the co-fragment need to be considered to describe the charge transfer process. Further evidence was found for the importance of the mutual orientation of the CH_2Br fragment and the electron accepting iodine ion.

Fragmentation of the CH_2BrI molecule in the intense free-electron laser pulse has been compared in the context of the known fragmentation dynamics of the CH_2BrI, CH_3I and CH_3Br molecules in low flux synchrotron radiation. The observed fragment ion charge state is consistent with sequential ionization of the CH_2BrI molecule by the intense XUV pulse at inner-shell electrons of the bromine and iodine atoms followed by Auger relaxation of the inner-shell vacancy and fragmentation of the highly charged parent ion. The kinetic energies of the observed fragment ions were consistent with a simple Coulomb repulsion model in the neutral CH_2BrI geometry.

The application of multi-mass imaging using the PImMS2 sensor has proven to be a very efficient data-acquisition tool for experiments at the free-electron laser facility. While about 320,000 FEL shots were fired to acquire the data presented here, time-dependent velocity-map imaging data of more then 10 fragment ions under four different experimental conditions and across a UV/XUV delay range of up to 4 ps were recorded and analyzed. Therefore, the highly sought-after, experimental time

at this facility was efficiently used. The multi-mass capability of the PImMS2 sensor comes at the expense of a reduced detection efficiency as described in Section 1.2.7. In later experiments at the same facility, data was acquired with an improved version of the PImMS2 sensor with largely enhanced detection efficiency.

Following this work, the PImMS2 sensor was used in three additional experiments at the FLASH facility. These experiments are not described in the context of this thesis but benefited greatly from further integration of the PImMS2 sensor into the beamline. For example, the correlation problems between the facilities FEL shot ID and the PImMS camera frame number was resolved, as described in Appendix A.

Chapter 4

Velocity-map imaging of electron ionization products

In this chapter, a study of the fragmentation dynamics following electron ionization of trifluoroiodo-methane (CF_3I) is presented for electron energies up to 100 eV. Product ions originating from fragmentation of singly, doubly and triply-charged parent ions are observed and their kinetic energy and angular distributions are recorded using multi-mass velocity-map imaging. Singly charged parent ions are found to show distinctly different fragmentation dynamics for dissociation of the C-F and C-I bond. While the C-F bond seems to be broken impulsively forming CF_2I^+ fragments, the C-I dissociation producing CF_3^+ ions appears to occur statistically after vibrational relaxation to the ground state. A comparison to photoionization studies gives further insight into the set of potential energy surfaces on which the fragmentation dynamics occur. Covariance analysis of the velocity-map images elucidates the fragmentation of doubly and triply-charged parent ions giving evidence for Coulomb explosion along the C-I bond and neutral fission of the C-F bond either in a concerted or sequential mechanism.

4.1 Introduction

Electron-molecule collisions play an important role for the chemistry in environments such as high energy plasmas or the Earth's upper atmosphere [17, 197–199]. Depending on the collision energy, different electron-induced processes take place. For collision energies much higher than the ionization threshold, the impinging electron strikes out an electron from the molecule, forming a cation. This process is referred to as electron ionization [200], and it is used for quasi-universal ionization in many mass-spectrometry experiments [201, pp.23]. For collision energies below the ionization threshold the colliding electron may be captured by the molecule, forming an anion. Ion-pair formation is a process in which the electron-molecule collision leads to fragmentation of the parent molecule into a positively and negatively charged product. It is observed for collision energies around the ionization threshold. Ions formed in electron-molecule collisions are often highly internally excited, and fragment to form neutral and charged products. Auto-ionization and multiple ionization in electron-molecule collisions have also been observed [202]. The work presented in this chapter is focussed on the fragmentation of molecular cations formed by electron ionization at collision energies between 20 and 100 eV.

While electron ionization is of importance for a wide range of processes, no universal theory to predict the relative yield of fragmentation products has been developed yet. On the way to a universal description of electron ionization, it is yet to be understood, how much energy is transferred in the molecule electron collision, and how this energy is distributed among the internal degrees of freedom of the molecule and its fragmentation products.

Halocarbons, such as CF_3I which are the subject of this study, are well suited for mass-spectrometry studies. The sample is easy to handle, and the fragmenta-

tion does not produce any ions with identical mass-to-charge ratios. Furthermore, CF_3I has been studied previously with a number of complementary theoretical and experimental methods. Results from these studies are available to compare with the experimental results of the present work. The fragmentation dynamics of CF_3I, on both singly-charged [203–207] and doubly-charged [208] potential surfaces, have been the subject of a range of photoionization studies. CF_3I is also of wider interest due to its use as a plasma etching gas with relatively low environmental impact [209].

An important quantity when describing the fragmentation dynamics is the partial ionization cross-section (PICS), $\sigma_i(E_{\mathrm{el}})$, which describes the relative yield of a specific fragment ion at a given incident electron energy E_{el}. The total ionization cross-section (TICS), $\sigma(E_{\mathrm{el}})$, is the sum of all PICS,

$$\sigma(E_{\mathrm{el}}) = \sum_i \sigma_i(E_{\mathrm{el}}). \tag{4.1}$$

Possible fragmentation mechanisms following electron ionization can be separated into two categories: statistical and impulsive fragmentation [210]. While statistical fragmentation occurs relatively slowly, allowing the parent ion to relax to a ground electronic state and redistribute the available energy amongst a large number of internal states, impulsive fragmentation happens much faster on excited state potential energy surfaces.

Statistical fragmentation processes are reasonably well modelled by the activated complex theory of Rosenstock *et al.* [211]. Assuming a large number of coupled electronic states, the internal energy is redistributed into vibrational levels of the cationic ground state and all molecular states are in equilibrium before fragmentation occurs [211]. This theory can in principle describe the fragmentation processes in small hydrocarbon molecules such as CH_4 [212] and C_2H_6 [213], but it does not adequately describe impulsive fragmentation on excited state potential energy surfaces.

Statistical fragmentation products typically have an unstructured kinetic energy distribution with a maximum near zero kinetic energy.

One example of an impulsive mechanism is the ionizaton and fragmentation of the C_2F_6 molecule, in which the C-F bond is found to break faster than the timescale of one vibration forming a $C_2F_5^+$ fragment [214–216]. In this case, the statistical fragmentation model underestimates the yield of the $C_2F_5^+$ fragment ion, and instead it is found that the fragmentation occurs on an excited state potential energy surface with repulsive character [217]. Similary to photoionization studies, impulsive fragmentation of the parent ion can be distinguished into three types [218–220], depending on how much energy transfer occurs amongst the fragmentation partners. Two different forms of inter-molecular fragmentation and one form of intra-molecular fragmentation are differentiated. In the first inter-molecular case the electron-molecule collision leads to a vertical excitation into a repulsive excited state, which fragments along one molecular coordinate. During the fragmentation, the adjacent bonds adjust to the change in electronic configuration and become strongly vibrationally excited. This can lead to further fragmentation of the primary product. In the second case of inter-molecular fragmentation, the available energy is channelled almost exclusively into translation and the fragments' internal degrees of freedom remain unchanged. In the case of intra-molecular fragmentation, both fragments continue to interact, and redistribution of energy can take place during the dissociation. Impulsive fragmentation typically yields reaction products with higher kinetic energy than the statistical process. The intra-molecular type tends to yield products with kinetic energy distributions that resemble more a statistical dissociation, making it a borderline case between pure statistical and impulsive fragmentation.

While there are distinct examples for which either statistical or impulsive frag-

mentation mechanisms dominate, in general for ion dissociation the reaction dynamics tend to be a mixture of both mechanisms. Statistical fragmentation often becomes the more prominent pathway for larger molecules and in cases where more vibrational modes and electronic states couple, allowing for relaxation and redistribution of energy into vibrational energy levels of the electronic ground state.

In the present work, ionic fragmentation products are probed using velocity-map imaging employing both a conventional charged-coupled device (CCD) sensor and the PImMS2 sensor. In addition to the fragmentation products kinetic energy and angular distributions from velocity-map image data, this experiment yields partial ionization cross-sections for electron ionization of CF_3I at electron energies $20 < E_{el} < 100\,eV$.

This chapter is structured in three parts. After a description of the experimental set-up and of modifications made in the context of this work, the partial ionization cross-sections for the electron ionization of CF_3I will be discussed, followed by the presentation of product ion velocity-map image data. The results are compared with photoionization studies and based on this comparison a fragmentation mechanism is proposed. Finally, the outcomes from this study are summarized and an outlook on future work is given.

4.2 Experimental considerations

Velocity-map images of electron ionization products are recorded with an electron-molecule crossed-beam apparatus. The experiment has been described in detail previously [147, 222], and is shown schematically in Figure 4.1. A velocity-map imaging spectrometer with three lens elements, flight tube and imaging detector is housed within a high-vacuum chamber with a background pressure of $\sim 10^{-8}$ Torr. A

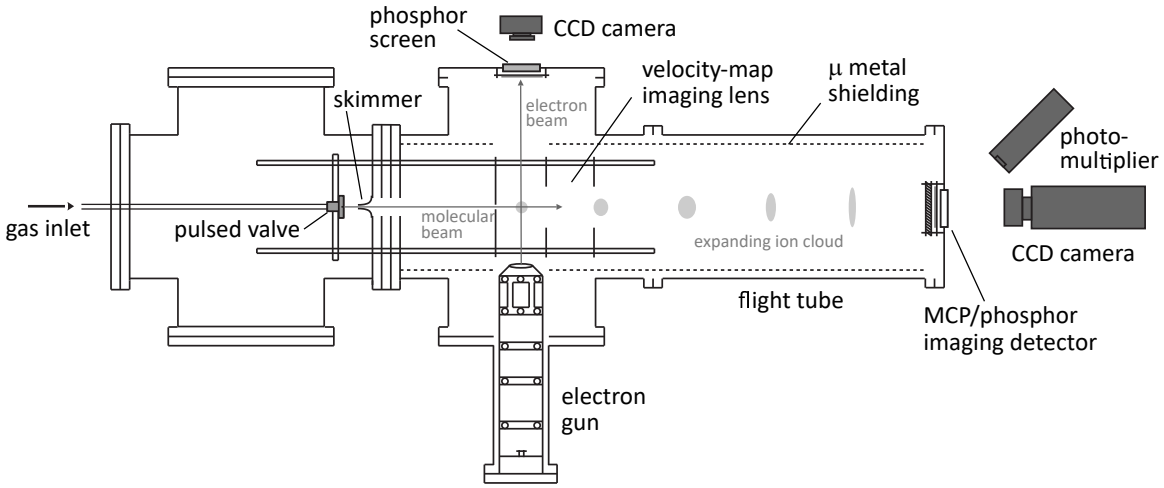


Figure 4.1: Set-up of the electron-molecule crossed-beam experiment: a molecular beam from the pulsed nozzle and an electron beam pulse collide inside a velocity-map imaging spectrometer; product ions are extracted after the electron beam has passed the interaction region and are velocity-mapped onto an imaging detector; the image is captured using a CCD camera or PImMS2 sensor; the total signal from the detector is acquired using a photo-multiplier pointing towards the screen; the electron beam can be characterized on a second detector opposite to the electron source; Reproduced from Reference [221] with permission from the PCCP Owner Societies.

molecular-beam pulse is formed *via* supersonic expansion in the source chamber and is collimated by a 1 mm skimmer before entering the differentially pumped scattering chamber. Details of the production of molecular beams *via* supersonic expansion and set-up of a velocity-map imaging spectrometer are discussed in Sections 1.2.1 and 1.2.5, respectively. In the scattering chamber, the molecular-beam pulse enters the velocity-map imaging (VMI) lens through an aperture (diameter: 2 mm) in the repeller plate and is intersected with an electron-beam pulse inside the spectrometer. The scattering distributions of cationic electron ionization products are velocity-mapped onto the imaging detector and recorded using a camera employing either a CCD or PImMS2 sensor. The total ion signal is recorded with a photo-multiplier tube (PMT, Hamamatsu, H10721-01). The extraction voltage and flight-tube length is adapted in order to optimize the image size projected onto the detector. Flight-tube lengths of 197 and 397 mm, measured from the ground-lens to the imaging detector,

and a typical extraction voltage of 2 kV have been employed in the experiments reported in this chapter. The electrostatic optics and flight tube are enclosed within a pair of μ-metal cylinders in order to screen the low energy electrons employed in the experiment from any external electric or magnetic fields. The electron beam can be steered through the grounded velocity-map imaging lens onto a phosphor-screen detector mounted opposite to the electron gun. By monitoring the signal on this phosphor screen the electron gun can be characterized in both continuous and pulsed beam mode.

The experiment is operated at a repetition rate of 10 Hz, and one experimental cycle is summarized in Figure 4.2. The molecular beam pulse is expanded *via* a pulsed nozzle at t_{MB} and the electron beam pulse (width: 170 ns) is released at $t_{\mathrm{e^-}}$ to intersect with the maximum of the molecule beam pulse (width: 200 μs) in the scattering chamber. The VMI lens is kept at ground potential for most of the experimental cycle but is rapidly pulsed up to the desired extraction potential at t_{VMI} as soon as the electron beam has cleared the interaction region. The relative delay between the electron beam and VMI extraction pulse, Δt_{VMI}, is characterized by monitoring the electron beam current on the detector facing the electron source, as described in more detail below. The relative timings of the electron beam and VMI extraction pulses were carefully adjusted and frequently checked to ensure the experiment was reproducible with good signal-to-noise ratio.

4.2.1 Modifications to the experimental set-up

The experiment was originally set up by J. Bull and J.W.L. Lee [147, 222]. In order to improve the signal quality, allow for an improved characterization of the electron source, and to speed up the data-acquisition, the original experimental set-up

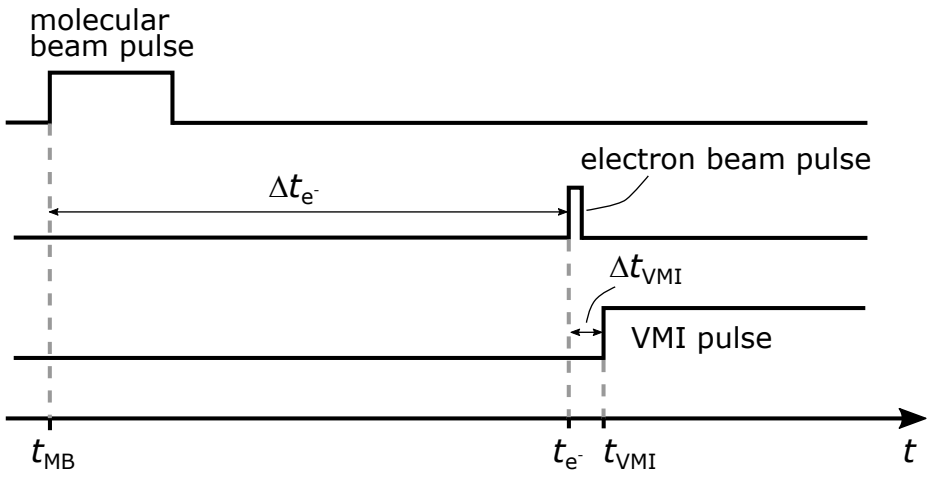


Figure 4.2: Pulse sequence for one experimental cycle: the relative timing of electron and molecular beam pulse, Δt_{e^-}, is optimized for the electron beam pulse to intersect with the maximum of the molecular beam; the relative timing of the VMI extraction pulse compared to the electron pulse, Δt_{VMI}, is optimized to ensure that the electron beam pulse has passed the interaction region before any voltage is applied across the interaction region.

was adapted for the present work. The main changes to the experiment by Bull *et al.* [222] are summarized in Figure 4.3.

Blue parts in Figure 4.3 have been removed in the modified version of the apparatus, and parts shown in red are added to the experiment. In the original set-up the electron gun was mounted on the top flange of the scattering chamber, pointing down-wards towards the turbo-molecular pump. After traversing the interaction region the electron pulse was collected on a grounded Faraday plate. In the new configuration the electron gun is mounted on the side of the scattering chamber as shown in Figure 4.1, and the electron beam can therefore be characterized using a position-sensitive detector mounted on the opposite side of the chamber.

To characterize the electron beam, a modified imaging detector with only a scintillator screen (P47) is used. The electron beam passes through the grounded velocity-map imaging lens onto the screen. A potential of 1 kV is applied to the screen to

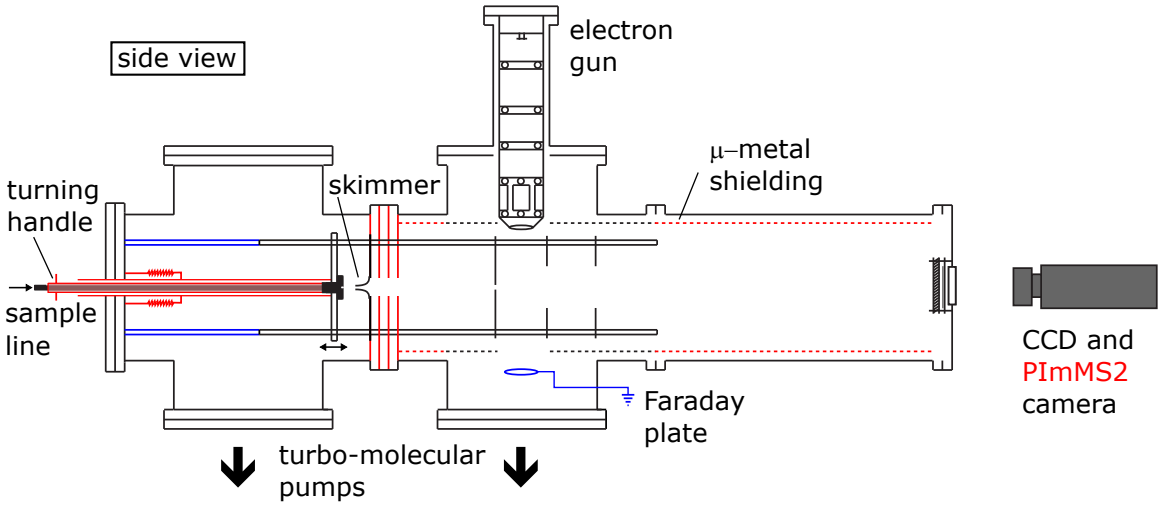


Figure 4.3: Summary of modifications to the set-up of the electron-molecule crossed-beam experiment in side view; parts shown in blue have been removed and red parts were added in the modified configuration; not shown here: the electron gun was moved from the top to a side flange of the scattering chamber pointing towards a secondary imaging detector (see Figure 4.1 for top view of the modified configuration).

accelerate the impinging electron beam. The fluorescence response of the scintillator is captured with a webcam (Logitech, C200) or PMT. Figure 4.4 (a) shows pictures of the electron beam profile (E_{el} = 100 eV) in continuous mode as acquired on the screen for four different focus conditions. The electron beam is focussed within the electron gun by an ion lens formed by an anode, focus and earth lens element, as shown in Figure 4.4 (b). In Figure 4.4 (a) it can be clearly seen how the focus is changed by applying different potentials, U_{foc}, to the focus element. For the routine optimization, the focus setting is adjusted for maximum yield of ionization products in the velocity-map imaging experiment, with a typical value of 95 V for an 100 eV electron beam.

To prepare an electron-beam pulse, the earth lens element (see Figure 4.4 (b)) is kept at a retarding potential for most of the experimental cycle and is pulsed down to ground potential for 170 ns using a custom-build voltage pulser. Typical retarding voltages are 40 V above the anode voltage. Thus, an approximately 170 ns

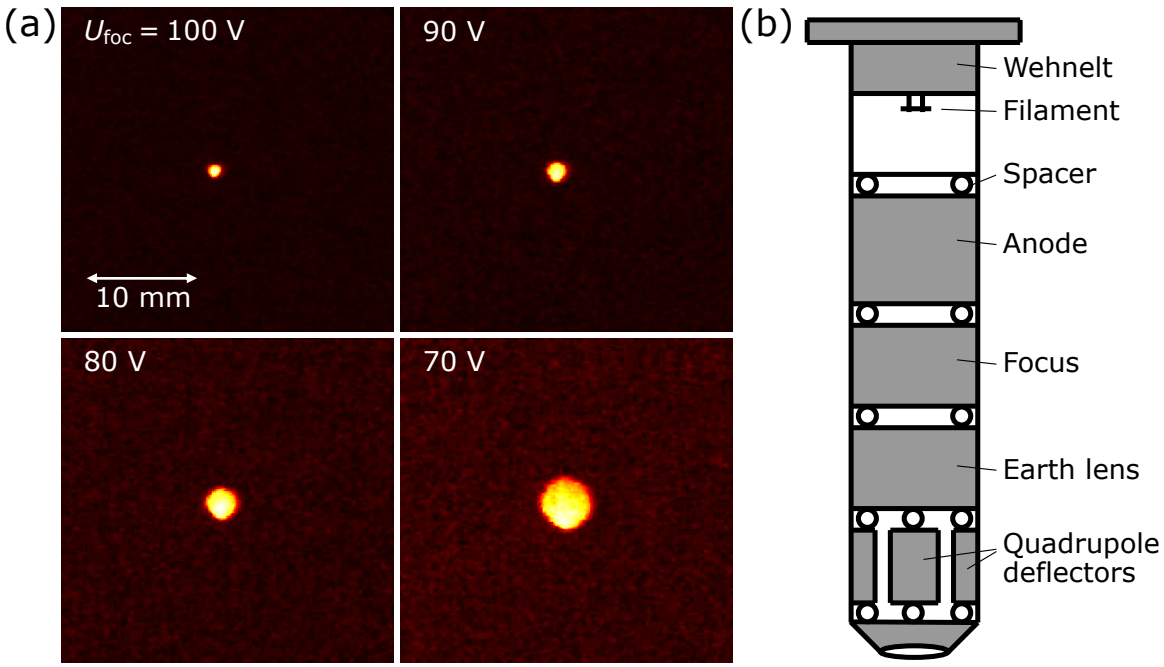


Figure 4.4: (a) Electron beam profile for four different focus voltages, U_{foc}; a continuous electron beam (E_{el} = 100 eV) passes through the grounded velocity-map imaging lens onto the scintillator screen on the opposite side of the spectrometer; a potential of 1000 V is applied to the screen to accelerate electrons and increase the scintillator fluorescence response, which is recorded with a webcam; (b) Schematic of the electron gun; electron are emitted thermally from the filament and accelerated towards the anode; the focus and earth elements form an ion lens which collimate the beam; the focussing voltage, U_{foc}, is applied to the focus element; the beam can be steered using two pairs of deflector plates.

long electron beam pulse is prepared. By capturing the total fluorescence response of the scintillator screen on arrival of the e^- pulse as the delay between the e^- pulse and VMI lens pulse is adjusted, the VMI extraction delay, Δt_{VMI}, can be characterized. Figure 4.5, shows the integral of the fluorescence signal over the electron pulse for different VMI-pulse delays, Δt_{VMI}. For very short delays, $\Delta t_{\mathrm{VMI}} < 100$ ns, the electron-beam pulse does not clear the velocity-mapping lens before the VMI field is applied, and is lost to the repeller plate. For delays 100 ns $< \Delta t_{\mathrm{VMI}} <$ 270 ns, part of the electron-beam pulse passes the interaction region. The pulse integral reaches a plateau value for delays $\Delta t_{\mathrm{VMI}} > 270$ ns, which indicates that the entire electron beam pulse is collected on the scintillator screen for delays in this range.

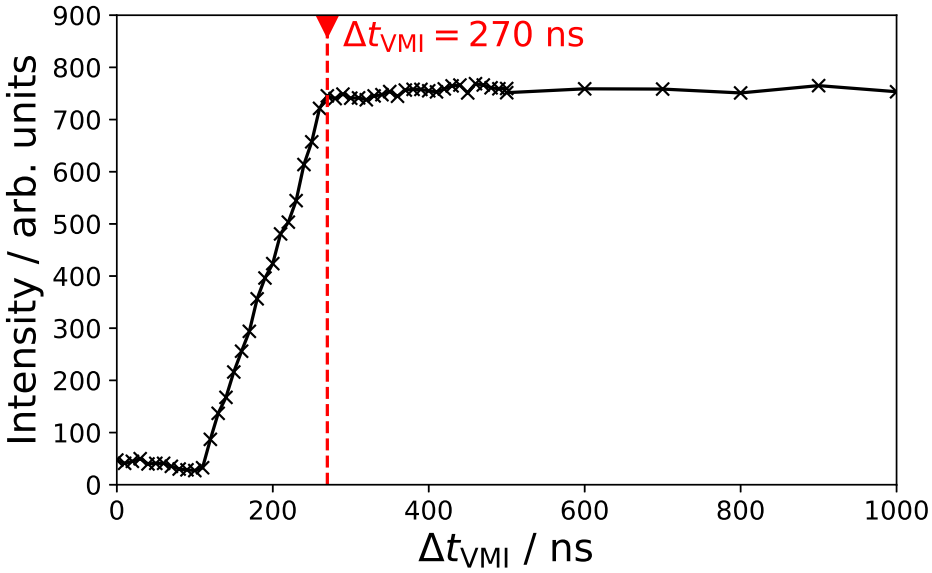


Figure 4.5: Electron-beam pulse signal on the scintilator screen for different VMI-pulse delays, Δt_{VMI}; a 180 ns long electron beam pulse passes the grounded velocity-map imaging lens, at varying VMI-pulse delays, Δt_{VMI}, the VMI-potential is pulsed up and ionization products are extracted; for $\Delta t_{\mathrm{VMI}} > 270\,\mathrm{ns}$ the VMI-pulse is applied after the electron pulse has fully cleared the velocity-map imaging lens.

In the original set-up the molecular beam nozzle, skimmer and VMI lens were mounted on a set of alignment rods attached to the back flange of the source chamber. On one hand, this configuration implicitly aligns all three elements of the experiment relative to each other, facilitating the experimental set-up. On the other hand, forming a proper vacuum seal to enable differential pumping between source and scattering chamber was difficult in this configuration. In the modified set-up, the alignment rods are instead attached to a flange, that isolates the two chambers from one another. The molecular beam valve is mounted inside the chamber in a way that allows the tension on the spring assembly that controls the valve opening and closing to be adjusted from outside the vacuum. The entire nozzle ensemble is mounted on a linear translator attached to the source chamber's rear flange, allowing the nozzle to skimmer distance to be altered in order to optimize the molecular beam. Figure 4.6 shows the time-profile of an optimized argon atom pulse prepared by supersonic ex-

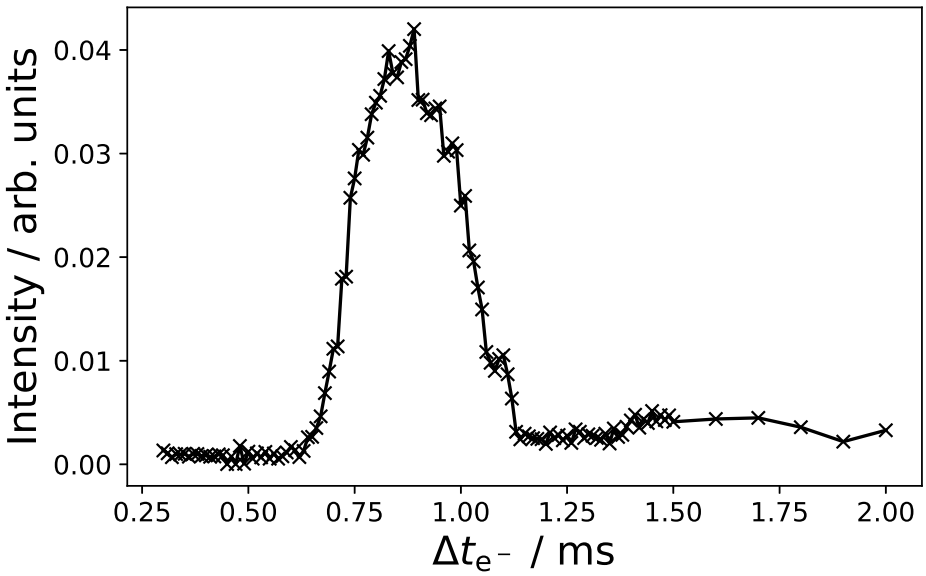


Figure 4.6: Intensity of an argon atom pulse as measured inside the velocity-map imaging lens; the delay of the electron beam pulse with respect to opening of the molecular beam valve, Δt_{e^-}, is varied from 300 μs to 2 ms and the signal for Ar^+ ionization products is recorded at the imaging detector with a PMT.

pansion from 2 bar stagnation pressure *via* a pulsed nozzle (Parker-Hannafin, Series 9, diameter: 0.8 mm) with an opening time of 200 μs.

The final modification to the experimental set-up, was replacing the CCD camera with a camera employing the PImMS2 sensor which enabled multi-mass imaging. This greatly increases the data acquisition speed by capturing velocity-map images of all fragment ions simultaneously, and increases the repetition rate of the experiment from 10 Hz to 20 Hz, in both cases limited by the readout speed of the camera.

4.3 Data analysis

4.3.1 Analysis of time-of-flight data

To record fragment time-of-flight spectra, spatial-map imaging potentials were applied to the velocity-mapping lens to ensure that all ions irrespective of their kinetic

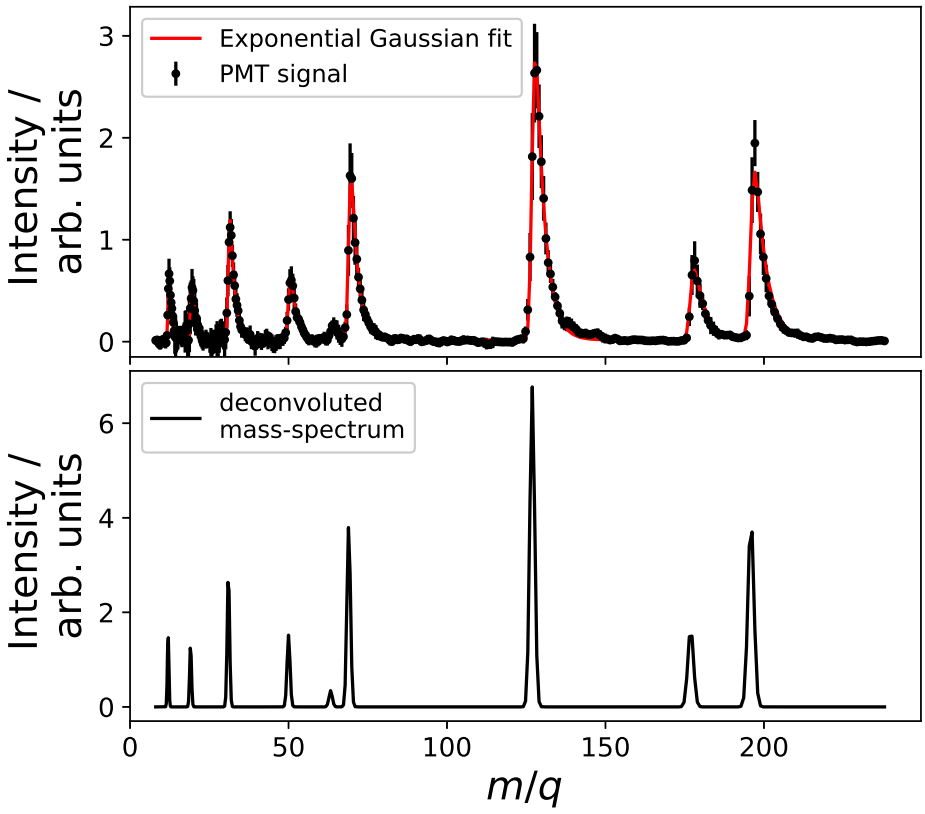


Figure 4.7: The mass-spectrum of framgentation products acquired by a PMT from the scintillator screen of the imaging detector is shown in the top-panel; a convolution of nine Gaussians with exponential decay functions in Equation (4.2) is fitted to the data (red line) to retrieve the deconvoluted fragment mass spectrum in the bottom-panel.

energy release are mapped onto the detector. The total ion signal at the imaging detector is recorded by a PMT behind the scintillator screen.

An example mass spectrum of CF_3I electron ionization products recorded at E_{el} = 100 eV is shown in Figure 4.7 (a). The peak shape of the PMT signal is determined by the approximately Gaussian-shaped ion time-of-flight signal and by the exponential fluorescence decay of the scintillator material (P47). To remove the contribution from the scintillator, a convolution of a Gaussian, P_{tof}, and exponential decay, $N(t)$, is fitted to each peak according to,

$$P = P_{tof}(t) * N(t) = \int_{-\infty}^{\infty} P_{tof}(t) N(t-\mu) d\mu. \tag{4.2}$$

The Gaussian distribution of arrival times for ion i, with centre t_i and the peak full-width at half maximum, $FWHM = 2\sqrt{2\ln 2}\sigma$, is given by:

$$P_{\text{tof}}(t; t_i, \sigma) = \frac{1}{\sqrt{2\pi\sigma^2}} e^{-\frac{(t-t_i)^2}{2\sigma^2}} \tag{4.3}$$

The exponential decay of the scintillator material, $N(t)$, is given by,

$$N(t) = e^{-\frac{t}{\tau}} \tag{4.4}$$

The exponential fluorescence lifetime τ of P47 was constrained to the reported value of 69.3 ns [223]. The nine observed ion peaks were fitted to Equation (4.2), and the deconvoluted ion time-of-flight distribution is given by the sum of the Gaussian components, before putting the time-of-flight distribution onto a mass scale. The fitting algorithm employed here was written by David Heathcote, based on the lmfit software package [224].

4.3.2 Analysis of velocity-map image data

Velocity-map image data presented in this chapter is handled and processed using the pyAbel software package [164]. Following centroiding of individual ion events to a single pixel (see Section 1.2.7), the centre of the velocity-map image is determined. The velocity-map image is then Abel-inverted using the pBasex algorithm and the ion kinetic energy and angular distributions are retrieved as outlined in Section 1.2.5. Basis functions employed in the inversion consist of one Gaussian function per radial element with a full-width-at-half-maximum of 0.7 pixel and Legendre polynomials up to $l = 2$.

The Abel inversion procedure requires the scattering distribution to have an axis of cylindrical symmetry parallel to the detector. The axis of symmetry of the product scattering distribution lies along the relative velocity vector of the collision $\vec{v}_{\text{MB}} - \vec{v}_{\text{e}^-}$

shown in Figure 4.8 for an electron-molecule collision. In this case, because the electron speed is much larger than the molecular beam speed, the relative velocity coincides to a very good approximation with the electron beam velocity. As described in in Section 1.2.2 for the general case of a bimolecular collision, a Newton diagram can be constructed for the scattering of an electron and molecular beam pulse.

This is shown in Figure 4.8 for a collision between an electron and molecular beam pulse with lab-frame velocities $\vec{v}_{e^-}$ and $\vec{v}_{MB}$, respectively. The centre-of-mass, CM, travels with velocity $\vec{v}_{CM}$. θ is defined as the angle between the relative velocity and the electron beam velocity vector, and can be derived using the definition of the tangents in a right-angled triangle,

$$\begin{aligned} \tan\theta &= \frac{v_{MB}}{v_{e^-}} \\ \theta &= \arctan\left(\frac{v_{MB}}{v_{e^-}}\right). \end{aligned} \tag{4.5}$$

Assuming a supersonic expansion of room-temperature CF_3I the maximum value for the molecular-beam speed, v_{MB} is given by,

$$v_{MB} = \sqrt{\frac{2C_pT_i}{m_{CF_3I}}} \tag{4.6}$$

where $C_p = 70.886\,J\,K^{-1}\,mol^{-1}$ [225] is the heat-capacity of CF_3I at room temperature, $T_i = 298\,K$ is the temperature of the expanding gas in the sample container and $m_{CF_3I} = 196\,g\,mol^{-1}$ is the molecular mass of trifluoroiodomethane. Hence, a maximum molecular beam speed of $464\,m\,s^{-1}$ is obtained.

The velocity of an electron beam with a kinetic energy of 100 eV is:

$$v_{e^-} = \sqrt{\frac{2E_{el}}{m_{e^-}}} = 5930000\,m\,s^{-1} \tag{4.7}$$

where the electron mass is $m_{e^-} = 9.1093835 \cdot 10^{-31}\,kg$ [177].

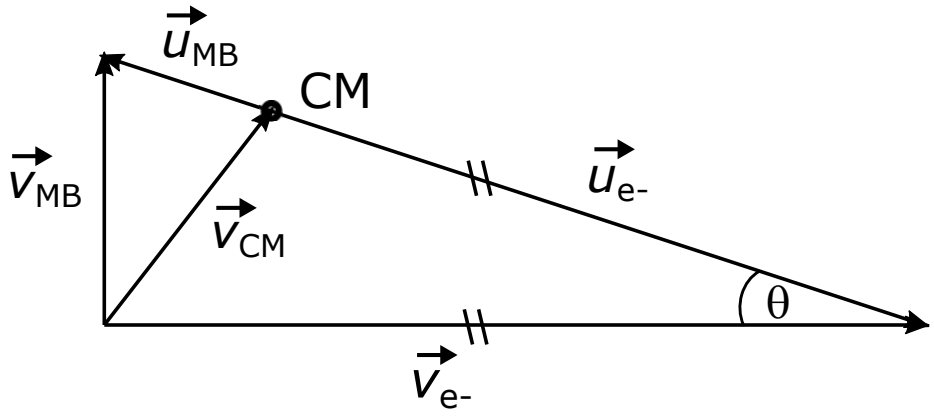


Figure 4.8: Newton diagram of an electron molecule collision in laboratory and centre-of-mass, CM, frame.

Using the electron and molecular beam velocities, calculated above, the angle θ is determined using Equation (4.5) to be 0.004°. Therefore, the electron beam axis lies approximately along the relative velocity vector of the electron-molecule collision and the recorded velocity-map images retain cylindrical symmetry along the electron beam. Therefore the pBASEX algorithm can be applied to obtain the Abel-inverted image.

As described in Section 1.2.5, fragment speed and kinetic energy distributions can be obtained from the Abel-inverted velocity-map image. The measured velocity distribution in pixel units is calibrated with trajectory simulations of charged particles in a model spectrometer using the SIMION software package [144]. In the following discussion of the results, the recorded velocity-map image is shown together with the Abel inverted image and the fragment kinetic energy distribution. For presentation purposes, the velocity-map images have been symmetrized along the electron beam axis.

4.4 Results and discussion

In the following, the partial ionization cross-sections and velocity-map imaging data for dissociative electron ionization of CF_3I are presented and discussed. The principal results of this study are compared with data from photoionization studies.

4.4.1 Partial ionization cross-sections

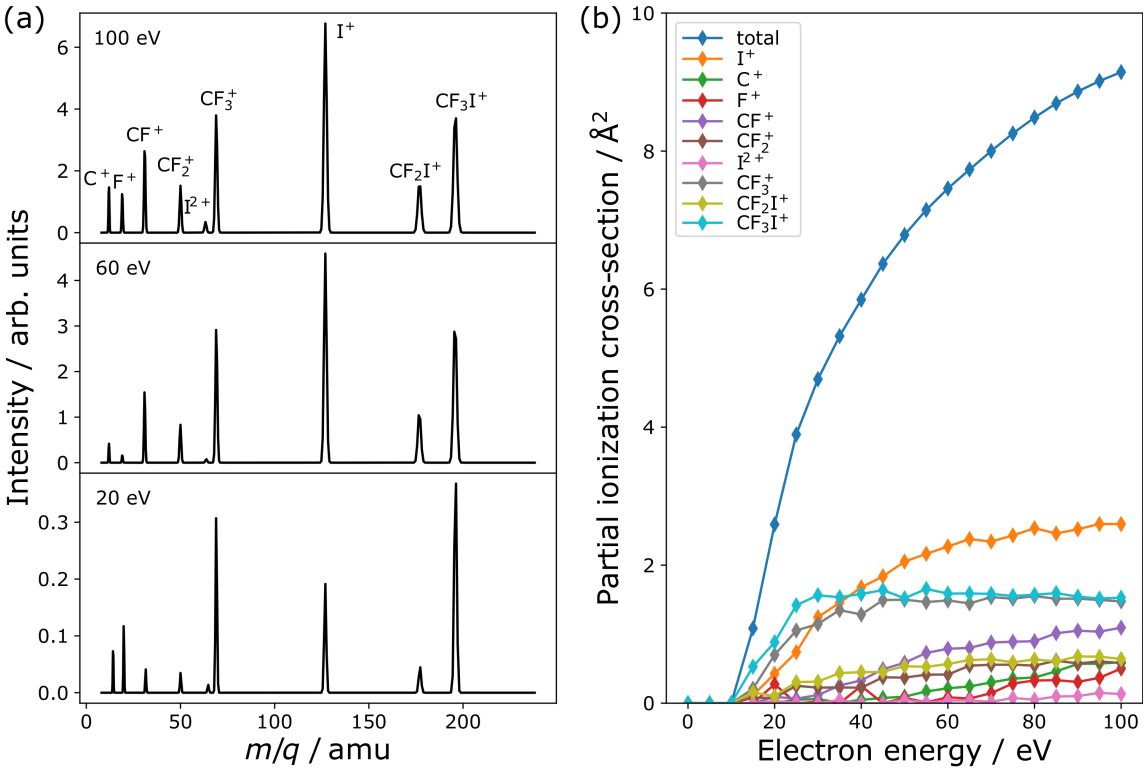


Figure 4.9: a) Deconvoluted mass-spectra derived as described in Section 4.3.1 for 100, 60 and 20 eV; b) Partial ionization cross-sections of the fragment ions.

Figure 4.9 (a) shows three example mass-spectra for the dissociative electron ionization products of CF_3I at electron energies of 100, 60 and 20 eV. The mass-spectra were deconvoluted from the photomultiplier signal as described in Section 4.3.1. The partial ionization cross-sections of the fragment ions are derived by integrating over

the relevant ion signal in the time-of-flight spectrum and normalizing the sum of individual ion yields to the total ionization cross-section for CF_3I measured in a separate experiment by Weiwei Zhou [221].

The mass spectrum resulting from 100 eV electron ionization of CF_3I shows that the dominant ions at this electron energy are the I^+ and CF_3^+ fragment ions and CF_3I^+ parent ion. While the fragment ion yield is generally observed to decrease with decreasing electron energy, the partial ionization cross-sections in the threshold region are in agreement with reported appearance energies for the electron ionization products listed in Table 4.1, from Dibeler *et al.* [226]. Two further studies [227, 228] of the fragment appearance energies support the values from Reference [226]. The fragment relative abundances at 100 eV observed in this study and listed in Table 4.1, are also in reasonable agreement with values reported in Reference [226]. In addition to CF_3I^+, I^+ and CF_3^+ a number of less abundant fragments are observed: CF_2I^+, CF_2^+, CF^+, F^+ and C^+. In contrast to the present work, the I^+ fragment is observed as a minor species relative to CF_3^+ and CF_3I^+ in the work reported in Reference [226]. One possibly explanation could be that in the studies reported in References [226], [227] and [228], CF_3I molecules were not prepared in a cooled molecular beam but as a thermal sample which could lead to a different fragmentation pattern due to the additional internal energy in the ionized species.

After the single ionization of the sample molecule, forming CF_3I^+, the most abundant fragment ions, CF_3^+ and I^+, originate from fission of the C-I bond with the charge remaining on the I^+ or CF_3^+ fragment,

$$CF_3I^+ \longrightarrow {CF_3}^+ + I \tag{4.8}$$

$$CF_3I^+ \longrightarrow CF_3 + I^+. \tag{4.9}$$

Fragment ion	m/q	Relative abundance at 100 eV	appearance energy / eV
CF_3I^+	196	0.167	10.0 ± 0.3
CF_2I^+	177	0.070	15.3 ± 0.3
I^+	127	0.284	13.6 ± 0.5
CF_3^+	69	0.161	11.4 ± 0.4
I^{2+}	63.5	0.014	-
CF_2^+	50	0.064	18.5 ± 0.6
CF^+	31	0.120	20.7 ± 1
F^+	19	0.055	33 ± 1
C^+	12	0.065	32.6 ± 1

Table 4.1: Ionic fragments from electron ionization of CF_3I with their mass-to-charge ratio m/q, observed relative abundance at an electron energy of 100 eV and appearance potentials for electron ionization taken from Reference [226].

CF_2I^+ and F^+ ions are also observed, resulting from C-F bond cleavage,

$$CF_3I^+ \longrightarrow CF_2I^+ + F \tag{4.10}$$

$$CF_3I^+ \longrightarrow CF_2I + F^+. \tag{4.11}$$

Smaller carbo-fluorides, CF^+ and CF_2^+, and the C^+ and F^+ fragment ions can also be formed from secondary dissociation of a larger fragment ion along a C-F bond. A small signal for I^{2+} ions, at a mass-to-charge ratio of 63.5 amu, indicates the fragmentation of a larger multiply charged ion, which could yield fragmentation into multiple charged and neutral fragments.

The velocity-map imaging data presented in the following section gives more information on the fragmentation pathways associated with the production of observed fragment ions.

4.4.2 Velocity-map image data

Velocity-map images were recorded for the three main fragment ions, I^+, CF_3^+ and CF_2I^+, for four different electron energies, 100, 80, 60 and 40 eV, and are presented in Figures 4.10 to 4.12 alongside the Abel-inverted images and the corresponding kinetic energy distributions. The data were recorded using a charged-coupled device (CCD) camera with the long drift-tube configuration of the velocity-map imaging spectrometer.

The kinetic energy distributions of all three fragment ions show no apparent differences for the four different kinetic energies, but for all three ions the observed kinetic energy is very small in comparison to the electron beam energy. Furthermore, the kinetic energy distributions of the CF_3^+ and CF_2I^+ fragments are qualitatively different from each other. While in the CF_3^+ image most of the ion signal is found in the image centre and the kinetic energy distribution falls off steeply towards the baseline by about 0.2 eV, the CF_2I^+ kinetic energy distribution shows a distinct, approximately 0.07 eV wide, feature centred at approximately 0.14 eV. The I^+ kinetic energy distribution is much broader and tails off by approximately 1 eV; the corresponding image intensity for the I^+ ions is at the maximum in its centre, uniformly decreasing towards higher kinetic energies.

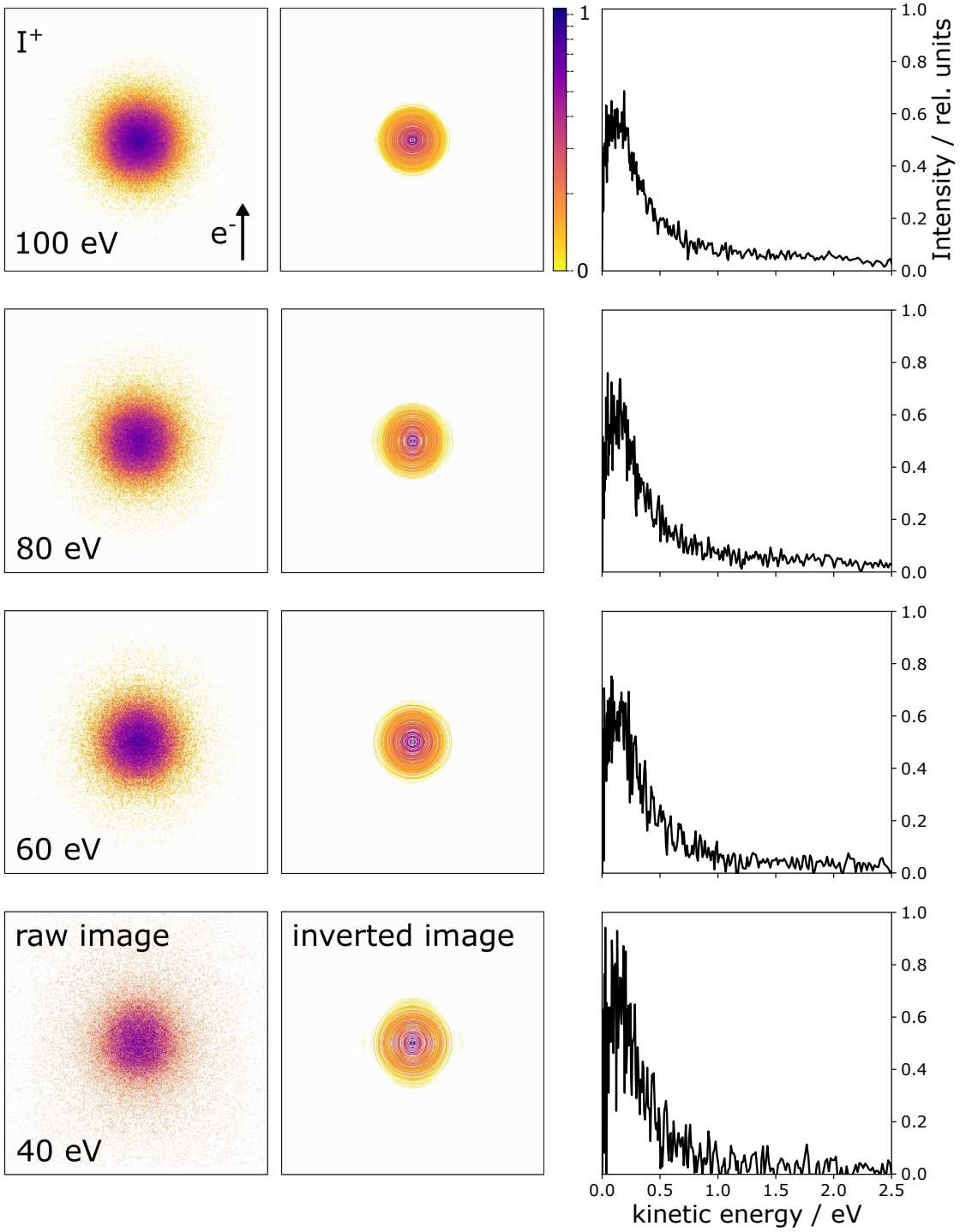


Figure 4.10: Velocity-map images, Abel-inverted images and kinetic energy distributions of the I^+ fragmentation product from electron ionization of CF_3I at electron energies of 100 eV, 80 eV, 60 eV and 40 eV; the electron beam propagates along the arrow shown in the top left image; the velocity-map imaging spectrometer was configured with the long drift-tube ensemble as described in the experimental section; presented kinetic energy distributions are smoothed using a three-point moving average.

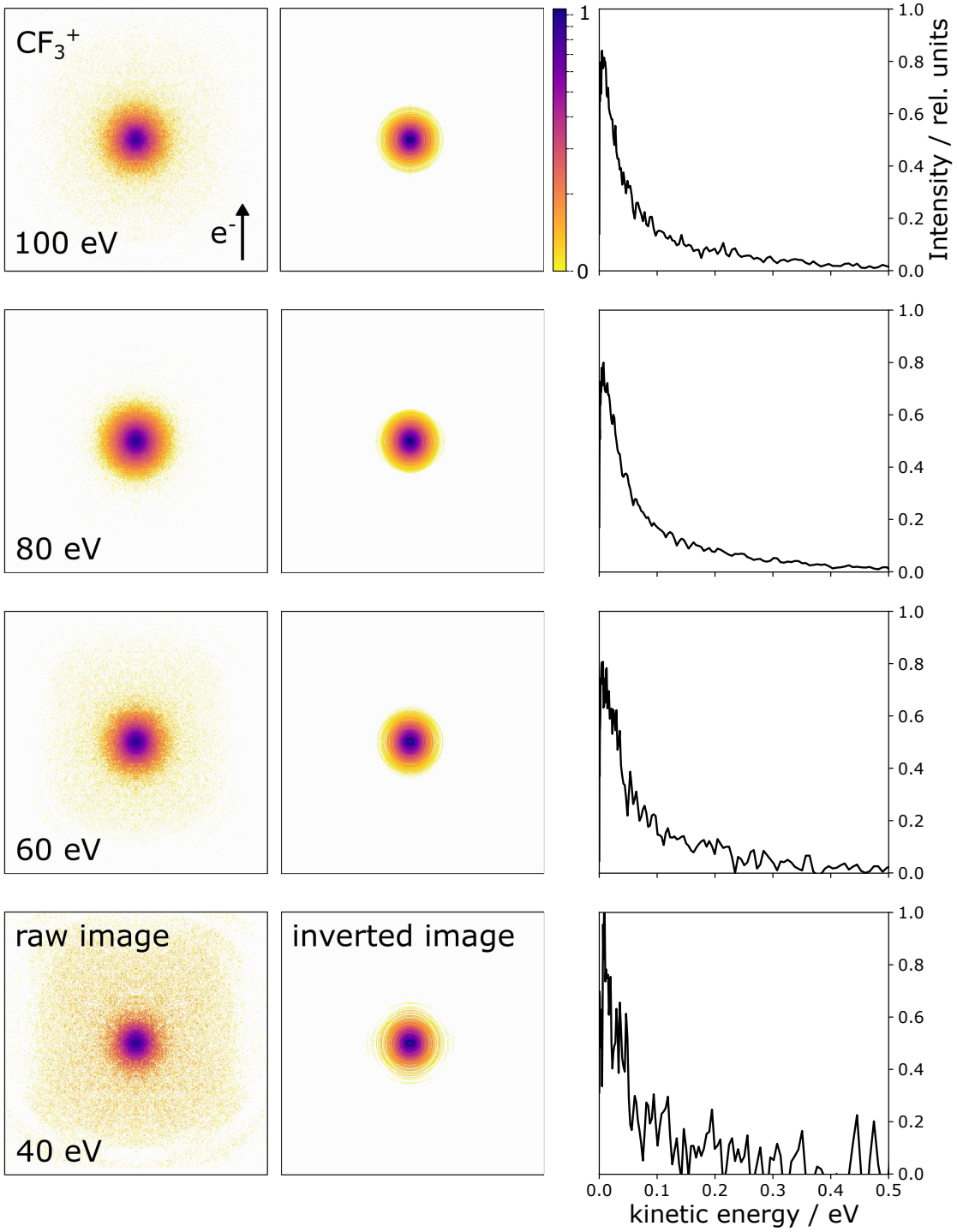


Figure 4.11: Velocity-map images, Abel-inverted images and kinetic-energy distributions of the CF_3^+ fragmentation product from electron ionization of CF_3I at electron energies of 100, 80, 60 and 40 eV; the electron beam propagates along the arrow shown in the top left image; the velocity-map imaging spectrometer was configured with the long drift-tube ensemble as described in the experimental section; presented kinetic energy distributions are smoothed using a three-point moving average.

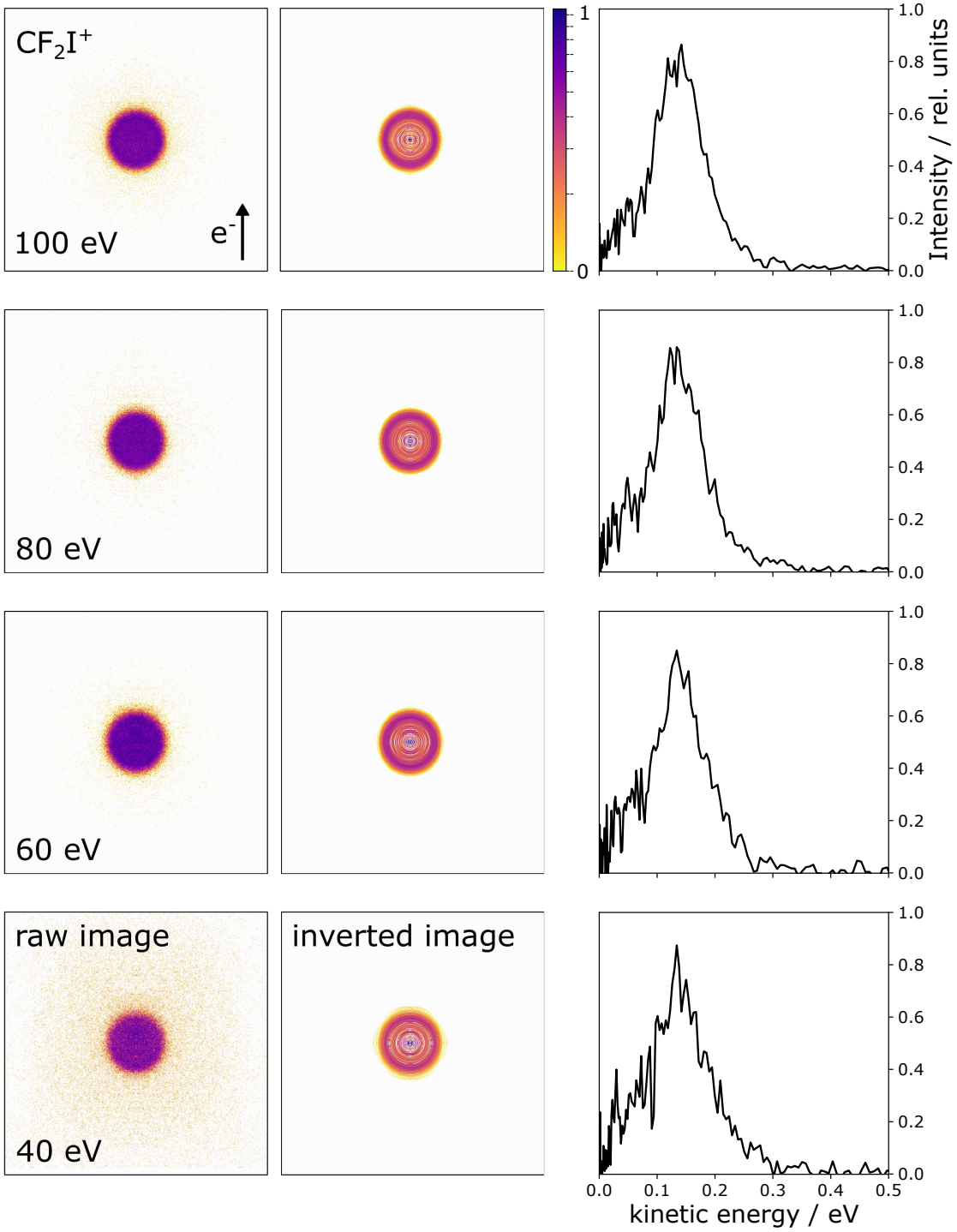


Figure 4.12: Velocity-map images, Abel-inverted images and kinetic energy distributions of the CF_2I^+ fragmentation product from electron ionization of CF_3I at electron energies of 100, 80, 60 and 40 eV; the electron beam propagates along the arrow shown in the top left image; the velocity-map imaging spectrometer was configured with the long drift-tube ensemble as described in the experimental section; presented kinetic energy distributions are smoothed using a three-point moving average.

The observations made for the CF_3^+ and I^+ ions are consistent with low resolution measurements of the fragment kinetic energy distribution following electron ionization at an energy of 70 eV by Dibeler *et al.* [226]. Using the beam deflection technique developed by Berry *et al.* [229], the authors observed a thermal kinetic energy distribution for the CF_3^+ species with similar width to the CF_3I^+ parent ion kinetic energy distribution. Similar to the present work the authors observe a much broader distribution for fragment kinetic energies in the I^+ than in the CF_3^+ channel. Here, the I^+ kinetic energy distribution still appears to be thermal but with significant contributions of ions with a kinetic energy of approximately 0.4 eV. Through comparison with data from photoionization and photofragmentation studies in Section 4.4.3, it will be shown that the observations made here are consistent with vibrational relaxation of the CF_3I^+ parent ion, producing thermal CF_3^+ ions, and that production of CF_2I^+ ions is consistent with impulsive fragmentation along the C-F bond on an excited potential energy surface.

Experiments with shorter drift-tube length revealed additional channels for higher energy fragment ions. Velocity-map imaging data was recorded with the PImMS2 sensor for all fragments at the same time. The velocity-map images are presented together with the Abel-inverted images and the fragment ion kinetic energy distributions in Figures 4.14 and 4.15, for an electron energy of 100 eV.

In Figure 4.14, velocity-map image data for the CF_2I^+, I^+, CF_3^+ and I^{2+} fragment ions are shown. In the kinetic energy range from 0 to 2.5 eV, observations made with the long drift-tube configuration (see Figures 4.10 to 4.12) were reproduced for the I^+, CF_3^+ and CF_2I^+ fragment ions. An additional channel is found in the CF_3^+ kinetic energy distribution at an energy of about 4 eV and for I^+ at approximately 2.3 eV. Although still in the measurement range of the long drift-tube configuration,

the high energy feature of I^+ ions is close to the detector edge, and is perceived as noise in Figure 4.10. As shown in the following, these higher I^+ and CF_3^+ ions arise from fragmentation of a doubly charged parent ion according to,

$$CF_3I^{2+} \longrightarrow {CF_3}^+ + I^+ \cdot \tag{4.12}$$

The kinetic energy distributions in Figure 4.14 are compared with fragment energies predicted from a Coulomb repulsion model, shown as downward pointing arrows at the relevant energies. The total kinetic energy of the fragments from the Coulomb repulsion, $E_{\mathrm{kin,total}}$, is derived assuming a two-body fragmentation process according to Coulomb's law,

$$E_{\mathrm{kin,total}} = \frac{1}{4\pi\epsilon_0} \cdot \frac{q_1 q_2}{r}. \tag{4.13}$$

Here, ϵ_0 is the vacuum permittivity and it is assumed that the two repelling charges, q_1 and q_2, are placed at the equilibrium positions of the atoms in the neutral geometry of CF_3I. The internuclear distances are taken from a microwave spectroscopy study published in Reference [230], and the relevant information on the molecular geometry are summarized in Figure 4.13. The total kinetic energy is distributed between the fragmentation partners, A and B, with masses, m_{A} and m_{B}, as described in Section 1.2.5, according to,

$$E_{\mathrm{kin,A}} = E_{\mathrm{kin,total}}/(1 + \frac{m_{\mathrm{A}}}{m_{\mathrm{B}}}). \tag{4.14}$$

While it is assumed here, that the distance between the repelling charges is given by the geometry of the neutral molecule, the geometry of the parent ion is most likely different. Eland *et al.* [208] performed CASSCF calculations on the CF_3I^{2+} dication to model the potential energy curves along the C-I and C-F bond distance and showed that the equilibrium C-I distance of the ground and most excited states of the dication are longer than in the neutral electronic ground state. Therefore, the model applied here slightly overestimates the fragment kinetic energy. Nevertheless,

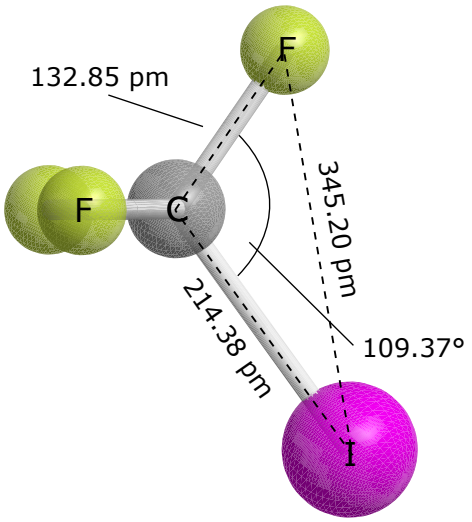


Figure 4.13: Structure of the CF_3I molecule; the F-C-F bond angle is 108.42°; information on bond angle and internuclear distances are taken from Reference [231].

reasonable agreement between the observed features and the predicted kinetic energies is found.

To derive the kinetic energy of the CF_2I^+ ion, the charges are placed onto the fluorine and iodine atom, and in the case of the I^+ fragments the repelling charges are placed on the carbon and iodine atoms. The CF_3^+ kinetic energy distribution is compared with predictions for two possible cases. One charge is placed on the iodine, and the partner charge is either placed on the carbon (black arrow) or fluorine atom (blue arrow). The dataset appears to be more consistent with a charge placed on the carbon centre rather than on the fluorine atom in the CF_3^+ fragment.

The high kinetic energy features in the I^+ and CF_3^+ fragment kinetic energy distributions are in good agreement with the Coulomb repulsion model describing the fragmentation of a doubly charged parent ion. While this leads to a single distinct feature in the CF_3^+ kinetic energy distribution, the high kinetic energy I^+ fragments form a much broader feature merging with the dissociative single ionization products

at lower kinetic energy. This is consistent with additional fragmentation of the CF_3^+ particle, losing one or more fluorine atoms in a multi-body break-up which carry excess energy and reduce the energy observed in the I^+ fragment. This is supported by the kinetic energy distributions of the CF_2^+, CF^+ and C^+ fragments which are presented and discussed in Figure 4.15. In order to be able to observe the effect of the secondary fragmentation in the I^+ product channel, the C-F fission happens either concerted with the I^+-CF_3^+ fragmentation or shortly after at a time when both fragments are in close enough proximity to interact with each other.

The kinetic energy distribution determined from the I^{2+} image shows a broad component with a maximum at about 1 eV, ranging up to approximate 5 eV and then sharply falling off. The kinetic energy distribution is compared with predictions of the Coulomb repulsion model in a similar way as for the I^+ fragment, for repulsion between the I^{2+} ion and a charge at the carbon atom of the CF_3^+ co-fragment. Similar to the kinetic energy distribution of the I^+ ion, the feature extends to lower kinetic energies indicating further fragmentation of the co-fragment. The formation of an I^{2+} ion partnered by a CF_3^+, CF_2^+ or CF^+ ion is further supported by covariance analysis of the velocity-map image data, discussed below. The observation of an I^{2+} ion together with a charged cofragment indicates the fragmentation of a triply charged parent ion according to,

$$CF_3I^{3+} \longrightarrow {CF_3}^+ + I^{2+}\cdot \tag{4.15}$$

Figure 4.15 shows the velocity-map image data and kinetic energy distributions of the CF_2^+, CF^+, F^+ and C^+ fragment ions. The CF_2^+ and CF^+ kinetic energy distributions show two features, one relatively low energy feature tailing off from 0 to 2 eV, and one higher energy feature appearing at approximately 3 to 6 eV. While the lower energy feature most probably originates from dissociative ionization of the

singly charged parent ion, the higher energy component is of similar energy to that predicted for CF_3^+ repelling from an I^+ ion. The C^+ ion shows a high kinetic energy component in the similar energy range, but with no low kinetic energy feature, indicating that this fragment ion is not formed by dissociative single ionization of the CF_3I molecule. The high kinetic energy ions might be formed by additional fragmentation of the CF_3^+ ion following the fragmentation reaction (4.12) or by a concerted multi-body fragmentation of a doubly charged parent ion in processes such as,

$$CF_3I^{2+} \longrightarrow CF_2{}^+ + I^+ + F \tag{4.16}$$

$$CF_3I^{2+} \longrightarrow CF^+ + I^+ + 2\,F \tag{4.17}$$

$$CF_3I^{2+} \longrightarrow C^+ + I^+ + 3\,F. \tag{4.18}$$

These pathways are observed in covariance analysis between the CF_x^+ and I^+ velocity-map images in the following.

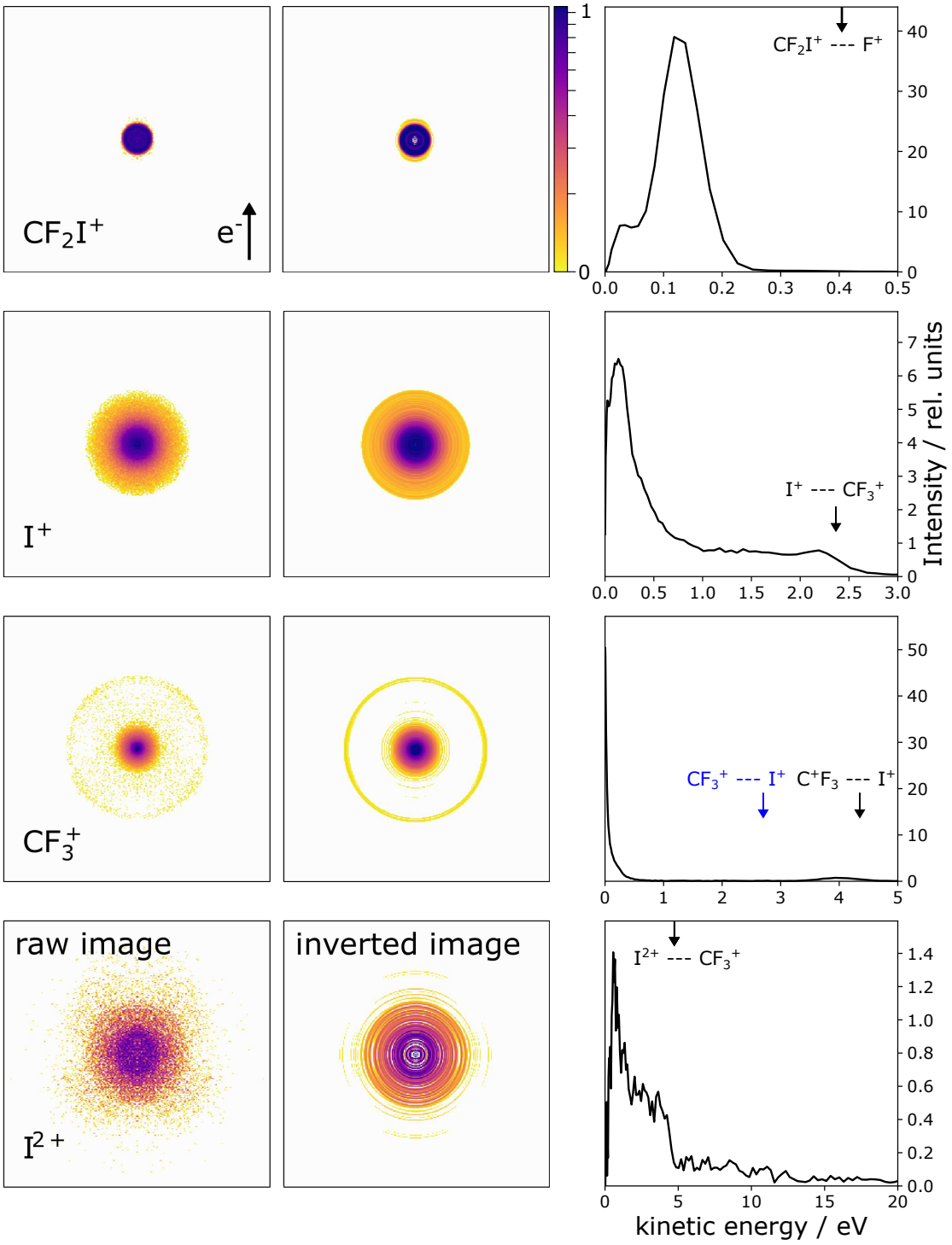


Figure 4.14: Velocity-map images, Abel-inverted images and fragments' kinetic energy distribution for CF_2I^+, I^+, CF_3^+ and I^{2+} ion from electron ionization at an electron energy of 100 eV; velocity-map images shown here and in Figure 4.15 are recorded in the same experiment with the PImMS sensor; the velocity-map imaging spectrometer was configured with the short drift-tube ensemble as described in Section 4.2.

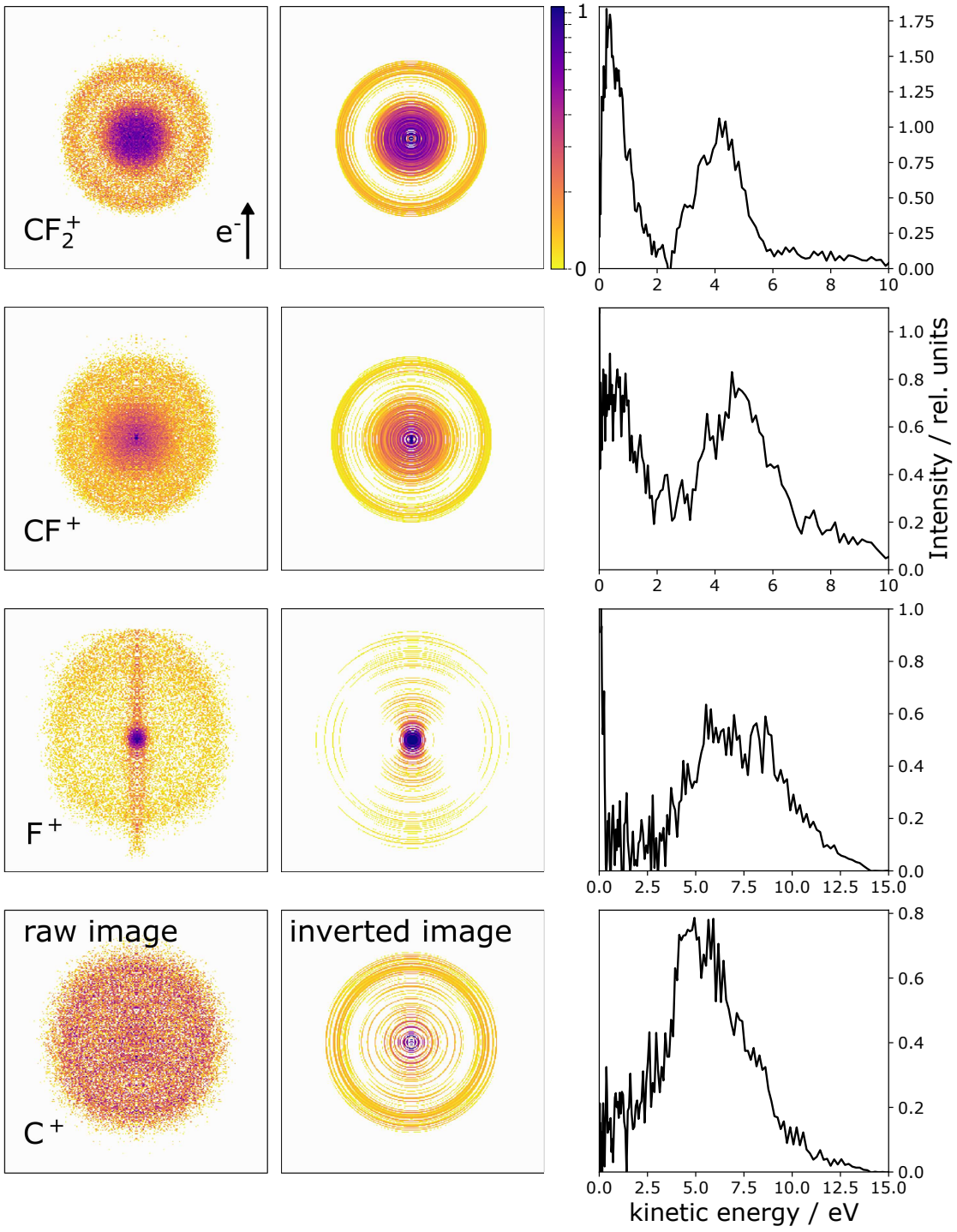


Figure 4.15: Velocity-map images, Abel inverted images and fragments' kinetic energy distribution for CF_2^+, CF^+, F^+ and C^+ ion from electron ionization at an electron energy of 100 eV; velocity-map images shown here and in Figure 4.15 are recorded in the same experiment with the PImMS sensor; the velocity-map imaging spectrometer was configured with the short drift-tube ensemble as described in Section 4.2.

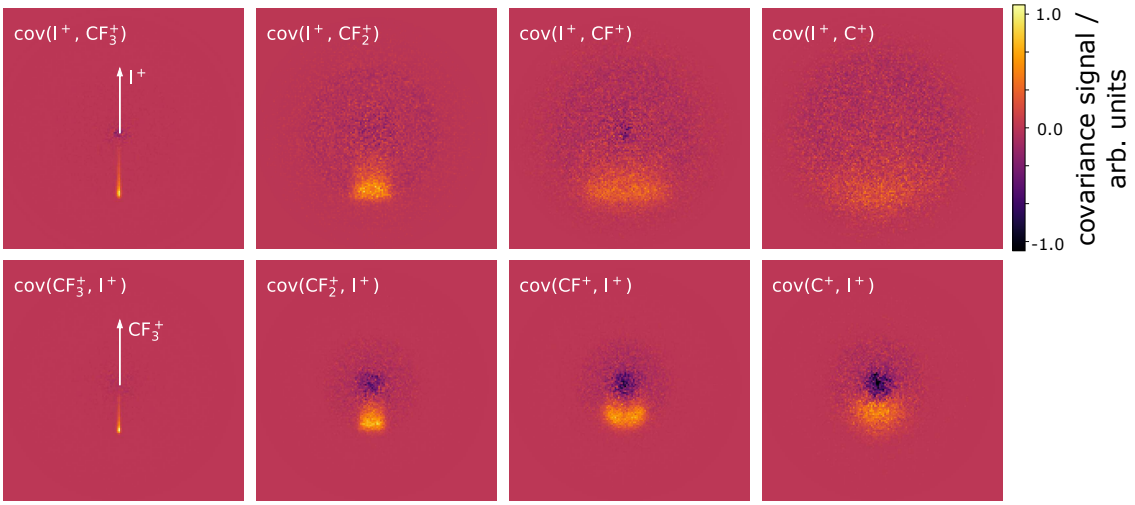


Figure 4.16: Angular covariance of the I^+ and CF_x^+ fragment ions for $x = 3, 2, 1, 0$ from left to right; in the top row covariance of the CF_x^+ fragment is shown in reference with the I^+ ion; in the bottom row covariance of the I^+ fragment is plotted in reference to the different CF_x^+ ions; the vertical arrow in the left hand site images shows the direction of the reference ion relative to the plotted covariance map; positive parts in the image describe a statistical correlation between the plotted and reference ions.

In order to confirm the assignment of the observed high kinetic energy ions to fragmentation products of the doubly and triply charged parent ions CF_3I^{2+} and CF_3I^{3+}, covariance analysis was performed between the velocity-map images of the fragment ions for an electron energy of 100 eV as outlined in Section 1.2.6. The angular covariance of the CF_3^+, CF_2^+, CF^+ and C^+ fragments in the recoil frame with the reference I^+ ion pointing upwards is shown in the top row of Figure 4.16. The bottom row shows the covariance of the I^+ ion in reference to the CF_3^+, CF_2^+, CF^+ and C^+ fragments.

The I^+-CF_3^+ covariance pair shows a sharp feature of positive covariance at 180° relative to the reference ion. The feature is most intense in the outer part of the velocity-map image and, hence, confirms the assignment of those ions to Coulomb explosion of CF_3I^{2+} to form CF_3^+ and I^+. Covariances between I^+ and CF_2^+, CF^+, and C^+, respectively, show that a third body is involved in this fragmentation leading to deflection of the partner ion from the C-I recoil axis. This is consistent with both a

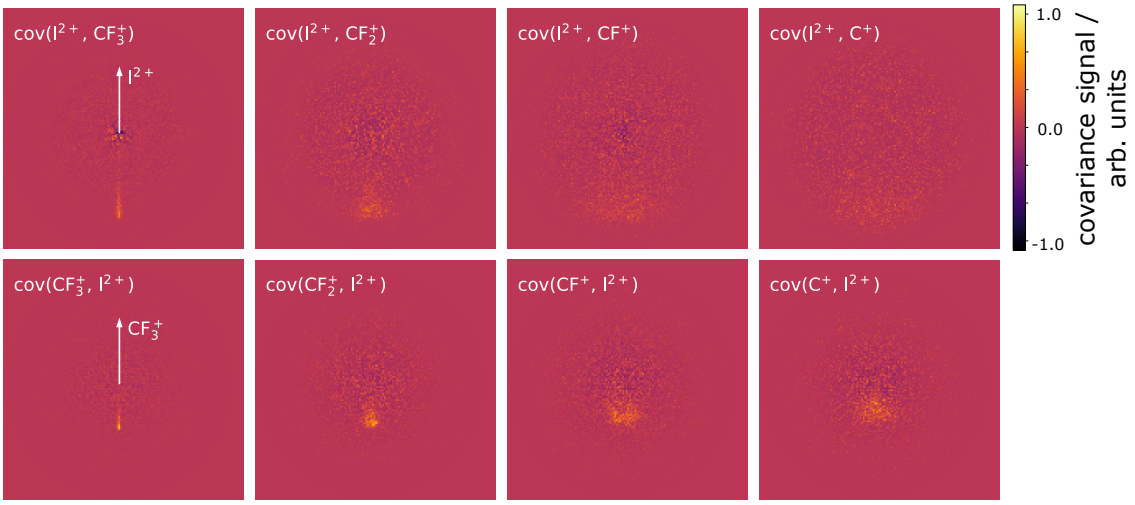


Figure 4.17: Angular covariance of the I^{2+} and CF_x^+ fragment ions for $x = 3, 2, 1, 0$ from left to right; in the top row covariance of the CF_x^+ fragment is shown in reference with the I^{2+} ion; in the bottom row covariance of the I^{2+} fragment is plotted in reference to the different CF_x^+ ions; the vertical arrow in the left hand site images shows the direction of the reference ion relative to the plotted covariance map; positive parts in the image describe a statistical correlation between the plotted and reference ions.

concerted and sequential secondary fragmentation. Further simulations and experimental work is needed to differentiate the contributions of both mechanisms.

Covariances between the I^{2+} fragment and the CF_3^+, CF_2^+, CF^+ and C^+ fragments are presented in Figure 4.17. The results are very similar to those observed for singly charged I^+ with the same co-fragments. I^{2+} is observed to recoil from a CF_3^+ partner ion, confirming the formation and fragmentation of a triply charged parent ion in Reaction (4.15). Additional fragmentation pairs correlating with the CF_2^+, CF^+ and C^+ fragments are also observed, and show a similar angular deflection from a third recoil partner as seen in the covariance maps for the I^+ fragment ion.

Covariance analysis involving the F^+ fragment velocity-map image did not reveal any correlations with other detected ionic fragments. This is consistent with the CF_2I^+ kinetic energy distribution which did not show any evidence for ions formed

in a CF_2I^+-F^+ fragmentation, further indicating that fragmentation of the multiply charged parent ion into a F^+ ion and another charged particle is not a significant contribution to the dissociative ionization pathways of CF_3I^+ at an electron energy of 100 eV. Several fragmentation pathways of a multiply charged parent ion or primary fragmentation products along the C-F bond are in principle conceivable. The counts for the F^+ image are relatively low because of the relatively low partial ionization cross-section of the F^+ ion and because the available counts for the relatively high kinetic energy ions are distributed over more camera pixels, further reducing the counts in each pixel for the covariance analysis. Because of these effects covariances between features in the F^+ ion and partner ions might not be perceivable within the available statistics.

While the production and fragmentation of doubly or higher charged parent ions upon electron impact has been reported previously [232–235], no report on the fragmentation of multiply charged ions upon electron ionization of CF_3I was found in the available literature. Electron ionization of CF_4 at 100 eV [234] and 43.7 eV [235] was studied in a covariance mapping experiment employing a pulsed electron beam and an effusive molecular beam source. The authors record electrons and ions with a double-sided time-of-flight spectrometer constructed around the scattering centre of the molecular and electron beam. Covariance analysis between the time-of-flight of recorded ions illustrates correlations between the F^+ fragments and CF^+, CF_2^+ and CF_3^+ ions. A quantitative analysis of the covariance result indicates that the momentum distribution between the F^+ ion and partner fragment is close to a two-body break-up where both fragments carry equal and opposite momentum. Thus, Bruce *et al.* [234] concluded that most of the momentum is carried away by the detected ion pair and, in the case of the CF_2^+-F^+ and CF^+-F^+ ion pair channels the additional fragmentation partner carries only little momentum.

In the present study, no conclusive evidence for polar C^+-F^+ fragmentation channels is found. The data shows a significant deviation of the CF_2^+-I^+ and CF^+-I^+ recoil from a two body break up observed in the CF_3^+-I^+ ion pair. This suggests that the polar fragmentation of the CF_3I^{2+} parent ion along the C-I bond coordinate is comparably impulsive as the most likely neutral C-F fission. This is consistent with the energy of primary C-F fission products attributed to dissociative single ionization and C-I fission associated to Coulomb fragmentation of a doubly-charged parent ion in the present study. Based on the observed fragment kinetic energies of the CF_2I^+ and I^+ fragment ions and using Equation (4.14), total kinetic energy releases of 1.3 eV and 6.3 eV were derived for the CF_2I^+-F and CF_3^+-I^+ fragmentations, respectively. Both values are within the same order of magnitude.

In order to retrieve more information on the secondary fragmentation mechanism, a more quantitative analysis of the recoil frame angular covariance maps is needed. In the current state of the analysis, the un-oriented correlations of ion pairs in the velocity-map images are aligned relative to the direction of one reference ion (see Section 1.2.6 for more details). If more than two partner fragments contribute to the particle velocities, the covariance map becomes a two-dimensional projection of the three-dimensional distribution of covariance events as the additional fragmentation partner is not aligned in the recoil frame. If the third fragmentation partner is charged and also detected three-fold covariance methods can be used to gain more information on the correlation between the three partner fragments [20]. More work is needed to develop additional analytical or experimental approaches to retrieve information of the three-dimensional distribution of covariances from its two-dimensional projection.

4.4.3 Comparison to photoionization studies

In the following the observations made for the fragmentation of CF_3I upon electron ionization are compared with data from dissociative photoionization experiments employing pulsed lasers and XUV sources. The main difference between electron ionization and photoionization is that the photoabsorption step is governed by selection rules, only allowing transitions from the ground state to an excited state for which the transition-dipole moment is non-zero. Nevertheless, the comparison with these studies elucidates a set of excited state potential energy surfaces on which the fragmentation may occur.

The dissociative ionization of the CF_3I molecule has been subject of a number of studies focussed on photoelectron and photoion products [203–207] and a summary of the reported fragmentation pathways of a singly charged parent ion is shown in Figure 4.18. Low *et al.* [204] correlated fragmentation products to the molecular states of the CF_3I^+ cation in a photoelectron-photoion coincidence experiment, identifying which electronic state of the parent ion is correlated with which product pathway. It was concluded that fragmentation from the $\widetilde{X}^2\mathrm{E}$ ground state leads to production of $\mathrm{CF}_3^+(\widetilde{X}^1\mathrm{A}_1)$ ions and $\mathrm{I}(^2\mathrm{P}_{3/2})$ atoms in their respective ground states. The kinetic energy distribution observed for the CF_3^+ fragment strongly suggests a statistical fragmentation of the parent ion and, thus, would be consistent with fragmentation from the $\widetilde{X}^2\mathrm{E}_{1/2}$ ground state of a singly charged CF_3I^+ parent ion. Fragmentation from the excited $\widetilde{A}^2\mathrm{A}_1$ state was found to produce both $\mathrm{CF}_3^+(^1\mathrm{A}_1)/\mathrm{I}(^2\mathrm{P}_{1/2})$ and $\mathrm{CF}_3(^2\mathrm{A}_1)/\mathrm{I}^+(^3\mathrm{P}_2)$ fragment pairs. The cationic $\widetilde{A}$-state can be accessed by ionization of a C-I bonding electron, and fragmentation yielding I^+ then proceeds on a strongly repulsive potential energy surface. This is inconsistent with the observations made in the I^+ kinetic energy distribution within the present work. Direct fragmentation on an excited potential energy surface would yield a distinct non-zero feature in the kinetic

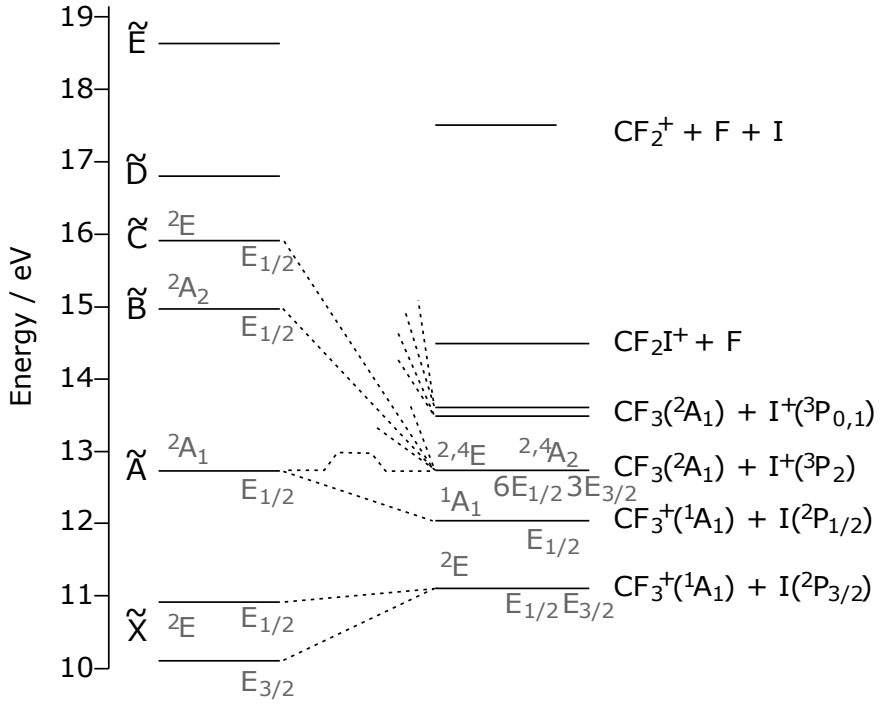


Figure 4.18: Partial correlation diagram summarizing the product pathways of the $\widetilde{X}$, $\widetilde{A}$, $\widetilde{B}$, $\widetilde{C}$, $\widetilde{D}$ and $\widetilde{E}$ electronic states in the CF_3I^+ cation from photoelectron studies [204, 205, 207, 236, 237]; state symmetries in the C_{3v} and extended point groups are also shown; Reproduced from Reference [221] with permission from the PCCP Owner Societies.

energy distribution. The I^+ kinetic energy distribution observed in this work peaks close to zero and is almost featureless. Therefore, it appears unlikely for the observed I^+ fragments to be formed on the $\widetilde{A}$-state potential energy surface. CF_3^+ fragments formed *via* the $\widetilde{A}$-state could undergo non-radiative relaxation to the ground state and blend into the $\widetilde{X}$-state fragmentation products.

Following photoionization, the cationic $\widetilde{B}(^2A_2)$, $\widetilde{C}(^2E)$ and $\widetilde{D}$ states are found to correlate with fragmentation along the C-F bond, yielding CF_2I^+ + F as the most abundant product pair [204]. Fragmentation after photoionization to this set of states is observed with distinct non-zero total kinetic energy release, approximately 0.9 to 1.0 eV for the $\widetilde{B}$-state and 1.1 to 1.2 eV for the $\widetilde{C}$ and $\widetilde{D}$-states. This compares well with the kinetic energy distribution of CF_2I^+ observed in this study, with a maximum

at 0.13 eV. If the electron ionization and subsequent fragmentation of the cation proceeds in a two step process, the total kinetic energy can be deduced from the CF_2I^+ fragment kinetic energy to be 1.3 eV using Equation (4.14). Dissociative photoionization also yields I^+ as a minor product from the $\widetilde{B}$ and $\widetilde{C}$-states and a more prominent product from the $\widetilde{D}$ and $\widetilde{E}$-states. For the latter two states, Low *et al.* [204] report a kinetic energy for the I^+ fragments of 0.4 and 0.6 eV, respectively. The I^+ fragments observed in this work form a rather featureless distribution peaking at about 0.2 eV kinetic energy and extending out to about 1 eV. While the kinetic energy distribution of I^+ fragments does not show any specific features at the kinetic energies observed for fragments in photodissociation studies, the general range of kinetic energies indicates the involvement of these higher lying electronic states of the CF_3I^+ cation in the production of I^+.

Eland *et al.* [208] used pulsed XUV light to ionize the CF_3I molecule and studied the double photoionization spectrum of CF_3I in a photoelectron-photoelectron coincidence (PEPECO) experiment and the fragmentation mechanism of the CF_3I^{2+} dication in photoelectron-photoion-photoion coincidence and photoelectron-photoelectron-photoion-photoion (PEPEPIPICO) experiments. From the photoionization spectrum, the authors estimated the vertical double ionization energy as 28 eV. Below this threshold, formation of the CF_3^+/I^+ ion pair is attributed to single ionization forming a doubly charged ion core and highly excited electron which auto-ionizes, while the singly charged CF_3I^+ ion dissociates along the C-I bond. For higher photon energies, vertical ionization leads to the direct formation of a CF_3I^{2+} dication. While calculations suggest that this species is bound along the C-I and C-F bond, the potential well might be overcome by vibrational excitation of the parent dication. Thus, the authors suggest that the fragmentation of the CF_3I^{2+} dication along the C-I bond occurs on the 1^1E, 1^3E, 1^1A_1 and 2^1E states. At photon energies above 31 eV, Eland

et al. [208] observe the formation of a CF_2I^{2+} cation partnered by a neutral fluorine atom according to,

$$CF_3I \xrightarrow{XUV} CF_2I^{2+} + F. \tag{4.19}$$

The dication appears to be stable for photon energies up to 32.5 eV, and a comparison with electronic structure calculations [208] suggests that this species is formed in the $2^2A''$ and $2^2A'$ states. These are bound along the C-I coordinate by about 0.5 eV and along the C-F coordinate by less than 0.2 eV. Accordingly, for higher photon-energies this CF_2I^{2+} fragment is observed to break up further along the C-I and C-F bond according to,

$$CF_2I^{2+} \longrightarrow {CF_2}^+ + I^+ + F \tag{4.20}$$

$$CF_2I^{2+} \longrightarrow CF^+ + I^+ + 2\,F. \tag{4.21}$$

The authors conclude that for higher photon energies these processes occur faster, making it no longer possible to distinguish a difference between sequential and concerted fragmentation mechanisms.

Observations presented in Section 4.4.2 show clear evidence for the fragmentation of doubly charged parent ions formed in electron ionization. The findings in the photofragmentation study by Eland *et al.* [208] suggest a possible mechanism for the secondary fragmentation of the CF_3I^{2+} dication *via* a CF_2I^{2+} intermediate. While the presented velocity-map image data are qualitatively consistent with such a mechanism, other fragmentation pathways including a primary C-I fission and either concerted or sequential fragmentation of the CF_3^+ ion are also feasible. Contributions from these three mechanisms cannot be distinguished in the presented covariance data without a quantitative analysis of the recoil frame covariance maps presented in this chapter, and further advances of the data analysis are ongoing.

4.5 Conclusion and outlook

A comprehensive study of the fragmentation following electron ionization of CF_3I has been presented for an energy range from 20 to 100 eV. The presented observations are consistent with the fragmentation of singly, doubly and triply charged parent ions, formed in the initial ionizing collision.

Fragmentation of the singly-charged parent ion can be classified into two distinct fragmentation mechanisms, both producing relatively low energy fragment ions. Fragmentation along the C-F bond yielding CF_2I^+ fragments, is observed to occur impulsively, whilst fragmentation along the C-I bond produces thermal CF_3^+ with very low kinetic energy. This suggests vibrational relaxation of the parent ion before the fragmentation takes place on a ground or low lying excited state. I^+ fragments, which are also born in a C-I dissociation, appear to result from an intermediate case between both these mechanisms, and the formation of I^+ fragment ions is carefully attributed to an intramolecular impulsive mechanism where the fragmentation occurs on an excited potential energy surface but progresses sufficiently slowly so that some energy can be distributed into the cofragments internal degrees of freedom. The kinetic energy of all detected ions is much lower than that of the incident electron beam, which is consistent with the low efficiency of energy transfer in electron ionization [17]. A comparison to photofragmentation and photoionization studies suggests that CF_2I^+ is produced *via* the $\widetilde{B}$, $\widetilde{C}$ and $\widetilde{D}$ states and I^+ ions appear to, at least partially, be produced on the excited $\widetilde{D}$ and $\widetilde{E}$ states. In contrast, CF_3^+ ions appear to fragment on the ground state potential energy surface.

Product ions from the fragmentation of a multiply charged parent ions appear to arise from a Coulomb explosion along the C-I bond either in the parent ion or a CF_2I^{2+} intermediate. This yields highly vibrational fragment ions which can undergo

successive fragmentation losing neutral fluorine atoms.

In the work presented here, data acquisition using the PImMS2 sensor and the accompanying use of angular covariance analysis played a key role in the identification and study of fragmentation processes of multiply charged fragment ions. The low count rate observed in this experiment makes the multi-mass imaging technique a valuable experimental tool, as velocity-map images of all eight fragmentation products can be recorded simultaneously.

Experimentally it would be useful to extend the apparatus to simultaneously record both ionic products and secondary and scattered electrons. This would yield further insight into the ionization step, which can so far only be studied indirectly. One potential experimental arrangement would be to place imaging detectors on the top and bottom of the scattering chamber, and extract electrons with a negative extraction potential on one and ions with a positive extraction potential on the other detector. In this configuration the molecular beam would be steered directly into the turbo-molecular pump on the side of the spectrometer, perhaps further reducing the background gas in the scattering chamber.

To support the experimental findings of this study it would be interesting to perform simulations of Coulomb explosion dynamics similar to those recently performed by Zhou [238]. The charge distribution in the multiply charged parent ion is determined by an electronic structure calculation and the equations of motion of the fragment ions are evaluated. While the geometry is changed, charge distributions are re-determined step-by-step.

Finally, it would be interesting to study more sample molecules which have a similar structural motive as CF_3I, *i.e.* one strong and one much weaker bond, such as C_2F_6. These molecules are expected to similarly exhibit contrasting impulsive and statistical fragmentation. One other group of molecules with perhaps more biological applications are proteins, with their strong backbone bond and comparably more weakly bound side chain. Although cumbersome to prepare in the gas-phase, the laser-induced acoustic desorption technique [239, 240] could be one approach preparing overall neutral amino-acids in the gas-phase, and such a source could further complement the experimental set-up.

Chapter 5

Conclusion

The capabilities of multi-mass velocity-map imaging to study molecular fragmentation dynamics have been illustrated on three example experiments.

Velocity-map imaging has proven a powerful tool to investigate the photofragmentation and photoionization dynamics of niobium oxide (NbO) in the visible part of the spectrum. Velocity-map images of the NbO photofragmentation products show a complex set of features which have been discussed in context of the great number of combinations of accessible niobium atom and oxygen atom product states. Further analysis of the photoion velocity-map images yielded refined dissociation energies of NbO and NbO^+ as $60,650 \pm 124$ cm^{-1} and $57,414 \pm 124$ cm^{-1}, respectively. Photoelectron imaging has been used for the first time on this experimental apparatus, and utilising this technique the vibrational constant of the NbO^+ $X^3\Sigma^-$ state has been measured as 1002 ± 11 cm^{-1}. Upon review of the available literature published to date, this appears to be the first reported experimental value for the vibrational constant of the NbO^+ ground state. Recent modifications of the experiment to mass-selectively prepare and fragment charged metal-ligand clusters have been illustrated, and future experiments employing the multi-mass imaging technique to complement the existing velocity-map imaging spectrometer have been outlined.

A study of the UV-dissociation of bromoiodomethane (CH_2BrI) upon absorption of a UV photon in the A-absorption band has been presented. The fragmentation dynamics have been studied using a UV-pump XUV-probe experiment and multi-mass velocity-map imaging was employed to record the kinetic energy and angular distributions of the product ions. Three different XUV probe-photon energies, 66.7 eV, 70.1 eV, and 138.5 eV have been compared. The observations are largely consistent with previous experimental [7, 149, 152–154] and theoretical studies [150, 151]. Kinetic energy distributions and yield of the XUV ionization products are consistent with fragmentation of highly charged parent ions which are formed in sequential inner-shell ionization and Auger-relaxation of the inner-shell vacancy in the highly intense XUV pulse from the free-electron laser. As the UV-fragmentation products drift apart, charge transfer is observed between the highly charged iodine cation and the neutral CH_2Br co-fragment. A more detailed analysis for the time-dependence of the charge transfer for different iodine ion charge states shows some evidence for the rotational dynamics of the CH_2Br co-fragment.

A multi-mass velocity-map imaging study of the electron ionization dynamics of CF_3I has been presented for electron energies up to 100 eV. The data shows clear evidence for fragmentation of singly, doubly, and triply-charged parent ions. Singly-charged parent ions seem to fragment along the C-F bond on a distinctly direct pathway forming CF_2I^+ ions and statistically forming CF_3^+ ions along the C-I bond after vibrational relaxation to the ground state. The fragmentation mechanism forming I^+ fragment ions appears to be best described by an intramolecular impulsive mechanism, presenting evidence of both a direct and statistical pathway. A comparison to photoionization studies [203–207] suggests a set of potential energy surfaces on which the fragmentation dynamics may occur. Fragmentation of doubly and triply-charged parent ions are clearly identified by observing the correlation of singly and

doubly charged fragments obtained in covariance analysis between ions detected in velocity-map images of the product ions. Secondary fragmentation along the C-F bond, which is also observed, is discussed in comparison to a double-photoionization and photofragmentation study [208].

The application of multi-mass velocity-map imaging to experiments described in Chapters 3 and 4 complemented the available experimental set-up in two ways. Firstly, the time taken to acquire velocity-map imaging data for all observed fragment ions has been reduced significantly because velocity-map images of all fragment ions can be recorded simultaneously. This is of particular advantage for the experiments described in Chapter 3 which were conducted on a free-electron laser facility with limited experimental time. Secondly, the acquisition of velocity-map imaging data of multiple fragment ions in the same experimental cycle allows for correlations between fragment ions to be elucidated in form of covariances. As shown in Chapter 4, the application of covariance analysis to the recorded data yields detailed insight into the fragmentation mechanism which would otherwise not be obtainable in a conventional velocity-map imaging experiment.

Because of its limited sensor array size of only 324x324 pixels, the application of multi-mass imaging using the PImMS2 sensor reduces the kinetic energy resolution compared to velocity-map imaging using a CCD sensor with a typical array-size on the order of 1000x1000 pixels. The reduced kinetic energy resolution would be of particular disadvantage for experiments described in Chapter 2 because the precise determination of the *d*-metal oxides dissociation energy requires high kinetic energy resolution to distinguish between kinetic energy features from product channels of similar energy. Furthermore, the photo-active area of a pixel in the PImMS2 sensor is smaller than in a CCD sensor pixel of similar size as some of the PImMS2 active

array size is reserved for other parts of the chip architecture such as the memory registers. This leads to reduced light sensitivity of the PImMS2 sensor and, in some cases, requires the application of higher gain voltages to the detector which can lead to saturation of the imaging detector at high signal levels.

Further improvement of the time and energy resolution, along with the light sensitivity of the PImMS2 sensor are needed to make multi-mass velocity-map imaging using the PImMS2 sensor an even more powerful tool for the investigation of molecular fragmentation dynamics in the gas phase. One significant improvement has been achieved recently with application of an array of micro-lenses onto the PImMS2 sensor array and this version of the sensor was employed in the experiments described in Chapter 4. Each lens of the micro-lens array is placed on four pixel and focusses the light onto the photo-active area of the sensor. Thus, a significant improvement of the light sensitivity of the sensor could been achieved.

Bibliography

(1) Eyring, H.; Polanyi, M. *Z. Phys. Chem. B* **1931**, 12, 279.

(2) Born, M.; Oppenheimer, R. *Ann. Phys.* **1927**, 389, 457–484.

(3) Dunoyer, L. *Sc. Paris* **1911**, 152, 594.

(4) Yang, X. *Annu. Rev. Phys. Chem.* **2007**, 58, 433–459.

(5) Ashfold, M. N. R.; Ingle, R. A.; Karsili, T. N. V.; Zhang, J. *Phys. Chem. Chem. Phys.* **2019**, 21, 13880–13901.

(6) Chandler, D. W.; Farneth, W. E.; Zare, R. N. *J. Chem. Phys.* **1982**, 77, 4447–4458.

(7) Butler, L. J.; Hintsa, E. J.; Shane, S. F.; Lee, Y. T. *J. Chem. Phys.* **1987**, 86, 2051–2074.

(8) Maiman, T. H. *Nature* **1960**, 187, 493–494.

(9) Chin, S. L. *Phys. Rev. A* **1971**, 4, 992–996.

(10) Zandee, L.; Bernstein, R. B. *J. Chem. Phys.* **1979**, 71, 1359–1371.

(11) Chandler, D. W.; Houston, P. L. *J. Chem. Phys.* **1987**, 87, 1445–1447.

(12) Eppink, A. T. J. B.; Parker, D. H. *Rev. Sci. Inst.* **1997**, 68, 3477–3484.

(13) Parker, D. H.; Eppink, A. T. J. B. *J. Chem. Phys.* **1997**, 107, 2357–2362.

(14) Sarma, G.; Marinakis, S.; ter Meulen, J. J.; Parker, D. H.; McKendrick, K. G. *Nat. Chem.* **2012**, 4, 985–989.

(15) Harding, D. J.; Neugebohren, J.; Hahn, H.; Auerbach, D. J.; Kitsopoulos, T. N.; Wodtke, A. M. *J. Chem. Phys.* **2017**, 147, 013939.

(16) Neugebohren, J.; Borodin, D.; Hahn, H. W.; Altschäffel, J.; Kandratsenka, A.; Auerbach, D. J.; Campbell, C. T.; Schwarzer, D.; Harding, D. J.; Wodtke, A. M.; Kitsopoulos, T. N. *Nature* **2018**, 558, 280–283.

(17) Märk, T. D.; Dunn, G. H., *Electron Impact Ionization*; Springer Verlag: Vienna, 1985.

(18) Jungmann, J. H.; Gijsbertsen, A.; Visser, J.; Visschers, J.; Heeren, R. M. A.; Vrakking, M. J. J. *Rev. Sci. Inst.* **2010**, 81, 103112.

(19) Slater, C. S.; Blake, S.; Brouard, M.; Lauer, A.; Vallance, C.; John, J. J.; Turchetta, R.; Nomerotski, A.; Christensen, L.; Nielsen, J. H.; Johansson, M. P.; Stapelfeldt, H. *Phys. Rev. A* **2014**, 89, 011401(R).

(20) Pickering, J. D.; Amini, K.; Brouard, M.; Burt, M.; Bush, I. J.; Christensen, L.; Lauer, A.; Nielsen, J. H.; Slater, C. S.; Stapelfeldt, H. *J. Chem. Phys.* **2016**, 144, 161105.

(21) Burt, M.; Amini, K.; Lee, J. W. L.; Christiansen, L.; Johansen, R. R.; Kobayashi, Y.; Pickering, J. D.; Vallance, C.; Brouard, M.; Stapelfeldt, H. *J. Chem. Phys.* **2018**, 148, 091102.

(22) Allum, F.; Burt, M.; Amini, K.; Boll, R.; Köckert, H.; Olshin, P. K.; Bari, S.; Bomme, C.; Braußе, F.; Cunha de Miranda, B.; Düsterer, S.; Erk, B.; Géléoc, M.; Geneaux, R.; Gentleman, A. S.; Goldsztejn, G.; Guillemin, R.; Holland, D. M. P.; Ismail, I.; Johnsson, P.; Journel, L.; Küpper, J.; Lahl, J.; Lee, J. W. L.; Maclot, S.; Mackenzie, S. R.; Manschwetus, B.; Mereshchenko, A. S.; Mason, R.; Palaudoux, J.; Piancastelli, M. N.; Penent, F.; Rompotis, D.; Rouzée, A.; Ruchon, T.; Rudenko, A.; Savelyev, E.; Simon, M.; Schirmel, N.; Stapelfeldt, H.; Techert, S.; Travnikova, O.; Trippel, S.; Underwood, J. G.; Vallance, C.; Wiese, J.; Ziaee, F.; Brouard, M.; Marchenko, T.; Rolles, D. *J. Chem. Phys.* **2018**, 149, 204313.

(23) Lee, J. W.; Köckert, H.; Heathcote, D.; Popat, D.; Chapman, R.; Majchrzak, P.; Springate, E.; Vallance, C. **2019**, in preparation.

(24) Scoles, G., *Atomic and molecular beam methods*; Oxford University Press: New York, 1992.

(25) Chase, M. W. *J. Phys. Chem. Ref. Data* **1998**, 9, 1–1951.

(26) Moore, J. H.; Davis, C. C.; Coplan, M. A.; Greer, S. C., *Building Scientific Apparatus*; Cambridge University Press: Cambridge, 2009.

(27) Dietz, T. G.; Duncan, M. A.; Powers, D. E.; Smalley, R. E. *J. Chem. Phys.* **1981**, 74, 6511–6512.

(28) Bondybey, V. E.; English, J. H. *J. Chem. Phys.* **1981**, 74, 6978–6979.

(29) Deng, H. T.; Kerns, K. P.; Castleman, A. W. *J. Phys. Chem.* **1996**, 100, 13386–13392.

(30) Shen, M. H.; Winniczek, J. W.; Farrar, J. M. *J. Phys. Chem.* **1987**, 91, 6447–6449.

(31) Duncan, M. A. *Rev. Sci. Inst.* **2012**, 83, 041101.

(32) Hayes, T.; Bellert, D.; Buthelezi, T.; Brucat, P. *Chem. Phys. Lett.* **1998**, 287, 22–28.

(33) LaiHing, K.; Wheeler, R. G.; Wilson, W. L.; Duncan, M. A. *J. Chem. Phys.* **1987**, 87, 3401–3409.

(34) Brouard, M.; Vallance, C., *Tutorials in Molecular Reaction Dynamics*; The Royal Society of Chemistry: Cambridge, 2012.

(35) Levine, R. D., *Molecular Reaction Dynamics*; Cambridge University Press: Cambridge, 2005.

(36) Lee, Y. T. *Atomic and Molecular Beam Methods*; Oxford University Press: New York, 1988; Vol. 1.

(37) Zare, R.; Herschbach, D. *Proc. IEEE* **1963**, 51, 173–182.

(38) Zare, R. N. *Mol. Photochem.* **1972**, 4, 1–37.

(39) Porter, G. *Proc. R. Soc. A* **1950**, 200, 284–300.

(40) Tango, W. J.; Link, J. K.; Zare, R. N. *J. Chem. Phys.* **1968**, 49, 4264–4268.

(41) Geusic, J. E.; Hensel, M. L.; Smith, R. G. *Appl. Phys. Lett.* **1965**, 6, 175–177.

(42) Schnürer, M.; Cheng, Z.; Hentschel, M.; Tempea, G.; Kálmán, P.; Brabec, T.; Krausz, F. *Phys. Rev. Lett.* **1999**, 83, 722–725.

(43) Emma, P.; Akre, R.; Arthur, J.; Bionta, R.; Bostedt, C.; Bozek, J.; Brachmann, A.; Bucksbaum, P.; Coffee, R.; Decker, F.-J.; Ding, Y.; Dowell, D.; Edstrom, S.; Fisher, A.; Frisch, J.; Gilevich, S.; Hastings, J.; Hays, G.; Hering, P.; Huang, Z.; Iverson, R.; Loos, H.; Messerschmidt, M.; Miahnahri, A.; Moeller, S.; Nuhn, H.-D.; Pile, G.; Ratner, D.; Rzepiela, J.; Schultz, D.; Smith, T.; Stefan, P.; Tompkins, H.; Turner, J.; Welch, J.; White, W.; Wu, J.; Yocky, G.; Galayda, J. *Nat. Photonics* **2010**, 4, 641–647.

(44) Oepts, D.; van der Meer, A.; van Amersfoort, P. *Infrared Phys. Technol.* **1995**, 36, 297–308.

(45) Hargrove, L. E.; Fork, R. L.; Pollack, M. A. *Appl. Phys. Lett.* **1964**, 5, 4–5.

(46) Demtröder, W., *Laser Spectroscopy*, 4th ed.; Springer Verlag: Heidelberg, 2008; Vol. 2.

(47) Spence, D. E.; Kean, P. N.; Sibbett, W. *Opt. Lett.* **1991**, 16, 42.

(48) Kerr, J. *Philos. Mag.* **1875**, 50, 337–348.

(49) Laser Chart., Luxottica Exciton, https://exciton.luxottica.com/pub/media/luxexciton/laser-chart-graph.jpg, 25.05.2019.

(50) Demtröder, W., *Laser Spectroscopy*, 4th ed.; Springer Verlag: Heidelberg, 2008; Vol. 1.

(51) Hercher, M. *Appl. Opt.* **1969**, 8, 1103.

(52) Kulatilaka, W.; Anderson, T.; Lucht, R. *(CLEO). Conference on Lasers and Electro-Optics, 2005.* IEEE: Baltimore, MD, USA, 2005; Vol. 3, 1975–1977.

(53) Madey, J. M. J. *J. Appl. Phys.* **1971**, 42, 1906–1913.

(54) Kondratenko, A. M.; Saldin, E. L. *Part. Accel.* **1980**, 10, 207–216.

(55) Bonifacio, R.; Pellegrini, C.; Narducci, L. *Opt. Commun.* **1984**, 50, 373–378.

(56) Ackermann, W. et al. *Nat. Photonics* **2007**, 1, 336–342.

(57) McNeil, B. W. J.; Thompson, N. R. *Nat. Photonics* **2010**, 4, 814–821.

(58) Ullrich, J.; Rudenko, A.; Moshammer, R. *Annu. Rev. Phys. Chem.* **2012**, 63, 635–660.

(59) Frühling, U.; Wieland, M.; Gensch, M.; Gebert, T.; Schütte, B.; Krikunova, M.; Kalms, R.; Budzyn, F.; Grimm, O.; Rossbach, J.; Plönjes, E.; Drescher, M. *Nat. Photonics* **2009**, 3, 523–528.

(60) Weast, R. C., *Handbook of Chemistry and Physics*, 56th ed.; CRC Press: Cleveland, Ohio, 1976.

(61) Schmidt, P. C.; Schäfer, R., *Methods in Physical Chemistry*; John Wiley & Sons, Incorporated: Weinheim, 2012; 41-45.

(62) Keldysh, L. V. *Sov. Phys. JETP* **1965**, 20, 1307.

(63) DeWitt, M. J.; Levis, R. J. *J. Chem. Phys.* **1999**, 110, 11368–11375.

(64) Wiley, W. C.; McLaren, I. H. *Rev. Sci. Inst.* **1955**, 26, 1150–1157.

(65) Auerbach, D. J. *Atomic and Molecular Beam Methods*; Oxford University Press: New York, 1988; Vol. 1, 373.

(66) Hall, G. E.; Loo, R. O.; Harri, H.-P.; Sivakumar, N.; Chawla, G. K.; Houston, P. L.; Chandler, D. W.; Hepburn, J. W.; Burak, I. *Ber. Bunsen-Ges.* **1988**, 92, 281–288.

(67) Baldwin, D. P.; Buntine, M. A.; Chandler, D. W. *J. Chem. Phys.* **1990**, 93, 6578–6584.

(68) Whitaker, B. J. *Research in Chemical Kinetics*; Elsevier: Amsterdam, 1993, 307–346.

(69) Chandler, D. W.; Houston, P. L.; Parker, D. H. *J. Chem. Phys.* **2017**, 147, 013601.

(70) Suits, A. G. *Rev. Sci. Inst.* **2018**, 89, 111101.

(71) Garcia, G. A.; Nahon, L.; Powis, I. *Rev. Sci. Inst.* **2004**, 75, 4989–4996.

(72) Bordas, C.; Paulig, F.; Helm, H.; Huestis, D. L. *Rev. Sci. Inst.* **1996**, 67, 2257–2268.

(73) Abel, N. *J. reine angew. Math.* **1826**, 1826, 153–157.

(74) Whitaker, B. J., *Imaging in Molecular Dynamics*; Cambridge University Press: Cambridge, 2003.

(75) Dribinski, V.; Ossadtchi, A.; Mandelshtam, V. A.; Reisler, H. *Rev. Sci. Inst.* **2002**, 73, 2634–2642.

(76) Dick, B. *Phys. Chem. Chem. Phys.* **2014**, 16, 570–580.

(77) Gebhardt, C. R.; Rakitzis, T. P.; Samartzis, P. C.; Ladopoulos, V.; Kitsopoulos, T. N. *Rev. Sci. Inst.* **2001**, 72, 3848–3853.

(78) Townsend, D.; Minitti, M. P.; Suits, A. G. *Rev. Sci. Inst.* **2003**, 74, 2530–2539.

(79) Krems, M.; Zirbel, J.; Thomason, M.; DuBois, R. D. *Rev. Sci. Inst.* **2005**, 76, 093305.

(80) Lipciuc, M. L.; Buijs, J. B.; Janssen, M. H. M. *Phys. Chem. Chem. Phys.* **2006**, 8, 219–223.

(81) Tonokura, K.; Suzuki, T. *Chem. Phys. Lett.* **1994**, 224, 1–6.

(82) Ali, I.; Dörner, R.; Jagutzki, O.; Nüttgens, S.; Mergel, V.; Spielberger, L.; Khayyat, K.; Vogt, T.; Bräuning, H.; Ullmann, K.; Moshammer, R.; Ullrich, J.; Hagmann, S.; Groeneveld, K.-O.; Cocke, C.; Schmidt-Böcking, H. *Nucl. Instrum. Methods Phys. Res., Sect. B* **1999**, 149, 490–500.

(83) Frasinski, L. J. *J. Phys. B: At. Mol. Opt. Phys.* **2016**, 49, 152004.

(84) Frasinski, L. J.; Codling, K.; Hatherly, P. A. *Science* **1989**, 246, 1029–1031.

(85) Mikosch, J.; Patchkovskii, S. *J. Mod. Opt.* **2013**, 60, 1426–1438.

(86) Zhaunerchyk, V.; Frasinski, L. J.; Eland, J. H. D.; Feifel, R. *Phys. Rev. A* **2014**, 89, 053418.

(87) Slater, C. S.; Blake, S.; Brouard, M.; Lauer, A.; Vallance, C.; Bohun, C. S.; Christensen, L.; Nielsen, J. H.; Johansson, M. P.; Stapelfeldt, H. *Phys. Rev. A* **2015**, 91, 053424.

(88) Frasinski, L. J.; Zhaunerchyk, V.; Mucke, M.; Squibb, R. J.; Siano, M.; Eland, J. H. D.; Linusson, P.; v.d. Meulen, P.; Salén, P.; Thomas, R. D.; Larsson, M.; Foucar, L.; Ullrich, J.; Motomura, K.; Mondal, S.; Ueda, K.; Osipov, T.; Fang, L.; Murphy, B. F.; Berrah, N.; Bostedt, C.; Bozek, J. D.; Schorb, S.; Messerschmidt, M.; Glownia, J. M.; Cryan, J. P.; Coffee, R. N.; Takahashi, O.; Wada, S.; Piancastelli, M. N.; Richter, R.; Prince, K. C.; Feifel, R. *Phys. Rev. Lett.* **2013**, 111, 073002.

(89) Kornilov, O.; Eckstein, M.; Rosenblatt, M.; Schulz, C. P.; Motomura, K.; Rouzée, A.; Klei, J.; Foucar, L.; Siano, M.; Lübcke, A.; Schapper, F.; Johnsson, P.; Holland, D. M. P.; Schlathölter, T.; Marchenko, T.; Düsterer, S.; Ueda, K.; Vrakking, M. J. J.; Frasinski, L. J. *J. Phys. B: At. Mol. Opt. Phys.* **2013**, 46, 164028.

(90) Slater, C. S., *Studies of Photoinduced Molecular Dynamics Using a Fast Imaging Sensor*; Springer International Publishing: Cham, 2016.

(91) Christensen, L.; Nielsen, J. H.; Brandt, C. B.; Madsen, C. B.; Madsen, L. B.; Slater, C. S.; Lauer, A.; Brouard, M.; Johansson, M. P.; Shepperson, B.; Stapelfeldt, H. *Phys. Rev. Lett.* **2014**, 113, 073005.

(92) Amelio, G. F.; Tompsett, M. F.; Smith, G. E. *Bell Syst. Tech. J.* **1970**, 49, 593–600.

(93) Edmund Optics, Ltd, FLIR Flea 3 USB 3.0 Cameras, Product description, 2019.

(94) Nomerotski, A.; Brouard, M.; Campbell, E.; Clark, A.; Crooks, J.; Fopma, J.; John, J. J.; Johnsen, A. J.; Slater, C.; Turchetta, R.; Vallance, C.; Wilman, E.; Yuen, W. H. *J. Instrum.* **2010**, 5, C07007–C07007.

(95) Llopart, X.; Ballabriga, R.; Campbell, M.; Tlustos, L.; Wong, W. *Nucl. Instrum. Methods Phys. Res., Sect. A* **2007**, 581, 485–494.

(96) John, J. J.; Brouard, M.; Clark, A.; Crooks, J.; Halford, E.; Hill, L.; Lee, J. W. L.; Nomerotski, A.; Pisarczyk, R.; Sedgwick, I.; Slater, C. S.; Turchetta, R.; Vallance, C.; Wilman, E.; Winter, B.; Yuen, W. H. *J. Instrum.* **2012**, 7, C08001–C08001.

(97) Vallance, C.; Brouard, M.; Lauer, A.; Slater, C. S.; Halford, E.; Winter, B.; King, S. J.; Lee, J. W. L.; Pooley, D. E.; Sedgwick, I.; Turchetta, R.; Nomerotski, A.; John, J. J.; Hill, L. *Phys. Chem. Chem. Phys.* **2014**, 16, 383–395.

(98) Clark, A. T.; Crooks, J. P.; Sedgwick, I.; Turchetta, R.; Lee, J. W. L.; John, J. J.; Wilman, E. S.; Hill, L.; Halford, E.; Slater, C. S.; Winter, B.; Yuen, W. H.; Gardiner, S. H.; Lipciuc, M. L.; Brouard, M.; Nomerotski, A.; Vallance, C. *J. Phys. Chem. A* **2012**, 116, 10897–10903.

(99) Sauval, A. J. *Astron. Astrophys.* **1978**, 62, 295–298.

(100) Davis, D. N.; Keenan, P. C. *Publications of the Astronomical Society of the Pacific* **1969**, 81, 230.

(101) Balducci, G.; Gigli, G.; Guido, M. *Ber. Bunsen-Ges.* **1987**, 91, 635–641.

(102) Sievers, M. R.; Chen, Y.; Armentrout, P. B. *J. Chem. Phys.* **1996**, 105, 6322–6333.

(103) Dyke, J. M.; Ellis, A. M.; Fehėr, M.; Morris, A.; Paul, A. J.; Stevens, J. C. H. *J. Chem. Soc., Faraday Trans. 2* **1987**, 83, 1555–1565.

(104) Loock, H.-P.; Simard, B.; Wallin, S.; Linton, C. *J. Chem. Phys.* **1998**, 109, 8980–8992.

(105) Rayner, D. M.; Mitchell, S. A.; Bourne, O. L.; Hackett, P. A. *J. Opt. Soc. Am. B* **1987**, 4, 900.

(106) Parry, I. S.; Hermes, A. C.; Kartouzian, A.; Mackenzie, S. R. *Phys. Chem. Chem. Phys.* **2014**, 16, 458–466.

(107) Cooper, G. A.; Kartouzian, A.; Gentleman, A. S.; Iskra, A.; van Wijk, R.; Mackenzie, S. R. *J. Chem. Phys.* **2015**, 143, 124302.

(108) Cooper, G. A.; Gentleman, A. S.; Iskra, A.; Mackenzie, S. R. *J. Chem. Phys.* **2017**, 147, 013921.

(109) Gentleman, A. S.; Iskra, A.; Köckert, H.; Mackenzie, S. R. *Phys. Chem. Chem. Phys.* **2019**, 21, 15560–15567.

(110) Maner, J.; Mauney, D.; Duncan, M. *Chem. Phys. Lett.* **2017**, 671, 182–185.

(111) Johnston, M. D.; Pearson, W. L.; Wang, G.; Metz, R. B. *Rev. Sci. Inst.* **2018**, 89, 014102.

(112) Maner, J. A.; Mauney, D. T.; Duncan, M. A. *J. Phys. Chem. Lett.* **2015**, 6, 4493–4498.

(113) Johnston, M. D.; Lockwood, S. P.; Metz, R. B. *J. Chem. Phys.* **2018**, 148, 214308.

(114) Johnston, M. D.; Gentry, M. R.; Metz, R. B. *J. Phys. Chem. A* **2018**, 122, 8047–8053.

(115) Lessen, D. E.; Asher, R. L.; Brucat, P. J. *J. Chem. Phys.* **1991**, 95, 1414–1416.

(116) Citir, M.; Altinay, G.; Metz, R. B. *J. Phys. Chem. A* **2006**, 110, 5051–5057.

(117) Citir, M.; Metz, R. B. *J. Chem. Phys.* **2008**, 128, 024307.

(118) Wrede, E.; Laubach, S.; Schulenburg, S.; Brown, A.; Wouters, E. R.; Orr-Ewing, A. J.; Ashfold, M. N. R. *J. Chem. Phys.* **2001**, 114, 2629–2646.

(119) James, A. M.; Kowalczyk, P.; Langlois, E.; Campbell, M. D.; Ogawa, A.; Simard, B. *J. Chem. Phys.* **1994**, 101, 4485–4495.

(120) Saloman, E. B.; Kramida, A. *Astrophys. J., Suppl. Ser.* **2017**, 231, 18.

(121) Saloman, E. B.; Kramida, A. *Astrophys. J., Suppl. Ser.* **2019**, 240, 41.

(122) *Panther EX OPO and EX PLUS OPO Operation and Maintenance Manual*; Continuum: 2000.

(123) Datasheet - Cobra Dye Laser., Sirah Lasertechnik GmbH, 2019.

(124) Iskra, A. *Photofragmentation Studies of Metal Ion-Molecule Complexes and Metal Oxides*, DPhil thesis, Oxford: University of Oxford, 2017.

(125) Cheval, G.; Femenias, J.-L.; Merer, A.; Sassenberg, U. *J. Mol. Spectrosc.* **1988**, 131, 113–126.

(126) Kingston, C.; Liao, C.-K.; Merer, A.; Tang, S. *J. Mol. Spectrosc.* **2001**, 207, 104–112.

(127) Brom, J. M.; Durham, C. H.; Weltner, W. *J. Chem. Phys.* **1974**, 61, 970–981.

(128) Femenias, J.; Cheval, G.; Merer, A.; Sassenberg, U. *J. Mol. Spectrosc.* **1987**, 124, 348–368.

(129) Launila, O.; Schimmelpfennig, B.; Fagerli, H.; Gropen, O.; Taklif, A.; Wahlgren, U. *J. Mol. Spectrosc.* **1997**, 186, 131–143.

(130) Rao, V. R. *Indian J. Phys.* **1950**, 24, 35–49.

(131) Uhler, U. *Ark. Fys.* **1954**, 8, 265.

(132) Merer, A. J.; Sassenberg, U.; Féménias, J.; Cheval, G. *J. Chem. Phys.* **1987**, 86, 1219–1224.

(133) Adam, A. G.; Azuma, Y.; Barry, J. A.; Merer, A. J.; Sassenberg, U.; Schröder, J. O.; Cheval, G.; Féménias, J. L. *J. Chem. Phys.* **1994**, 100, 6240–6262.

(134) Herzberg, G., *Spectra of Diatomic Molecules*, 2nd ed.; Krieger Publishing Company: Malabar, FL, 1950; Vol. 1.

(135) Klynning, L.; Lindgren, B.; Aslund, N. *Ark. Fys.* **1965**, 30, 141.

(136) Martin, R. W.; Merer, A. J. *Canad. J. Phys.* **1973**, 51, 125–143.

(137) Carlson, R. C.; Bates, J. K.; Dunn, T. M. *J. Mol. Spectrosc.* **1985**, 110, 215–241.

(138) Western, C. PGOPHER version 10.1., 2018.

(139) Moore, C. E., *Atomic energy levels as derived from the analyses of optical spectra 24Cr to 41Nb*; National Bureau of Standards: Gaithersburg, MD, 1971; Vol. 2.

(140) Moore, C. E., *Tables of Spectra of Hydrogen, Carbon, Nitrogen, and Oxygen Atoms and Ions*; CRC Press: Boca Raton, FL, 1993; 339 pp.

(141) Sevy, A.; Matthew, D. J.; Morse, M. D. *J. Chem. Phys.* **2018**, 149, 044306.

(142) Bharate, N. S.; Kalkote, A. D.; Behare, S. H. *Indian J. Phys.* **1990**, 64, 228–231.

(143) Loh, S. K.; Lian, L.; Armentrout, P. B. *J. Am. Chem. Soc.* **1989**, 111, 3167–3176.

(144) Manura, D. J.; Dahl, D. D. Simion., version 8.1, 2013.

(145) Saloman, E. B.; Kramida, A. *Astrophys. J., Suppl. Ser.* **2017**, 231, 19.

(146) Sodupe, M.; Branchadell, V.; Rosi, M.; Bauschlicher, C. W. *J. Phys. Chem. A* **1997**, 101, 7854–7859.

(147) Lee, J. W. L. *Novel developments in time-of-flight particle imaging*, DPhil Thesis, University of Oxford, 2016.

(148) Zhao, A.; van Beuzekom, M.; Bouwens, B.; Byelov, D.; Chakaberia, I.; Cheng, C.; Maddox, E.; Nomerotski, A.; Svihra, P.; Visser, J.; Vrba, V.; Weinacht, T. *Rev. Sci. Instr.* **2017**, 88, 113104.

(149) Lee, S. J.; Bersohn, R. *J. Phys. Chem.* **1982**, 86, 728–730.

(150) Liu, K.; Zhao, H.; Wang, C.; Zhang, A.; Ma, S.; Li, Z. *J. Chem. Phys.* **2005**, 122, 044310.

(151) Liu, Y.-J.; Ajitha, D.; Krogh, J. W.; Tarnovsky, A. N.; Lindh, R. *ChemPhysChem* **2006**, 7, 955–963.

(152) Burt, M.; Boll, R.; Lee, J. W. L.; Amini, K.; Köckert, H.; Vallance, C.; Gentleman, A. S.; Mackenzie, S. R.; Bari, S.; Bomme, C.; Düsterer, S.; Erk, B.; Manschwetus, B.; Müller, E.; Rompotis, D.; Savelyev, E.; Schirmel, N.; Techert, S.; Treusch, R.; Küpper, J.; Trippel, S.; Wiese, J.; Stapelfeldt, H.; de Miranda, B. C.; Guillemin, R.; Ismail, I.; Journel, L.; Marchenko, T.; Palaudoux, J.; Penent, F.; Piancastelli, M. N.; Simon, M.; Travnikova, O.; Brausse, F.; Goldsztejn, G.; Rouzée, A.; Géléoc, M.; Geneaux, R.; Ruchon, T.; Underwood, J.; Holland, D. M. P.; Mereshchenko, A. S.; Olshin, P. K.; Johnsson, P.; Maclot, S.; Lahl, J.; Rudenko, A.; Ziaee, F.; Brouard, M.; Rolles, D. *Phys. Rev. A* **2017**, 96, 043415.

(153) Marggi Poullain, S.; Chicharro, D. V.; Navarro, E.; Rubio-Lago, L.; González-Vázquez, J.; Bañares, L. *Phys. Chem. Chem. Phys.* **2018**, 20, 3490–3503.

(154) Murillo-Sánchez, M. L.; Marggi Poullain, S.; Bajo, J. J.; Corrales, M. E.; González-Vázquez, J.; Solá, I. R.; Bañares, L. *Phys. Chem. Chem. Phys.* **2018**, 20, 20766–20778.

(155) Li, Q.-X.; Ran, Q.; Chen, C.-X.; Sheng, L.-S.; Yu, S.-Q.; Zhang, Y.-W.; Ma, X.-X. *Chem. J. Chin. Univ.* **1996**, 17, 268–272.

(156) Attar, A. R.; Piticco, L.; Leone, S. R. *J. Chem. Phys.* **2014**, 141, 164308.

(157) Erk, B.; Boll, R.; Trippel, S.; Anielski, D.; Foucar, L.; Rudek, B.; Epp, S. W.; Coffee, R.; Carron, S.; Schorb, S.; Ferguson, K. R.; Swiggers, M.; Bozek, J. D.; Simon, M.; Marchenko, T.; Kupper, J.; Schlichting, I.; Ullrich, J.; Bostedt, C.; Rolles, D.; Rudenko, A. *Science* **2014**, 345, 288–291.

(158) Boll, R.; Erk, B.; Coffee, R.; Trippel, S.; Kierspel, T.; Bomme, C.; Bozek, J. D.; Burkett, M.; Carron, S.; Ferguson, K. R.; Foucar, L.; Küpper, J.; Marchenko, T.; Miron, C.; Patanen, M.; Osipov, T.; Schorb, S.; Simon, M.; Swiggers, M.; Techert, S.; Ueda, K.; Bostedt, C.; Rolles, D.; Rudenko, A. *Struct. Dyn.* **2016**, 3, 043207.

(159) Amini, K.; Savelyev, E.; Brauße, F.; Berrah, N.; Bomme, C.; Brouard, M.; Burt, M.; Christensen, L.; Düsterer, S.; Erk, B.; Höppner, H.; Kierspel, T.; Krecinic, F.; Lauer, A.; Lee, J. W. L.; Müller, M.; Müller, E.; Mullins, T.; Redlin, H.; Schirmel, N.; Thøgersen, J.; Techert, S.; Toleikis, S.; Treusch, R.; Trippel, S.; Ulmer, A.; Vallance, C.; Wiese, J.; Johnsson, P.; Küpper, J.; Rudenko, A.; Rouzée, A.; Stapelfeldt, H.; Rolles, D.; Boll, R. *Struct. Dyn.* **2018**, 5, 014301.

(160) Erk, B.; Müller, J. P.; Bomme, C.; Boll, R.; Brenner, G.; Chapman, H. N.; Correa, J.; Düsterer, S.; Dziarzhytski, S.; Eisebitt, S.; Graafsma, H.; Grunewald, S.; Gumprecht, L.; Hartmann, R.; Hauser, G.; Keitel, B.; von Korff Schmising, C.; Kuhlmann, M.; Manschwetus, B.; Mercadier, L.; Müller, E.; Passow, C.; Plönjes, E.; Ramm, D.; Rompotis, D.; Rudenko, A.; Rupp, D.; Sauppe, M.; Siewert, F.; Schlosser, D.; Strüder, L.; Swiderski, A.; Techert, S.; Tiedtke, K.; Tilp, T.; Treusch, R.; Schlichting, I.; Ullrich, J.; Moshammer, R.; Möller, T.; Rolles, D. *J. Synchrotron Radiat.* **2018**, 25, 1529–1540.

(161) Savelyev, E.; Boll, R.; Bomme, C.; Schirmel, N.; Redlin, H.; Erk, B.; Düsterer, S.; Müller, E.; Höppner, H.; Toleikis, S.; Müller, J.; Kristin Czwalinna, M.; Treusch, R.; Kierspel, T.; Mullins, T.; Trippel, S.; Wiese, J.; Küpper, J.; Braue, F.; Krecinic, F.; Rouzée, A.; Rudawski, P.; Johnsson, P.; Amini, K.; Lauer, A.; Burt, M.; Brouard, M.; Christensen, L.; Thøgersen, J.; Stapelfeldt, H.; Berrah, N.; Müller, M.; Ulmer, A.; Techert, S.; Rudenko, A.; Rolles, D. *New J. Phys.* **2017**, 19, 043009.

(162) Tiedtke, K.; Feldhaus, J.; Hahn, U.; Jastrow, U.; Nunez, T.; Tschentscher, T.; Bobashev, S. V.; Sorokin, A. A.; Hastings, J. B.; Möller, S.; Cibik, L.; Gottwald, A.; Hoehl, A.; Kroth, U.; Krumrey, M.; Schöppe, H.; Ulm, G.; Richter, M. *J. Appl. Phys.* **2008**, 103, 094511.

(163) Schulz, S.; Grguraš, I.; Behrens, C.; Bromberger, H.; Costello, J. T.; Czwalinna, M. K.; Felber, M.; Hoffmann, M. C.; Ilchen, M.; Liu, H. Y.; Mazza, T.; Meyer, M.; Pfeiffer, S.; Predki, P.; Schefer, S.; Schmidt, C.; Wegner, U.; Schlarb, H.; Cavalieri, A. L. *Nat. Commun.* **2015**, 6, 5938.

(164) Gibson, S.; Danhickstein; Yurchak, R.; Dhrubajyoti Das; Shih, G.; Furii; Ellisje624; PhantomYuan Pyabel 0.7.6., 2017.

(165) Amini, K. *Studies of ultrafast molecular photofragmentation and dynamics using fast imaging sensors*, DPhil thesis, Oxford: University of Oxford, Merton College, 2017.

(166) Gahl, C.; Azima, A.; Beye, M.; Deppe, M.; Döbrich, K.; Hasslinger, U.; Hennies, F.; Melnikov, A.; Nagasono, M.; Pietzsch, A.; Wolf, M.; Wurth, W.; Föhlisch, A. *Nat. Photonics* **2008**, 2, 165–169.

(167) Eckert, S.; Beye, M.; Pietzsch, A.; Quevedo, W.; Hantschmann, M.; Ochmann, M.; Ross, M.; Minitti, M. P.; Turner, J. J.; Moeller, S. P.; Schlotter, W. F.; Dakovski, G. L.; Khalil, M.; Huse, N.; Föhlisch, A. *Appl. Phys. Lett.* **2015**, 106, 061104.

(168) Braußе, F.; Goldsztejn, G.; Amini, K.; Boll, R.; Bari, S.; Bomme, C.; Brouard, M.; Burt, M.; de Miranda, B. C.; Düsterer, S.; Erk, B.; Géléoc, M.; Geneaux, R.; Gentleman, A. S.; Guillemin, R.; Ismail, I.; Johnsson, P.; Journel, L.; Kierspel, T.; Köckert, H.; Küpper, J.; Lablanquie, P.; Lahl, J.; Lee, J. W. L.; Mackenzie, S. R.; Maclot, S.; Manschwetus, B.; Mereshchenko, A. S.; Mullins, T.; Olshin, P. K.; Palaudoux, J.; Patchkovskii, S.; Penent, F.; Piancastelli, M. N.; Rompotis, D.; Ruchon, T.; Rudenko, A.; Savelyev, E.; Schirmel, N.; Techert, S.; Travnikova, O.; Trippel, S.; Underwood, J. G.; Vallance, C.; Wiese, J.; Simon, M.; Holland, D. M. P.; Marchenko, T.; Rouzée, A.; Rolles, D. *Phys. Rev. A* **2018**, 97, DOI: 10.1103/PhysRevA.97.043429.

(169) Bozek, J. D. *Eur. Phys. J.: Spec. Top.* **2009**, 169, 129–132.

(170) Sorokin, A. A.; Wellhöfer, M.; Bobashev, S. V.; Tiedtke, K.; Richter, M. *Phys. Rev. A* **2007**, 75, 051402.

(171) Erk, B.; Rolles, D.; Foucar, L.; Rudek, B.; Epp, S. W.; Cryle, M.; Bostedt, C.; Schorb, S.; Bozek, J.; Rouzee, A.; Hundertmark, A.; Marchenko, T.; Simon, M.; Filsinger, F.; Christensen, L.; De, S.; Trippel, S.; Küpper, J.; Stapelfeldt, H.; Wada, S.; Ueda, K.; Swiggers, M.; Messerschmidt, M.; Schröter, C. D.; Moshammer, R.; Schlichting, I.; Ullrich, J.; Rudenko, A. *Phys. Rev. Lett.* **2013**, 110, 053003.

(172) Rudenko, A.; Inhester, L.; Hanasaki, K.; Li, X.; Robatjazi, S. J.; Erk, B.; Boll, R.; Toyota, K.; Hao, Y.; Vendrell, O.; Bomme, C.; Savelyev, E.; Rudek, B.; Foucar, L.; Southworth, S. H.; Lehmann, C. S.; Kraessig, B.; Marchenko, T.; Simon, M.; Ueda, K.; Ferguson, K. R.; Bucher, M.; Gorkhover, T.; Carron, S.; Alonso-Mori, R.; Koglin, J. E.; Correa, J.; Williams, G. J.; Boutet, S.; Young, L.; Bostedt, C.; Son, S.-K.; Santra, R.; Rolles, D. *Nature* **2017**, 546, 129–132.

(173) Olney, T. N.; Cooper, G.; Fat Chan, W.; Burton, G. R.; Brion, C.; Tan, K. *Chem. Phys.* **1997**, 218, 127–149.

(174) Olney, T. N.; Cooper, G.; Brion, C. *Chem. Phys.* **1998**, 232, 211–237.

(175) Yeh, J.; Lindau, I. *At. Data Nucl. Data Tables* **1985**, 32, 1–155.

(176) Atkins, P.; de Paula, J., *Physical Chemistry*, 10th ed.; Oxford University Press: Oxford, 2014; 43 pp.

(177) Mohr, P. **1994**, dataset, DOI: `10.18434/T4WW24`.

(178) Bailleux, S.; Duflot, D.; Taniguchi, K.; Sakai, S.; Ozeki, H.; Okabayashi, T.; Bailey, W. C. *J. Phys. Chem. A* **2014**, 118, 11744–11750.

(179) Papula, L., *Mathematische Formelsammlung*, 10th ed.; Vieweg + Teubner: Wiesbaden, 2009.

(180) Dunford, R. W.; Southworth, S. H.; Ray, D.; Kanter, E. P.; Krässig, B.; Young, L.; Arms, D. A.; Dufresne, E. M.; Walko, D. A.; Vendrell, O.; Son, S.-K.; Santra, R. *Phys. Rev. A* **2012**, 86, 033401.

(181) Lee, M.; Kim, H.; Lee, Y. S.; Kim, M. S. *J. Chem. Phys.* **2005**, 123, 024310.

(182) Becker, U.; Szostak, D.; Kerkhoff, H. G.; Kupsch, M.; Langer, B.; Wehlitz, R.; Yagishita, A.; Hayaishi, T. *Phys. Rev. A* **1989**, 39, 3902–3911.

(183) Ryufuku, H.; Sasaki, K.; Watanabe, T. *Phys. Rev. A* **1980**, 21, 745–750.

(184) Niehaus, A. *J. Phys. B: At. Mol. Phys.* **1986**, 19, 2925–2937.

(185) Frenking, G.; Fau, S.; Marchand, C. M.; Grützmacher, H. *J. Am. Chem. Soc.* **1997**, 119, 6648–6655.

(186) Li, Z.; Francisco, J. S. *J. Chem. Phys.* **1999**, 110, 817–822.

(187) Bailleux, S.; Dréan, P.; Zelinger, Z.; Godon, M. *J. Mol. Spectrosc.* **2005**, 229, 140–144.

(188) Li, Y.; Francisco, J. S. *J. Chem. Phys.* **2001**, 114, 2879–2882.

(189) Ozeki, H.; Okabayashi, T.; Tanimoto, M.; Saito, S.; Bailleux, S. *J. Chem. Phys.* **2007**, 127, 224301.

(190) Dunning, T. H. *J. Chem. Phys.* **1989**, 90, 1007–1023.

(191) Wilson, A. K.; Woon, D. E.; Peterson, K. A.; Dunning, T. H. *J. Chem. Phys.* **1999**, 110, 7667–7676.

(192) Kendall, R. A.; Dunning, T. H.; Harrison, R. J. *J. Chem. Phys.* **1992**, 96, 6796–6806.

(193) Andrews, L.; Dyke, J. M.; Jonathan, N.; Keddar, N.; Morris, A. *J. Phys. Chem.* **1984**, 88, 1950–1954.

(194) Frisch, M. J.; Trucks, G. W.; Schlegel, H. B.; Scuseria, G. E.; Robb, M. A.; Cheeseman, J. R.; Scalmani, G.; Barone, V.; Petersson, G. A.; Nakatsuji, H.; Li, X.; Caricato, M.; Marenich, A. V.; Bloino, J.; Janesko, B. G.; Gomperts, R.; Mennucci, B.; Hratchian, H. P.; Ortiz, J. V.; Izmaylov, A. F.; Sonnenberg, J. L.; Williams-Young, D.; Ding, F.; Lipparini, F.; Egidi, F.; Goings, J.; Peng, B.; Petrone, A.; Henderson, T.; Ranasinghe, D.; Zakrzewski, V. G.; Gao, J.; Rega, N.; Zheng, G.; Liang, W.; Hada, M.; Ehara, M.; Toyota, K.; Fukuda, R.; Hasegawa, J.; Ishida, M.; Nakajima, T.; Honda, Y.; Kitao, O.; Nakai, H.; Vreven, T.; Throssell, K.; Montgomery Jr., J. A.; Peralta, J. E.; Ogliaro, F.; Bearpark, M. J.; Heyd, J. J.; Brothers, E. N.; Kudin, K. N.; Staroverov, V. N.; Keith, T. A.; Kobayashi, R.; Normand, J.; Raghavachari, K.; Rendell, A. P.; Burant, J. C.; Iyengar, S. S.; Tomasi, J.; Cossi, M.; Millam, J. M.; Klene, M.; Adamo, C.; Cammi, R.; Ochterski, J. W.; Martin, R. L.; Morokuma, K.; Farkas, O.; Foresman, J. B.; Fox, D. J., *Gaussian09 Revision D.01*; Gaussian Inc.: Wallingford CT, 2013.

(195) Murillo-Sánchez, M. L.; Marggi Poullain, S.; Bajo, J. J.; Corrales, M. E.; González-Vázquez, J.; Solá, I. R.; Bañares, L. **2018**, private communication.

(196) Stapelfeldt, H.; Constant, E.; Corkum, P. B. *Phys. Rev. Lett.* **1995**, 74, 3780–3783.

(197) Christophorou, L. G.; Olthoff, J. K. *Appl. Surf. Sci.* **2002**, 192, 309–326.

(198) Laube, J. C.; Hogan, C.; Newland, M. J.; Mani, F. S.; Fraser, P. J.; Brenninkmeijer, C. A. M.; Martinerie, P.; Oram, D. E.; Röckmann, T.; Schwander, J.; Witrant, E.; Mills, G. P.; Reeves, C. E.; Sturges, W. T. *Atmos. Chem. Phys.* **2012**, 12, 4081–4090.

(199) Mühle, J.; Ganesan, A. L.; Miller, B. R.; Salameh, P. K.; Harth, C. M.; Greally, B. R.; Rigby, M.; Porter, L. W.; Steele, L. P.; Trudinger, C. M.; Krummel, P. B.; O'Doherty, S.; Fraser, P. J.; Simmonds, P. G.; Prinn, R. G.; Weiss, R. F. *Atmos. Chem. Phys.* **2010**, 10, 5145–5164.

(200) Todd, J. F. J. *Pure Appl. Chem.* **1991**, 63, 1541–1566.

(201) Ekman, R., *Mass spectrometry: instrumentation, interpretation, and applications*; John Wiley & Sons: Hoboken, N.J, 2009; 371 pp.

(202) Müller, A. *Advances In Atomic, Molecular, and Optical Physics*; Elsevier: 2008; Vol. 55, 293–417.

(203) Powis, I.; Dutuit, O.; Richard-Viard, M.; Guyon, P. M. *J. Chem. Phys.* **1990**, 92, 1643–1652.

(204) Gek Low, K.; Hampton, P. D.; Powis, I. *Chem. Phys.* **1985**, 100, 401–413.

(205) Roeterdink, W. G.; Janssen, M. H. M. *Phys. Chem. Chem. Phys.* **2002**, 4, 601–612.

(206) Yates, B. W.; Tan, K. H.; Bancroft, G. M.; Tse, J. S. *J. Chem. Phys.* **1986**, 85, 3840–3850.

(207) Downie, P.; Powis, I. *Faraday Disc.* **2000**, 115, 103–117.

(208) Eland, J. H. D.; Feifel, R.; Hochlaf, M. *J. Chem. Phys.* **2008**, 128, 234303.

(209) Christophorou, L. G.; Olthoff, J. K. *J. Phys. Chem. Ref. Data* **2000**, 29, 553–569.

(210) Bull, J. N.; Bart, M.; Vallance, C.; Harland, P. W. *Phys. Rev. A* **2013**, 88, 062710.

(211) Rosenstock, H. M.; Wallenstein, M. B.; Wahrhaftig, A. L.; Eyring, H. *Proc. Natl. Acad. Sci. USA* **1952**, 38, 667.

(212) Stockbauer, R. *J. Chem. Phys.* **1973**, 58, 3800–3815.

(213) Prasil, Z.; Forst, W. *J. Phys. Chem.* **1967**, 71, 3166–3177.

(214) Simm, I. G.; Danby, C. J.; Eland, J. H. D.; Mansell, P. I. *J. Chem. Soc., Faraday Trans. 2* **1976**, 72, 426.

(215) Simm, I.; Danby, C.; Eland, J. *Int. J. Mass Spectrom. Ion Phys.* **1974**, 14, 285–293.

(216) Inghram, M. G.; Hanson, G. R.; Stockbauer, R. *Int. J. Mass Spectrom. Ion Phys.* **1980**, 33, 253–261.

(217) Lifshitz, C.; Long, F. A. *J. Phys. Chem.* **1965**, 69, 3746–3751.

(218) Busch, G. E.; Wilson, K. R. *J. Chem. Phys.* **1972**, 56, 3626–3638.

(219) Riley, S. J.; Wilson, K. R. *Faraday Discuss. Chem. Soc.* **1972**, 53, 132.

(220) Mitchell, R. C.; Simons, J. P. *Discuss. Faraday Soc.* **1967**, 44, 208.

(221) Köckert, H.; Heathcote, D.; Lee, J. W. L.; Zhou, W.; Richardson, V.; Vallance, C. *Phys. Chem. Chem. Phys.* **2019**, 21, 14296–14305.

(222) Bull, J. N.; Lee, J. W. L.; Vallance, C. *Phys. Rev. A* **2015**, 91, 022704.

(223) Winter, B.; King, S. J.; Brouard, M.; Vallance, C. *Rev. Sci. Inst.* **2014**, 85, 023306.

(224) Newville, M.; Stensitzki, T.; Allen, D. B.; Ingargiola, A. LMFIT: Non-Linear Least-Square Minimization and Curve-Fitting for Python., version 0.8.0, 2014.

(225) Linstrom, P. NIST Chemistry WebBook, NIST Standard Reference Database 69., dataset, 1997.

(226) Dibeler, V. H.; Reese, R. M.; Mohler, F. L. *J. Res. Natl. Bur. Stan.* **1956**, 57, 113.

(227) Marriott, J.; Crauus, J. D. *J. Electronics* **1956**, 1, 405–420.

(228) Dorman, F. H. *J. Phys. Chem.* **1964**, 41, 2857–2859.

(229) Berry, C. E. *Phys. Rev.* **1950**, 78, 597–605.

(230) Walters, S. W.; Whiffen, D. H. *J. Chem. Soc., Faraday Trans. 2* **1983**, 79, 941.

(231) Cox, A. P.; Duxbury, G.; Hardy, J. A.; Kawashima, Y. *J. Chem. Soc., Faraday Trans. 2* **1980**, 76, 339.

(232) Bruce, M. R.; Bonham, R. A. *Z. Phys. D.* **1992**, 24, 149–154.

(233) Bruce, M.; Bonham, R. *Int. J. Mass Spectrom. Ion Process.* **1993**, 123, 97–100.

(234) Bruce, M. R.; Mi, L.; Sporleder, C. R.; Bonham, R. A. *J. Phys. B: At. Mol. Opt. Phys.* **1994**, 27, 5773–5794.

(235) Mi, L.; Sporleder, C.; Bonham, R. *Chem. Phys. Lett.* **1996**, 251, 252–258.

(236) Aguirre, F.; Pratt, S. T. *J. Chem. Phys.* **2003**, 119, 9476–9485.

(237) Aguirre, F.; Pratt, S. T. *J. Chem. Phys.* **2003**, 118, 6318–6326.

(238) Zhou, W. *Ionization and fragmentation dynamics of singly and multiply charged ions*, DPhil thesis, Oxford: University of Oxford, Exeter College, 2018.

(239) Hutchins, D.; Dewhurst, R.; Palmer, S.; Scruby, C. *Appl. Phys. Lett.* **1981**, 38, 677–679.

(240) Pérez, J.; Ramırez-Arizmendi, L. E.; Petzold, C. J.; Guler, L. P.; Nelson, E. D.; Kenttämaa, H. I. *Int. J. Mass Spectrom.* **2000**, 198, 173–188.

(241) Lee, J. W. L. PImMS Software Documentation v1.8., project internal document Oxford, 2011.

(242) Henke, B.; Gullikson, E.; Davis, J. *At. Data Nucl. Data Tables* **1993**, 54, 181–342.

(243) Keitel, B. **2019**, private communication.

Appendix A

Integration of the PImMS sensor at the FLASH1 beamline

The PImMS sensor and the acquisition software have been integrated into the CAMP instrument by Jason W.L. Lee in cooperation with the FLASH team. The PImMS camera sensor was used in the context of this work and is not permanently installed at the beam-line. Instruments which are permanently installed are integrated directly into the beam-line diagnostics system. Hence, data acquired at the CAMP end-station and by diagnostics tools in the beam-line are directly associated with the unique FEL shot ID. Opposed to that, the camera is receiving its trigger signal from the master-oscillator and a personal computer with the acquisition software [241] was used to receive the FEL shot ID of the experimental cycle and assign it to the acquired data. The integration of the PImMS sensor outside of the DAQ system led to problems with the unique assignment of PImMS camera frames to shot IDs. This section discusses the origin of these assignment problems, the applied corrections in the data analysis and the changes that have been implemented for future experiments.

Figure A.1 shows the integration of the PImMS camera-sensor with the CAMP instrument. At the start of each acquisition cycle the "Master oscillator" triggers the free-electron laser generation, the DAQ diagnostics system and starts the PImMS acquisition cycle (indicated with blue arrows in Figure A.1). Secondly, shown as orange

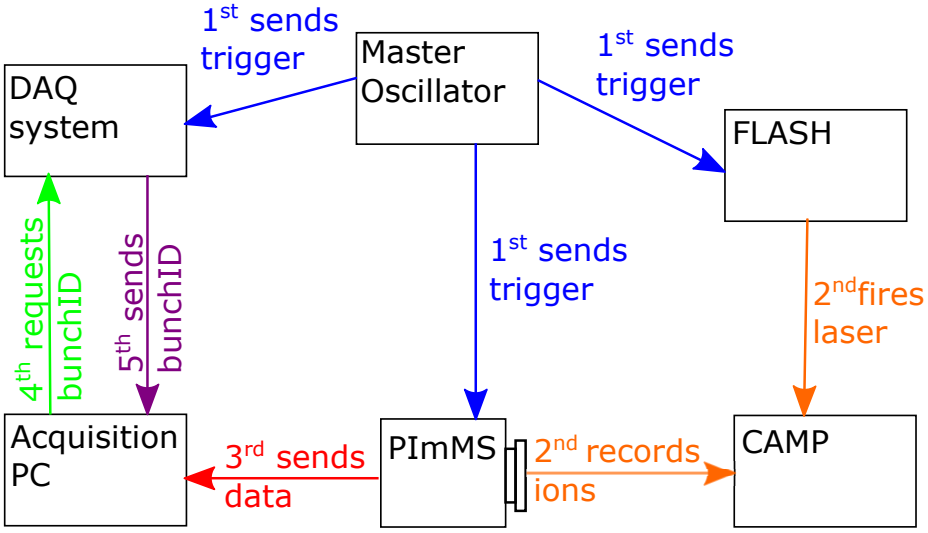


Figure A.1: Schematic acquisition cycle of the PImMS sensor at the CAMP instrument. The master oscillator triggers the free-electron laser FLASH, the PImMS camera sensor and the beam-line DAQ system (blue arrows), the camera records data (orange arrows) and sends a data package to a computer in the FLASH hall (red arrow), a shot ID of the current experimental cycle is requested from the DAQ system (green arrow) and the data is written to the hard-drive once the shot ID is received (purple arrow).

arrows, the EUV laser pulse is generated and the PImMS camera records ion signals generated in the CAMP instrument. At this point, the DAQ system also assigns a new shot ID and records parameters characterising the operation of the beam-line. Upon completion of the camera acquisition cycle, the PImMS camera sends the camera frame data to a computer handling the PImMS acquisition software [241] (red arrow). Once the data is received, the PC requests the shot ID from the DAQ system (green arrow). Finally in the fifth step (purple arrow), the DAQ system sends the shot ID to the acquisition software and the data is written to the hard-drive. Here, the shot ID replaces the frame number, usually written out by the software for application in conventional laboratories.

The experimental cycle is repeated at 10 Hz and the cycle has to be completed within < 100 ms to avoid overlap with the subsequent experimental cycle. However,

the duration of the data transfer in step 3 and the handling of the shot ID request by the DAQ system between step 4 and 5 may fluctuate. With increasing number of ions recorded by the PImMS sensor in a single frame, the read-out from chip and transfer of the data may exceed the available time before the DAQ system receives the trigger for the following acquisition cycle. In this case, a wrong shot ID is stored in the PImMS data file. The mismatch between PImMS frames and the unique shot IDs, leads to a poor correlation between beam-line diagnostics parameters such as electron-bunch arrival times or EUV pulse intensities to signal recorded by the PImMS camera sensor. Furthermore, the assignment of a PImMS data package with the subsequent shot ID can lead to two camera frames bearing the same shot ID.

In context of this work, the mismatch between the PImMS camera frame and the shot ID is corrected in two steps. At first, camera frames which have the same shot ID are reassigned. Next, camera frames are adjusted to FEL shot IDs in chunks of 50 frames by shifting the shot IDs and comparing the correlation of ion signal to FEL pulse energy.

Figure A.2 shows two-dimensional histograms of the ion count per frame as a function of the FEL pulse energy for the different stages of the correlation correction. The example shown here is taken from a UV/XUV delay scan at a photon wavelength of $\lambda = 18.6\,\mathrm{nm}$ with about 22500 frames. The histogram of the raw data in (a) shows two distinct features, one with an average of 40 ions per frame at a pulse energy of $60\,\mu\mathrm{J}$ and one having twice the ion signal at a comparable pulse energy. As described above, the latter feature corresponds to two frames which got assigned the same shot ID, thus seemingly doubling the ion counts for this shot ID. These frames can easily be identified as they contain more then the four camera registers which are saved for each active pixel (see Section 1.2.7). Furthermore, the assignment of two frames to

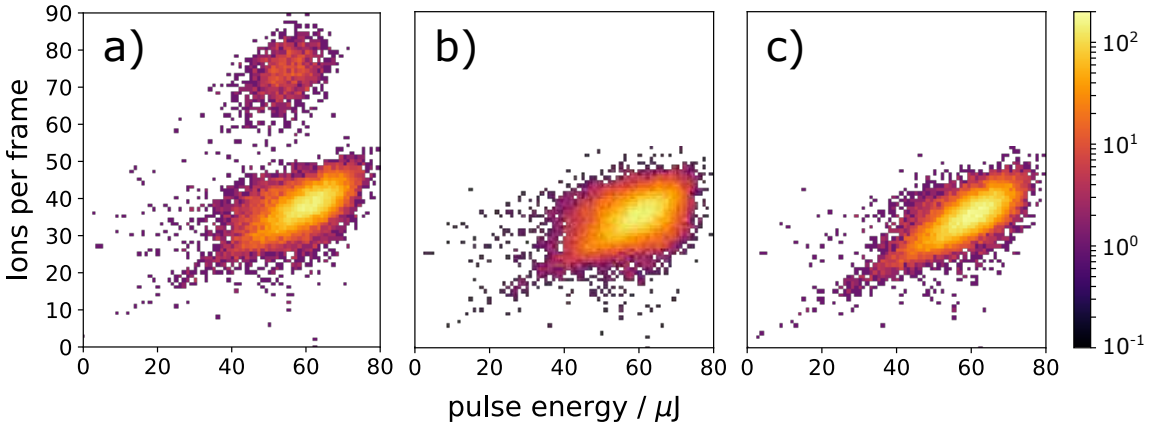


Figure A.2: Improvement of the correlation between total ion signal recorded with the PImMS sensor and the FEL pulse energy to correct for the mismatch between PImMS frames and FEL shot IDs; the raw data (a) contains cases where FEL shot IDs are assigned to multiple PImMS camera frames, forming a distinct feature with about 80 ions at 60 μJ; (b) shows the result of the rearrangement; the remaining mismatch is corrected in (c) by altering the shot ID of 50 frames at a time and testing the correlation between signal intensity and pulse energy by comparing the residuals of linear fits to the results.

a single shot ID creates a preceding shot ID without an attached camera frame. To correct for the double assignment, the misreferenced frame is assigned to a previously unassigned shot ID. In cases where this unassigned shot ID is not directly preceding the doubly assigned ID, it is assumed that the misreference has brought a series of frames out of synchronisation and camera frames are collectively assigned backwards towards the next unassigned shot ID. In the example shown in Figure A.2 about 10% of the dataset had to be reassigned. The result is shown in (b). Here, the two features from (a) have merged but the histogram still shows a portion of uncorrelated frames that overlap with a feature of linear correlation between signal and pulse energy.

From panel (b) it can be seen that the total ion signal is approximately proportional to the pulse energy, for these experimental conditions. The correlation between shot ID and camera frames is mostly restored. To further improve the correlation, the data-set is split into chunks of 50 camera frames. For each of these chunks the

original shot ID assignment is compared to a reassignment of the entire chunk towards the preceding shot ID. The configuration yielding an improved correlation between ion signal and EUV pulse energy is carried forward into the final data set. A better correlation is given for smaller residuals of a least square fit to a linear function of the form:

$$I(P) = m \cdot P + I(P = 0) \tag{A.1}$$

Here, I is the ion count per frame and P is the pulse energy. As the reassignment of frames, depending on their correlation, will inevitably lead to double-assignments of frames to single shot IDs at the edges of the shifted chunks, overlapping shot IDs of shifted chunks are omitted from the dataset. This leads to an overall loss of about 1% of frames in this example. The result of both correction steps, are shown, in panel c). It can be seen that the double assignment of frames to shot IDs is resolved and the correlation between signal and FEL pulse energy is largely enhanced.

The mismatch between the PImMS camera frames and the shot IDs is a result of the response jitter of the DAQ server and the time-delay in the data transfer from the PImMS sensor to the acquisition PC. For future experiments with PImMS at this beam-line this has been solved in a two-step approach. Firstly, an auxiliary server has been introduced into the DAQ network for the communication with PImMS which presents the shot ID to PImMS upon request more rapidly and with largely reduced response jitter. Secondly, each camera frame is assigned a unique marker before it is transferred to the acquisition PC. This marker is iterated with the master oscillator and allows for an unambiguous reconstruction of the frame to shot ID assignment if either device gets out of synchronisation. These changes have been implemented in later experiments and have proven to yield reliable assignments between the PImMS camera frame and the shot ID.

Appendix B

Calculation of XUV photon numbers

In Section 3.4.1 XUV fragmentation of CH_2BrI is compared for different photon energies. In order to quantitatively compare data sets acquired at different XUV photon energies, total ion yields are normalized to the photon number of each free-electron laser (FEL) shot. The gas-monitor detector (GMD) is used to measure the shot-to-shot intensity of the FEL as delivered from the undulator. The number of photons in each laser pulse N_{Photon} can be derived by comparing the measured pulse intensity I to the energy of a single photon E_{Photon}.

$$N_{\mathrm{Photon}} = \frac{I[\mathrm{J}]}{E_{\mathrm{Photon}}[\mathrm{J}]} \tag{B.1}$$

The photon energy is given by the Planck equation:

$$E_{\mathrm{Photon}} = \frac{hc}{\lambda} \tag{B.2}$$

Here, $h = 6.626 \cdot 10^{-34}\,\mathrm{Js}$ [177] is the Planck constant, $c = 2.99 \cdot 10^{8}\,\mathrm{ms}^{-1}$ [177] is the speed of light in vacuum and λ is the XUV wavelength. The spectrum of the XUV pulse is measured while the FEL laser beam is set up for a new output wavelength.

The spectrum of an FEL pulse varies from shot-to-shot because of the stochastic nature of the SASE process, and the averaged spectrum will therefore not show

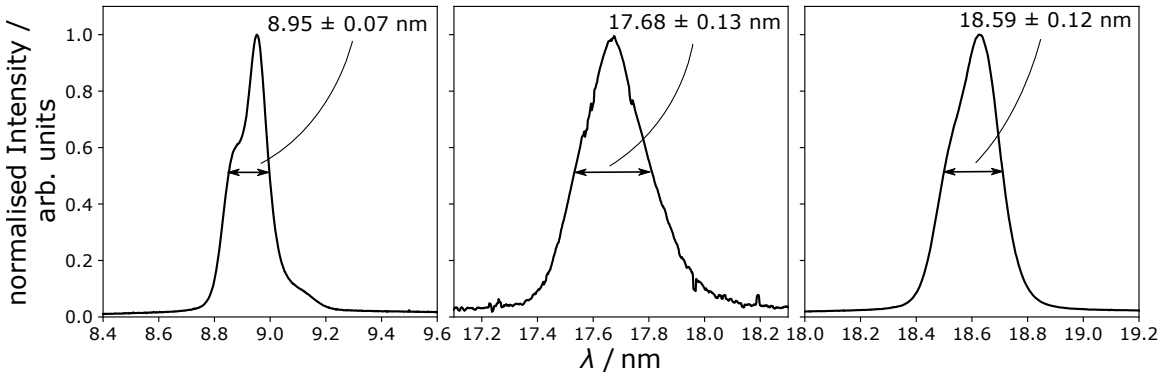


Figure B.1: Wavelength spectra of free-electron laser pulses used in this work. The central wavelength and the full-width at half maximum is given for each distribution; the spectra are normalized to a maximum of 1.0.

a normal distribution. The pulse spectra are shown in Figure B.1 and the central wavelengths of the XUV pulses are measured as weighted means of each distribution: $8.95 \pm 0.07\,\mathrm{nm}$, $17.68 \pm 0.13\,\mathrm{nm}$ and $18.59 \pm 0.12\,\mathrm{nm}$. Using Equation (B.2), photon energies of $138.5 \pm 1.1\,\mathrm{eV}$, $70.1 \pm 0.5\,\mathrm{eV}$ and $66.7 \pm 0.4\,\mathrm{eV}$ are derived.

Along the beam path to the CAMP instrument, part of the XUV pulse intensity is absorbed at the beam-line mirrors and filter elements given by the transmission of the beam-line T_{BL} and the two exchangeable filters T_{filter1} and T_{filter2}.

$$N_{\mathrm{Photon}} = \frac{I[\mathrm{J}]}{E_{\mathrm{Photon}}[\mathrm{J}]} \cdot T_{\mathrm{BL}} \cdot T_{\mathrm{filter1}} \cdot T_{\mathrm{filter2}} \tag{B.3}$$

The transmission of the beamline has been calculated and measured by Erk *et al.* [160]. The calculated transmission values are based on theoretical reflectivities [242] of the carbon coated mirrors in the beam-line. As can be seen in Figure B.2 the calculated transmissions agree well with two measurements of the beam-line transmission shown here as orange diamonds. To this purpose, the authors compared the intensity of free-electron laser pulses delivered from the undulator and behind the CAMP apparatus. The original intensity has been measured with a gas-monitor detector at the front of the beam-line and a second mobile GMD was used to measure the intensity

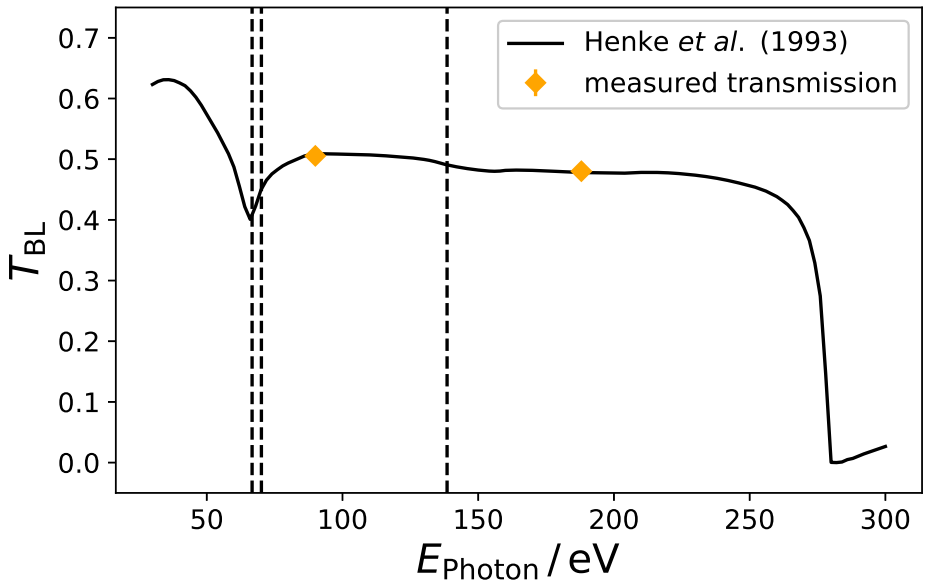


Figure B.2: Transmission of the beamline, T_{BL}, calculated based on values from Reference [242] (black line) in comparison with measured transmissions by Erk *et al.* [160] (orange diamonds). The dashed lines indicate the wavelengths used in the context of this work.

behind the CAMP instrument. Because of the good agreement between calculated and measured values, the beam-line transmission T_{BL} from the tabulated theoretical values [242] can be regarded as good estimate. The vertical lines in Figure B.2 indicate the photon energies used in this work.

The FEL beam can be attenuated with up to two transmission filters. Circular films of silicon, niobium, aluminium and zirconium with different thicknesses are mounted in two wheels which allow for easy exchange of the filters. In the context of this work, 420 nm thick silicon, 297 nm thick zirconium and 400 nm thick niobium filters have been used. Figure B.3 shows tabulated theoretical transmission values [242] in comparison with transmissions measured at the synchrotron BESSY2 at the *Physikalisch-Technische Bundesanstalt* (PTB), Berlin [243]. Here, the silicon and zirconium filters transmissions have been measured for 221.9 nm and 287.5 nm thick films, respectively. According to the Beer-Lambert law[176, p.479], transmis-

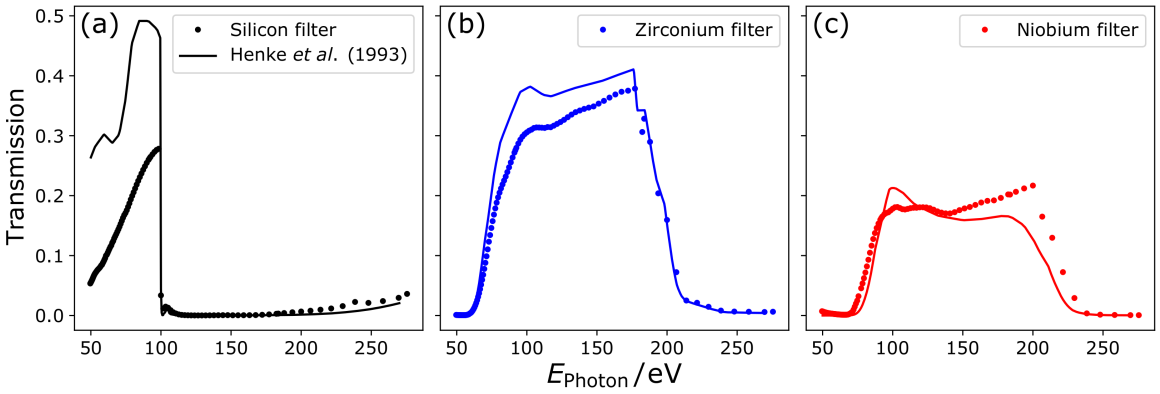


Figure B.3: Transmission of 420 nm thick silicon, 297 nm thick zirconium and 385 nm thick niobium films; measured transmissions [243] (dots), and tabulated theoretical transmissions [242] (solid lines) are shown; the transmissions of the silicon and zirconium filters are measured for 221.9 nm and 287.5 nm thick films, respectively, and transmissions for thicker films are derived according to Equation (B.5).

sion I/I_0 of a material decreases exponentially with its thickness d and absorption coefficient γ,

$$T = \frac{I}{I_0} = e^{-\gamma d} \tag{B.4}$$

Thus, the transmission of a filter with thickness d_2 can be derived if the transmission is known for thickness d_1, according to

$$T(d_2) = e^{-|\log(T(d_1))| \cdot \frac{d_2}{d_1}} \tag{B.5}$$

Based on Equation (B.5) the available experimental transmissions of the silicon and zirconium filters are extrapolated to the thickness used in the current experiment, shown as dots in Figure B.3 (a), (b) and (c).

E_{Photon}/eV	T_{BL}	$T_{\text{Si 420 nm}}$	$T_{\text{Zr 297 nm}}$	$T_{\text{Nb 385 nm}}$
66.7	0.408	0.129	0.044	not used
70.1	0.451	0.146	0.084	not used
138.5	0.491	not used	0.343	0.170

Table B.1: Transmissions of the beamline and attenuation filters, for the three different photon energies used in this work.

Transmissions of the beamline and the filters used in this work are summarized in Table B.1. Using Equation (B.3) and shot-to-shot measurements of the FEL intensity, absolute photon numbers in the interaction region have been calculated for the different combinations of photon energies and attenuation filters, used in this work. The results are summarized in Figure 3.3 in Section 3.2 of the main text.